

**DEVELOPMENT OF MULTI-FUNCTIONAL
BLAST RESISTANT WATER FAÇADE SYSTEM**

Wang Yonghui

(B. Eng., Harbin University of Science and Technology;

M. Eng., Harbin Institute of Technology)

**A THESIS SUBMITTED
FOR THE DEGREE OF DOCTOR OF PHILOSOPHY**

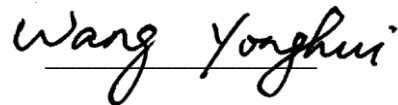
**DEPARTMENT OF CIVIL & ENVIRONMENTAL ENGINEERING
NATIONAL UNIVERSITY OF SINGAPORE**

2015

DECLARATION

I hereby declare that the thesis is my original work and it has been written by me in its entirety. I have duly acknowledged all the sources of information which have been used in the thesis.

This thesis has also not been submitted for any degree in any university previously.

A handwritten signature in black ink that reads "Wang Yonghui". The signature is written in a cursive style with a horizontal line underneath the text.

Wang Yonghui

5 Jan 2015

Acknowledgement

Firstly, I would express my sincerest appreciation and gratitude to my supervisor, Prof. Liew Jat Yuen, Richard for his support, supervision, encouragements, constructive advices and generous guidance on my research work during my PhD study.

The special thank also goes to Dr. Lee Siew Chin for her encouragement, support and invaluable advices for my research work.

I would like to thank Prof. Koh Chan Ghee and Assoc. Prof. Chua Kim Huat David for their precious judgments and comments on my research work.

My sincere appreciation is dedicated to Dr. Zheng Min, Dr. Wang Tongyun, Dr. Xiong Mingxiang, Dr. Ma Chenyin, Dr. Li Ya, Dr. Xiong Dexin, Dr. Yan Jiabao, Mr. Huang Zhenyu, Dr. Wang Yanbo, Dr. Wang Yu and Mr. Yang Yi for their continuous supports on research works and discussions.

My thanks also extend to all staff members at Concrete and Structural Engineering Laboratory. Special thanks go to Mr. Koh Yian Kheng, Mr. Ang Beng Oon and Mr. Ishak Bin A Rahman for their generous, patient and continuous help during the experiments. The kind assistance from Mr. Low Chee Wah of NUS Impact Mechanics Laboratory is deeply appreciated.

Financial support of graduate research scholarship from the National University of Singapore is gratefully appreciated. Sincere thanks are also extended to the Ministry of Home Affairs (MHA), Singapore for providing the research project grant through the Centre for Protective Technology (CPT) for this study.

I would thank all my friends and colleagues during my study in NUS. The special thank also goes to my friend Dr. Yan Shijun for his encouragement and help.

Last but not least, I would thank my wife (Ms. Zhan Tingting), my parents and my brother for their moral supports, continuous love, understanding and encouragements. Thank you for making this study possible and May God bless all of you.

Contents

Acknowledgement	i
Contents	iii
Summary	vii
List of Tables	x
List of Figures	xi
List of Symbols	xvii
Chapter 1 Introduction	1
1.1 Overview	1
1.2 Background	3
1.3 Objectives and Scopes	5
1.4 Outline of Thesis	6
Chapter 2 Literature Review	11
2.1 Introduction	11
2.2 Hybrid Solar Photovoltaic-Thermal System	11
2.3 Water Effects in Mitigating Blast Load	12
2.4 Blast Resistant Wall/Panel	14
2.4.1 Masonry wall/panel	15
2.4.2 Reinforced Concrete Wall/Panel	16
2.4.3 Steel Wall/Panel	18
2.4.4 Steel-Concrete Composite Wall/Panel	19
2.5 Blast Load and Test Method	20
2.5.1 Blast Load	20
2.5.2 Blast Load Generation Method	21
2.5.3 Lateral Pressure Load Generation Method	23
2.6 Analytical Method	23

Chapter 3 Energy Performance of Water Façade Systems	29
3.1 Introduction	29
3.2 Test Setup	29
3.2.1 Monitoring Station	29
3.2.2 Mock-ups	30
3.2.3 Automated Water Circulation System	31
3.2.4 Instrumentation and Remote Data Monitoring	32
3.3 Test Results and Discussion	33
3.3.1 Water Filled Tank VS Bare Wall	33
3.3.2 Water Filled Tank VS Water Filled Tank-Sandwich Panel	38
3.4 Summary	41
Chapter 4 Performance of Water Façade Systems under Lateral Pressure Load	57
4.1 Introduction	57
4.2 Material Properties	57
4.2.1 Steel	58
4.2.2 Cement Grout	58
4.3 Preparation of Specimens	60
4.4 Test Setup and Instrumentation	61
4.5 Discussion on Test Results	62
4.5.1 Load–Displacement Response and Failure Mode	62
4.5.2 Load–Strain Response	65
4.5.3 Deflection Shapes	67
4.5.4 Contact Area	68
4.6 Analysis of Specimens Subject to Lateral Pressure Load	69
4.6.1 Water Tank	69
4.6.2 SCS Sandwich Panels	71
4.6.3 Comparison with Test Results	73
4.7 Finite Element Analysis of Specimens under Lateral Pressure Load 74	
4.7.1 Material Models	75
4.7.2 Element Type and Formulation	82
4.7.3 Contact and Loading Approach	82

4.7.4 Finite Element Model.....	84
4.7.5 Discussion on Finite Element Results.....	84
4.8 Summary	91
Chapter 5 Performance of Water Façade Systems under Dynamic Pressure Load	129
5.1 Introduction.....	129
5.2 Preparation of Specimens	129
5.3 Test Setup and Instrumentation	130
5.4 Discussion on Test Results.....	131
5.4.1 Deformation Modes.....	132
5.4.2 Impact Force and Air Pressure	134
5.4.3 Displacement Response.....	135
5.4.4 Strain Response	137
5.5 Analysis of Specimens under Dynamic Pressure Load.....	139
5.5.1 SDOF System Establishment.....	139
5.5.2 Parameters Calculation	140
5.5.3 Comparison with Test Results.....	142
5.6 Finite Element Analysis of Specimens under Dynamic Pressure Load	143
5.6.1 Material Models	143
5.6.2 Element Type and Formulation	145
5.6.3 Contact and Loading Approach.....	145
5.6.4 Finite Element Model.....	147
5.6.5 Discussion on Finite Element Results.....	147
5.7 Summary	151
Chapter 6 Analytical Methods for Predicting Deformation of Water Façade Systems under Blast Loading	174
6.1 Introduction.....	174
6.2 Analytical Method for Water Filled Tank.....	175
6.2.1 SDOF System	175
6.2.2 Free Vibration Analysis	181

6.2.3 Shock Spectrum	182
6.2.4 Generation of P–I Diagram.....	185
6.2.5 Lagrange Equation Method.....	186
6.3 Analytical Method for Water Filled Tank-Sandwich Panel.....	191
6.3.1 SDOF System.....	191
6.3.2 Lagrange Equation Method.....	203
6.3.3 Comparison with Finite Element Results	204
6.4 Design implications	205
6.5 Summary	207
Chapter 7 Conclusions and Recommendations	217
7.1 Review on Completed Research Work	217
7.2 Conclusions	219
7.3 Recommendations for Future Studies	223
References.....	225
Appendix A: Figures of Mock-ups for Monitoring Test.....	235
Appendix B: Contact Area Approximation	237
Publications	239

Summary

The objective of the current study is to develop a multi-functional water façade system that can be used to harness the solar energy, reduce solar heat penetration into building and at the same time acts as a protective envelope against blast. Since the probability of blast threat on buildings is usually low, it is of significance advantage to carry out the investigation on the multi-functional water façade system in order to maximize the benefits of adopting a blast-mitigating design while improving the building performance in terms of energy usage. The proposed multi-functional water façade system is an innovative design, it is also the objective of this research to evaluate its energy saving and blast resistant performance.

The stainless steel water tank infilled with water, which is named Steel-Water-Steel (SWS), was proposed as one type of water façade system and can be installed at the outer skin of the building to achieve energy saving and to resist blast load. Since the blast resistance of stainless steel water tank is low, the Steel-Concrete-Steel (SCS) sandwich panel, which was proven with high blast resistant capacity, was attached at the rear of the stainless steel water tank to form another type of water façade system which is named SWS-SCS.

To assess the energy saving performance of the water façade systems, field monitoring studies on the SWS and SWS-SCS mock-ups were conducted. The energy performance of the proposed water façade systems was evaluated in two aspects, i.e. thermal efficiency and space cooling load. The thermal efficiency gauges the

efficiency of water façade system in storing the solar energy as warm water and the space cooling load gauges the solar energy that penetrates into room. The field monitoring results showed that the SWS-SCS panel performed better than the SWS panel which in turn performed better than the control bare brick wall that directly exposed to solar radiation. This field test confirmed the energy saving function of the proposed water façade systems.

The structural response of water façade systems under lateral pressure load was experimentally, numerically and analytically studied and the resistance-deflection functions, deflection shapes and failure modes were obtained, which are necessary for conducting the simplified analysis on the water façade systems under dynamic pressure loading. The inflated high pressure airbag was used to apply the lateral pressure load in the experimental study. Due to the limitation of airbag lifting capacity, the SWS-SCS configuration was divided into SWS and SCS which were tested separately. Finite Element analyses were then conducted to investigate the effect of water on the static response of SWS tank and the load transfer mechanism between face plate and concrete core of SCS panel.

Dropping weight on inflated high pressure airbag was adopted to generate the dynamic pressure loading. This test method is to simulate the dynamic blast load and can be easily conducted in the laboratory. The Single-Degree-of-Freedom (SDOF) method was adopted to predict the responses of the specimens under dynamic pressure loading. Due to the limitation of the adopted test method with load duration longer than that of direct blast test, the performance of water façade systems under

blast loading was investigated using Finite Element method.

An analytical method, based on energy principle, was adopted to predict the blast response of the pin-pin supported water façade systems. The accuracy of the method was validated with the established Finite Element models and the design implication of water façade systems was discussed.

List of Tables

Table 3.1 Categorized results for October 2013	43
Table 3.2 Properties of materials (Welty <i>et al.</i> , 2001)	43
Table 3.3 Thermal efficiency of SWS mock-up	44
Table 3.4 Space cooling load	45
Table 3.5 Categorized results for June 2014.....	46
Table 3.6 Thermal efficiency of SWS and SWS-SCS mock-up.....	47
Table 3.7 Space cooling load of SWS and SWS-SCS mock-up.....	48
Table 4.1 Material properties of stainless steel and mild steel	94
Table 4.2 Material properties of cement grout.....	94
Table 4.3 Details of static test specimens	94
Table 4.4 Lateral pressure test results.....	94
Table 4.5 Comparisons between experimental and analytical results	94
Table 5.1 Summary of impact test results.....	154
Table 5.2 Midpoint displacement of SAS and SWS tanks (mm).....	154
Table 5.3 Midpoint displacement of SCS50 and SCS75 sandwich panels (mm)	154
Table 5.4 Comparison of maximum displacements between test and SDOF (mm)	154
Table 6.1 Maximum displacement comparison	209
Table 6.2 Minimum plate thickness of façade systems under blast load.....	209

List of Figures

Fig. 1.1 The proposed water façade systems.....	9
Fig. 2.1 Posttest configuration for masonry walls: no bonding (left) and bonding (right) between wall and polymer coating (Davidson <i>et al.</i> , 2005).....	27
Fig. 2.2 Local buckling of the corrugation after blast test (Langdon and Schleyer, 2005a).....	27
Fig. 2.3 Typical pressure–time profile for blast wave in free air (Smith and Hetherington, 1994)	28
Fig. 2.4 Test setup for blast load simulation system (Mostaghel, 2003).....	28
Fig. 3.1 Photo of monitoring station	49
Fig. 3.2 Layout of the monitoring station	49
Fig. 3.3 Schematic diagram of circulating system: (a) SWS VS bare wall, (b) SWS VS SWS-SCS.....	50
Fig. 3.4 Temperature sensing points for roof (Each dot represents one temperature sensor probe)	51
Fig. 3.5 Temperature sensing points for walls (Each dot represents a pair of temperature sensor probes on the internal and external surfaces of the wall)	51
Fig. 3.6 Temperature sensing points for SWS and SWS-SCS mock-ups (Each dot represents one temperature sensor probe at the center)	52
Fig. 3.7 Wireless data relay from central control station to industrial computer	52
Fig. 3.8 HOBO weather station.....	53
Fig. 3.9 Temperature profiles of water inside the SWS tank in Oct 2013.....	53
Fig. 3.10 Temperature profiles of external west wall of Room A1 and A2 in Oct 2013.....	54
Fig. 3.11 Relationship between thermal efficiency and solar energy.....	54
Fig. 3.12 Temperature profiles on 2 October 2013	55
Fig. 3.13 Temperature profiles of water of SWS and SWS-SCS mock-ups in June 2014.....	55
Fig. 3.14 Temperature profiles of external west wall of Room A1 and A2 in June 2014.....	56

Fig. 3.15 Relationship between thermal efficiency and solar energy	56
Fig. 4.1 Specification for tensile coupon test (in mm)	95
Fig. 4.2 Stress–strain curves of (a) stainless steel (b) mild steel	96
Fig. 4.3 Coupons after tensile test: (a) stainless steel (b) mild steel.....	97
Fig. 4.4 Uniaxial compression test setup	97
Fig. 4.5 Uniaxial compression stress–strain curves of cement grout: (a) longitudinal direction (b) transverse direction.....	98
Fig. 4.6 Diagram of splitting test	98
Fig. 4.7 Notation for SAS and SWS tanks.....	99
Fig. 4.8 Notation for SCS sandwich panel	99
Fig. 4.9 Schematic of SAS and SWS tanks (in mm)	100
Fig. 4.10 Schematic of SCS sandwich panel (in mm)	101
Fig. 4.11 Static test setup	102
Fig. 4.12 Test control and data acquisition system	102
Fig. 4.13 Instrumentation layout (bottom view): (a) LVDTs on SAS and SWS (b) strain gauges on SAS and SWS (c) LVDTs on SCS50 and SCS75 (d) strain gauges on SCS50 and SCS75 (in mm)	103
Fig. 4.14 Load–midpoint displacement (LVDT D0) of SAS and SWS tanks under lateral pressure load	104
Fig. 4.15 Flexural failure of SAS tank.....	104
Fig. 4.16 Buckling on top plate of SAS tank.....	105
Fig. 4.17 Fracture of weld between bottom plate and stiffener of SWS tank....	105
Fig. 4.18 Load–midpoint displacement of SCS50 and SCS75 panels under lateral pressure load	106
Fig. 4.19 Deformation of SCS50: (a) before shear failure (b) after shear failure	106
Fig. 4.20 Load–midpoint displacement of re-tested SCS75 panel under line load	107
Fig. 4.21 Flexure failure of SCS75 panel under line load	107
Fig. 4.22 Load–strain curves of SAS: Strain distribution (a) along span direction (b) along width direction (c) at midpoint.....	108
Fig. 4.23 Load–strain curves of SWS: Strain distribution (a) along span direction	

(b) along width direction (c) at midpoint	109
Fig. 4.24 Load–strain curves of SCS50: Strain distribution (a) along span direction (b) along width direction (c) in side plate	110
Fig. 4.25 Load–strain curves of SCS75: Strain distribution (a) along span direction (b) along width direction (c) in side plate	111
Fig. 4.26 Deflection shape in span direction	112
Fig. 4.27 Deflection shapes in width direction	113
Fig. 4.28 Contact area–load curves	114
Fig. 4.29 Effective cross-section of SAS under bending (in mm)	114
Fig. 4.30 Deformation of SCS sandwich panel under lateral pressure load	115
Fig. 4.31 Compression zone along the concrete core.....	115
Fig. 4.32 Cross-section of SCS sandwich panel at mid-span.....	116
Fig. 4.33 Force distribution on each section	116
Fig. 4.34 Varying contact area in the FE model of SAS (quarter model)	117
Fig. 4.35 Applied loading curves in FE model.....	117
Fig. 4.36 FE model of (a) water tank and (b) SCS sandwich panel in lateral pressure test (quarter model).....	118
Fig. 4.37 Comparison of FE predicted load–midpoint displacement with test results: (a) SAS (b) SWS.....	119
Fig. 4.38 Deformation of SAS in the FE analysis (top surface): (a) Plastic hinge at mid-span (b) Buckling in the top surface (c) Deformation of stiffener..	120
Fig. 4.39 Comparison of face plate depth between SAS and SWS.....	121
Fig. 4.40 Variation of the resistance of SAS with moving stiffener.....	121
Fig. 4.41 Comparison of FE predicted load–midpoint displacement with test results: (a) SCS50 (b) SCS75	122
Fig. 4.42 Shear failure of SCS50	123
Fig. 4.43 Compression zone of the concrete core along span direction.....	123
Fig. 4.44 Axial stress distribution (Z-direction) in the bottom plate (quarter model)	124
Fig. 4.45 Axial stress distribution (Z-direction) in top plate (quarter model)....	124
Fig. 4.46 Installation of façade tanks to floor beam.....	125
Fig. 4.47 Load–displacement curves of SAS and SWS tanks.....	126

Fig. 4.48 Failure modes of SWS: (a) pin-roller supported (b) pin-pin supported	126
Fig. 4.49 Load–displacement curves of SCS sandwich panels	127
Fig. 4.50 Failure modes of SCS50: (a) pin-roller supported (b) pin-pin supported	127
Fig. 5.1 Drop-weight impact test machine.....	155
Fig. 5.2 Drop-weight impact test setup.....	155
Fig. 5.3 Overview of data acquisition system: (a) photo (b) schematic drawing	156
Fig. 5.4 Instrumentation layout: (a) LVDTs on SAS and SWS (b) strain gauges on SAS and SWS (c) LVDTs on SCS50 and SCS75 (d) strain gauges on SCS50 and SCS75 (in mm)	157
Fig. 5.5 Deformed shape of SAS tank: (a) after 1 st impact (b) after 2 nd impact	158
Fig. 5.6 Buckling on top surface of SAS tank after 2 nd impact	158
Fig. 5.7 Deformed shape of SWS: (a) after 1 st impact (b) after 2 nd impact.....	159
Fig. 5.8 Top surface of SWS after 2 nd impact.....	159
Fig. 5.9 Permanent deformation of SAS and SWS after 2 nd test	160
Fig. 5.10 Deformed shape of SCS50 panel after impact	160
Fig. 5.11 Deformed shape of SCS50 and SCS75 panels after impact.....	160
Fig. 5.12 Impact force–time history of (a) SAS (b) SWS (c) SCS sandwich panel	161
Fig. 5.13 Air pressure–time history of (a) SAS and (b) SWS tanks	162
Fig. 5.14 Air pressure and impact force–time history of SAS under first impact	162
Fig. 5.15 Air pressure–time history of SCS sandwich panel	163
Fig. 5.16 Air pressure and impact force–time history of SCS50 panel	163
Fig. 5.17 Displacement–time histories of SAS and SWS tanks	163
Fig. 5.18 Displacement–time and air pressure–time histories of SWS tank under first impact.....	164
Fig. 5.19 Comparison of maximum displacements of SAS and SWS tanks in the load–deflection curves	164
Fig. 5.20 Displacement–time histories of SCS50 and SCS75 sandwich panels	164

Fig. 5.21 Strain–time histories of SAS tank under first impact: (a) along span direction (b) along width direction.....	165
Fig. 5.22 Strain–time histories of SWS tank under first impact: (a) along span direction (b) along width direction.....	166
Fig. 5.23 Longitudinal strain–time history of SCS50 under impact	167
Fig. 5.24 Longitudinal strain–time history of SCS75 under impact	167
Fig. 5.25 Comparison of displacement–time histories between test and SDOF	168
Fig. 5.26 Strain rate effects of mortar under tension.....	168
Fig. 5.27 Relationship between pressure and relative volume for water	169
Fig. 5.28 Applied pressure–time history of SAS.....	169
Fig. 5.29 FE model of (a) SWS and (b) SCS sandwich panel in dynamic pressure test	170
Fig. 5.30 Comparison of FE predicted displacement–time histories with test...	171
Fig. 5.31 Internal energy of water and stainless steel in FE analysis.....	171
Fig. 5.32 Comparison of FE predicted displacement–time histories with test...	172
Fig. 5.33 Internal energy of steel and core material of SCS50	172
Fig. 5.34 Midpoint displacement–time histories of SAS and SWS	173
Fig. 5.35 Midpoint displacement–time histories of SCS sandwich panels	173
Fig. 6.1 Simplified half model for pin-pin supported SWS tank	210
Fig. 6.2 Details of membrane action	210
Fig. 6.3 Comparison of pressure–mid-span displacement response	210
Fig. 6.4 Comparison of deflection shape of SWS tank	211
Fig. 6.5 Numerical generated constant value κ	211
Fig. 6.6 Shock spectrum for SWS tank	211
Fig. 6.7 Dimensionless P–I diagram for SWS tank	212
Fig. 6.8 Comparison of dimensionless P–I diagram	212
Fig. 6.9 Comparison of maximum displacement	212
Fig. 6.10 Comparison of strain rate effect.....	213
Fig. 6.11 Simplified half model for pin-pin supported SWS-SCS panel	213
Fig. 6.12 Force distribution and neutral axis on the concrete core	214
Fig. 6.13 Deformation profile across the concrete core depth	214
Fig. 6.14 Comparison of pressure–mid-span displacement curves between	

analytical method and FE analysis	214
Fig. 6.15 Comparison of deflection shapes of SWS-SCS panel.....	215
Fig. 6.16 Configuration of infinitesimal element along span	215
Fig. 6.17 Flow chart for determining equation of motion	216

List of Symbols

η_{th}	Thermal efficiency
ε	Strain
$\dot{\varepsilon}$	Strain rate
$\dot{\varepsilon}_{eff}^p$	Effective plastic strain rate
$\dot{\varepsilon}_p$	Plastic strain rate
$\dot{\varepsilon}'_{ij}$	Deviatoric strain rate
ε_{wall}	The emission coefficient of wall
ε_y	Yield strain
α	Hardening coefficient of the elastic-plastic-hardening constitutive model
$\bar{\beta}$	Volumetric thermal expansion coefficient
ν	Kinematic viscosity
γ_f	Strain rate enhancement factor
γ_{M0}	Partial factor for structural steel
γ_0	Gruneisen gamma
σ	Stress
σ'_{ij}	Deviatoric (viscous) stress
$\Delta\sigma_y$	Initial yield deviatoric stress
$\Delta\sigma_m$	Maximum deviatoric stress
$\Delta\sigma_r$	Residual deviatoric stress
η	The distance between compressive layer and neutral axis
λ	Effective plastic strain parameter
ρ	Density
$\phi_1(x)$	Deflection shape function along x direction
$\phi_2(y)$	Deflection shape function along y direction

ϕ	Deflection shape function
$\bar{\mu}$	Dynamic viscosity
ϑ	Support rotation
θ	Angle
χ	Dimensionless displacement
χ_y	Dimensionless displacement at yield point
ω	Circular frequency
A	Area
A_y	Shear area
a	Bulk sound speed of water
a_{ij}	Parameters defining the failure surface in MAT_72R3
B	Width
C_i	Generalized displacement
$c_{p,w}$	Specific heat capacity of water
D	Strain rate parameters in Cowper-Symonds model
E	Young's modulus
$E_{cooling}$	Space cooling load
E_c	Elastic modulus of concrete
E_s	Solar energy
E_{ss}	Elastic modulus of steel plate
E_T	Internal energy per unit width by tension force
E_{T+B}	Total internal energy per unit width due to tension and bending
E_w	The energy stored in water
$F(t)$	Force
F_c	Compression force in concrete
F_e	Equivalent force
F_{end}	Compression force given by end plate
f_c	Cylinder compressive strength of concrete

f_y	Yield stress
G_f	Fracture energy
Gr	Grashof number
h	Element size
h_a	The convection coefficient of air
h_c	Concrete core depth
I	Impulse
\bar{I}	Dimensionless impulse
I_0	Pressure asymptote
K	Kinetic energy
K_c	Curvature
K_e	Equivalent curvature
K_L	Load factor
K_{LM}	Load mass factor
k_a	Conductivity of air
k_{ep}	Equivalent plastic stiffness
k_s	Stiffness
L_e	The length of compression zone
ΔL_s	Elongation of steel plate
M	Moment capacity
M_e	Equivalent mass
m	Mass
m_a	Mass per unit area
m_w	The total mass of water inside the water tank
m_{xi}	Mass per unit length in x direction
m_{yi}	Mass per unit length in y direction
Nu	Nussel number
P	Pressure

\bar{P}	Dimensionless pressure
P_{e0}	Pressure asymptote
P_{em}	Initial maximum pressure \times span
P_r	Reflected pressure
Pr	Prandtl number
Q_s	The intensity of solar radiation
q	Strain rate parameters in Cowper-Symonds model
R	Resistance
R_c	Resistance contributed by concrete core
R_e	Equivalent resistance
$r(z)$	Pressure-deflection function
S_{ij}	Stress deviatoric tensor
T	Free vibration period
\bar{T}	Tension force per unit width
t'	The distance to neutral axis
T_c	The effective compression depth of concrete core
T_{iww}	Internal west wall temperature
T_{room}	Room temperature
t	Time
t_c	Top plate thickness of SCS panel
t_d	Load duration
t_n	Neutral axis
t_r	Bottom plate thickness of SCS panel
U	Strain energy
U_D	Strain energy considering strain rate effect
u	Internal energy of concrete core per unit area
V	Potential energy
\tilde{V}	Volume of top/bottom steel plate

V_C	The tensor viscosity coefficient
V_c	Shear resistance of concrete core
$V_{pl,Rd}$	Design value of the plastic resistance to vertical shear
V_{rd}	Shear resistance of SCS panel
V_{sp}	Shear resistance of side plates
v_0	Initial velocity
W_y	Elastic section modulus
x_{max}	Maximum displacement
\ddot{y}	Acceleration
y_m	Mid-span displacement
$y_{m,m}$	A value of mid-span displacement
$y_{m,max}$	Maximum mid-span displacement
$y_{m,n}$	The minimum of $y_{m,max}$ and $y_{m,m}$

Chapter 1 Introduction

1.1 Overview

The façade of a building plays an important role as a protective envelope that shields its occupants from natural elements and in some cases, the more extreme threats such as accidental blast attack. Recently, the energy saving façade is increasingly used to improve the energy efficiency of a building. To combine the blast resistance and energy saving function into one façade system, a novel multi-functional façade system was developed in this study.

In hot climate region like Singapore, a fair amount of solar radiation is transmitted through the external walls or facades of buildings throughout the day. The solar thermal energy can cause the surface temperature of the wall/façade to rise to 20 °C above the ambient temperature, leading to high energy consumption for space cooling with air-conditioning. To minimize the solar thermal loading, façade systems made of double-glazed glass, low-emissivity glass and aluminum claddings, to name a few, are often specified for a building project. Although these systems are aesthetically pleasing, they are costly and do not utilize the abundant solar energy effectively. On the other hand, the Building Integrated Photovoltaic (BIPV) façade system has been used to harness the solar energy but it is a more complex and costly option. In view of cost and efficiency, water is an ideal insulation medium for harnessing the solar energy due to its high specific heat capacity. This motivated the development of

stainless steel water storage tank to provide an economical and efficient solution for buildings to reduce solar heat penetration and store the solar energy for daily usages. In addition to the savings on the building operational cost, the reduction in electricity consumption due to lower 'heat gain' and the use of solar energy for providing a source of warm water will also reduce fuel burning and hence lessen the greenhouse gas emissions from power generation plants.

The use of water to mitigate blast energy has been quite extensively studied through experimental and numerical methods (Keenan and Wager, 1992; Shin *et al.*, 1998; Chong *et al.*, 1999) and significant reduction of peak pressure and impulse was observed especially when the water was stored close to the explosive. The underlying principle of water in mitigating blast loading is that the high pressure shock wave produced by detonation aerosolizes the water placed close to the explosive and causes both a phase change of water and the redistribution of internal and kinetic energy over the detonation gases, blast wave and barrier material (Chen *et al.*, 2005). These studies were based on the scenario that water was directly exposed to blast wave. For confined water in a tank, such as the water storage façade, little research has been done in this field and studies are therefore required to understand the effect of confined water on the response of water storage façade.

Since the probability of a blast threat is usually low, the water storage façade system was developed and investigated in this study to achieve both energy saving and blast resistance function in order to maximize the benefits of adopting blast-mitigating design besides improving the building performance.

1.2 Background

Solar collectors have been used for decades to harness solar energy and provide heating source. An active system typically consists of a glazed thermal collector that absorbs heat using liquid storage medium which is then circulated to a heat tank for storage during daytime. At night, the stored heat in the liquid is redistributed for heating. However, the passive system, which does not require power supply, has a thermal storage mass, such as water and sand to store the thermal energy (Baer and Mingenbach, 2002; Maloney, 1981; Lee *et al.*, 2005). The advantage of using water as thermal storage mass is that it is economical and easy to operation. Besides this, the specific heat capacity of water is higher than sand, which makes water store more solar energy per unit temperature difference as compared to sand. Another advantage of using water as thermal storage mass is that it has high potential for reducing blast loading (Keenan and Wager, 1992; Shin *et al.*, 1998; Chong *et al.*, 1999). Hence, water appears to be an ideal choice to achieve both energy saving and blast resistance function.

Thinner and lighter blast resistant façade/wall systems such as the unitized wall, stick wall and metal stud wall systems (Swartz *et al.*, 2009; Hallissy *et al.*, 2005) have been wider application in recent years in favors of space-saving, easier installation and handling as well as aesthetic appeal. Some of these systems have been tested and were shown to survived low blast pressure. Heavier and stiffer system constructed using ductile poured-in-place reinforced concrete (RC), such as the perimeter blast-resistant wall (Nanayakkara, 2004), will provide higher level of protection against blast loading but not easy to be installed as the façade system.

RC panel is commonly used in structure and its performance against blast loading has been studied by experimental (Silva and Lu, 2009) and numerical methods (Zhou *et al.*, 2008). Based on the test and numerical studies, some simplified methods to predict the response of RC panel subjected to blast loading were proposed (Natio and Wheaton, 2006; Silva and Lu, 2009). Since concrete is brittle under tension, the fractured flying debris would pose serious risk to the occupants and building itself. Fibers were therefore added to increase the ductility of concrete under tension. The experimental and numerical studies showed that fiber-reinforced concrete (FRC) performed better under blast loading as compared to conventional RC structures (Foglar and Kovar, 2013). Other than this, it has been shown that the maximum deformation of concrete panel retrofitted with steel plate could be reduced as compared to the non-retrofitted concrete panel and the scabbing can be prevented by retrofitted steel plates (Yun *et al.*, 2013). Steel concrete composite structures like the retrofitted concrete panel have been adopted as the protective layer against accidental load, such as impact and blast threat. Experimental and numerical studies showed that the Steel-Concrete-Steel (SCS) sandwich panels displayed good performance against blast loading (Lan *et al.*, 2005; Liew and Wang, 2011). The SCS sandwich panel, which is prior to other panels in terms of blast resistance and spalling protection, would be an ideal choice as a blast resistance layer that can be attached to the water storage façade to improve its blast resistance capacity. Hence, the lighter and thinner Steel-Water-Steel (SWS) water storage façade would be ideal for protection against low level blast and Steel-Water-Steel-Steel-Concrete-Steel (SWS-SCS) with the additional composite layer as shown in Fig. 1.1 could be adopted to resist high level blast. In terms of energy saving performance, the SWS-SCS with additional SCS layer

may perform better than the SWS in maintaining the thermal heat in the water and providing extra insulation to reduce the solar penetration into rooms.

To date, study on such multi-functional blast-resistant façade system with energy saving function has not been found in public references. Hence, this study is undertaken to develop the multi-functional façade system and evaluate its energy saving and blast resistance performance to facilitate the application of such façade system in actual project.

1.3 Objectives and Scopes

The objective of this study was to develop a novel multi-functional water façade system and evaluate its energy saving and blast resistance performance. To achieve the main objective, the specific objectives are outlined as follow:

1. Design a water storage façade system that is effective in harnessing the solar energy and resisting blast loading.
2. Determine the energy savings by using the water storage façade to harness the solar energy in the form of warm water for usage and reduce solar heat penetration into building.
3. Evaluate the performance of water storage façade under static, dynamic and blast pressure loading.
4. Develop analytical methods for predicting the response of water storage façade under blast loading in order to facilitate the blast resistant design of the system.

To achieve the aforementioned objectives, the scope of this study area is as follow:

1. Conduct literature reviews and patent search to examine existing technologies on blast resistant façade/wall and solar energy harvesting façade system to address the design for the multi-functional water façade system.
2. Conduct field monitoring on the mock-ups of the proposed water storage façade system. The mock-ups will be mounted onto actual building with west facing brick wall. Through the field monitoring study, the energy saving performance of the proposed systems in terms of warm water collection and space cooling load reduction will be evaluated.
3. Conduct lateral pressure test on SWS tank and add-on SCS blast resistant panel. The resistance–deflection and deflection shape function obtained from the test will be applied to establish the simplified blast analysis method.
4. Conduct drop-weight impact test on SWS tank and SCS panel to study their responses under dynamic pressure loading.
5. Establish and verify the FE models of SWS tank and SCS panel against test results and to apply the models for further study on SWS tank and SCS panel under blast loading.
6. Carry out theoretical analysis on the water storage façade and develop analytical methods to evaluate the blast response of the proposed system.

1.4 Outline of Thesis

In chapter 1, the motivation behind the development of the multi-functional blast resistant water façade system is explained and the concept of the water storage façade is presented. The need for research is then identified, based on which the main objectives and scope of the study are outlined.

Chapter 2 provides a comprehensive review on existing energy saving façade systems and blast resistant façades or walls that have been reported in the literature. Besides this, research findings on the water effects in mitigating blast loading are presented, followed by description on the utilization of analytical methods for predicting the blast response of structures.

Chapter 3 describes the field monitoring on the mock-ups of the proposed water storage façade system. Based on the monitoring results, its energy saving performance is reported in terms of thermal efficiency and space cooling load.

In chapter 4, the performance of the water façade system under lateral pressure load was investigated through experimental, analytical and numerical study. Analysis and discussion on the experimental results are presented, followed by verification of the FE models against the test data. The verified models were applied to further study the behavior of the water storage façade under lateral pressure load.

The performance of the water façade system under dynamic pressure loading is discussed in chapter 5. Both experimental and numerical results are presented and the experimentally-verified FE models were applied to study the response of the façade under blast pressure loading.

Analytical methods to predict the blast response of the water storage façade are presented in chapter 6. These include the Single-Degree-of-Freedom (SDOF) method, Lagrange Equation method and Pressure–Impulse diagram method. The validation of

the analytical methods was conducted by comparing with the FE simulations.

Chapter 7 completes the thesis with a set of conclusions derived from present experimental, numerical and analytical investigations. Lastly, recommendations are proposed for further studies.

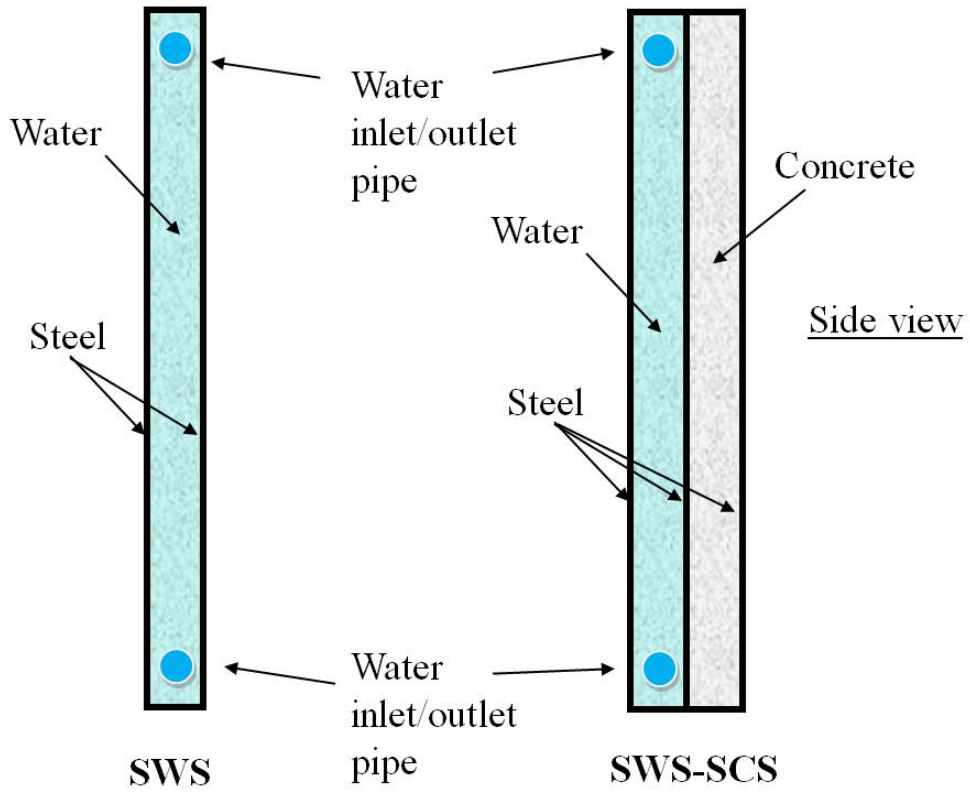


Fig. 1.1 The proposed water façade systems

Chapter 2 Literature Review

2.1 Introduction

The proposed multi-functional water façade system is a novel design concept that has yet to be fully developed. The concept stemmed from the use of the thermal and blast mitigation properties of water to harness solar energy and reduce blast response. The use of water as a heat storage medium in hybrid solar photovoltaic-thermal (PVT) system to harness the solar energy is first reviewed. Research findings on the effects of water in mitigating blast loading were examined, followed by the reviews on the blast performance of blast resistant walls/panels. The characteristics of blast loading and the methods used to simulate blast loading and lateral pressure loading are also reviewed in order to find the suitable experimental method. Finally, existing analytical methods to predict the responses of structural members against blast loading are discussed.

2.2 Hybrid Solar Photovoltaic-Thermal System

The façade-integrated photovoltaic/water-heating system developed by Chow *et al.* (2007) is a hybrid solar technology that integrates the PV and solar thermal components in one single system. The hybrid solar PVT system utilized water to cool down the PVT components that exposed directly to solar radiation and store the solar thermal energy. Since a part of solar radiation fallen on the building façade is directly

converted to useful thermal and electric power, the portion of solar energy penetrated into the building is reduced. Hence, the hybrid solar PVT system can store the solar energy as electric and thermal energy and also reduce the space cooling load. The thermal efficiency at zero reduced temperature and the cell conversion efficiency of the tested hybrid solar PVT system in Hong Kong were 38.9% and 8.56%, respectively. The thermal efficiency at zero reduced temperature is the optical efficiency of the collector and can be obtained by multiplying transmission coefficient τ_t with absorbed factor α_t (Eicker, 2003). In addition, the space cooling load, which is the heat gains from the environment, could be reduced by 50% in peak summer of Hong Kong where temperature can reach 35.4 °C. The natural circulation of water by means of thermosyphon principle and forced circulation of water using pump were compared in the experimental study, which showed that the collector performance of natural circulation could be as good as forced circulation (Chow *et al.*, 2007). An explicit dynamic thermal model of the hybrid solar PVT system was also developed by Chow *et al.* (2008) to evaluate the annual performance of building-integrated photovoltaic/water-heating system (Chow *et al.*, 2009). It was found that the year-round thermal and cell conversion efficiencies were 37.5% and 9.39%, respectively, under typical Hong Kong weather conditions and the space cooling load could be reduced by 38%.

2.3 Water Effects in Mitigating Blast Load

The erection of a water wall around an explosive has been found to be an effective method of mitigating the shock wave and blast pressure of an explosion (Cheng *et al.*, 2005). The encouraging earlier findings and low cost of water have motivated the

research on its blast mitigation effects. To date, a number of experiments have been carried out (Keenan and Wager, 1992; Vretblad and Eriksson, 1994; Joachime and Lunderman, 1997; Chabin and Pitiot, 1998; Absil *et al.*, 2000) and it was demonstrated that the peak pressure and impulse were reduced significantly when the water was stored close to the explosive. This could be attributed to the significant amount of energy loss from the shock to break up the water into small droplets, which in turn, enhances the process of phase change from liquid to gas state (Cheng *et al.*, 2005). The effects of water wall on blast wave mitigation were studied in scale model tests by Chabin *et al.* (1998). The influence of different parameters such as the thickness of the wall and the distance between the explosive charge and the water barricade was calculated. Nomographs were used to give overpressure as a function of wall thickness, charge-to-wall distance and charge-to-location distance. Besides, several small-scale tests showed that water (contained in plastic bags or containers) placed in the proximity of explosives stored in a confined space could reduce the internal gas pressure and impulse from a detonation by up to 90% (Malvar and Tancreto, 1998).

Besides the experimental investigations, numerical studies on the mitigation effects of water have been conducted as well. Shin *et al.* (1998) modeled the mitigation effects of water shield around the explosive on shock waves. It was found that the magnitude of peak pressure generally decreased and the shock arrival time increased with increasing thickness of water shield for the case that the water shield was in contact with explosive. A series of studies using the AUTODYN software was conducted by Birnbaum *et al.* (1998) to simulate three small-scale feasibility tests of explosions inside a rigid chamber. A user subroutine was used to account for heat transfer effects

that are not represented in the standard version of the program. It was shown that the model with heat transfer effects between explosive products and water/vapor was better than that without it. Cheng *et al.* (2005) utilized a multi-material Eulerian finite element technique to study the influence of the design parameter, such as the water-to-explosive weight ratio, the water wall thickness, the air-gap and the cover area ratio of water on the effectiveness of the water mitigation concept. It was shown that the higher the water-to-explosive weight ratio, the more significant was the reduction in peak pressure of the explosion. Typically, water-to-explosive weight ratios in the range of 1-3 were found to be most effective (Cheng *et al.*, 2005).

Since the aforementioned researches on blast wave mitigation effects by water were based on the scenario that the water was exposed to blast wave before and during the event of the explosion, different mechanism would be expected from the confined water in the proposed water storage façade in the current study. Hence, experimental and numerical studies were carried out to determine the effects of water on the response of water storage façade under static, dynamic and blast pressure loading.

2.4 Blast Resistant Wall/Panel

In the event of blast attack, the wall/panel tends to sustain higher blast loading due to its larger exposed area as compared with column and beam. Therefore, the blast performance, failure mechanism and retrofitting of wall/panel is an important research area on the blast resistance of structures. To date, numerous experimental, numerical and analytical studies have been carried out to investigate the blast response of different kinds of walls/panels, including masonry, reinforced concrete, steel and

composite walls/panels.

2.4.1 Masonry wall/panel

Masonry or brick is commonly used for building walls due to its easy construction and low cost. However, unreinforced masonry is very brittle and prone to become debris hazard to the building occupants in the event of blast. The debris hazard of masonry wall caused by blast load has been studied (Wang *et al.*, 2009; Baylot *et al.*, 2005) and retrofitting techniques were developed to mitigate the debris hazard (Baylot *et al.*, 2005). Wang *et al.* (2009) adopted the numerical method to study the probabilistic fragment size distribution and launch distance. The analysis results indicated that the masonry fragments approximately followed the Weibull distribution, which was consistent with the empirical fragment distribution. A series of physical experiments were conducted by Baylot *et al.* (2005) to develop methods for predicting the hazard levels associated with concrete masonry units (CMU) walls. The CMU is commonly known as concrete blocks. The experiments included nonretrofitted CMU walls and three types of retrofits, including fiber reinforced polymer (FRP), sprayed-on polyurea and hot-dipped galvanized A-36 steel. It was found that the debris velocity was directly related to the applied impulse and the retrofit techniques were successful at reducing the hazard level.

The performances of unreinforced masonry walls under blast loading were studied by Wei and Stewart (2010) using numerical method. A new model for strain rate effects and a new dynamic plastic damage model were used for brick and mortar in their numerical model. It was found that the boundary condition and wall thickness significantly affected the blast responses of unreinforced masonry walls, while the

effect of material strength was relatively small. For reinforced masonry walls, the reinforcements commonly used include reinforcing steel bars, FRP and elastomeric polymer. According to the experimental study by Mayrhofer (2002), the dynamic force enhancement of reinforced masonry wall by reinforcing steel bars increased by a factor of four in comparison with unreinforced masonry wall. Tan and Patoary (2009) proposed an approximate analysis method to determine the blast resistance of FRP-strengthened masonry walls, based on which, 18 full-scale masonry walls reinforced with three different FRP systems were designed and subjected to field explosions. No visible crack or debonding was observed due to the low blast pressure load. A full-scale blast test was carried out by Urgessa *et al.* (2010) on eight masonry walls reinforced with two and four layers of carbon fibers and two types of polymer matrices. Based on the test results and analysis, a retrofit design procedure was proposed to design the amount of retrofits for masonry walls retrofitted with FRPs. More recently, the focus has shifted from applying stiff fiber-reinforced composites to using lower-strength higher-elongation elastomeric polymers that can be easily applied to the interior masonry wall. The spray-on polymer approach could overcome the problems of stiff composites, such as high material costs, challenges in bonding the material to the wall and difficulties in anchoring the material to the host structures (Davidson *et al.*, 2005). Fig. 2.1 shows the bonding effects of polymer coating on the blast resistance of masonry wall and the improvement of blast resistance with bonding could be observed.

2.4.2 Reinforced Concrete Wall/Panel

Extensive analytical, numerical and experimental studies have also been conducted to investigate the performance of the widely used reinforced concrete (RC) wall/panel.

Since concrete is also a brittle material, the same debris hazard as masonry wall is likely to occur under blast loading. The design guide has provided the charts to predict the spalling of concrete (UFC, 2008). Besides this, spalling criteria for different levels of spalling can also be determined using numerical method (Xu and Lu, 2006).

The blast resistance of RC structures can be improved by adopting ultrahigh-strength concrete (UHSC) as shown in the experimental investigation by Ngo *et al.* (2007), where UHSC panel suffered less damage as compared to normal strength concrete (NSC) panel. However, the UHSC is normally more brittle than NSC, which limits its energy absorbing capacity. The use of fibers were effective in improve the ductility of concrete and energy absorbing capacity. For examples, the superior performance of ultra-high performance fiber reinforced concrete (UHPFRC) against blast loading was also demonstrated through numerical analysis by Mao *et al.* (2014). The UHPFRC is a concrete material with both high strength concrete and fiber reinforcement. It was concluded that steel fibers and reinforcing bar were of similar effect in increasing the resistance of UHPFRC panel under far field blast loading, while the significant improvement was observed under near field blast loading. Long carbon fibers added to RC panels were also shown to improve the blast spalling resistance of concrete (Tabatabaei *et al.*, 2013). The deflection of RC panel could also be reduced by increasing the panel thickness and the ratio of reinforcing bar as evident from the numerical investigation by Lin *et al.* (2014). The efficiency of FRP strengthening schemes for improving the performance of RC panel against single and multiple blast loads has been demonstrated by Wu *et al.* (2009) and Tanapornraweekit *et al.* (2011), respectively. The FRP-strengthen RC panels could survive multiple explosions and brittle shear failure with FRP debonding was observed after the explosion

(Tanapornraweekit *et al.*, 2011).

The SDOF method is a simple method that is usually adopted to predict the response of RC panel under blast loading (UFC, 2008). The SDOF combined with the displacement based design (DBD) method was presented by Silva and Lu (2009) to assess the blast response of RC panel. Comparison with experimental results demonstrated that this method was suitable for the cases where punching shear failure was not the governing failure mode. This was likely because the punching shear failure mode was not considered in the SDOF model. Naito and Wheaton (2006) presented a method that combined basic section analysis, SDOF modeling and a static FE pushover analysis to calculate the blast resistance of an existing RC shear wall. Pressure–Impulse curves were also developed to quantify the blast resistance of the wall.

2.4.3 Steel Wall/Panel

As opposed to concrete and masonry, steel has higher ductility and strength to resist blast loading. However, due to the higher cost, steel structural elements tend to be slender and less massive than concrete structures. Therefore, global and local buckling is more likely to occur in steel structures under blast loading. To improve the stiffness of steel panel, corrugated and profiled sections are normally adopted. The profiled stainless steel panels under blast loading were investigated experimentally by Langdon and Schleyer (2005a). It was found that the connection detail could significantly influence the response of the panel under blast loading. Besides this, large permanent plastic deformations were sustained by the panels without rupture, and localized buckling developed at the center of the corrugations as shown in Fig.

2.2 (Langdon and Schleyer, 2005a). An analytical approach based on Lagrange Equation method was proposed to assess the response of profiled panel against blast loading. The modeling approaches predicted less deformation of profiled panel as compared to current design guidance due to the inclusion of supports and membrane action (Langdon and Schleyer, 2005b). To improve the blast resistance of profiled blast panels, an innovative passive barrier system was developed by Boh *et al.* (2005) to delay the tearing of the horizontal welds at the connections. The effects of strain rates on the response of the stainless steel firewall under hydrocarbon explosion were also investigated by Boh *et al.* (2004). It was found that the enhancement due to strain rates on the deflection of the panel were effective before weld failure, after which the enhancement effects might be governed by failure criteria.

2.4.4 Steel-Concrete Composite Wall/Panel

The steel-concrete composite panels have higher ductility than concrete panels and higher buckling resistance than steel panels and therefore are commonly adopted as blast resistant panels. The Steel-Concrete-Steel (SCS) sandwich panel that consists of a concrete core sandwiched in between two steel faceplates is a favorable type of steel-concrete composite elements for blast resistance due to its high energy absorbing capacity and spalling protection. The composite action of SCS sandwich structure is achieved by using shear connectors to bond the two face plates to the concrete core. Therefore, several types of shear connectors were developed, including headed shear studs (Odeyemi and Wright, 1989), angle shear connectors (Malek *et al.*, 1993), Bi-steel (Foundoukos, 2005) and interlocked J-hook connectors (Liew *et al.*, 2008). Although a number of researches have been conducted to study the performance SCS sandwich panels under static loading, there are very limited work on their blast

performance (Kang, 2012; Liew and Wang, 2011; Lan *et al.*, 2005). Kang (2012) carried out the field blast test on the SCS sandwich panels with and without shear connectors. It was found that the SCS sandwich panel without shear connectors could perform as well as those with shear connectors, including headed studs and J-hook connectors. In view of easy fabrication and low cost, the SCS sandwich panel without shear connectors would be an ideal choice as the add-on layer to improve the blast resistance of water storage façade system.

2.5 Blast Load and Test Method

2.5.1 Blast Load

A blast is characterized by a rapid expansion of gases generating a pressure wave propagating from the source of the explosion (Smith *et al.*, 2009). The effects of a blast are in the form of a shock wave composed of a high-intensity shock front which expands outward from the surface of the explosive into the surrounding air. As the wave expands, it decays in strength, lengthens in duration, and decreases in velocity (UFC, 2008). The shape of the blast wave depends on the nature of the energy release. When the explosive is located on or near to the ground, the blast is considered to be a surface burst. The incident blast wave is reflected and amplified by the ground and the reflected wave then merges with the incident wave to form a hemispherical blast wave. When the explosive is far from any reflecting surface, the blast is considered to be an air burst and is a spherical blast wave (Smith and Hetherington, 1994).

The typical pressure–time profile for blast wave in free air is shown in Fig. 2.3, which includes positive and negative phase. In the positive phase, the incident pressure P_s

decays to the ambient pressure P_o within the time duration t_d known as positive phase duration. For the following negative phase, the peak negative pressure is typically small as compared to the peak pressure in positive phase. Hence, the negative phase is usually ignored in the blast resistant design (UFC, 2008; ASCE, 2010; ASCE 2011). The positive phase of surface blast can be described by the modified Friedlander Equation (Baker, 1973) as

$$P(t) = P_r \left(1 - \frac{t}{t_d} \right) \exp \left(-\frac{\bar{\theta} t}{t_d} \right) \quad (2.1)$$

where $\bar{\theta}$ is the coefficient that describes the rate of decay of the pressure–time curve. Parameters P_r , t_d and $\bar{\theta}$ can be obtained using blast loading predictive tool ConWep (Hyde, 1991) by given TNT charge and standoff distance. Herein the reflected pressure P_r is used, since the blast wave is reflected and magnified with higher reflected pressure when it impinges onto the face of a target. In the blast resistant design, the pressure–time profile in positive phase can be further simplified as a bi-linear or triangular shape (UFC, 2008; ASCE, 2011), which was adopted in the theoretical study.

2.5.2 Blast Load Generation Method

Field explosive detonation is a direct method to generate the blast loading (Liew and Wang, 2011; Lan *et al.*, Clubley 2014; Forglar and Kovar, 2013; Arora *et al.*, 2011; Tabatabaei *et al.*, 2013). This method can be used to test several specimens simultaneously and is able to replicate the actual condition of the detonation of high explosives (Remennikov *et al.*, 2009). However, field blast test is generally expensive and requires remote and often very large testing site. Besides, the test data may be easy to lose due to the damage of transducers, cables or data acquisition equipment.

Therefore, other methods such as shock tube and non-explosive test method have been devised to simulate the high pressure and short duration of a blast loading. In the shock tube test method, which is less expensive than field blast test, the generated impulse loading can be well controlled. However, the specimen size is limited by the size of the shock tube and the load duration is relatively longer compared with field blast test (Schleyer *et al.*, 2007; Lacroix *et al.*, 2014). In the laboratory test by Whisler and Kim (2014), a non-explosive test method was developed to generate dynamic blast-type pressure pulse loading. However, only the impulse could be recorded and not the pressure–time history, which is necessary for analyzing the response of specimen in the dynamic and quasi-static response regimes. Another simple blast load simulation system that comprises of a test panel and a membrane mounted within a frame system as shown in Fig. 2.4 was proposed by Mostaghel (Mostaghel, 2003). The membrane combined with the panel forms an airtight chamber, which is inflated with air before testing. The plate is dropped onto the membrane at various heights to achieve the required impulse magnitude and duration. Even though the load duration is longer than those obtained directly from field blast detonation, this method is simple and can be easily conducted in the laboratory and was adopted by some researchers to generate blast-type pressure loading (Remennikov *et al.*, 2009; Chen and Hao, 2014). Remennikov *et al.* (2009) adapted this method with an inflated airbag acting as the airtight chamber to test columns under impulse loading. The similar method was also adapted by Chen and Hao (2014) to investigate the response of multi-arch double-layered panel under impulse loading. As the use of airbag to generate pressure loading with short duration in the laboratory appeared to be an easy and economical way, this method was adopted in the present study to generate dynamic pressure loading to assess the response of water storage façade system.

2.5.3 Lateral Pressure Load Generation Method

To apply lateral pressure load on panel specimens, Malo (2001) developed an experimental device that used water as the pressure medium. Although this method can be used to apply uniform pressure load on specimens, the test operation is more complex than using inflated airbag (Patoary, 2004; Derakhshan *et al.*, 2013). For instance, the instruments have to be water-proof if they are immersed in the water medium, such as strain and displacement transducers. In view of easy operation and low cost, the inflated airbag loading method was also adopted to investigate the response of the water storage façade under lateral pressure load.

2.6 Analytical Method

The equivalent SDOF method was proposed by Biggs (1964) as a simple method to evaluate the response of continuous member under blast loading. This method has been widely adopted to evaluate the structural response (UFC, 2008; ASCE, 2010; ASCE, 2011; Rigby *et al.*, 2014; Morison, 2006) and several modifications have been made to more accurately consider the strain rate effects (Nassr *et al.*, 2012; Garta and Stochino, 2013) and different failure modes (Krauthammer *et al.*, 1986; Astarlioglu *et al.*, 2013). In the SDOF method, a structural member is made equivalent to the SDOF system through transformation factor K_{LM} , which is a function of its deflection shape (Biggs, 1964). Hence, a good and representative deflection shape function would provide a closer estimate of the actual response. Normally, the deflection shape function is obtained by analyzing the member under uniformly distributed static load. In reality, the deflection shape changes during motion due to the existence of inertia force which, together with the uniform pressure load, changes the load distribution on

the member. It is accepted that deflection shape function has little effect on the structural response if the adopted deflection shapes are in accordance with the boundary conditions. However, the difference in maximum displacement obtained using different assumed shape functions may be over 10% in elastic range and may be even more when the member enters into plastic range (Baker *et al.*, 1983). Hence, the Lagrange Equation method with combined shape functions was adopted in this study to accurately predict the response of water storage façade under all three response regimes, i.e. quasi-static, dynamic and impulsive.

A constant Dynamic Increase Factor (DIF) is usually included in the SDOF analysis to represent the average strain rate effect on material strength (UFC, 2008; ASCE, 2010; ASCE, 2011). Since the DIF is a function of strain rate, it also varies during motion. Hence, adopting a constant DIF may not accurately capture the strain rate effect. To overcome this limitation, Nassr *et al.* (2012) proposed a strain rate model that defines the maximum strain rate in terms of scaled distance for beam column. Different DIF values can be generated under different blast loads, but the model is still unable to capture the varying DIF with strain rate during motion. The varying DIF was recently included in the continuous beam model (Carta and Stochino, 2013; Jones *et al.*, 2009) and SDOF model (Carta and Stochino, 2013) to analyze simply-supported RC panels under blast loading. The DIF was introduced by updating the resistance at each time step according to the strain rate at the corresponding time step and the predictions by including varying DIF were more accurate than those with constant DIF by comparing with test results. Since this method was not easy to be introduced in the Lagrange Equation model, the energy principle would be used to include the varying DIF into the SDOF and Lagrange Equation methods to accurately

capture the strain rate effect.

The Pressure–Impulse (P–I) diagram, which is an iso-damage curve (Cormie *et al.*, 2009) for a particular structural member loaded with a particular blast load history, is normally utilized to evaluate the damage level of structures for a given blast scenario. There are mainly two methods to construct the P–I diagram, i.e. the commonly adopted SDOF (Li and Meng, 2002; Li and Meng, 2002b; Fallah and Louca, 2006; Krauthammer *et al.*, 2008; Dragos and Wu, 2013) and the more recently applied FE methods (Shi *et al.*, 2008; Mutalib and Hao, 2011). The advantage of SDOF method is that the parameters relationship of structural member can be directly constructed. For example, the pressure and impulse asymptotes, which are two critical parameters of P–I diagram, can be given as functions related to structural parameters such as stiffness, mass and allowable maximum displacement. In the SDOF method, deformation is utilized to gauge the damage level, which would be reasonable for members such as beam and slab but not so much for column since the failure is more likely to be governed by its residual axial strength. Therefore, researchers have increasingly used the FE method to construct the P–I diagram of such structures. For instance, Shi *et al.* (2008) and Mutalib *et al.* (2011) applied the FE method to generate the P–I diagram for RC and FRP strengthened RC columns, respectively. In their studies, the residual axial strength was simulated and applied as the damage level indicator, which is more representative than maximum displacement for column. The disadvantage of FE method is that the pressure and impulse asymptotes cannot be directly defined. Parametric studies and curve-fitting are usually utilized to establish these parameters. In the present study, the dimensionless P–I diagram involving pressure and impulse asymptotes would be constructed using SDOF method and its

accuracy would be verified by comparing with FE investigations.

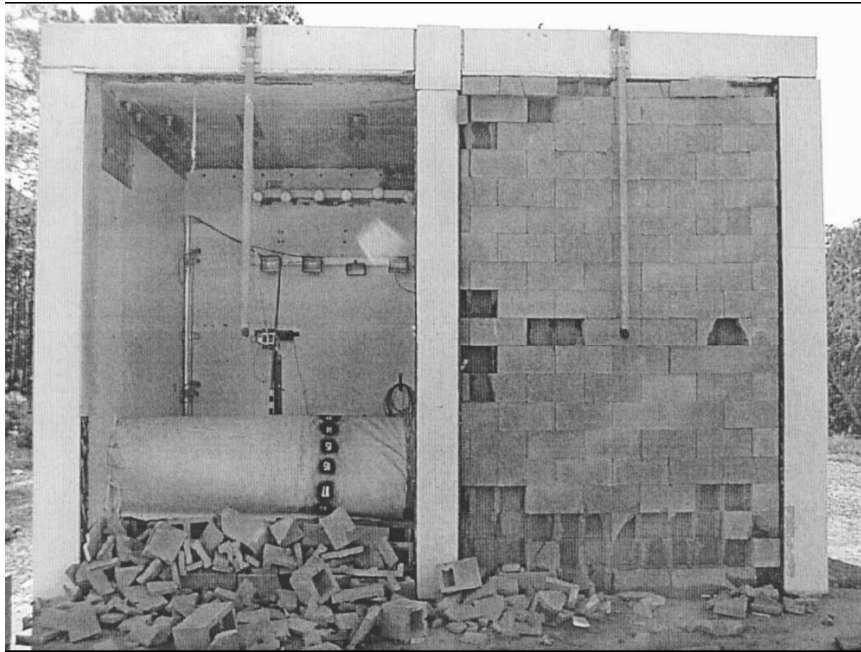


Fig. 2.1 Posttest configuration for masonry walls: no bonding (left) and bonding (right) between wall and polymer coating (Davidson *et al.*, 2005)

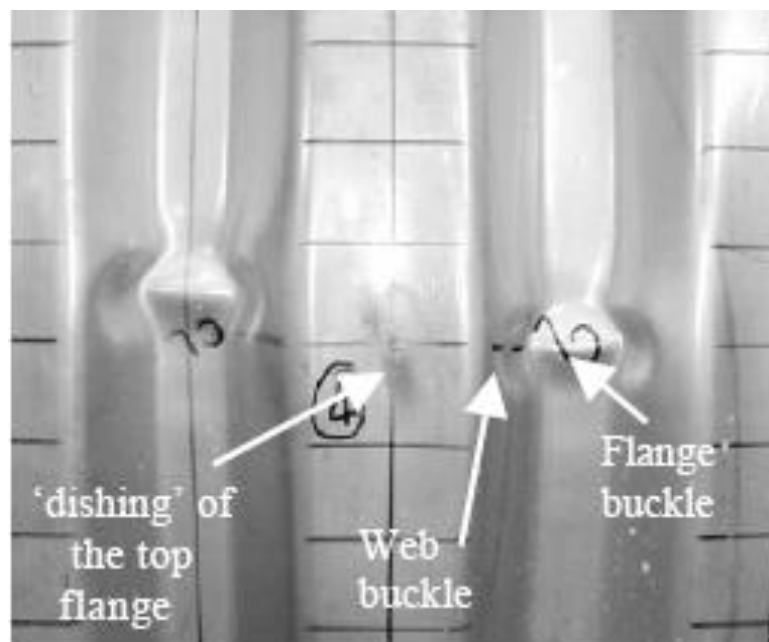


Fig. 2.2 Local buckling of the corrugation after blast test (Langdon and Schleyer, 2005a)

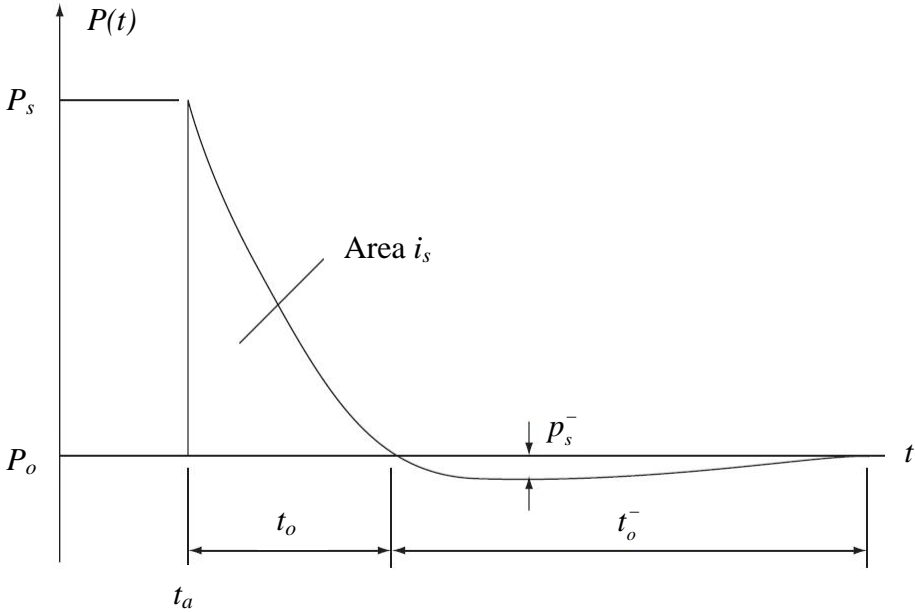


Fig. 2.3 Typical pressure–time profile for blast wave in free air (Smith and Hetherington, 1994)

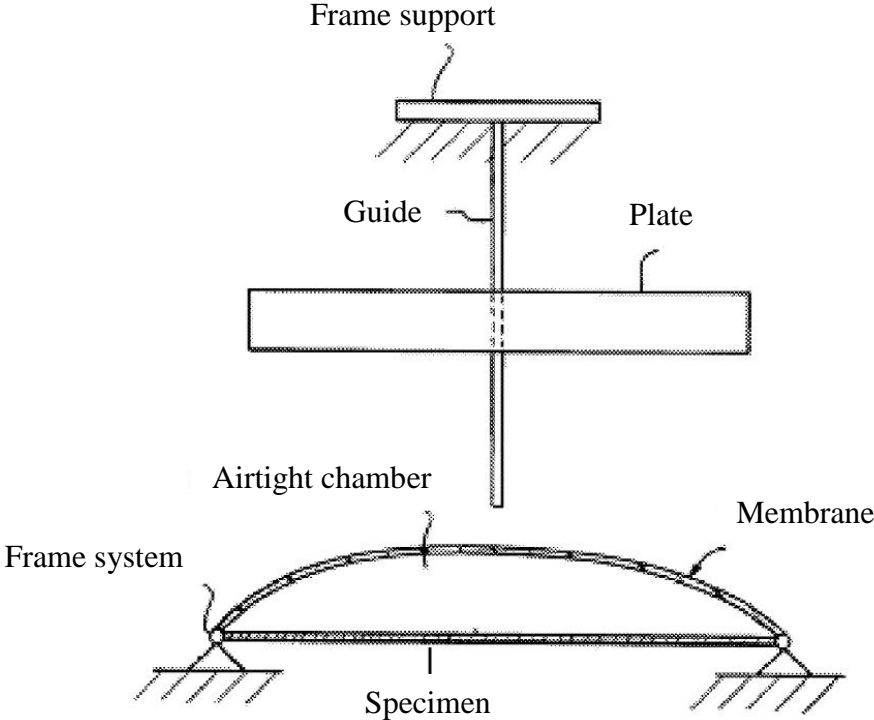


Fig. 2.4 Test setup for blast load simulation system (Mostaghel, 2003)

Chapter 3 Energy Performance of Water Façade Systems

3.1 Introduction

Mock-ups of the water façade tank with and without the Steel-Concrete-Steel (SCS) sandwich layer were designed, fabricated and installed at a monitoring station to evaluate the energy savings performance of the proposed water façade system in terms of thermal efficiency and space cooling load. The two design configurations of the mock-ups denoted as Steel-Water-Steel (SWS) and SWS-SCS, monitoring station, water circulation, automated control, instrumentation and remote data monitoring system are described in the following sections. The weather data and temperature profiles of the water façade mock-ups, building walls and indoor air were recorded based on which the thermal efficiency and space cooling load reduction of the water façade system were evaluated. The SWS mock-up was installed on the external west wall of Room A2 and it was compared to the control bare external west wall of Room A1 from 1 August 2013 to 21 March 2014 before the SWS-SCS mock-up was put up on 22 March 2014.

3.2 Test Setup

3.2.1 Monitoring Station

Two identical rooms on the second level of a two story monitoring station at Tuas, Singapore were used to conduct the temperature monitoring, as shown in Fig. 3.1. Fig.

3.2 shows the layout and dimension of the two rooms, A1 and A2, with directly west facing brick wall (wall 1) and three other walls (wall 3) made of 100 mm thick drywall.

Both of the rooms were provided with a Mitsubishi Heavy Duty Jetflow air-conditioning unit on the internal east wall. The units were fitted with timer control to automatically start and stop the controlled room temperature daily at the preset times.

3.2.2 Mock-ups

The drawings of the SWS and SWS-SCS mock-ups are given in Appendix A and the dimensions are summarized as follow:

- i. SWS - Steel plate thickness: $t = 10$ mm
 - SWS tank size: $2500 \text{ mm (W)} \times 2500 \text{ mm (H)} \times [t + 50 \text{ mm} + t] \text{ (D)}$
 - SWS tank capacity: 312.5 liter
- ii. SWS-SCS - Steel plate thickness: $t = 10$ mm
 - SWS tank size: $2500 \text{ mm (W)} \times 2500 \text{ mm (H)} \times [t + 50 \text{ mm} + 1/2t] \text{ (D)}$
 - SWS tank capacity: 312.5 liter
 - SCS panel size: $2500 \text{ mm (W)} \times 2725 \text{ mm (H)} \times [1/2t + 50 \text{ mm} + t] \text{ (D)}$

(W – Width, H – Height, D – Depth)

Since the proposed water storage façade was intended as a solar energy harvesting system whereby the warm water heated by the solar thermal energy is stored in a supply tank to be circulated to end-users, stainless steel 316 material was adopted for the SWS tank to fulfill the potability requirement of the Public Utilities Board of

Singapore. For the SCS panel, which was not in direct contact with water, mild steel with 2-coats painted external surfaces was applied. Pre-mixed Parvex Dacvo cement grout without coarse aggregate was adopted for the core material of SCS panel since it is easier to be pumped into the panel as compared to normal concrete with coarse aggregate.

3.2.3 Automated Water Circulation System

The mock-ups were equipped with automated control water circulation system to drain and then refill the SWS tank to and from the collection and feed tanks, respectively, once the target water temperature of 38 °C was attained. As illustrated in Fig. 3.3, the collection tank was placed on the top of the feed tank. The tanks were of the same size of 1500 mm (Length) × 1500 mm (Width) × 1050 mm (Height) and designed to a specified volume capacity that equals to six drainages from the SWS and SWS-SCS mock-ups combined. Water in the collection tank was left to cool overnight and the actuated valve between the feed tank and collection tank was opened at 06:00 daily to circulate the cold water back to the feed tank. Hence, at the start of each day at 06:00, the water circulation system was reset to full feed tank and empty collection tank condition using the timer control. When the water temperature in the mock-up reached the target temperature of 38 °C, the valve was automatically opened and warm water was drained through gravity outflow to the collection tank. After the tank was completely drained, the outlet valve was automatically closed and the inlet valve was opened using a timer control. At the same time, the pump was triggered and started to draw water from the feed tank to refill the mock-up.

3.2.4 Instrumentation and Remote Data Monitoring

The DS18B20 temperature sensor probe, which is accurate to ± 0.3 °C under ambient temperature of 20 to 50 °C and to ± 0.5 °C across its entire measurement range of -10 to +85 °C, was applied to measure the temperature at 5 minutes logging frequency. The layout of temperature probes are shown in Fig. 3.4 to Fig. 3.6 and summarized as follow:

- i. Above the ceiling for both rooms (2 probes)
- ii. Below the ceiling for both rooms (2 probes)
- iii. Center of internal and external surfaces of East and West walls of each room (8 probes)
- iv. Internal and external surface of North and South walls (above the door) of each room (4 probes)
- v. Center of each room (2 probes)
- vi. SWS mock-up (3 probes)
- vii. SWS-SCS mock-up (3 probes)

Web based data transmission was achieved by using a central control station to send the temperature data wirelessly to an industrial computer running Linux as shown in Fig. 3.7. A custom written program uploaded the sensor data online via a 3G modem to a database.

For the weather condition onsite, a solar powered U30/NRC USB HOBO outdoor weather station was deployed on the west corridor (see Fig. 3.8) in between the two rooms to monitor the ambient temperature, relative humidity (RH), wind speed and solar radiation using plug-and-play smart sensors. The measured data were also

logged at 5 minutes interval and the smart sensors automatically communicated the data information to the HOBO data logger. The S-THB-M002 12-bit temperature and RH smart sensor was installed within a solar radiation shield as shown in Fig. 3.8. The S-WSA-M003 wind speed smart sensor that offers measurement range from 0 to 45 m/s recorded the average wind speed and highest 3 seconds gust at each logging interval. The solar radiation was measured using three S-LIB-M003 silicon pyranometers that offer measurement range from 0 to 1280 W/m² over a spectral range of 300 to 1100 nm. Two of the pyranometers were placed on the west corridor with one facing perpendicularly away from the west wall and the other facing vertically towards sky. The third pyranometer faced perpendicularly away from the east wall.

Lutron DW-601 power analyzer was mounted on the internal east wall of both rooms to carry out measurement of live mains voltage to the air-conditioning units in order to determine the power consumption by the units. Since the measured quantity is an integrated quantity (summation), the frequency of data logging was not a concern. The update rate of the power analyzer was set to 5 minutes to match the temperature sensor probes logging rate.

3.3 Test Results and Discussion

3.3.1 Water Filled Tank VS Bare Wall

The monitoring data in October 2013 was selected to evaluate the energy efficiency of the SWS mock-up as compared to the control bare wall. Throughout the month, the air-conditioning units in both the monitoring rooms were operated at 24 °C, daily

from 08:00 to 17:00.

3.3.1.1 Temperature Profile

Fig. 3.9 shows the temperature profiles of water from 1 to 7 October 2013. It can be seen that the water temperature immediately reduced after the warm water was automatically drained out and replaced with cold water once the target temperature of 38 °C was reached. All of the recorded draining occurred after 12:00, which can be related to the position of the SWS mock-up that was facing the west side and hence, shielded from direct solar radiation in the morning.

25 days of recorded data (excluding 6 days with partially missing data, i.e. 17, 18, 19, 23, 24 and 31 October due to temporary disruption of temperature probe) in October 2013 were categorized into three groups in Table 3.1 according to the number of draining in a day, i.e. Group 1 (number of drains = 0), Group 2 (number of drains = 1) and Group 3 (number of drains = 2). The target temperature was reached on 9 out of the 25 days with one day of two draining.

From the comparison of the temperature profiles of external west walls of the two rooms in Fig. 3.10, it was noted that the maximum temperature of Room A2 with SWS mock-up was much lower than the bare wall of Room A1. Besides, the air-conditioning unit in Room A1 was unable to halt the temperature gain of the external west wall while the influence of controlled room temperature was evident from the temperature profile of the wall behind the SWS mock-up. This indicates the heat shield effect by the SWS mock-up that reduced the penetration of solar radiation into the room.

3.3.1.2 Thermal Efficiency of SWS mock-up

The thermal efficiency of the SWS mock-up is defined as the ratio of energy stored in water E_w to the solar energy E_s , as shown in Eq. (3.1).

$$\eta_{th} = \frac{E_w}{E_s} \quad (3.1)$$

where

$$E_w = \sum_{i=0}^n c_{p,w} m_w (T_{i+1} - T_i) \quad \text{for } T_{i+1} > T_i \quad (3.2)$$

$$E_s = \sum_{i=0}^n Q_s A \Delta t_i \quad (3.3)$$

In the above equations, $c_{p,w}$ is the specific heat capacity, m_w is the total mass of water in the SWS, T is the water temperature as measured by the temperature probe, Q_s is the intensity of solar radiation as measured by the HOBO, A is the front surface area of SWS and Δt_i is the time interval. Density and specific heat capacity of water are given in Table 3.2 (Welty *et al.*, 2001). The thermal efficiency was calculated from 08:00 to 17:00 in accordance with the running time of the air-conditioning units.

The calculated thermal efficiency for the 22 days of recorded data in October 2013 is tabulated in Table 3.3 and it ranges from 12.87% to 28.50%. The thermal efficiency of the SWS mock-up can be conveniently and effectively improved by painting the exposed front surface of the tank with high absorptivity paint in order to increase the solar absorptivity of stainless steel (0.4768). It was observed that the higher the solar energy, the higher was the number of draining as compared for the three groups of data. This indicates that higher solar energy would lead to higher energy stored in water and consequently higher number of draining, which translated to higher thermal

efficiency. This is illustrated in Fig. 3.11, where it can be seen that the thermal efficiency generally increases with increasing solar energy.

3.3.1.3 Space Cooling Load

Since Rooms A1 and A2 were identical except for their west walls, it is reasonable to assume that the heat penetration into both rooms through the other three walls and roof was the same. Therefore, only the heat penetration through west wall was determined in order to compare the space cooling load of the two rooms.

The difference in space cooling load between the two rooms can be evaluated from the difference in solar energy that penetrates through their respective west wall. By assuming that the temperature of the internal west wall was uniform across its entire surface and the room temperature was uniform over the confined space, the energy transferred from the internal west wall to indoor air through convection and radiation can be calculated as follow:

$$E_{cooling} = \sum_{i=0}^n \left[h_a (T_{iww} - T_{room}) + \varepsilon_{wall} \bar{h} (T_{iww}^4 - T_{room}^4) \right] A \Delta t_i \quad (3.4)$$

where h_a is the convection coefficient of air, T_{iww} and T_{room} are the temperatures of internal west wall and indoor air, ε_{wall} is the emission coefficient of wall, \bar{h} is the Stefan-Boltzmann constant ($5.676 \times 10^{-8} \text{ W/m}^2 \cdot \text{K}^4$), A is the surface area of the west wall and Δt_i is time interval.

The convection coefficient of air, h_a , can be obtained from the following equations:

$$Gr = \frac{g \bar{\beta} L^3 (T_{iww} - T_{room})}{\nu^2} \quad (3.5)$$

$$Nu = \left\{ 0.825 + \frac{0.387 (Gr Pr)^{1/6}}{\left[1 + (0.49/Pr)^{9/16} \right]^{8/27}} \right\}^2 \quad (3.6)$$

$$h_a = k_a Nu / L \quad (3.7)$$

where Gr is Grashof number, g is gravity, $\bar{\beta}$ is volumetric thermal expansion coefficient, L is the characteristic length, ν is kinematic viscosity, Nu is Nussel number, Pr is Prandtl number and k_a is conductivity of air.

The calculated space cooling load for the same period as the thermal efficiency calculations is given in Table 3.4 based on the recorded temperatures of internal west walls and indoor air of the two rooms. The space cooling loads of both Rooms A1 and A2 were shown to increase with increasing number of draining, as expected due to the higher solar energy. The difference in space cooling load between Rooms A1 and A2 also increases with increasing solar energy. This suggests that the SWS mock-up was effective as solar heat shield to the building on days with high solar radiation to reduce the space cooling load. Five days of negative space cooling load saving for Room A2 with SWS mock-up was observed in Table 3.4, which includes 2, 5, 8, 21 and 27 October 2013. To find out the reasons that caused the higher space cooling load for Room A2, the temperature profiles on 2 October 2013 are analyzed as plotted in Fig. 3.12. It was found that the temperature of the internal west wall of Room A1 with bare wall was generally lower than Room A2 during the running time of air-conditioning units from 08:00 to 17:00. Since the internal west wall temperature was mainly influenced by heat transfer between the external and internal west wall through conduction, the higher temperature of the external wall of Room A2 as compared to its internal wall temperature from 00:00 to 08:00 means that the heat was

transferred from the external wall to the internal wall during this period. In comparison, the external wall temperature of Room A1 was lower than its internal wall for the same period. Hence, the internal west wall of Room A2 cooled down slower to a higher temperature than Room A1 before the air-conditioning units were turned on at 08:00. Thus, the SWS mock-up was acting as a heat barrier that reduced heat loss from the external west wall behind it. This heat barrier effect could be alleviated by automatically replacing the water in the SWS mock-up with much cooler water in order to rapidly and effectively bring down the temperature.

Between the period of 08:00 to 17:00, it was noted in Fig. 3.12 that the temperature difference of the west wall of Room A1 was lower than Room A2 before 11:30. This indicates that the heat penetration through west wall of Room A1 by conduction was lower than Room A2. Hence, less space cooling load would be required to bring down the internal west wall temperature of Room A1 between 08:00 and 11:30. After 11:30, the external west wall temperature of Room A1 increased at a faster rate than Room A2 due to the increasing direct solar radiation. As the intensity of solar radiation from the west only started to increase after 12:00 and would reach the highest value after 16:00, the SWS mock-up was more effective as a solar heat shield after 12:00. Due to the remaining solar radiation after 17:00 and the thermal mass effect of the brick wall, the space cooling load was not fully captured as the air-conditioning units were turned off at 17:00. Higher saving of space cooling load would be expected if the air-conditioning units were running into the evening or through the night.

3.3.2 Water Filled Tank VS Water Filled Tank-Sandwich Panel

The temperature data in June 2014 were analyzed to compare energy savings

performances of the SWS and SWS-SCS mock-ups. The air-conditioning units in both rooms were maintained at 24 °C from 08:00 to 20:00 in this month. Automatic replacement of water in the mock-ups with cooler water from the feed tank was conducted at 21:30 each day in order to bring down the west wall temperature.

3.3.2.1 Temperature Profile

Fig. 3.13 compares the water temperature in the SWS and SWS-SCS mock-ups from 15 to 22 June 2014. The target temperature was reached on six days in the week due to the higher solar radiation in that month. As seen in the figure, the water temperature in the SWS-SCS mock-up increased faster than the SWS mock-up after 12:00, which indicates that the energy storage capacity of SWS-SCS mock-up was higher than that of the SWS mock-up.

From the recorded number of draining in the month of June as summarized in Table 3.5, the SWS mock-up was drained once in 7 days and twice in 3 days as compared to 10 and 5 days for the SWS-SCS mock-up. More significantly, a record of triple draining was achieved by the SWS-SCS in 2 days on 20 and 21 June 2014. Overall, the SWS-SCS mock-up achieved one additional draining under the same weather condition as compared to the SWS mock-up on 13 days, as marked (*) in the table. This higher energy storage capacity of the SWS-SCS mock-up was due to the thermal mass and heat barrier effect of the additional SCS layer that reduced the heat loss through the back surface of the SWS tank.

The temperature profiles of the external west wall of Rooms A1 and A2 from 15 to 22 June 2014 are compared in Fig. 3.14. The external west wall temperature of Room A1

with SWS-SCS mock-up was generally lower than Room A2 with SWS mock-up. Besides, the external west wall temperature of Room A1 also increased slower than Room A2 after 12:00 as the intensity of the solar radiation began to increase significantly. This demonstrates the better performance of the SWS-SCS mock-up in reducing the solar heat penetration as compared to the SWS mock-up.

3.3.2.2 Thermal Efficiency of SWS and SWS-SCS mock-ups

The thermal efficiencies of the two mock-ups were calculated using Eq. (3.1) for the daily period from 08:00 to 20:00 in accordance with the running time of the air-conditioning units. The calculated solar energy, energy stored in water and thermal efficiency of SWS and SWS-SCS mock-ups based on the recorded temperatures and weather data are tabulated in Table 3.6. The thermal efficiency of the SWS mock-up was found to range from 18.85% to 29.44% with an average of 23.01% for the 30 days in June 2014. In comparison, a higher thermal efficiency ranging from 21.40% to 40.62% with an average of 30.85% was observed for the SWS-SCS mock-up. This is in consistent with earlier observations that the SWS-SCS mock-up stored higher solar energy than the SWS mock-up. The relationships between the thermal efficiency and solar energy for the SWS and SWS-SCS mock-ups are shown in Fig. 3.15. Again, the thermal efficiency is shown to be generally increasing with increasing solar energy. It can be seen from the fitted curve that the thermal efficiency of SWS-SCS mock-up was higher than that of the SWS mock-up under the same solar energy. The thermal efficiency of the SWS-SCS mock-up was 5.4% higher than the SWS mock-up when the solar energy was 4.5 kWh and the difference rose to 9.4% under solar energy of 21.2 kWh. Hence, it appears that the thermal efficiency difference between the SWS-SCS and SWS mock-up is more significant when the solar energy is higher.

3.3.2.3 Space Cooling Load

The performance of the SWS and SWS-SCS mock-ups in reducing the space cooling load are discussed in this section. Similar to the comparison in Section 3.3.1.3, only heat penetration into Rooms A1 and A2 through their respective west wall was compared to evaluate the space cooling load by the two different configurations of the water façade systems.

Table 3.7 summarizes the space cooling load of Room A2 with SWS mock-up and Room A1 with SWS-SCS mock-up and the difference (A2-A1) between them. It was noted that the space cooling load of both Rooms A1 and A2 generally increased with increasing number of draining, which implies that higher space cooling load was required under higher solar energy. It was also noted that the space cooling load of Room A1 was less than that of Room A2 for all the whole month in June 2014. Hence, it was shown that the SWS-SCS mock-up with additional SCS layer can better reduce solar heat penetration into the room as compared to the SWS mock-up.

3.4 Summary

In this chapter, the field monitoring on the SWS and SWS-SCS mock-ups were presented, based on which the energy savings potential was evaluated in two aspects, i.e. thermal efficiency and space cooling load. The key findings are summarized as follow:

- i) The target water temperature of 38 °C for daily usage can be achieved using water storage façade and automated control of the water circulation system to drain and refill the water façade. The number of draining in a day was

dependent on the weather condition with higher draining on days with higher solar radiation. The SWS-SCS mock-up with additional SCS layer was shown to be capable of storing higher solar thermal energy as compared to the SWS mock-up. This was attributed to the thermal mass and heat barrier effect of the SCS that reduced the heat loss through the back surface of the water tank.

- ii) In the two months of data that was analyzed, the thermal efficiency of the SWS and SWS-SCS mock-up was found to be ranging from 12.87% to 23.01% and from 21.40% to 40.62%, respectively. The thermal efficiency of the SWS-SCS mock-up was 7.84% higher than that of SWS mock-up under the same weather condition. Generally, the thermal efficiency increases with increasing input solar energy.
- iii) The SWS mock-up was shown to be effective as a solar heat shield to reduce heat penetration into the building as compared to the control bare wall. The external west wall temperature behind the mock-up was lower than the control wall during daylight.
- iv) Although the SWS mock-up was effective as solar heat shield, negative space cooling load saving as compared to the bare wall was observed on certain days with lower solar radiation due to cloud or rain. Besides, the heat barrier effect of the SWS mock-up also hindered the heat loss from the wall behind it during the night. But, the SWS mock-up achieved overall space cooling load reduction of 0.0484 kWh per day averaging over a month period compared to the bare wall.

Table 3.1 Categorized results for October 2013

Group 1 (No. of drain=0)	2, 3, 7, 10, 11, 12, 13, 14, 20, 21, 22, 26, 27, 28, 29, 30 October 2013
Group 2 (No. of drain=1)	1, 4, 5, 6, 8, 9, 15, 25 October 2013
Group 3 (No. of drain=2)	16 October 2013

Table 3.2 Properties of materials (Welty *et al.*, 2001)

Material	Parameters	Temperature (K)		
		280	300	320
Brick	Emissivity	0.65	0.65	0.65
	Density (kg/m ³)	1.2614	1.1769	1.1032
Air	Conductivity (W/m*K)	0.024671	0.026240	0.027785
	Kinematic viscosity (m ² /s)	1.3876×10 ⁻⁵	1.5689×10 ⁻⁵	1.7577×10 ⁻⁵
	Thermal diffusivity (m ² /s)	1.9488×10 ⁻⁵	2.2156×10 ⁻⁵	2.5003×10 ⁻⁵
	Prandtl number	0.713	0.708	0.703
	Volumetric thermal expansion coefficient	3.5659×10 ⁻³	3.3329×10 ⁻³	3.1343×10 ⁻³
		Temperature (K)		
		273	293	313
Water	Density (kg/m ³)	999.3	998.2	992.2
	Specific heat capacity (J/kg*K)	4226	4182	4175

Table 3.3 Thermal efficiency of SWS mock-up

Date Oct 2013	Solar energy* (kWh) (1)	Energy stored in water* (kWh) (2)	Thermal efficiency (%) (2)/(1)×100%
Group 1			
7	12.45	3.26	26.16
10	5.07	0.90	17.84
11	13.35	3.33	24.96
12	8.07	1.04	12.87
13	10.83	2.33	21.51
14	11.32	2.62	23.18
20	13.94	3.17	22.71
21	7.72	1.27	16.42
22	11.06	2.58	23.34
26	9.31	2.28	24.50
27	7.28	1.94	26.71
28	10.70	2.78	26.02
29	6.82	1.51	22.19
30	6.21	1.27	20.42
Group 2			
4	17.27	4.52	26.15
5	17.03	4.25	24.96
6	16.66	4.75	28.50
8	14.16	3.78	26.70
9	14.63	3.87	26.43
15	15.29	3.86	25.26
25	12.95	3.46	26.72
Group 3			
16	16.79	4.43	26.37
Total	258.90	63.20	-
Average	11.77	2.87	24.38

*The energy is obtained by summing the respective energy from 08:00 to 17:00.

Table 3.4 Space cooling load

Date Oct 2013	Space cooling load* in Room A1 (kWh) (1)	Space cooling load* in Room A2 (kWh) (2)	Difference (kWh) (1)-(2)
Group 1			
2	0.872	1.020	-0.1480
3	0.996	0.934	0.0624
7	0.865	0.804	0.0607
10	1.102	1.084	0.0177
11	0.799	0.785	0.0139
12	1.026	1.013	0.0121
13	1.069	0.876	0.1930
14	0.999	0.935	0.0634
20	0.959	0.840	0.1200
21	0.867	0.920	-0.0532
22	0.854	0.743	0.1110
26	1.048	0.949	0.0998
27	0.797	0.848	-0.0502
28	0.843	0.777	0.0662
29	0.952	0.903	0.0489
30	0.950	0.903	0.0470
Average	0.937	0.896	0.0415
Group 2			
1	1.090	0.946	0.1440
4	1.033	0.909	0.1240
5	0.927	0.992	-0.0650
6	0.915	0.883	0.0321
8	0.996	1.030	-0.0342
9	0.916	0.911	0.0058
15	1.036	0.958	0.0779
25	1.031	0.899	0.1320
Average	0.993	0.941	0.0521
Group 3			
16	1.256	1.128	0.1280
Total	24.199	22.989	1.2100
Average (total)	0.968	0.920	0.0484

*Space cooling load is obtained by summing the transferred energy from 08:00 to 17:00.

Table 3.5 Categorized results for June 2014

Group 1 (No. of drain=0)	1, 2, 3, 4, 5, 6, 9, 10*, 12*, 13*, 14, 15, 16*, 22, 24*, 25*, 27, 28, 29*, 30 June 2014
Group 2 (No. of drain=1)	7, 11*, 17*, 18*, 19*, 23, 26 June 2014
Group 3 (No. of drain=2)	8, 20* 21* June 2014

Note: The date marked with (*) indicates that the SWS-SCS mock-up has one more time drain than SWS mock-up.

Table 3.6 Thermal efficiency of SWS and SWS-SCS mock-up

Date Jun 2014	Solar energy* (kWh)	SWS-SCS mock-up		SWS mock-up	
		Energy stored in water* (kWh)	Thermal efficiency (%)	Energy stored in water* (kWh)	Thermal efficiency (%)
	(1)	(2)	(2)/(1)×100%	(3)	(3)/(1)×100%
Group 1					
1	9.76	2.60	26.61	1.86	19.02
2	9.11	2.31	25.37	1.76	19.35
3	11.18	3.13	28.03	2.46	22.03
4	8.79	2.03	23.10	1.84	20.96
5	4.53	0.97	21.40	0.85	18.85
6	4.67	1.47	31.59	1.25	26.70
9	7.33	2.98	40.62	1.46	19.97
10	11.42	3.80	33.23	2.55	22.35
12	13.27	4.61	34.74	3.35	25.22
13	12.39	3.32	26.82	2.55	20.61
14	4.53	1.20	26.55	0.97	21.51
15	11.69	3.19	27.27	2.53	21.67
16	12.66	3.77	29.82	2.49	19.66
22	8.34	2.35	28.12	1.97	23.62
24	14.24	4.13	29.03	2.87	20.15
25	17.43	5.54	31.76	3.98	22.81
27	5.09	1.26	24.82	1.14	22.34
28	12.72	3.37	26.47	2.76	21.70
29	12.69	3.73	29.38	3.12	24.62
30	6.78	1.45	21.43	1.08	15.98
Group 2					
7	16.90	6.01	35.56	4.98	29.44
11	15.91	5.24	32.91	3.89	24.47
17	18.41	5.81	31.54	4.09	22.20
18	20.67	7.11	34.41	5.15	24.91
19	21.22	6.69	31.53	4.79	22.56
23	14.29	3.88	27.17	2.96	20.72
26	15.44	4.68	30.29	3.55	22.97
Group 3					
8	18.59	6.53	35.11	4.97	26.72
20	20.30	6.64	32.71	4.84	23.82
21	18.72	7.14	38.13	5.15	27.50
Total	379.07	116.93	-	87.20	-
Average	12.64	3.90	30.85	2.91	23.01

*The energy is obtained by summing the respective energy from 08:00 to 20:00.

Table 3.7 Space cooling load of SWS and SWS-SCS mock-up

Date Jun 2014	Space cooling load* in Room A2 (kWh) (1)	Space cooling load* in Room A1 (kWh) (2)	Difference (kWh) (1)-(2)
Group 1			
2	1.594	1.544	0.051
3	1.370	1.226	0.144
4	1.257	1.159	0.098
5	1.048	1.002	0.046
6	1.006	0.839	0.168
9	1.834	1.755	0.079
10	1.549	1.338	0.211
12	1.227	1.173	0.053
13	1.480	1.199	0.281
16	1.480	1.317	0.163
24	1.551	1.379	0.172
25	1.287	1.218	0.069
27	1.024	1.021	0.003
30	1.341	1.317	0.024
Average	1.361	1.249	0.112
Group 2			
11	1.526	1.277	0.250
17	1.520	1.213	0.308
18	1.230	1.187	0.043
19	1.370	1.128	0.242
23	1.840	1.710	0.130
26	1.414	1.163	0.251
Average	1.483	1.280	0.204
Group 3			
20	1.574	1.262	0.312
Total	29.522	26.427	3.098
Average (total)	1.406	1.258	0.148

*Space cooling load is obtained by summing the transferred energy from 08:00 to 20:00.



Fig. 3.1 Photo of monitoring station

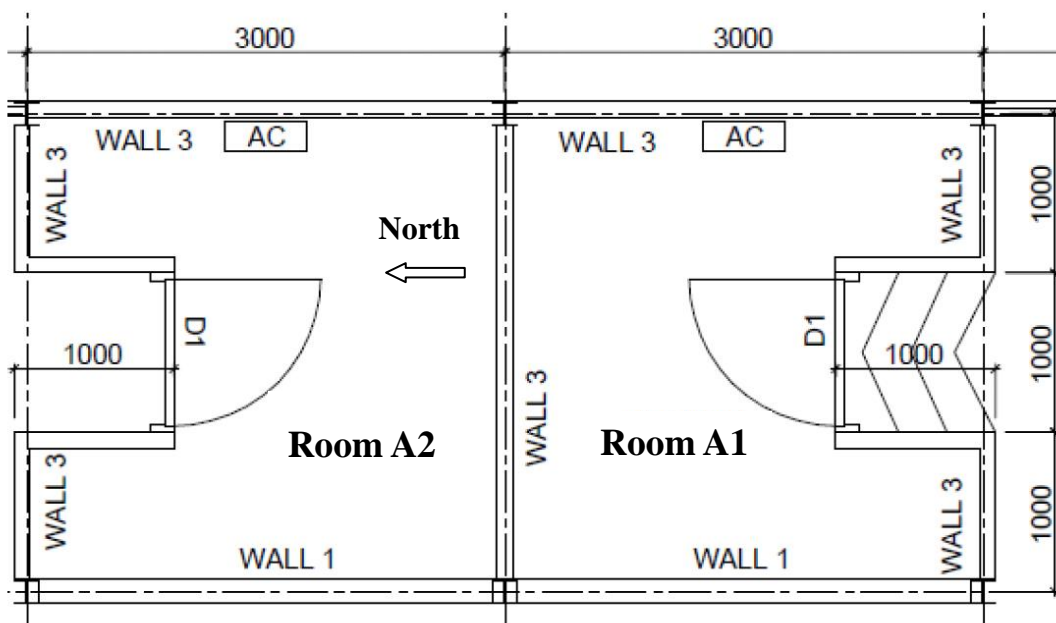
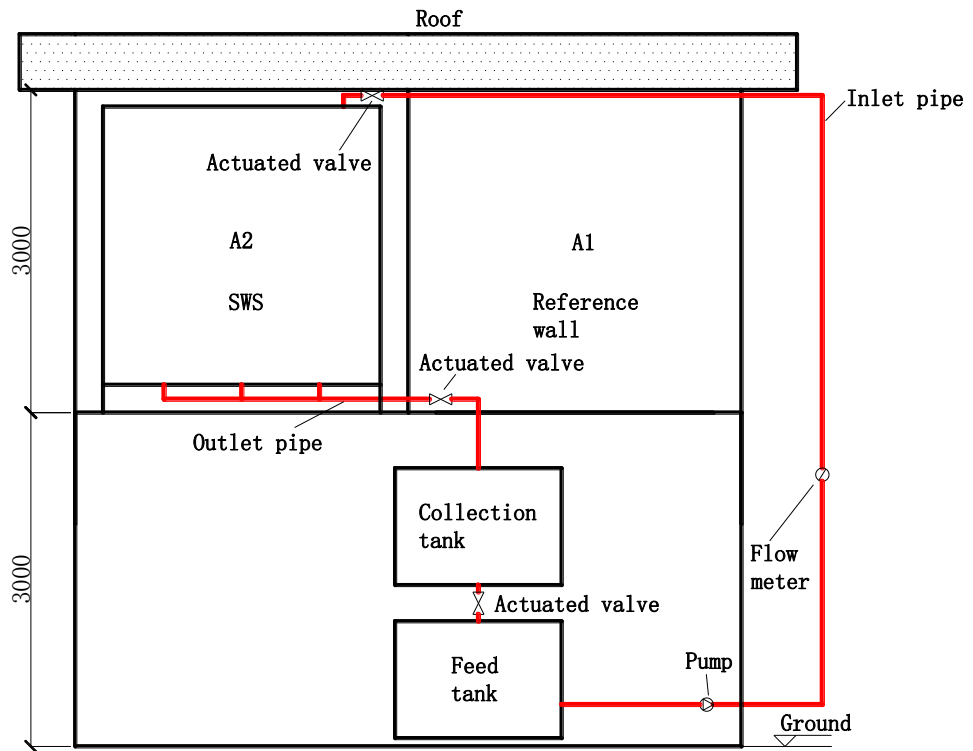
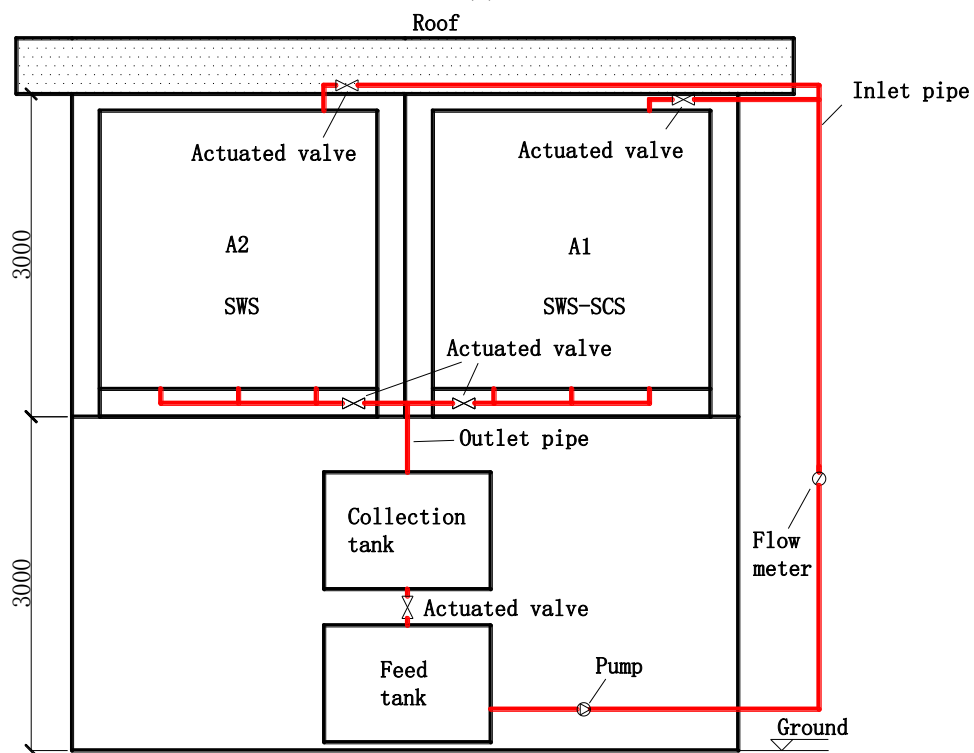


Fig. 3.2 Layout of the monitoring station



(a)



(b)

Fig. 3.3 Schematic diagram of circulating system: (a) SWS VS bare wall, (b) SWS VS SWS-SCS

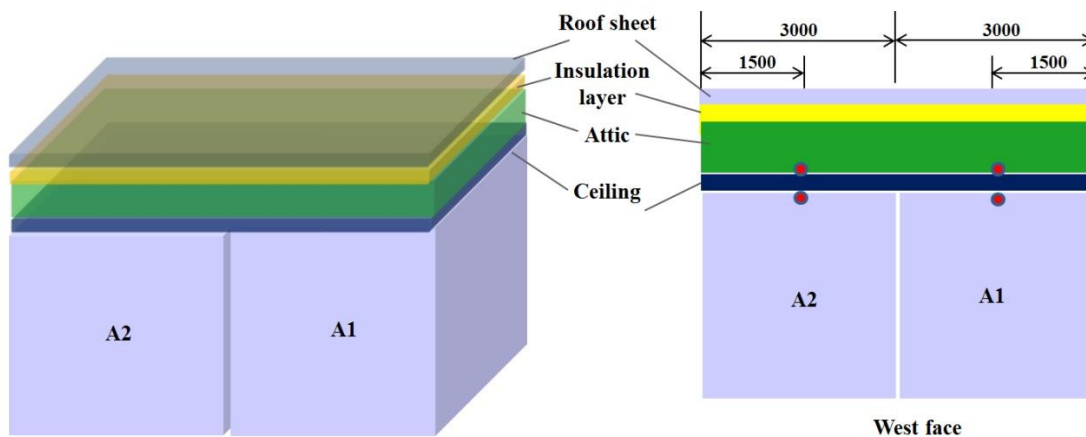


Fig. 3.4 Temperature sensing points for roof (Each dot represents one temperature sensor probe)

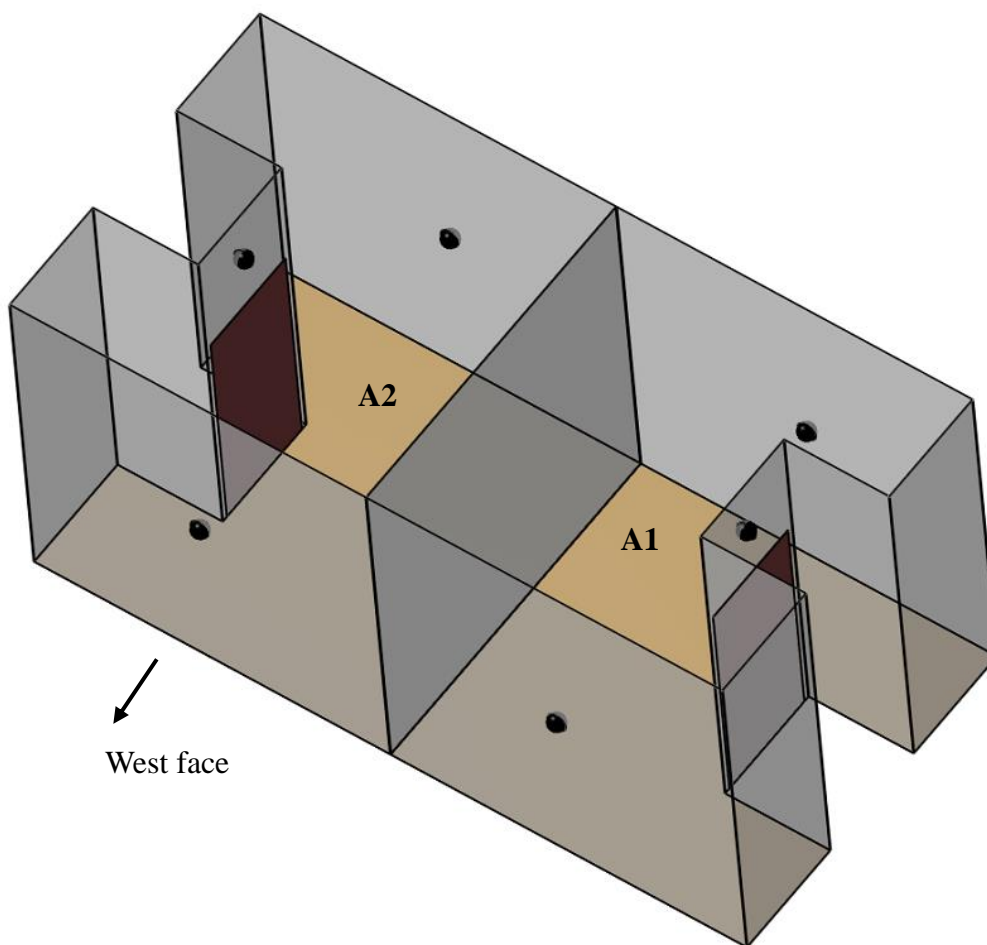


Fig. 3.5 Temperature sensing points for walls (Each dot represents a pair of temperature sensor probes on the internal and external surfaces of the wall)

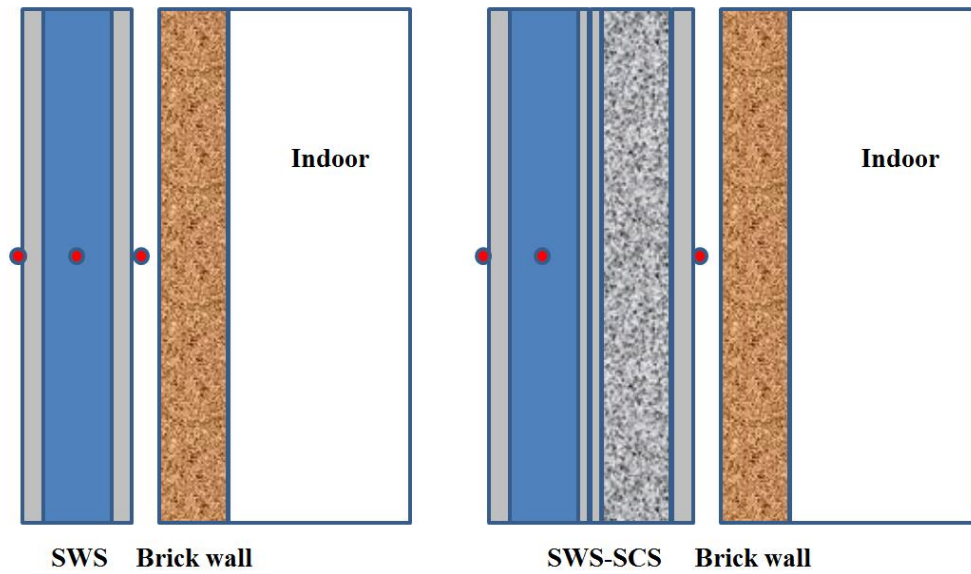


Fig. 3.6 Temperature sensing points for SWS and SWS-SCS mock-ups (Each dot represents one temperature sensor probe at the center)



(a) Central control station



(b) Industrial computer running Linux

Fig. 3.7 Wireless data relay from central control station to industrial computer

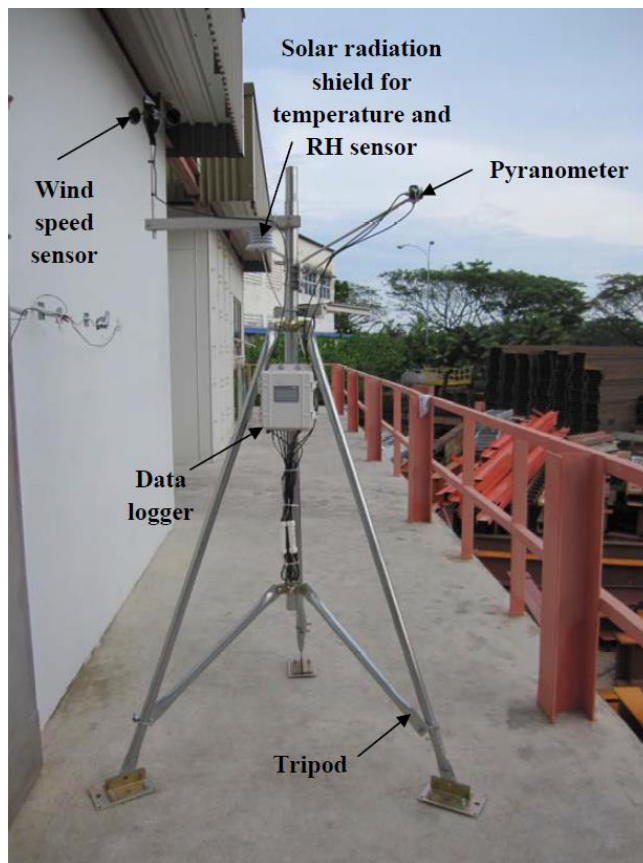


Fig. 3.8 HOBO weather station

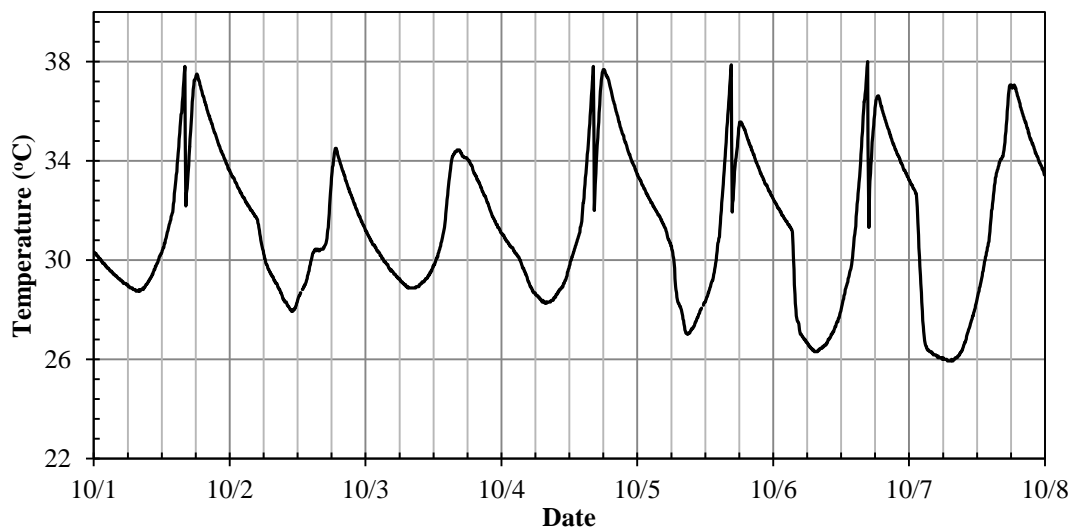


Fig. 3.9 Temperature profiles of water inside the SWS tank in Oct 2013

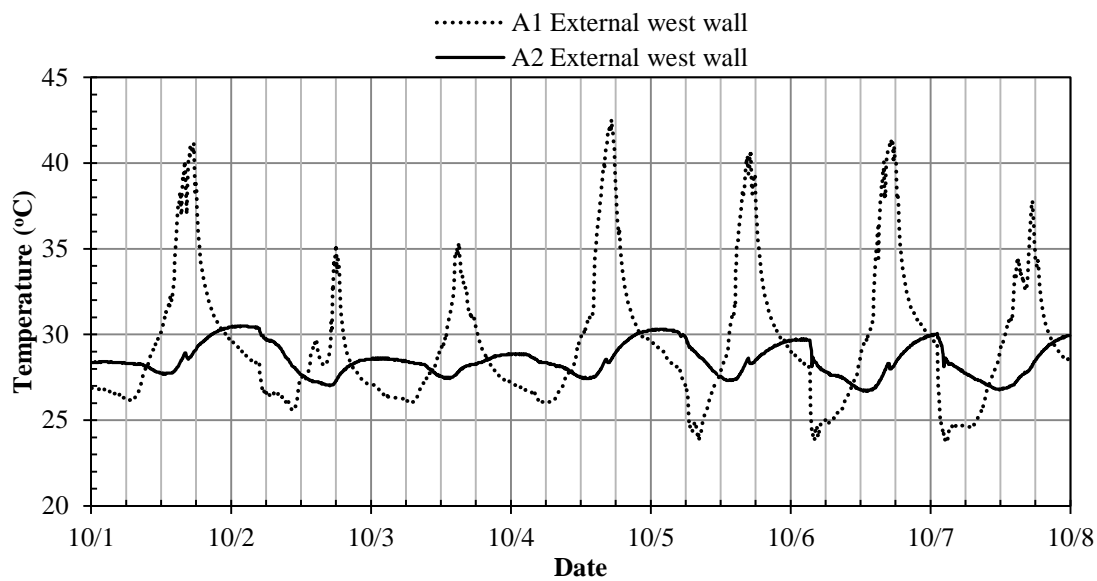


Fig. 3.10 Temperature profiles of external west wall of Room A1 and A2 in Oct 2013

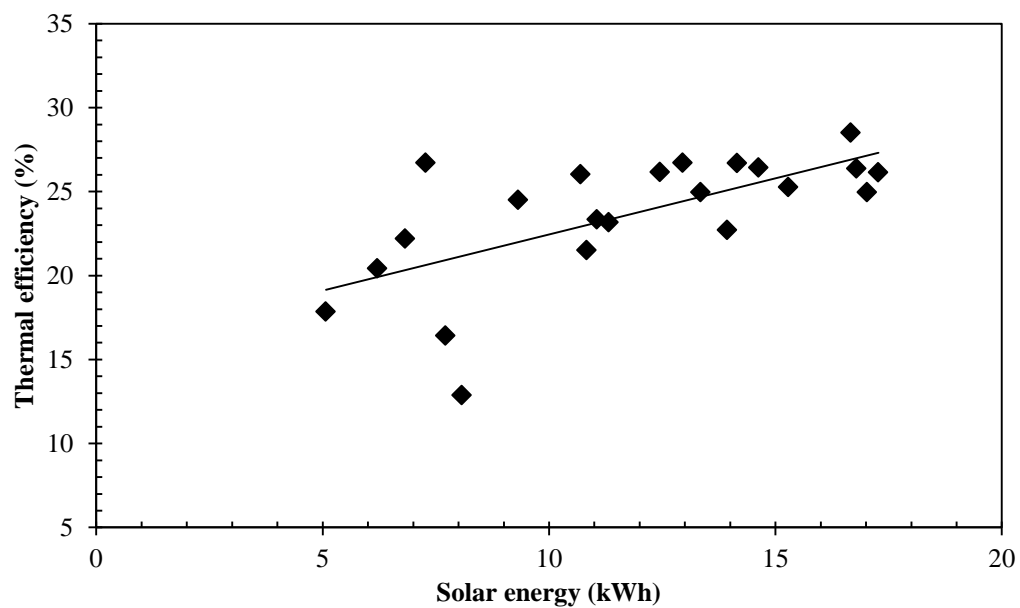


Fig. 3.11 Relationship between thermal efficiency and solar energy

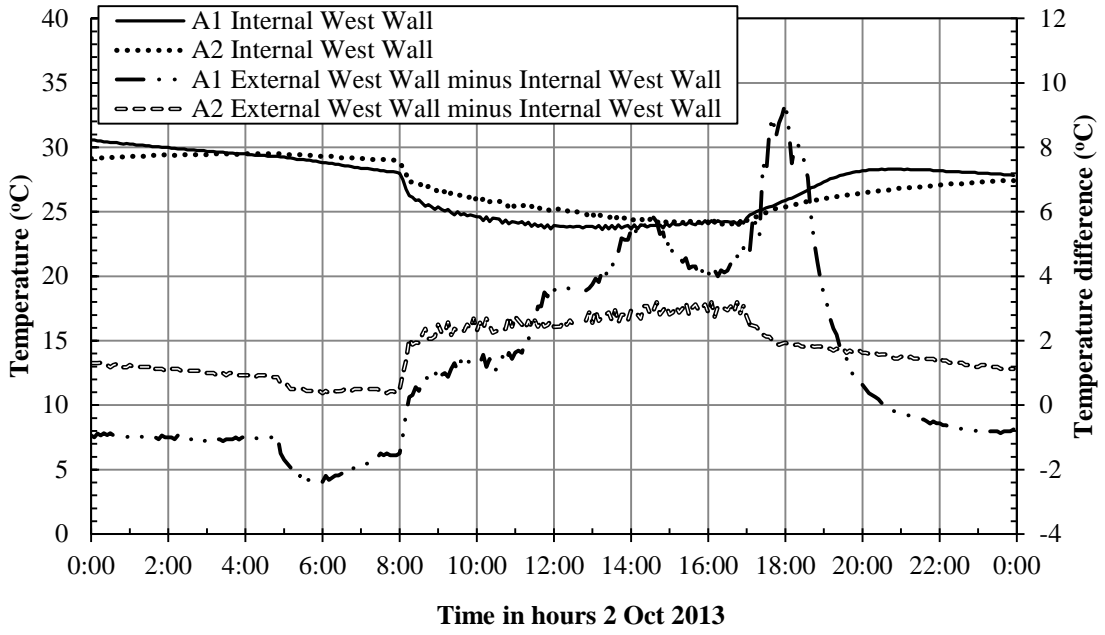


Fig. 3.12 Temperature profiles on 2 October 2013

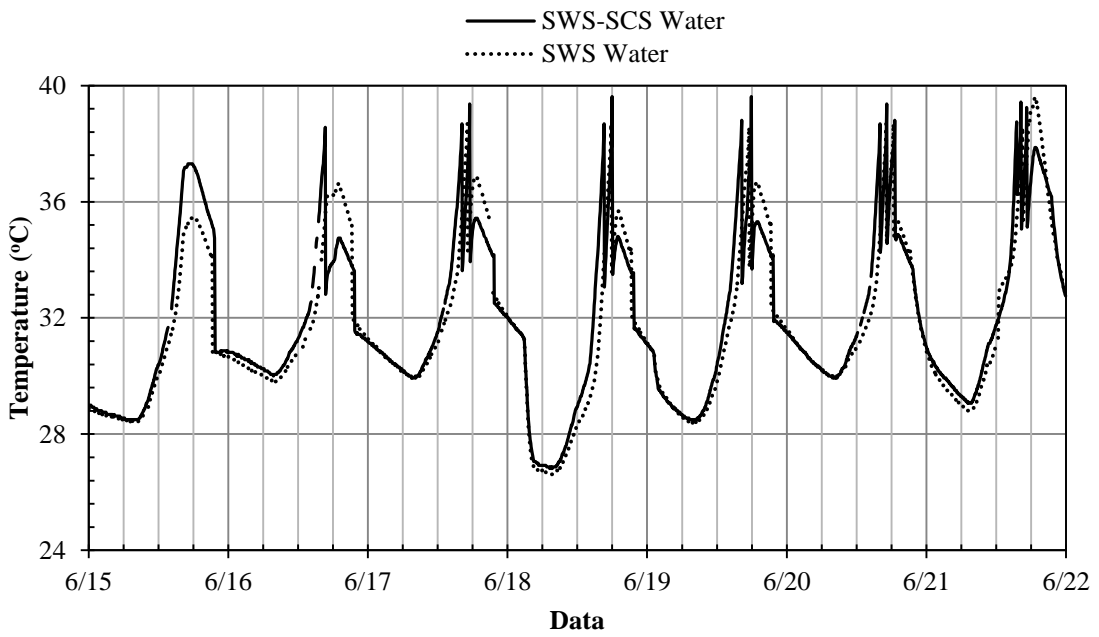


Fig. 3.13 Temperature profiles of water of SWS and SWS-SCS mock-ups in June 2014

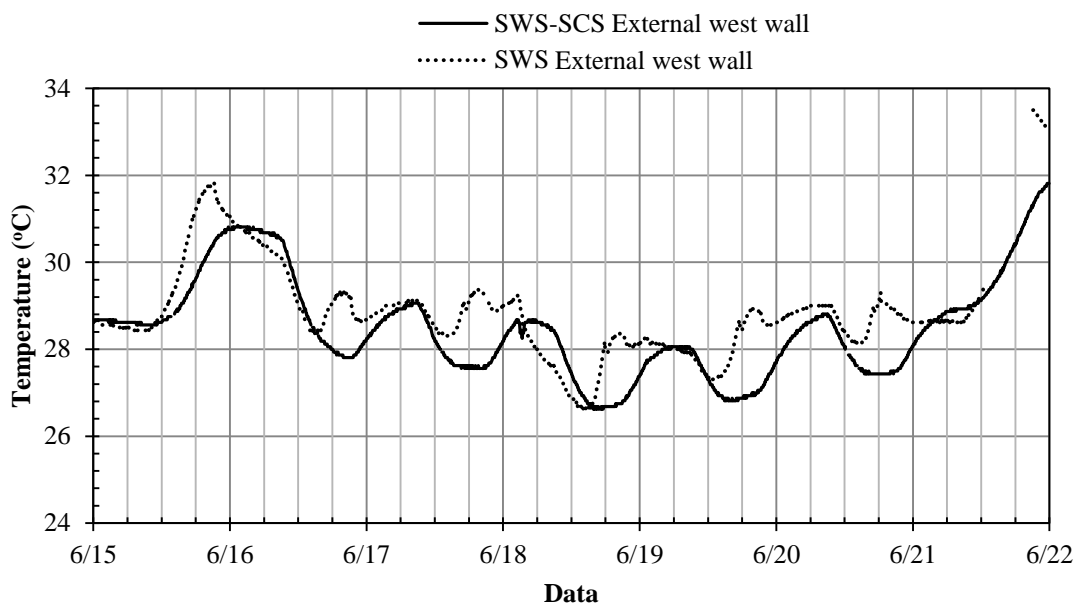


Fig. 3.14 Temperature profiles of external west wall of Room A1 and A2 in June 2014

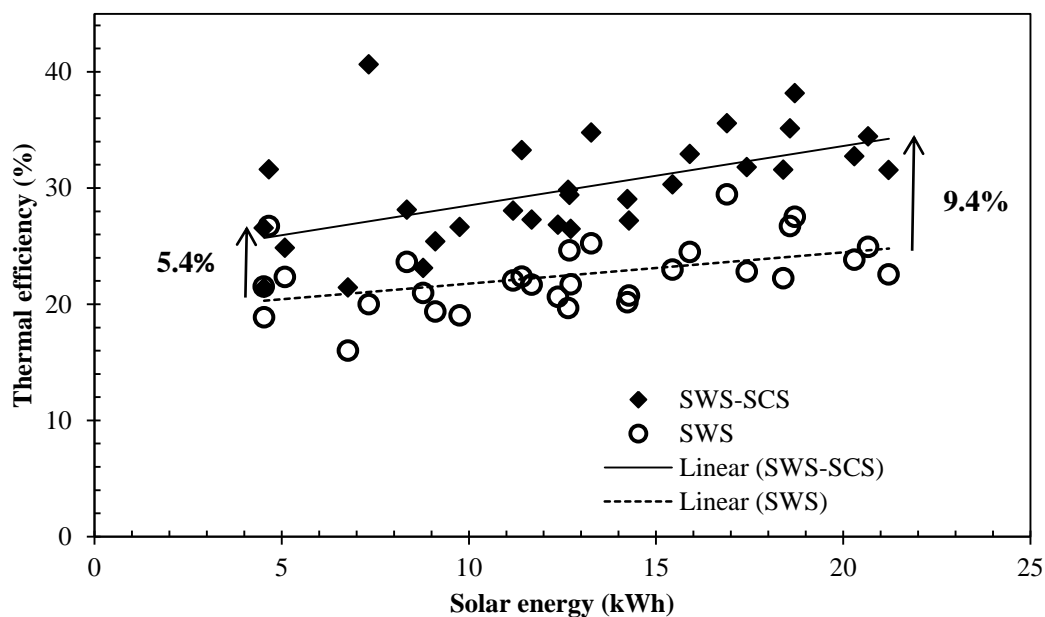


Fig. 3.15 Relationship between thermal efficiency and solar energy

Chapter 4 Performance of Water Façade Systems under Lateral Pressure Load

4.1 Introduction

The structural responses of water façade systems under lateral pressure load were experimentally, analytically and numerically investigated in this chapter. The loading was applied using hydraulic actuator on an inflated high pressure airbag to assert lateral pressure on the specimens in the experimental study. Due to the limitation of airbag lifting capacity, which has maximum allowable pressure of 0.8 MPa, the SWS-SCS configuration was divided into SWS and SCS which were tested separately. The resistance–deflection curves, deflection shapes and strain responses were obtained from the experiments to understand their behaviors under lateral pressure load. In addition, the effects of water and concrete core depth on the resistances of SWS and SCS were experimentally investigated. Analytical models were developed to predict the resistances of the specimens and the analytical predictions were verified with the test results. FE models of the test specimens under lateral pressure load were established. The experimentally-verified FE models were applied to investigate the effects of water on the resistance of SWS tank and the load transfer mechanism between face plate and concrete core of SCS panel.

4.2 Material Properties

The material properties of the stainless steel, mild steel and cement grout used to

fabricate the SES, SWS and SCS specimens were determined under static loading condition in accordance to the ASTM laboratory test standards. The material test procedure and results are reported in the following subsections.

4.2.1 Steel

Three coupon specimens for each of the 3 mm thick mild steel and stainless steel plates were machined according to ASTM E8E (2004) recommendation as shown in Fig. 4.1. The center of both faces of the coupon was attached with a 5 mm post yield strain gauge to capture the tensile strain while extensometer was used to record the displacement beyond the strain gauge limit. In the test setup, one end of the coupon was gripped by the loading arm of the test machine while the other end was secured to an immobile base. Displacement-controlled loading rate of 0.1 mm/min was applied up to yield and then increased to 1 mm/min between yield and fracture.

The average yield stress of the stainless steel 316 at 0.2% proof strain is 260.9 MPa while the mild steel has slightly higher average yield stress of 309.2 MPa, as determined from their respective tensile stress–strain curves in Fig. 4.2. However, the ultimate engineering stress and strain of the stainless steel are higher than the mild steel as compared in Table 4.1. All the coupon specimens failed with tensile necking as shown in Fig. 4.3. It was noted that the fracture point did not occur exactly at the center of specimen, particularly for the mild steel. Hence, it is necessary to capture the post yield extension of the coupons by using extensometer.

4.2.2 Cement Grout

Due to the small depth of the SCS sandwich panel as compared to its length and width,

it was proposed that the confined core space was filled with concrete by using pump in order to eliminate the need for welding after pouring and also to ensure better casting quality. Self-compacting concrete (SCC) with 6 mm maximum aggregate size was initially proposed in view of its superior workability as compared to normal concrete for such space constraint. After several trial mixes to verify the workability and pumpability of the SCC mix using the IMER pump, it was finally confirmed that the pump was unable to provide sufficient pressure to consistently move the SCC without bleeding or segregation. As a result, the pre-mixed Parvex Davco cement grout with minimum compressive strength of 40 MPa was sourced to replace the SCC mix. Based on the supplier recommendation of 3.5 to 5 liter of water per bag of grout (25 kg), 4 liter water per bag mix proportion was selected and trial mix was conducted to ensure that the grout was pumpable and segregation-free with sufficient workability and setting time before the actual casting. During the casting of SCS sandwich panels for the structural test, nine 100 × 200 mm cylinders and six 100 mm cubes samples were prepared for material test. The grout was pumped from the top of the cylinder and cube moulds without compaction or vibration in order to mimic the casting of the panels.

The uniaxial compression test was carried out in accordance to the ASTM C39/C39M (2005) test standard. The cylinder samples were loaded using the 1000 kN MTS machine under displacement-controlled rate of 0.1 mm/min as shown in Fig. 4.4. Two 30 mm post yield strain gauges were used to measure the longitudinal strain and another two were applied for the transverse strain. The softening response was captured by using four Linear Variable Displacement Transducers (LVDT) as seen in the uniaxial compression stress–strain curves plotted in Fig. 4.5.

Tensile splitting test on three cylinder samples were carried out to determine the tensile stress of the cement grout. Each cylinder was placed horizontally between the loading surfaces of the compression test machine as shown in Fig. 4.6. The compression load was applied diametrically and uniformly along the length of cylinder until the failure of the cylinder along the vertical diameter.

The material properties of the cement grout as determined from the uniaxial compression test (ASTM C469, 2002) are summarized in Table 4.2. The average compressive and tensile stresses were obtained as 50.3 MPa and 4.9 MPa.

4.3 Preparation of Specimens

Stainless steel (SS316) tanks with and without infilled water (SWS and SAS) were investigated to study the influence of water on the resistance of the steel tank structure. Two stiffeners with cut-out holes for water flow were welded to the top and bottom plates and the tank was enclosed by four side plates. As seen in Fig. 4.7, a 20mm ($\frac{3}{4}$ inch) inlet pipe and an outlet pipe of the same size, both with threaded plug, were provided so that the SWS tank can be filled with water before test. For comparison purpose, the pipes were also included in the SAS tank.

Two SCS sandwich panels with different core depth of 50 and 75 mm were fabricated from mild steel plates that were fillet welded together to form the outer skin as shown in Fig. 4.8. 32 mm ($\frac{1}{4}$ inch) inlet pipe with stopper ball valve and 32 mm ($\frac{1}{4}$ inch) outlet pipe with threaded cap were provided at the side and end plates of the panels

for the pumping of cement grout into the core. The schematic drawings of the four specimens are shown in Fig. 4.9 and Fig. 4.10 and the details are summarized in Table 4.3.

4.4 Test Setup and Instrumentation

For the lateral pressure load test setup, the specimen was roller-supported at two ends by 80 mm (diameter) round bars. The clear span between the bars was 900 mm as shown in Fig. 4.11. The load was applied at the mid-span point through an inflated airbag which was placed on top of the test specimen via a 1000 mm × 1000 mm × 30 mm thick transfer steel plate. The distance between the transfer plate and specimen was kept at 120 mm throughout the test. To load the specimen, the airbag was continuously charged using a compressed air pump so that the inflating airbag, which was restrained on the top by the fixed transfer plate, will apply increasing pressure onto the specimen. This loading method allows a slower change in contact area between airbag and specimen as compared to displacing the actuator at a certain displacement-controlled rate. The rate of displacement at the mid-span point of the test specimen was kept within the static loading rate of less than 1 mm/min throughout the test. The air supply pressure was also manually controlled using the regulator as shown in Fig. 4.12 to maintain an approximately constant deformation rate for the specimen.

Fig. 4.13 shows the positions of LVDTs and strain gauges at the bottom plate of the specimen. Seven LVDTs were provided to measure the displacements and deflection shapes along the span length and across the width direction. For the SAS and SWS

tanks, strain gauges S0, S1 and S2 were used to capture the strain distribution along the span direction while S0, S4, S5 and S6 were used to measure the strain distribution across the width direction. For the SCS sandwich panels, three additional strain gauges were used to record the strain distribution across the side plate at mid-span. The strain and displacement data were recorded using the data logger as seen in Fig. 4.12. Other than this, the non-contact area from edge of specimen to contacting edge of airbag and specimen was measured at every loading interval of 20 kN or less.

4.5 Discussion on Test Results

4.5.1 Load–Displacement Response and Failure Mode

4.5.1.1 SAS and SWS Tanks

Both of the SAS and SWS tanks underwent large ductile deformation beyond peak load as observed from their respective pressure load–displacement curves in Fig. 4.14. For the SWS tank, its maximum resistance is about 30% higher than the SAS tank. The comparison shows that the infilled water is effective to maintain the shape of the steel tank during loading and delay the occurrence of local buckling. At the post failure range, the resistance of SWS tank was decreased due to cracking of the welds and leakage of water.

Fig. 4.15 shows the flexure failure of the SAS and SWS tanks with plastic hinge at mid-span. Buckling was observed near mid-span of the side plates of both tanks, as shown in Fig. 4.16 for the SAS tank. This is attributable to the unsymmetrical load acting on the side plates, which could be visualized as web of a C-channel with the

top and bottom plates as flanges. Buckling of top plate along the stiffener at the weaker cut-out positions was also observed from the figure. At the post failure range, leakage of water from the SWS tank occurred due to cracking of welds between the stiffener and bottom plate as shown in Fig. 4.17. The final deformed shape of the SWS tank after leakage were similar to that of the SAS tank, which highlights the role of water in the improved resistance.

4.5.1.2 SCS50 and SCS75 Sandwich Panels

The pressure load–displacement responses of the SCS50 and SCS75 sandwich panels are compared in Fig. 4.18. A short plateau before yielding can be seen in both curves. This is likely due to the occurrence of debonding between the steel plates and grout core which results in lower stiffness and weakened composite action between the steel plates and grout core.

The deformed shapes of the SCS50 sandwich panel before and after the occurrence of shear failure are compared in Fig. 4.19. The shear failure was brittle, sudden and accompanied by a loud cracking sound. Spalling of the grout can be seen through the failure of welds between the bottom plate and side plate and also the tearing from the side plate to top plate due to the large shear deformation. Without shear connectors, the shear resistance of SCS sandwich panel is contributed by the core layer, top plate and side plate, among which the grout core is the main contributor. Thus, the possible measures to avoid such brittle shear failure under pressure load are by (a) increasing the thickness of top steel plate, (b) applying embedded reinforcing bars to the concrete core within the zone with high shear force and (c) increasing the span to depth ratio.

Due to the limitation of the allowable maximum airbag pressure of 0.8 MPa, the relief valve on the airbag was opened before the SCS75 panel has reached its ultimate resistance. Thus, the SCS75 panel was re-tested to failure under line load after the lateral pressure load test and the load–displacement curve is plotted in Fig. 4.20. The panel failed under flexure as shown in Fig. 4.21. Debonding between top plate and grout layer and buckling of top plate can be seen from the deformed shape. The observed failure modes are consistent with the structural form of the panel without shear connectors, which would otherwise resist the transverse and longitudinal shear and also delay the debonding between the top plate and grout core.

4.5.1.3 Maximum Resistance and Failure Mode

The maximum resistances and failure modes of the four specimens are compared in Table 4.4. It can be seen that the thicker and stiffer SCS50 and SCS75 sandwich panels exhibited much higher resistance as compared to the stainless steel tanks. However, the SAS and SWS tanks, which failed under flexure with large deformation, were superior in terms of ductility.

The SCS50 sandwich panel failed suddenly in brittle shear mode at mid-span displacement of 52.3 mm. The shear failure would also occur in the SCS75 sandwich panel due to its higher thickness to span ratio. Meanwhile, the SAS tank was able to maintain 84.2% of its maximum resistance at mid-span displacement of 100.9 mm, which is equivalent to a high ductility ratio of 6.2. Similar ductility was also observed for the SWS tank albeit at a lower remaining resistance of 72.6% of maximum resistance after the leakage of water. Based on the static test results, it was deduced that the SCS sandwich panel can be applied as add-on layer to increase the blast resistance of SWS tank provided that the aforementioned measures to avoid shear

failure are adopted to improve its ductility.

4.5.2 Load–Strain Response

4.5.2.1 SAS and SWS Tanks

The development of strains with loading along the span and across the width of the specimen is plotted in Fig. 4.22 and Fig. 4.23 for the SAS and SWS tanks, respectively. Before reaching the peak load, the strain readings at mid-span and quarter-span (Fig. 4.22(a)) of the SAS tank were similar. Beyond that, the strains at both quarter-spans began to decrease while the one at mid-span continued to rise. This indicates that the plastic hinge was developing at mid-span after the peak load. Fig. 4.22(b) compares the strains along the width direction and the strain reading near the stiffener (S4) was largest among all four before the peak load, indicating that load was transferred more through the stiffener as compared to the side plate. As the SAS tank sustained further deformation beyond the peak load, the strain near side plate (S6) became larger than the rest, which was due to occurrence of buckling near the side plate. The readings of strain gauges S0 at mid-span and S5 between the stiffener and side plate were smaller in comparison to S4 and S6, which is attributable to the shear lag effect where normal strain/stress in flange (top and bottom plates) further from the web (stiffener/side plate) is smaller than those near the web for thin-walled flanged flexural members (Reissner, 1986; Moffatt *et al.*, 1975). Fig. 4.22(c) compares the two strain gauges at mid-span and the longitudinal strain reading (S0) was evidently larger than the transverse strain reading (S3). This observation is consistent with the response of one-way supported member.

Fig. 4.23(a) compares the strain readings of SWS tank along the span direction. The

two quarter-span strain gauges recorded higher tensile strain than mid-span from the beginning of loading. This was unexpected and likely caused by the geometric imperfection of the SWS tank. All three strain readings decreased after the leakage of water at load of 86.4 kN, which demonstrates the role of water in distributing the load to bottom plate and improving the overall resistance of the tank. Fig. 4.23(b) compares the strain readings along the width direction. Similar to the SAS tank, the strain reading of S4 near stiffener was largest before peak load and it continued to increase after the leakage while the strain readings of S0 and S5 decreased after the leakage. The development of strain reading S6 near side plate agreed with the buckling deformation shown in Fig. 4.17, which was slightly off from the mid-span. The shear lag effect of strain S5 between stiffener and side plate was less obvious as compared to the SAS tank, which also demonstrates the effect of water in distributing the load to bottom plate in the SWS tank. As shown in Fig. 4.23(c), the larger longitudinal strain, smaller transverse strain response of the one-way supported SWS tank is also similar to the SAS tank.

4.5.2.2 SCS50 and SCS75 Sandwich Panels

The strain distribution of the SCS50 and SCS75 along the span direction are plotted in Fig. 4.24(a) and Fig. 4.25(a), respectively. The strain readings at mid-span (S0) were larger than those at quarter-spans (S1 and S2). This is because the bending moment at mid-span is larger than the quarter-span under lateral pressure load. Consistent with the load–displacement response of the panels, the plateau that indicates the stress redistribution after the debonding between grout core and steel plates was also observed in the load–strain curves.

From the plots of the strain distribution across the width in Fig. 4.24(b) and Fig. 4.25(b) for the SCS50 and SCS75 panels respectively, it can be seen that the strain near side plate (S4) increased more than the mid- (S0) and quarter-width (S3) strains after the plateau. This shows that the stresses were transferred to the side plate after the debonding near the mid- and quarter-width area. For the SCS50 sandwich panel which was tested to failure, it can be seen that the load was distributed back to the mid-span near the failure load.

Fig. 4.24(c) and Fig. 4.25(c) show the strain distribution across the side plate at mid-span for the SCS50 and SCS75 sandwich panels, respectively. It can be seen that the plate was under bending in the test. The neutral axis moved from the center of the side plate towards the top plate with increasing pressure loading for both panels. Subsequently for the SCS50 panel, the center strain reading S9 was reversed from tension to compression near to the failure load. This could indicate the failure of grout core whereby the compressive stress was transferred to the steel plate after failure of the grout.

4.5.3 Deflection Shapes

The deflection shapes of the four specimens, which are required to establish the equivalent SDOF system, are drawn in Fig. 4.26 and Fig. 4.27 at selected load levels in span and width directions, respectively. The load levels were selected such that the displacement intervals of adjacent load levels were similar.

The deflection shape of beam bending under lateral pressure load is a polynomial function in elastic range and a bi-linear function in plastic range after the formation of

plastic hinge at mid-span (Biggs, 1964). It should be mentioned that the deflection shape was derived only considering the flexure deformation not the shear deformation. As seen in Fig. 4.26, the deflection shapes of all four specimens were not exactly a polynomial function in elastic range nor bi-linear function when the plastic hinge was formed. One reason is that the shear deformation also contributed to the deflection shapes of the test specimens. Besides, the specimen may not be treated as a true beam due to its more complex geometry and the composite action in the sandwich panels. Hence, the deflection shapes from test could be applied to obtain more accurate construction of the SDOF system. As seen in Fig. 4.26(b) for the SWS tank, the displacement at quarter-span was higher than mid-span, which corresponds to the unexpected higher quarter-span strain readings as discussed previously.

Although the specimens were roller-supported at two ends, the mid-span deflection shapes along the width direction were not the same particularly at the beginning of loading as compared in Fig. 4.27. This is likely due to the influence of side plates in all specimens and stiffeners in the tanks. Besides, the concave in SCS75 panel at low load level may be attributed to the geometric imperfections of the specimen. The measured deflection shapes along the width direction will also be used to obtain the more accurate representation of the SDOF model.

4.5.4 Contact Area

The contact area between airbag and specimen, which changes with air pressure, was measured continuously during the test. Fig. 4.28 compares the relationships between the measured contact area and applied load for the four specimens and the change in contact area decreased with increasing load as the airbag was progressing towards its

fully inflated state. The four contact area–load curves were also close to each other, thus, showing that the same loading method was consistently applied on the different specimens.

4.6 Analysis of Specimens Subject to Lateral Pressure Load

4.6.1 Water Tank

The cross-section of the SAS tank at mid-span consists of two C-shape and I-shape beams as shown in Fig. 4.29. Hence, the bending resistance of SAS tank can be obtained by summing the bending resistance of these beams. According to EN 1993-1-1, The cross-section classification of these beams are all class 4, which means that local buckling will occur before the attainment of yield stress in one or more parts of the cross-section (Eurocode 3, 2005). Hence, effective width may be used to make the allowances for reductions in resistance due to the effects of local buckling. Besides, shear lag effects in flanges should also be taken into account by the use of an effective width according to EN 1993-1-5. Therefore, the effective width of tension flange was calculated considering shear lag effects and the effective width of compression flange was calculated considering combined effects of shear lag and plate buckling. The calculated effective widths are given in Fig. 4.29.

The bending resistance of SWS tank is difficult to evaluate since the effect of water on the resistance has not been analytical studied and no design code has been found up to date. Since the shear resistance of water is negligible, it theoretically has no contribution to the shear lag. However, it was observed from the test that it could reduce the shear lag effect of bottom plate, which might be due to the maintained

shape of SWS tank by water. Since water is incompressible and maintained the volume of SWS tank, the local buckling of top plate was partially hindered due to the confinement by water and airbag. However, it is still difficult to quantify the buckling resistance by water and the quantification is out of this research scope. Based on above analysis, the effective width of compression flange considering water effect in resisting local buckling is suggested in Eq. (4.1).

$$b_{eff}^w = b_{eff}^{cs} + \tilde{\lambda} (b_{eff}^s - b_{eff}^{cs}) \quad (4.1)$$

where b_{eff}^w is the effective width considering water effects in resisting local buckling, b_{eff}^{cs} is the effective width considering combined effects of shear lag and plate buckling, b_{eff}^s is the effective width considering shear lag effects and $\tilde{\lambda}$ is the influencing factor of water effects on plate buckling. The influencing factor $\tilde{\lambda}$ is varying from 0 to 1, which stands for no effects and fully restriction on plate buckling, respectively. It is found that the prediction is close to the test result when $\tilde{\lambda} = 0.62$. This demonstrates that water can partially hinder the local buckling. However, the determination of influencing factor α may need further analytical and experimental study and is out of the current research scope.

Since the shear resistance of water is negligible, the shear resistance of the SAS and SWS tanks is the same and can be calculated by Eq. (4.2) based on EN 1993-1-1 (Eurocode 3, 2005).

$$V_{pl,Rd} = \frac{A_v (f_y / \sqrt{3})}{\gamma_{M0}} \quad (4.2)$$

where A_v is the shear area.

4.6.2 SCS Sandwich Panels

Although the bending resistance of a full or partial composite SCS sandwich beam is given by the EN 1994-1-1 (Eurocode 4, 2004), the SCS sandwich panel with side and end plates cannot be simply treated as a SCS sandwich beam. The load transfer mechanism between steel plates and concrete core has to be analyzed to determine the bending resistance of such panel. The configuration of SCS sandwich panel before and after deformation is shown in Fig. 4.30. Since the bond between steel plates and concrete core was negligible and no shear connector was used, the composite action between steel plates and concrete core of the SCS sandwich panel was contributed by the end plate. In the absence of end plate, the top/bottom plate and concrete core will bend separately. In such scenario, the length of top/bottom plate over its thickness is nearly unchanged due to the thin plates, while the top layer of concrete core shortens and the bottom layer extends. Due to the existence of end plate, the extension of concrete core at bottom layer will be constrained and therefore its bottom layer at end and top layer at mid-span are under compression. Then, the compression zone along the concrete core can be obtained in Fig. 4.31. It is noted that the end plate has the function similar to shear connectors to provide the composite action between top/bottom plate and concrete core. In terms of top/bottom plate, the bottom plate is in tension and the stress of top plate is mainly influenced by the side plate instead of concrete core due to the separation between the end plate and top layer of concrete core as shown in Fig. 4.30. Under bending, the top plate near the side plate is under compression while certain distance away may have little compression due to the shear lag effect. This shear lag effect will be taken into account to determine the effective width of top plate under compression.

Fig. 4.32 shows the cross-section of the SCS sandwich panel at mid-span, which can be divided into three sections to calculate the bending resistance based on the previous discussions. The force distributions in the cross-section of sections A, B and C are shown in Fig. 4.33. As the width in section B is determined by considering the shear lag effect according to BS EN 1993-1-5 (Eurocode 3, 2005), the top plate within sections B and A is under compression and zero stress, respectively.

In section A, the top layer of concrete core is under compression and bottom plate is under tension. Hence, the effective compression depth of concrete core T_c can be obtained in Eq. (4.3) based on force equilibrium.

$$T_c = \frac{f_y t_t}{\bar{\eta} f_c} \quad (4.3)$$

where f_y and f_c are the yield strength of bottom plate and compressive strength of concrete core; t_t is the thickness of bottom plate; $\bar{\eta} = 1.0$ for $f_c \leq 50$ MPa, $\bar{\eta} = 1.0 - (f_c - 50)/200$ for $50 < f_c \leq 90$ MPa (Eurocode 2, 2004). The bending resistance of section A can then be calculated as

$$M_A = f_y t_t (t_t/2 + h_c - T_c/2) B_A \quad (4.4)$$

where h_c is the concrete core depth and B_A is the width of section A. In section B, the top plate is under compression and bottom plate is under tension. Since these two plates are of equal thickness and strength, the bending resistance of the section is reached when the neutral axis of concrete core moves near to the lower surface of the top plate. Therefore, the bending resistance in Section B can be calculated as

$$M_B = f_y t (h_c + t) B_B \quad (4.5)$$

where t is the thickness of top or bottom plate and B_B is the width of section B. In

section C, the side plate is under bending and it can be treated as a beam with rectangular section. Hence, the bending resistance of section C is obtained as

$$M_C = f_y W_z \quad (4.6)$$

where W_z is the plastic section modulus.

The transverse shear resistance, V_{rd} , of the SCS sandwich panel without shear connectors is contributed by concrete core, top/bottom plates and side plates as follow:

$$V_{rd} = V_c + V_{sp} \quad (4.7)$$

in which the contribution of top/bottom plates is included by modifying the effective depth of concrete core (Yan *et al.*, 2014). The shear resistance of the concrete core can be calculated as (Yan *et al.*, 2014)

$$V_c = \left[C_{Rd,c} k \eta_1 (100 \rho_1 f_{ck})^{1/3} \right] B h_e \quad (4.8)$$

where $C_{Rd,c} = 0.18/\gamma_c$ for normal weight concrete; $k = 1 + \sqrt{200/h_c} \leq 2.0$ with h_c in mm; $\rho_1 = t_t/h_c \leq 0.02$ and $\eta_1 = 0.40 + 0.60\bar{w}/2200$ where \bar{w} is the density of concrete in kg/m^3 . Considering the influence of top/bottom plate, the effective depth of the panel needs to be modified to

$$h_e = h_c + t_c E_s / E_c \quad (4.9)$$

where t_c is the thickness of compression steel plate and E_s and E_c are the elastic modulus of steel plate and concrete, respectively. The transverse shear resistance of side plate can be calculated by Eq. (4.2) given by EN 1993-1-1 (Eurocode 3, 2005).

4.6.3 Comparison with Test Results

The analytical calculations are compared to the lateral pressure loading test results in

Table 4.5. The calculated bending resistance of SAS tank according to Eurocode 3 matches well with the test result. Since there is no analytical solution to quantify the water effects on the local buckling of compression plate, an influencing factor is proposed to calculate the effective width of compression flange and it is found that the prediction is close to the test result when the influencing factor equals to 0.62. It is noted that the calculated shear resistances of SAS and SWS tanks are smaller than the calculated bending resistances, while flexure failure mode was observed for both SAS and SWS tanks in the test. This indicates that the shear resistance formula given by Eurocode 3 is conservative. As discussed earlier, shear failure mode was observed in the test on the SCS50 sandwich panel and the calculated shear resistance agrees well with the test result. The calculated bending resistance is conservative as indicated by the actual failure mode of the SCS 50 sandwich panel. The conservative predictions are caused by neglecting friction forces between the face plates and concrete core and neglecting strength hardening after the yield of the steel face plate.

4.7 Finite Element Analysis of Specimens under Lateral Pressure Load

FE analysis was conducted using LS-DYNA to simulate the responses of water tanks and SCS sandwich panels under lateral pressure load. Compared to physical tests, FE analysis could provide more detailed information and comprehensive observations on the structural responses, which helps to understand their behaviors under lateral pressure load.

4.7.1 Material Models

4.7.1.1 Concrete Material Model

Concrete is a complex heterogeneous material that exhibits non-linear inelastic behavior under multi-axial stress states. To accurately predict the material response and failure modes under a variety of loading situations, the key characteristics including the influence of confinement on concrete strength and energy absorption capacity, compression hardening and softening behaviors, volumetric expansion upon cracking, tensile fracture and softening, biaxial response and strain rate effects under dynamic load (Crawford *et al.*, 2012) have to be captured in the constitutive model, which defines the relationship between flow variables that relate stress to deformation and internal energy (Hallquist, 2006).

The Karagozian & Case material model (MAT_72R3 in LS-DYNA) developed by Malvar *et al.* (1997) was adopted in this study to model the cement grout layer. The stress tensor of a material may be decoupled into a hydrostatic pressure and a deviatoric stress tensor (Chen and Han, 1998) and this decouple was adopted in this material model. Although the material model was built to simulate the response of concrete under dynamic load (Malvar *et al.*, 1997), it has been shown that the model reasonably captured the material response under both quasi-static loading (Malvar *et al.*, 1997; Malvar *et al.*, 2004; Crawford *et al.*, 2012) and dynamic loading (Malvar *et al.*, 1997; Lin *et al.*, 2014, Lei *et al.*, 2014).

The deviatoric response of MAT_72R3 is defined by three independent failure surfaces that describe the plastic behavior of concrete. The three surfaces are the

initial yield surface, maximum failure surface and residual surface written as follow:

$$\Delta\sigma_y = a_{0y} + \frac{P}{a_{1y} + a_{2y}P} \quad (\text{Initial yield surface}) \quad (4.10)$$

$$\Delta\sigma_m = a_0 + \frac{P}{a_1 + a_2P} \quad (\text{Maximum failure surface}) \quad (4.11)$$

$$\Delta\sigma_r = \frac{P}{a_{1f} + a_{2f}P} \quad (\text{Residual surface}) \quad (4.12)$$

where p is pressure and parameter a_{ij} , which defines the failure surfaces, can be determined through uniaxial tension, uniaxial compression and triaxial compression tests. Option to automatically generate a standard set of the eight a_{ij} parameters for a given compressive strength of normal concrete is available in LS-DYNA. If the compressive strength ratio of a new material to the reference material is r , then the new coefficients of failure surface can be written in terms of the old ones as

$$a_{0n} = a_0 r, \quad a_{1n} = a_1, \quad a_{2n} = a_2 / r \quad (4.13)$$

In this material model, if the current stress state lies between the yield and maximum surfaces, the current failure surface is linearly interpolated between the yield and maximum surfaces based on the value of damage parameter η for hardening stage, as shown in Eq. (4.14). A similar interpolation is performed between the maximum and residual surfaces for softening stage if the current stress state is located between the maximum and residual surfaces, as shown in Eq. (4.15).

$$\Delta\sigma = \eta(\Delta\sigma_m - \Delta\sigma_y) + \Delta\sigma_y \quad (4.14)$$

$$\Delta\sigma = \eta(\Delta\sigma_m - \Delta\sigma_r) + \Delta\sigma_r \quad (4.15)$$

In above equations, the damage parameter η varies between 0 and 1 depending on the accumulated effective plastic strain parameter λ . The η is 0 when $\lambda=0$ and 1

when $\lambda = \lambda_m$. The η then decrease to 0 at some larger value of λ . Since λ is defined to be non-decreasing, the $\Delta\sigma$ can sequentially take on the values $\Delta\sigma_y$, $\Delta\sigma_m$ and $\Delta\sigma_r$ (Malvar, *et al.*, 1997).

The above $\Delta\sigma$ versus p relationships define the compressive meridian of the failure surface in the principal stress space. Hence, it is needed to establish the relationship between any point in the failure surface and the compressive meridian to form the full failure surface. The deviatoric plane shape typically transitions from triangular curves with smooth corners at low pressures to circular at high pressures (Chen, 1982). Therefore, the third invariant, Lode angle θ , is adopted to describe the deviatoric plane of concrete and the shape proposed by Willam and Warnke is adopted to provide a smooth and convex triangular surface generated by elliptical segments. Then, the principal stress difference $\Delta\sigma$ between the tensile and compressive meridian can be obtained by multiplying the compressive meridian with a ratio r' , which is defined as

$$r' = \frac{2(1-Q^2)\cos\theta + (2Q-1)\sqrt{4(1-Q^2)\cos^2\theta + 5Q^2 - 4Q}}{4(1-Q^2)\cos^2\theta + (1-2Q)^2} \quad (4.16)$$

In Eq. (4.16), $Q = r_t/r_c$, where r_t and r_c are the radii of the tensile and compressive meridians, respectively.

To capture the varying deviatoric plane with increasing pressure, the ratio of radii of tensile meridian to compressive meridian Q is defined as a piecewise linear function of pressure p as follow

$$Q(p) = \begin{cases} 1/2 & p \leq 0 \\ 1/2 + 3f_t/2f_c' & p = f_c'/3 \\ \frac{\alpha f_c'}{a_0 + \frac{2\alpha f_c'/3}{a_1 + 2a_2\alpha f_c'/3}} & p = 2\alpha f_c'/3 \quad \text{with } \alpha = 1.15 \\ 0.753 & p = 3f_c' \\ 1 & p \geq 8.45f_c' \end{cases} \quad (4.17)$$

In MAT_72R3, the accumulated effective plastic strain parameter λ , which governs the stress–strain relationship, is defined as follow

$$\lambda = \int_0^{\varepsilon_p} \frac{d\varepsilon_p}{r_f (1 + p/r_f f_t)^{b_1}} \quad \text{for } p \geq 0 \quad (4.18)$$

$$\lambda = \int_0^{\varepsilon_p} \frac{d\varepsilon_p}{r_f (1 + p/r_f f_t)^{b_2}} \quad \text{for } p < 0 \quad (4.19)$$

where r_f is the strain rate enhancement factor, b_1 and b_2 are the damage scaling exponents and $d\varepsilon_p$ is the effective plastic strain increment given by $d\varepsilon_p = \sqrt{(2/3) \varepsilon_{ij}^p \varepsilon_{ij}^p}$. The damage scaling exponents b_1 and b_2 govern the softening of the unconfined uniaxial stress–strain curve in compression and tension, respectively (Malvar *et al.*, 1997). Whenever the stress path is close to the triaxial tensile test path, a volumetric damage increment is added to the deviatoric damage as follow

$$\Delta\lambda = b_3 f_d k_d (\varepsilon_v - \varepsilon_{v,yield}) \quad (4.20)$$

where b_3 is the input scalar multiplier, k_d is the internal scalar multiplier, ε_v is the volumetric strain and $\varepsilon_{v,yield}$ is the volumetric strain at yield. The factor f_d is used to limit the effect of this change to the paths close to the triaxial tensile path by

$$f_d = \begin{cases} 1 - \frac{|\sqrt{3J_2}/p|}{0.1}, & 0 \leq |\sqrt{3J_2}/p| < 0.1 \\ 0 & |\sqrt{3J_2}/p| \geq 0.1 \end{cases} \quad (4.21)$$

The smeared crack band model was adopted for MAT_72R3 to avoid spurious mesh sensitivity caused by strain-softening (Malvar *et al.*, 1997). In this model, to ensure the constant fracture energy dissipation, the value of b_2 is determined by iterative calculations until the area under the stress–strain curve for a uniaxial unconfined tensile test coincides with G_f/h , where G_f and h are the fracture energy and element size, respectively. Similarly b_3 and b_1 are found using hydrostatic triaxial tensile test and uniaxial unconfined compressive test, respectively. In this study, the fracture energy from uniaxial unconfined compressive test on the cement grout was used to determine b_1 . The fracture energy in tension-softening was referred from Ishiguro (2007) in Eq. (4.23) to determine b_2 .

$$G_f = 0.0251f_c^{0.105} \quad (4.22)$$

where f_c is the compressive strength of grout in MPa. In absence of test data, the value of b_3 is assumed to be 1.15 as suggested by Malvar *et al.* (1997). This parameter determines the energy dissipation in triaxial tensile path, which is relatively small compared with the energy dissipation in compressive path. Hence, this assumption has no significant effect on the structural response.

The volumetric response of concrete material is defined in MAT_72R3 by the tabulated Equation of State (EOS), numbered as EOS_8 in LS-DYNA. The EOS relates the hydrostatic pressure, p , the relative volume, V , and the internal energy, e_i . In the loading (compression) phase, the pressure is defined as

$$p = C(\varepsilon_v) + \gamma T(\varepsilon_v) e_i \quad (4.23)$$

where ε_v is the natural logarithm of the relative volume, C and T are coefficients given as function of ε_v and e_i is the internal energy. Unloading occurs at the slope corresponding to the bulk modulus at the peak (most compressive) volumetric strain. Reloading follows the unloading path to the point where unloading begins and continues on the loading path (Hallquist, 2006).

In this study, the thermal state of concrete $\gamma T(\varepsilon_v) e_i$ in Eq. (4.23) was not considered and the values of C and ε_v can be generated by using the automated generation option in MAT_72R3, which is based on uniaxial strain test on concrete material (Malvar *et al.*, 1997). Since the bulk modulus of grout is different from that of normal concrete, the bulk modulus of grout (13.83 GPa) obtained from uniaxial unconfined compressive test was applied to the parameters in EOS.

Since the strain rate effects may have significant influence on the strength and failure mode of concrete material (UFC, 2008; CEB, 1993; Ross *et al.*, 1989; Ross *et al.*, 1996; Grote *et al.*, 2001), the strain rate enhancement was captured in MAT_72R3 by modifying the failure surface and damage function λ through the modified damage function in Eqs. (4.18) and (4.19). A radial rate enhancement on the concrete failure surface was implemented and the enhanced strength $\Delta\sigma_e$ corresponding to pressure p is determined as follow (Malvar *et al.*, 1997):

$$\Delta\sigma_e = \gamma_f \Delta\sigma(p/\gamma_f) \quad (4.24)$$

where γ_f is the strain rate enhancement factor or Dynamic Increase Factor (DIF).

For the simulation of specimens under lateral pressure load in this chapter, the DIF

was not considered in the FE models.

4.7.1.2 Steel Material Model

The Piecewise_Linear_Plasticity material model (Mat_24) was adopted to simulate the stainless steel and mild steel materials. For this material model, an arbitrary stress versus strain curve, an arbitrary strain rate dependency and a failure based on plastic strain can be defined. The material properties of the stainless steel and mild steel were determined from tensile coupon test, which has been given in Section 4.2.1. The strain rate effect is described using the Cowper-Symonds model which scales the yield stress as follow:

$$\sigma_y(\varepsilon_{eff}^p, \dot{\varepsilon}_{eff}^p) = \sigma_y(\varepsilon_{eff}^p) \left[1 + \left(\frac{\dot{\varepsilon}_{eff}^p}{D} \right)^{1/q} \right] \quad (4.25)$$

where $\sigma_y(\varepsilon_{eff}^p)$ is the yield stress, $\dot{\varepsilon}_{eff}^p$ is the effective plastic strain rate, and D and q are the strain rate parameters. Similar to the concrete material, the DIF of steel was not included in the FE models when simulating the specimens under lateral pressure load in this chapter.

4.7.1.3 Water Material Model

The Mat_elastic_fluid model (Mat_1_fluid) in LS-DYNA (Hallquist, 2012) was adopted to simulate the behavior of water in the lateral pressure test, because this material model is applicable for Lagrange formulation which is suitable for simulating the static behavior of confined water without severe element distortion. Besides, the computing time is significantly less than Eulerian formulation.

The volumetric response of water is defined by the bulk modulus, and the value used

in this study was 2.2 GPa (Whita, 1986). Although the relationship between hydrostatic pressure and volumetric strain is nonlinear at high hydrostatic pressure (Gurtman *et al.*, 1971) and cannot be captured by this model, the linear relationship is still applicable for the low hydrostatic pressure level (less than 100 MPa) involved in this study. Meanwhile, the deviatoric response of water is defined by a tensor viscosity, S_{ij} , written in terms of the damping coefficient as follow

$$S_{ij} = V_c \Delta L a \rho \dot{\epsilon}_{ij} \quad (4.26)$$

where V_c is the tensor viscosity coefficient, ΔL is the characteristic element length, a is the bulk sound speed of water, ρ is the water density and $\dot{\epsilon}_{ij}$ is the deviatoric strain rate.

4.7.2 Element Type and Formulation

The S/R Hughes-Liu shell element (Hallquist, 2012) was employed for the face plates of water tank and SCS sandwich panel as it can capture the performance of thin plate components and reduce the computing time as compared to fine solid element. The water and cement grout core were both meshed using eight-point solid element with reduced integration. The Lagrangian formulation, which is generally suitable for elements without severe element deformation, was adopted for the stainless steel, mild steel, concrete and water in the lateral pressure test.

4.7.3 Contact and Loading Approach

In the FE model, the contacts between two “parts” are captured through ‘master-slave’ contact interfaces, which are defined by using the surface to surface contact option in LS-DYNA. The penalty-based contact approach is a generally used method where the

contact spring stiffness is determined by the algorithm according to the sizes and material properties of contact segments. Hence, it works more effectively when the material stiffness parameters between the contacting surfaces are of the same order-of-magnitude, such as that between the face plates and the bar support in this study. However, this contact might break down when materials with dissimilar stiffness come into contact, as the contact stiffness, which is roughly the minimum of the slave and master stiffness, may be too small. Therefore, the soft constraint-based contact approach, whose contact stiffness is independent of material parameters and well suited for treating contact between materials of different stiffness, was used to simulate the interaction between face plate and water or concrete.

Since the contact area between airbag and specimen varied continuously during the lateral pressure test as shown in Fig. 4.28, it is difficult to replicate the actual load area in the FE model. Therefore, four contact areas were selected from the measured area during test to represent the varying contact area in the FE model as illustrated in Fig. 4.34 for the SAS tank. The applied pressure–time curve for each of the load area was increased from zero to maintain a continuously increasing applied force as shown in Fig. 4.35. The pressure P_1 , P_2 , P_3 and P_4 were selected by ensuring similar pressure differences between the adjacent applied pressures, i.e. $P_4 - P_3 \approx P_3 - P_2 \approx P_2 - P_1 \approx P_1$.

The implicit solver was incorporated into LS-DYNA to simulate the response of structures under quasi-static loading whereas the explicit solver was meant for dynamic analysis. Since the pressure load acting on specimen is specified as load curves input in the implicit analysis, the softening stage cannot be properly captured.

Therefore, the explicit solver was adopted to capture the softening stage. The dynamic effect should be eliminated when using explicit solver to simulate the quasi-static response. Normally, the inertia force is checked to ensure it is within the tolerable level. Since the evolution of internal and kinetic energy is easier to obtained, it is more widely used to judge the dynamic effect (Rust and Schweizerhof, 2003). When the ratio of kinetic-to-internal energy is negligible, it is reasonable to treat the loading as a quasi-static manner (Egan *et al.*, 2012).

4.7.4 Finite Element Model

Due to symmetry, quarter FE models of the specimens and round bar supports were established as shown in Fig. 4.36. The round bar support in the test setup was welded to a rigid rectangular mounting frame and therefore the nodes along the bottom of the round bar support were restricted from translation and rotation in the FE model. The airbag was not explicitly modeled, since it has negligible contribution to the resistance of specimen due to its flexibility.

4.7.5 Discussion on Finite Element Results

4.7.5.1 Empty Steel Tank and Water Filled Tank

The FE simulated load–displacement curves are compared with the test results in Fig. 4.37 and the FE models are able to predict the responses of SAS and SWS tanks with reasonable accuracy. The difference in maximum load between FE predictions and test results for SAS and SWS tanks were 8.0% and 5.0%, respectively. Both the FE models underestimated the maximum load, especially for the SAS tank. This is because the pressure load applied onto the specimen in the test is not exactly symmetric and the maximum resistance of one-way supported panel under symmetric

pressure loading in the FE model is lower than that under unsymmetrical pressure load in the test. Besides, the geometric imperfections of the specimens may also cause this disparity.

The welding failure of SWS tank led to water leakage after the peak load and the final deformation mode was similar to that of SAS tank. Since it is difficult to capture the leaking in the FE model and the calculating of SWS tank stopped before the leaking, only the simulated deformation mode of SAS tank is compared with test results in Fig. 4.38. It can be seen from Fig. 4.38(a) that the FE model can reasonably predict the flexure failure mode of SAS tank with plastic hinge at mid-span. Fig. 4.38(b) shows the buckling on the top surface, which is in agreement with the observations from the test. The buckling of top plate along the stiffener near the weaker area with cut-out holes was observed in both FE and test results. This may be caused by the relatively large shear deformation of stiffener near the weaker area as shown in Fig. 4.38(c).

It was found from the test that the SWS tank exhibited up to 31% increase in resistance as compared to the SAS tank. The effects of water in improving the resistance can be attributed to the role of water in maintaining shape of SWS tank, which helped in delaying the occurrence of local buckling. To investigate this, the simulated mid-span clear distances between top and bottom plates of SAS and SWS tanks at their maximum bending resistances are compared in Fig. 4.39. It can be seen that the clear distance of 30 mm before test was maintained at the position of the stiffener and side plate for both the SAS and SWS tanks, while other points along the mid-span shows varying degree of reduction. It is noted from Fig. 4.39 that for both SAS and SWS tanks, the reduction degree of clear distance between stiffener and side

plate ($150\text{mm} < x < 450\text{mm}$) is more significant than that between two stiffeners ($0\text{mm} < x < 150\text{mm}$), although their spacing is same of 300 mm. This different reduction degree is attributed to the different boundary conditions. The rotation of top plate around span direction at stiffener can be treated to be fully constrained because of the symmetric load, while the rotation of top plate at side plate is not fully constrained because the load is unsymmetrical and the side plate cannot fully constrain the rotation of top plate. The current position of stiffener may not be optimal, since the reduction degree of clear distance at two sides of stiffener is different. The optimal position of stiffener is difficult to be directly determined and parametric studies by moving the stiffener is suggested. Fig. 4.40 shows the variation of maximum resistance of SAS tank with moving stiffener. The maximum resistance reaches the peak value when the spacing between side plate and stiffener is half of the spacing between stiffeners ($x=225$).

In comparison, larger clear distance, which indicates smaller deformation of top plate as compared to bottom plate, was observed for the SWS tank. This indicates the contribution of water in transferring part of the load from top plate to bottom plate. Besides, the larger clear distance also results in higher section modulus of SWS tank, which increases the bending resistance.

4.7.5.2 SCS Sandwich Panels

The FE simulated load–displacement curves of the SCS sandwich panels are compared with test results in Fig. 4.41 and the FE models are capable of predicting the resistance of both panels with reasonable accuracy. As discussed earlier in this chapter, the plateau in the load–displacement curves from test was caused by the

debonding between steel plate and grout core. Due to the numerical difficulties in including this weak bond in the FE models, which has little effect on the maximum resistance of the SCS sandwich panels, only the friction was considered in the contact model between steel plate and grout core. The omission of the bond is reflected in the comparison where the stiffness of the FE simulated curve was smaller at initial stage and coincided with the test result after the debonding plateau. In addition, the FE models with full composite between the steel plate and grout core were also established and it is able to reasonably predict the initial stiffness of both panels as shown in Fig. 4.41.

Fig. 4.42 shows the FE simulated shear failure mode of the SCS50 sandwich panel. The shear failure occurred in one side of the specimen as compared to symmetric failure in the simulation, which could be attributed to the geometric imperfection of the specimen and difficulty in achieving a perfectly symmetry uniform loading using the airbag in the test. The failure of weld observed in the test, which can be attributed to the lower strength and ductility of the weld as compared to the mild steel plate, was not captured in the FE model.

The load transfer mechanism between steel plates and concrete core, which is required to evaluate the bending resistance of SCS sandwich panel as discussed earlier in Section 4.6.2, was simulated using the FE model. Fig. 4.43 shows the contours of axial stress in grout core and the compression zone can be clearly seen. The top layer and bottom layer of concrete core are under compression and tension at mid-span, which is consistent to the previous analysis. It can be seen from the contours of axial stress in Fig. 4.44 that the bottom plate is under tension and the axial stress at

mid-span has been yielded. Fig. 4.45 shows the contours of axial stress in top plate. It can be seen that the top plate near the side plate is under compression and the top plate with certain distance away from the side plate is under tension. Therefore, the load transfer mechanism between steel plates and concrete core discussed in the analytical model was demonstrated through FE simulation.

4.7.5.3 Boundary Effects

In the lateral pressure loading tests, the roller-supported boundary conditions were adopted as fully rigid support is usually difficult to be achieved and often resulted in semi-rigid condition, which would complicate the analysis. However, semi-rigid boundary conditions are common in actual structures and hence, the FE models that were experimentally verified were applied to investigate the response of the pin-pin supported tanks and panels with axially restrained boundary. One of the approaches to achieve axially restrained boundary is shown in Fig. 4.46. The end of SWS tank or SCS sandwich panel is connected to anchor bars to achieve axial restriction. The steel plates are used to connect the top and bottom anchor bars to ensure them deforming together and thus increasing the stiffness of axial restriction. Besides, the steel plates can also be used to cancel part of axial force from top and bottom SWS tanks or SCS sandwich panels if both of them are simultaneously subjected to blast loading.

In this study, the same material models, element types and formulations as well as contact approaches discussed previously for the FE models were maintained while the lateral pressure load is now applied onto the full top face of the specimen. The pin-pin supported boundary was specified by restraining the displacement of the nodes along the two edges of both bottom and top plates in vertical and axial directions. This will

be compared to a pin-roller supported boundary whereby only the nodes along the two edges of bottom plate were restrained in vertical direction.

The load–displacement curves of the SWS tank with pin-roller and pin-pin supported boundaries and SAS tank with pin-pin supported boundary are compared in Fig. 4.47. The maximum load and corresponding displacement of pin-roller supported SWS is also given in Fig. 4.47. The resistance of the SWS tank with pin-pin supported boundary is improved significantly compared with the pin-roller supported boundary, which can be attributed to the tensile membrane action. For a pin-pin supported structural member, the resistance in initial stage is primarily contributed by the bending action while the membrane action may have significant contribution to the resistance after development of membrane force (Cormie *et al.*, 2009). The magnitude of improvement in resistance depends on the tensile strength of face plate. The similar load–displacement curves were observed for the SAS and SWS tanks with pin-pin supported boundary, which indicates that water has little effect on the resistance if the pin-pin supported boundary is adopted. For the pin-roller supported SWS tank, water helps to increase the resistance by maintaining the section modulus and delaying the occurrence of local buckling. However, for the pin-pin supported boundary, the local buckling of both SAS and SWS tanks is unlikely to occur and the resistance is mainly contributed by tensile membrane force, which is not affected by the section modulus.

Fig. 4.48 compares the failure modes of SWS tank with pin-roller and pin-pin supported boundaries. In this analysis, the failure strain of stainless steel was 0.636 based on the tensile coupon test results. The flexure failure mode is evident in the effective plastic strain contours of the pin-roller supported tank while the tensile

membrane failure mode is expected for the pin-pin supported SWS tank. Besides, the higher plastic strain appears at location of plastic hinge for the pin-roller supported SWS tank while the plastic strain at the end is relatively higher for the pin-pin supported SWS tank which may cause the tensile membrane failure start to occur at the end.

The load–displacement curves of the SCS50 sandwich panel with pin-roller and pin-pin supported boundaries and the SCS75 sandwich panel with pin-pin supported boundary are compared in Fig. 4.49. The maximum loads and corresponding displacements are also marked. By comparing the load–displacement curves of the SCS50 sandwich panel with pin-roller and pin-pin supported boundaries, it can be seen that both are similar at initial stage. This indicates that the SCS50 sandwich panel mainly relies on the bending action to resist the lateral pressure load at initial stage. After the failure of grout core, the load was taken over by the tensile membrane behavior of the steel plates that were axially restrained while the pin-roller supported panel behaved shear failure. By comparing the load–displacement curves of the pin-pin supported SCS50 and SCS75 sandwich panels, the increase in grout core depth improved the resistance at initial stage but has little effect on the final resistance and ductility. This is because the grout core has no or minimal contribution to the resistance after severe cracking of grout.

The scaled damage measure contours of the SCS50 sandwich panel with pin-roller and pin-pin supported boundaries are compared in Fig. 4.50. The scaled damage measure, which is a function of accumulated effective plastic strain parameter λ , is defined in MAT_72R3 to evaluate the damage level of concrete. When it ranges from

0 to 1, the material transitions from the yield failure surface to the maximum failure surface and when it ranges from 1 to 2, the material transitions from the maximum failure surface to the residual failure surface (Hallquist, 2012). The grout core of both panels underwent severe damage after failure. Shear failure mode can be seen from the plot for the pin-roller supported SCS50 sandwich panel while the tensile membrane failure is shown in the plot for the pin-pin supported panel. The failure strain of mild steel defined in the FE model was 0.307 based on the tensile coupon test results. Due to the different failure modes, the resistance of pin-roller supported panel mainly determined by the shear strength of grout, while the failure strain of mild steel governs the resistance of pin-pin supported panel.

4.8 Summary

The lateral pressure load tests were conducted on four 900 mm (width) × 900 mm (clear span) specimens, which include the empty steel tank (SAS), water filled tank (SWS) and sandwich panels (SCS50 and SCS75). In addition, the analytical and numerical methods were adopted to predict the responses of specimens. The main findings and observations in this chapter are summarized as follow:

- i) The SAS and SWS tanks failed under ductile flexure mode and the resistance of the SWS tank was increased by 31% as compared to the SAS tank. This is because water helped to maintain the section modulus and delayed the occurrence of local buckling.
- ii) The SCS50 sandwich panel failed under brittle shear mode with failure of weld between side plate and bottom plate as well as spalling of the grout core. Such failure mode is undesirable and should be avoided by improving the shear

- resistance within the high shear stress zone near the support. Based on the test results, it was deduced that the SCS sandwich panel with enhanced ductility could be applied as an add-on layer to improve the blast resistance of the SWS tank which has comparatively lower resistance but superior ductility.
- iii) The change in load distribution due to addition of water can be seen from the comparison of load–strain curves of the SWS and SAS tanks. The shear lag effects of strain between stiffener and side plate of the SWS tank was less obvious as compared to the SAS tank. In addition, the longitudinal strain readings at both quarter-spans of the SWS tank continued to increase after peak load while those in the SAS tank showed signs of unloading.
 - iv) Unlike one-way supported beam, the deflection shapes of the four specimens were not exactly a polynomial function in elastic range or bi-linear after the formation of plastic hinge. This could be due to the influences of side plates/stiffeners and also contribution of shear deformation to the overall deflection shapes of the specimens.
 - v) The consistency of the applied loading method was demonstrated by the similar contact area–load curves of the four specimens.
 - vi) The analytical solutions can provide close predictions on the resistances of specimens except for the SWS tank, since there is no analytical solution to quantify the water effects in resisting the local buckling of compression plate and the quantification is out of the current research scope.
 - vii) The analytical model to calculate the bending resistance of the SCS sandwich panel under lateral pressure load was developed and it was proven to be conservative by comparing with test results.

- viii) The established FE models were reasonable in predicting the load–displacement responses and failure modes of water tanks and SCS sandwich panels under lateral pressure load. In addition, the role of water in maintaining the section modulus during the loading was demonstrated in the FE investigation. Therefore, it can increase the resistance of roller-supported SWS tank. However, the buckling of both SAS and SWS tanks is unlikely to occur for the pin-pin supported boundary and the resistance is mainly contributed by tensile membrane force, which is not affected by the section modulus. Hence, water has little effect on the lateral pressure resistance of SWS tank when the pin-pin supported boundary is adopted.
- ix) The lateral pressure resistance can be significantly improved when adopting the pin-pin supported boundary and the failure mode is changed from flexure or shear failure to tensile membrane failure. The magnitude of improvement in lateral pressure resistance depends on the tensile strength and ultimate strain of face plate.

Table 4.1 Material properties of stainless steel and mild steel

Material	Young's modulus (GPa)	Yield stress (MPa)	Ultimate stress (MPa)	Ultimate strain
Stainless steel	197.5	260.9	603.0	0.636
Mild steel	205.2	309.2	452.4	0.307

Table 4.2 Material properties of cement grout

Density (kg/m ³)	Young's modulus (GPa)	Compressive stress (MPa)	Poisson's ratio	Tensile stress (MPa)
2152	24.9	50.3	0.2	4.9

Table 4.3 Details of static test specimens

Label	Material		Dimension (mm)	Thickness (mm)	Schematic drawing
	Skin	Core			
SAS	Stainless steel	-	1100 × 900	3-30-3	Fig. 4.9
SWS	Stainless steel	Water	1100 × 900	3-30-3	Fig. 4.9
SCS50	Mild steel	Grout	1100 × 900	3-50-3	Fig. 4.10
SCS75	Mild steel	Grout	1100 × 900	3-75-3	Fig. 4.10

Table 4.4 Lateral pressure test results

Specimen	Maximum resistance (kN)	Failure mode
SAS	80.3	Flexure
SWS	105.4	Flexure
SCS50	371.5	Shear
SCS75	>508.0	No failure
SCS75 (line load)	369.9	Flexure

Table 4.5 Comparisons between experimental and analytical results

Specimen	F _{exp} (kN) (1)	F _{bend} (kN) (2)	F _{shear} (kN) (3)	(1)/(2) ((1)/(3))	Failure modes
SAS	80.3	72.1	65.1	1.11	Flexure
SWS	105.4	105.2	65.1	1.00	Flexure
SCS50	371.5	337.1	365.5	(1.02)	Shear
SCS75	>508.0	543.5	503.9	(>1.01)	No failure

Note: F_{exp} = experimental load of specimen; F_{bend} = calculated bending resistance of specimen; F_{shear} = calculated shear resistance of specimen.

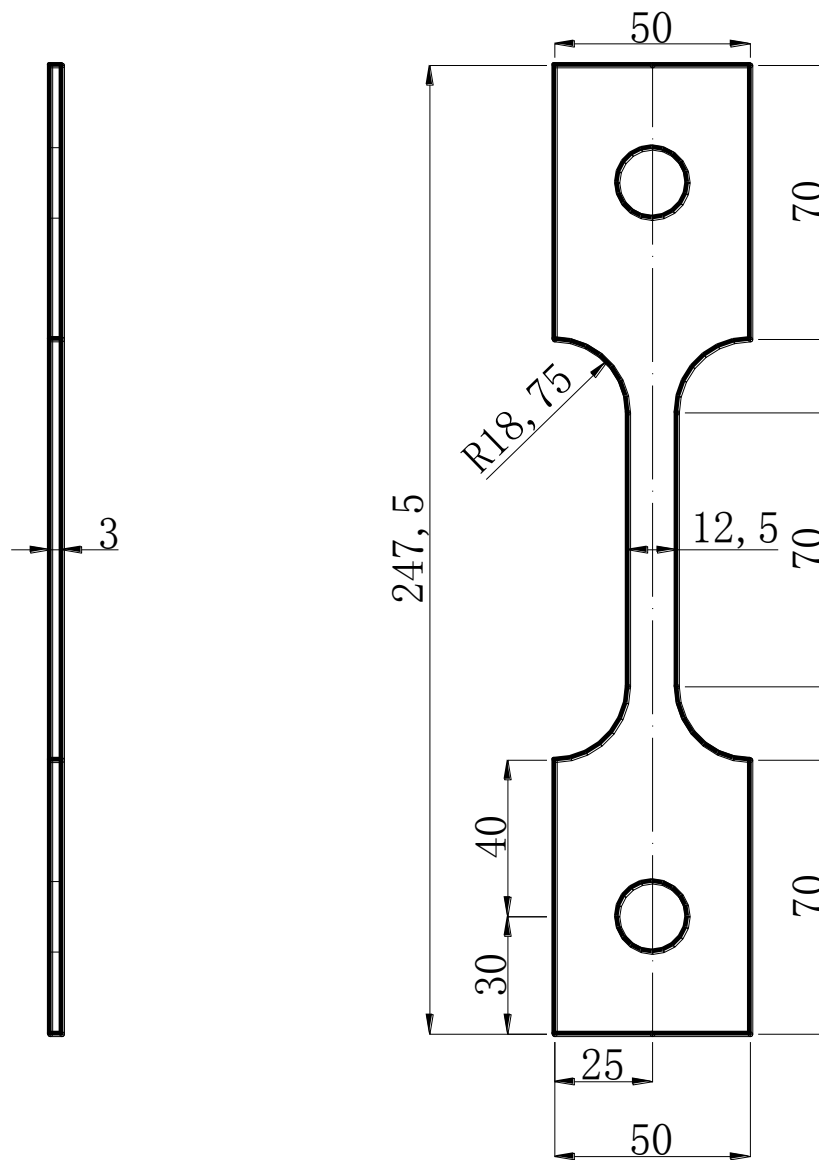


Fig. 4.1 Specification for tensile coupon test (in mm)

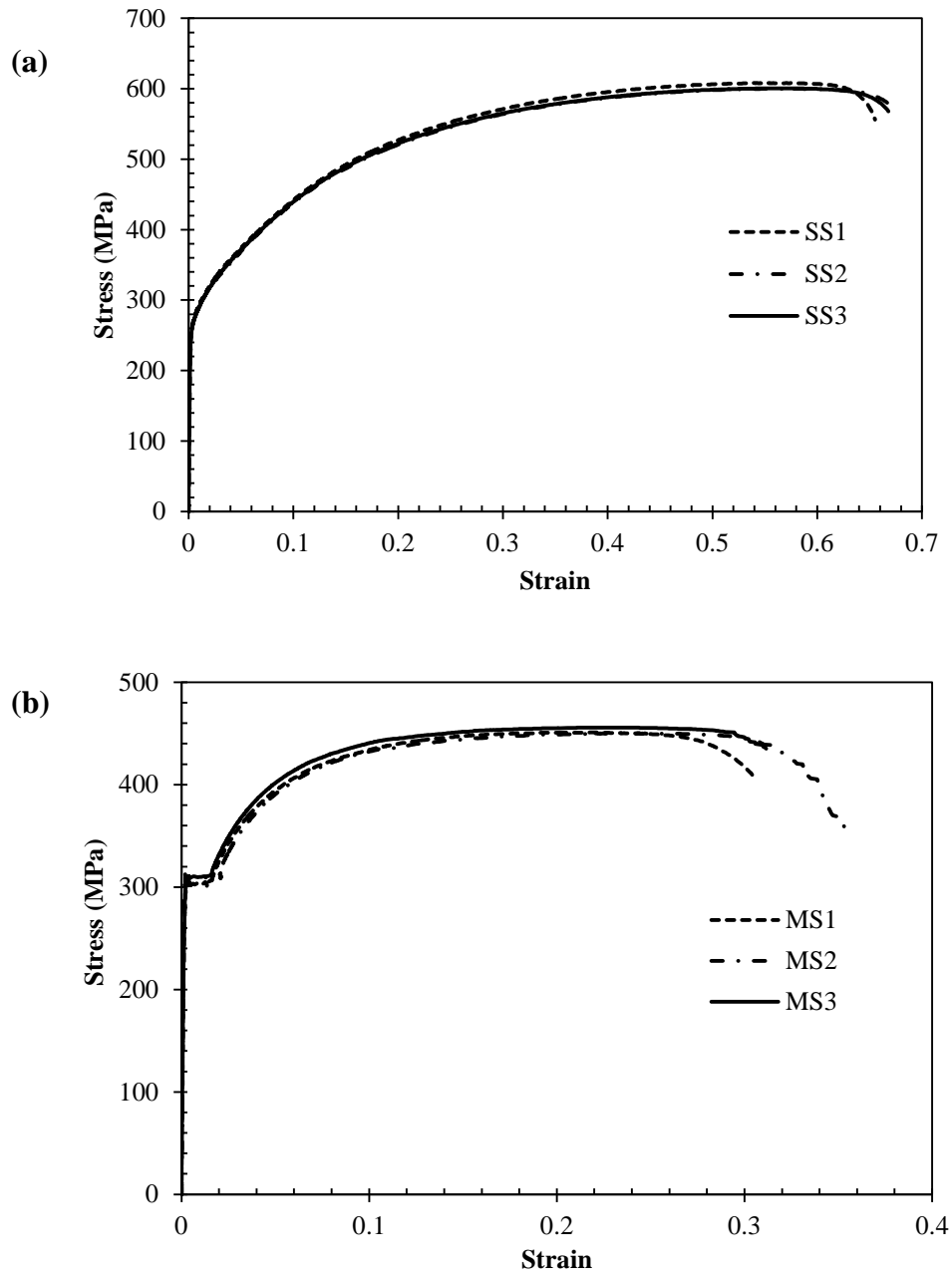


Fig. 4.2 Stress–strain curves of (a) stainless steel (b) mild steel

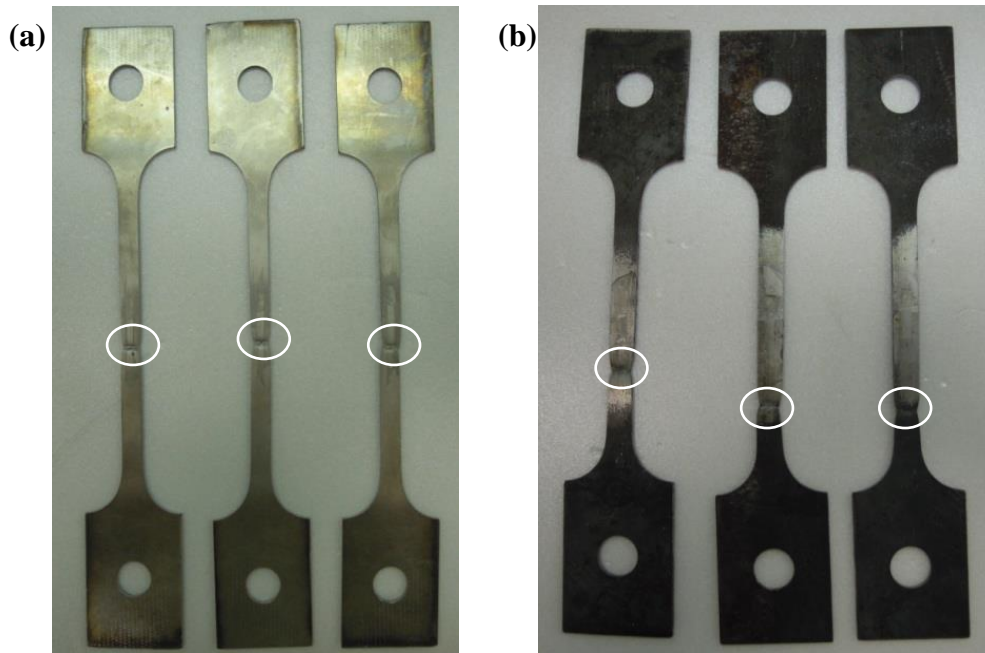


Fig. 4.3 Coupons after tensile test: (a) stainless steel (b) mild steel



Fig. 4.4 Uniaxial compression test setup

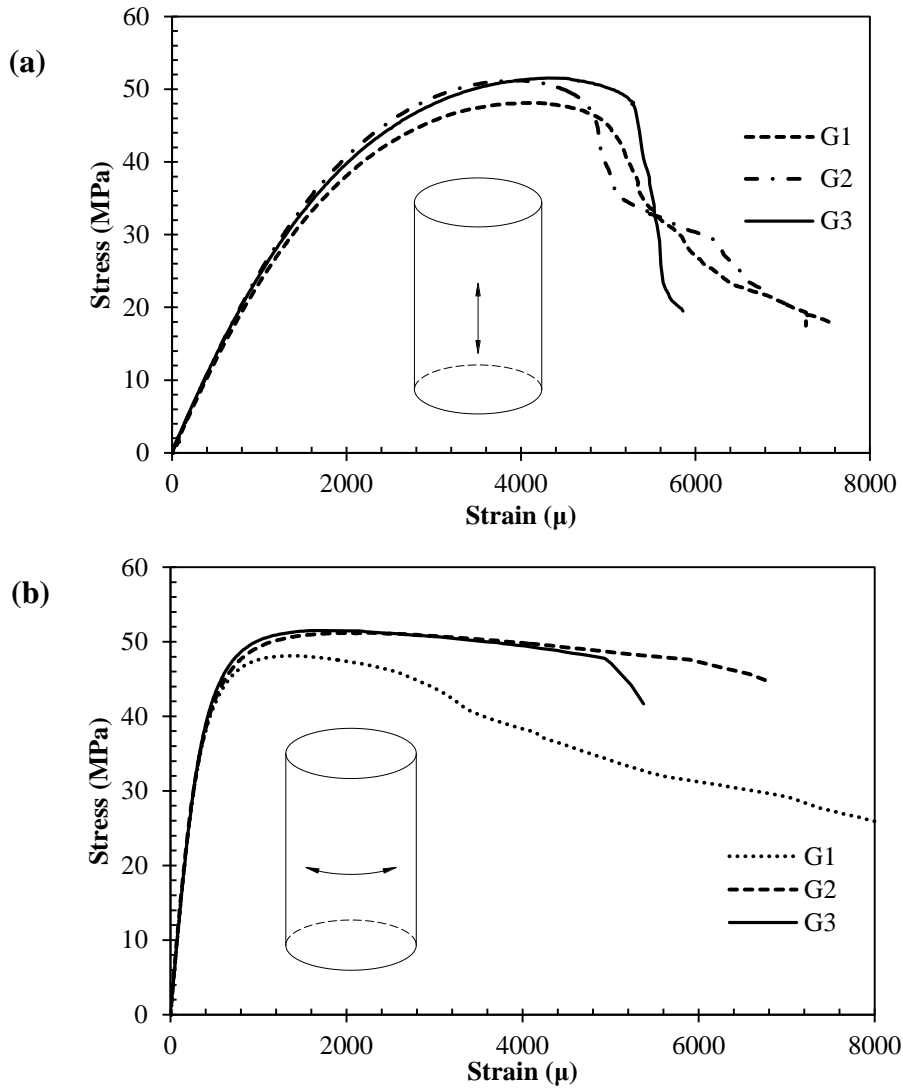


Fig. 4.5 Uniaxial compression stress–strain curves of cement grout: (a) longitudinal direction (b) transverse direction

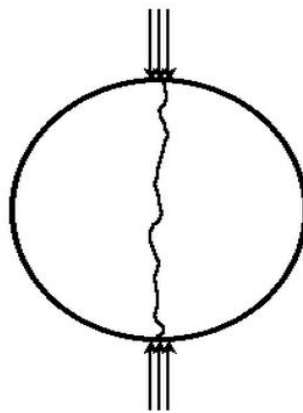


Fig. 4.6 Diagram of splitting test

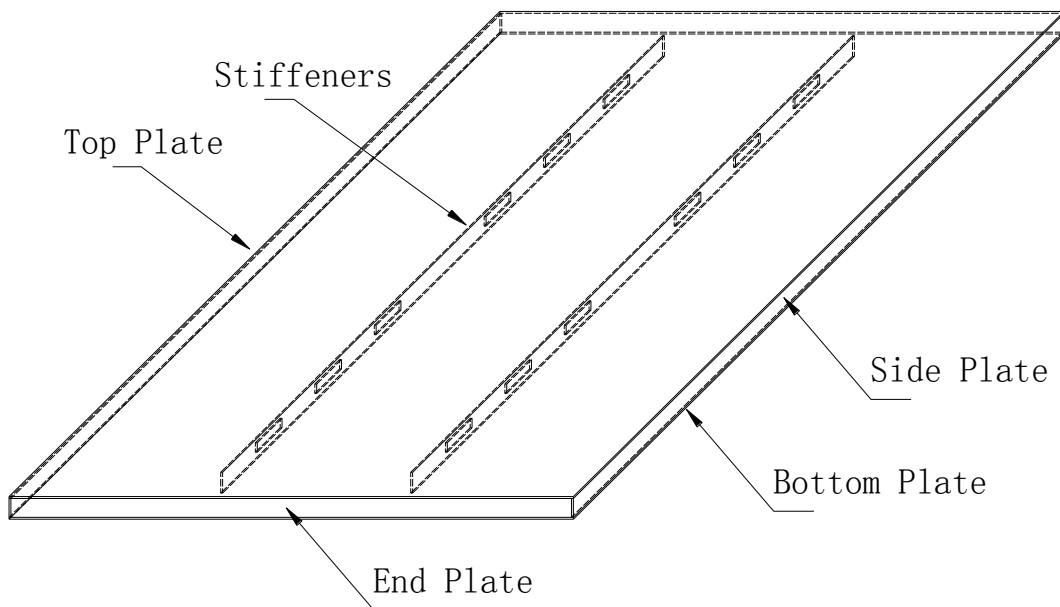


Fig. 4.7 Notation for SAS and SWS tanks

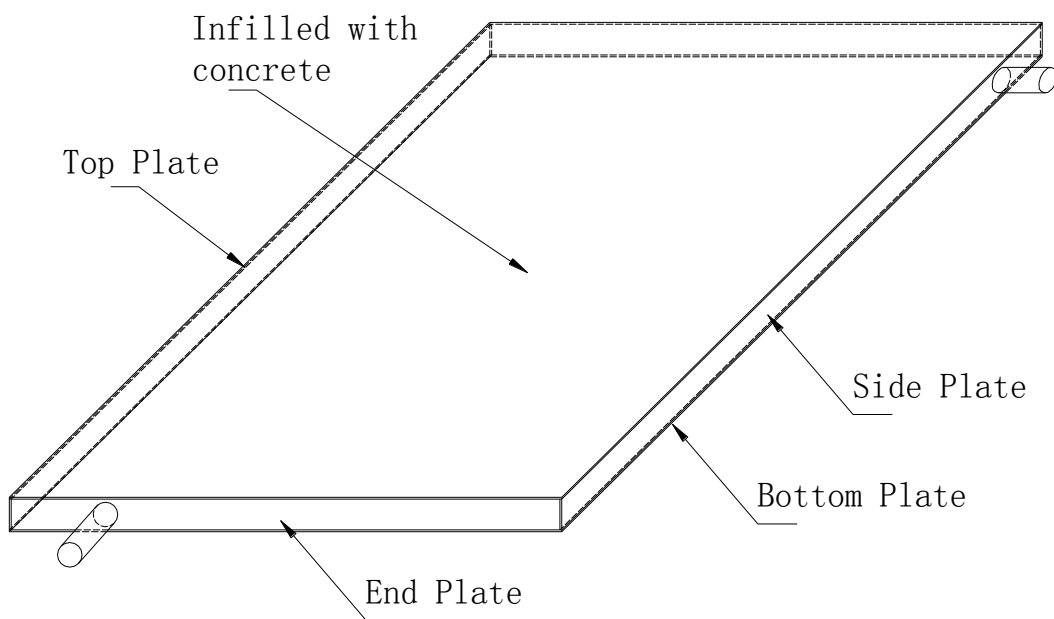


Fig. 4.8 Notation for SCS sandwich panel

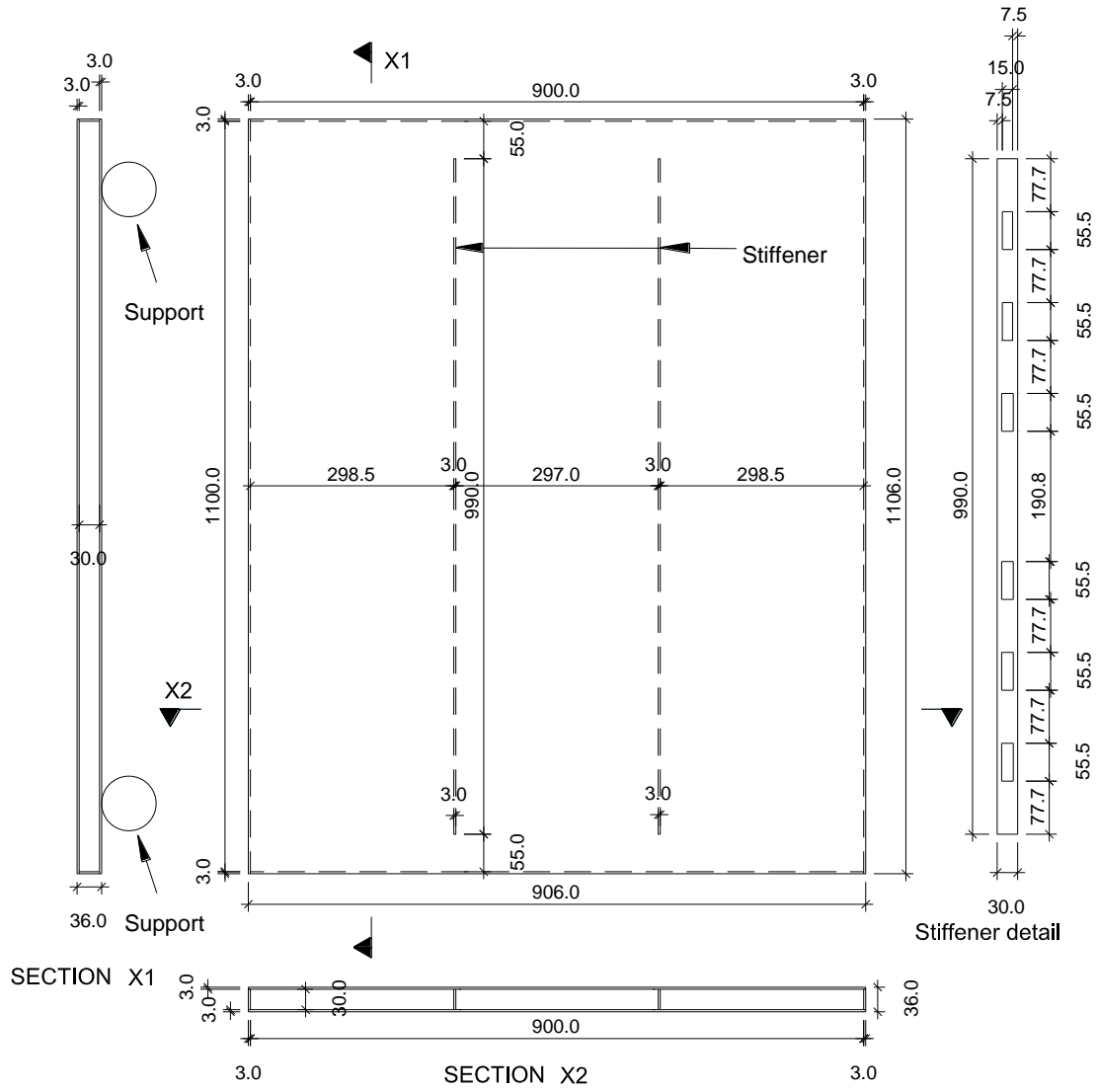


Fig. 4.9 Schematic of SAS and SWS tanks (in mm)

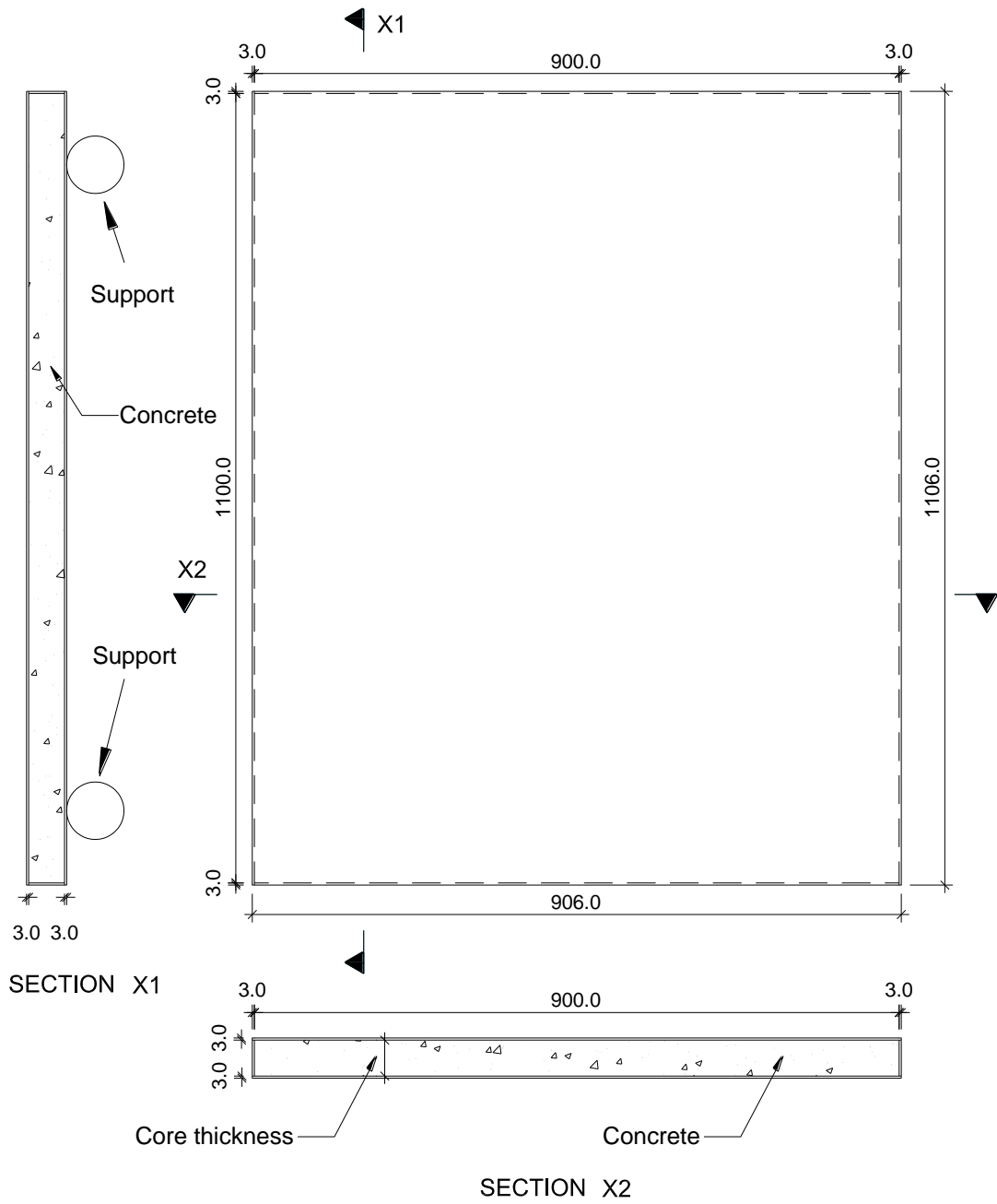


Fig. 4.10 Schematic of SCS sandwich panel (in mm)

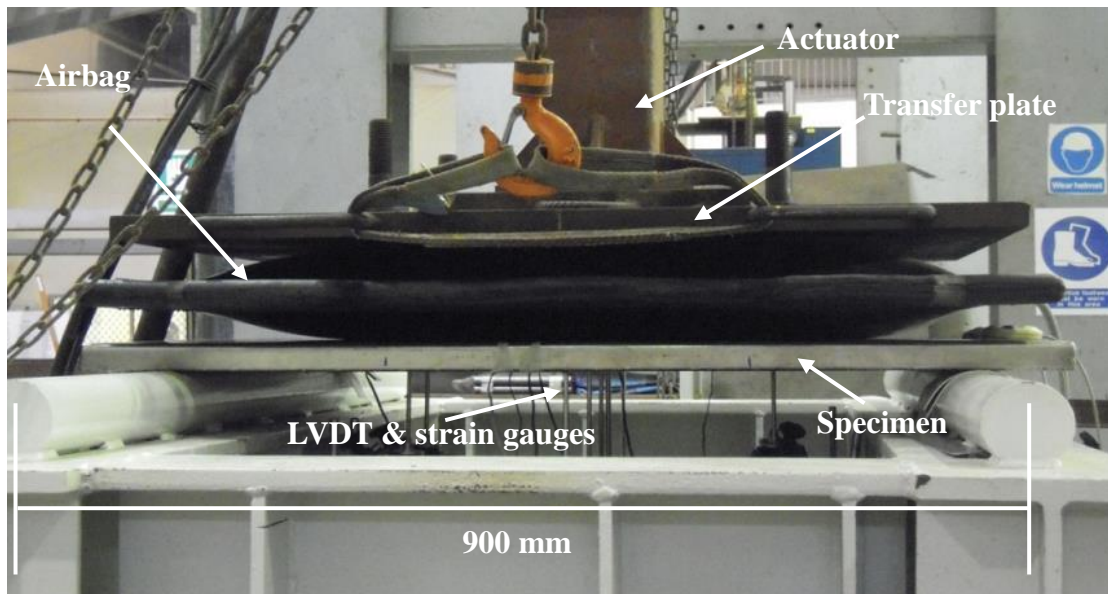


Fig. 4.11 Static test setup

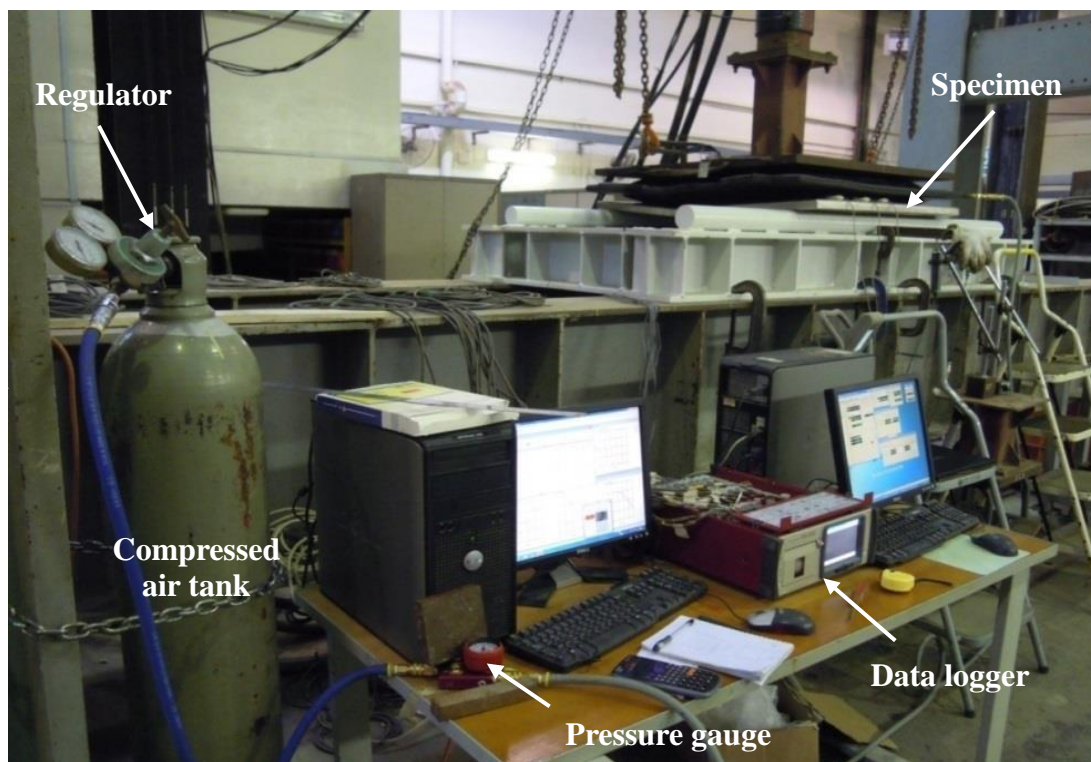


Fig. 4.12 Test control and data acquisition system

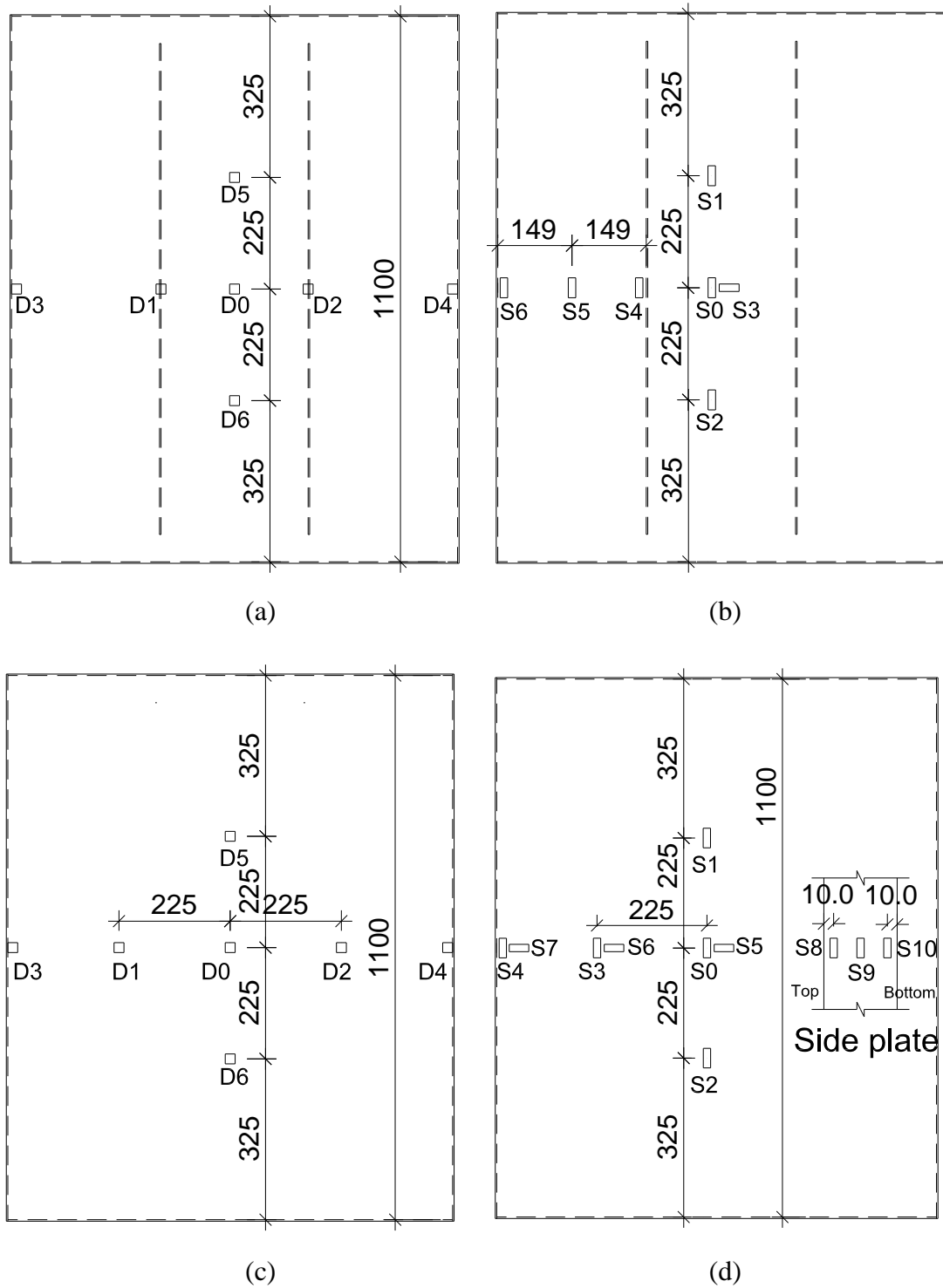


Fig. 4.13 Instrumentation layout (bottom view): (a) LVDTs on SAS and SWS (b) strain gauges on SAS and SWS (c) LVDTs on SCS50 and SCS75 (d) strain gauges on SCS50 and SCS75 (in mm)

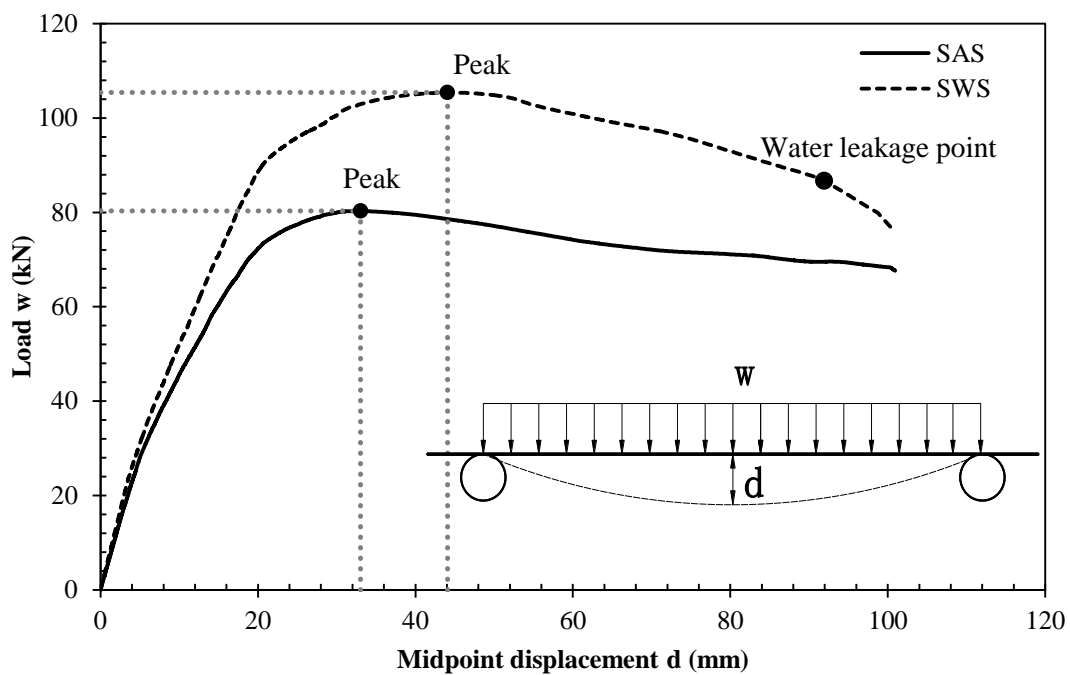


Fig. 4.14 Load–midpoint displacement (LVDT D0) of SAS and SWS tanks under lateral pressure load



Fig. 4.15 Flexural failure of SAS tank

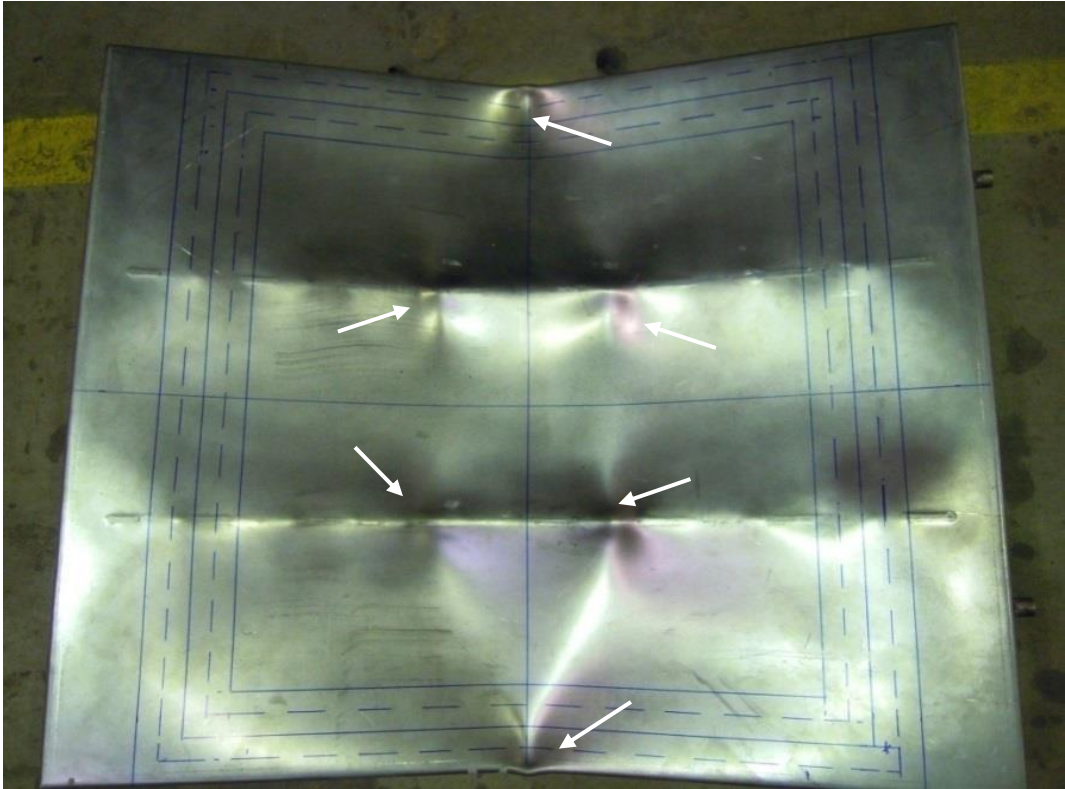


Fig. 4.16 Buckling on top plate of SAS tank

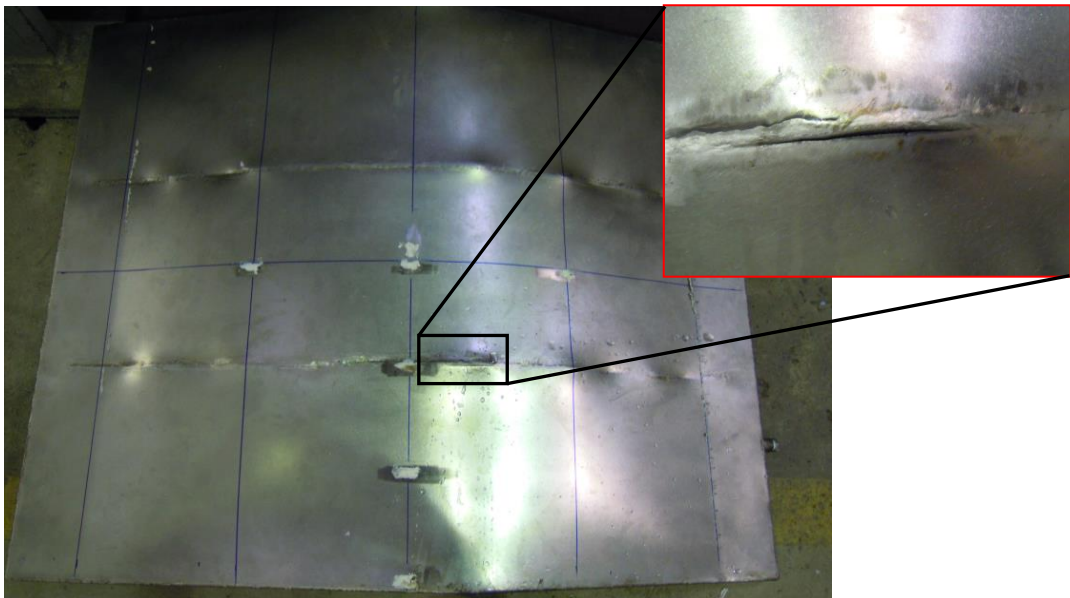


Fig. 4.17 Fracture of weld between bottom plate and stiffener of SWS tank

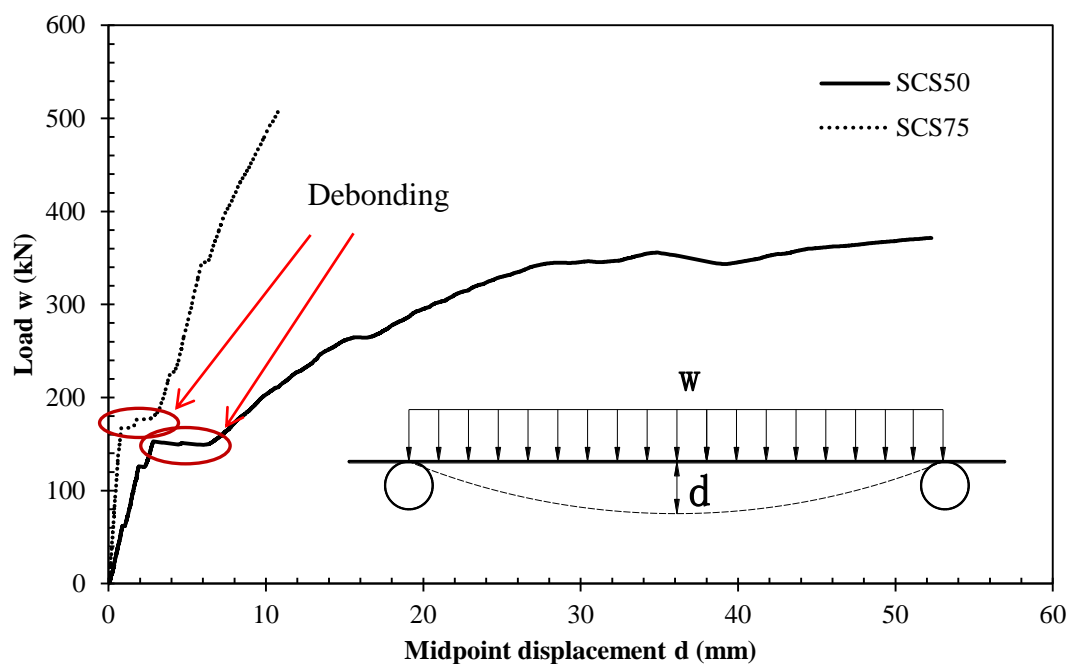


Fig. 4.18 Load–midpoint displacement of SCS50 and SCS75 panels under lateral pressure load

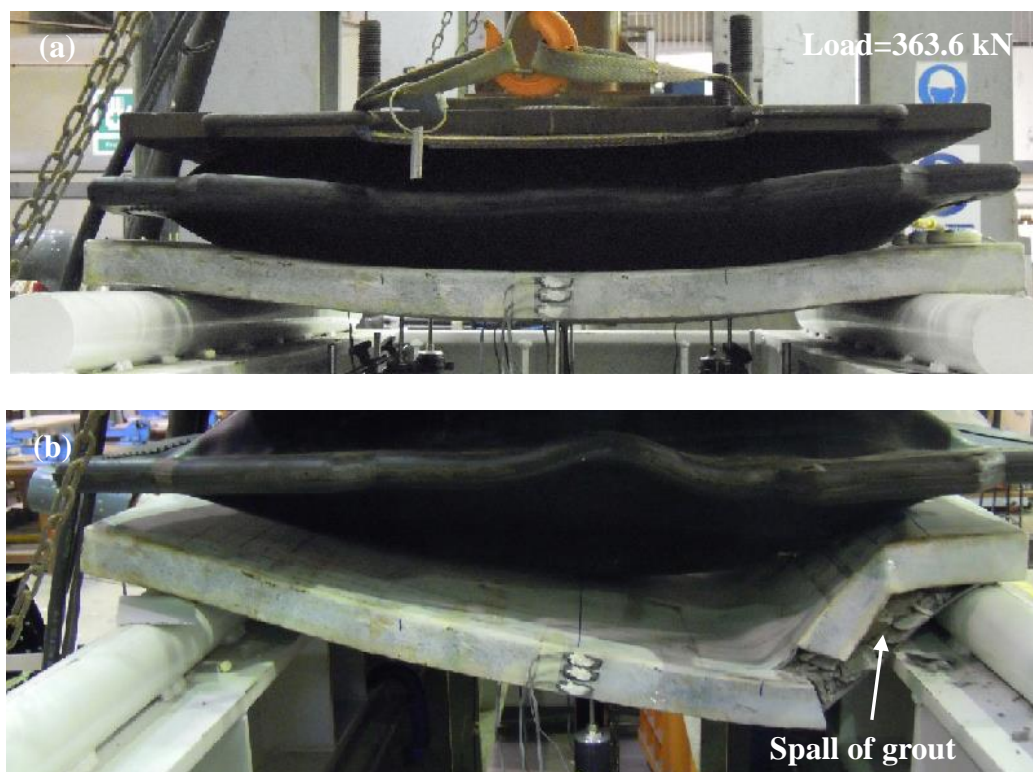


Fig. 4.19 Deformation of SCS50: (a) before shear failure (b) after shear failure

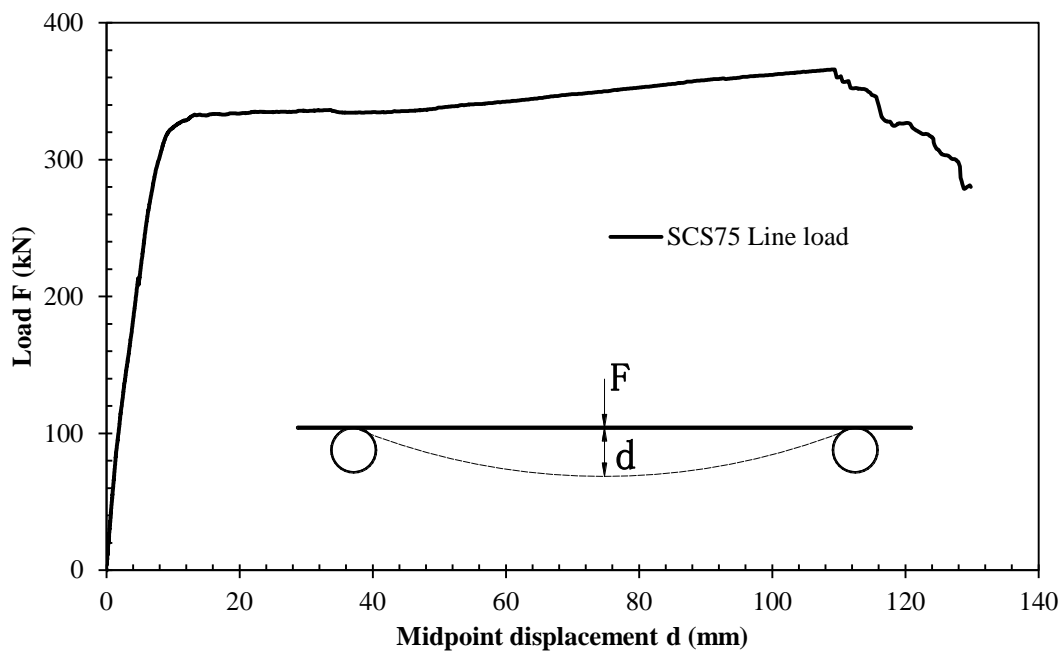


Fig. 4.20 Load–midpoint displacement of re-tested SCS75 panel under line load



Fig. 4.21 Flexure failure of SCS75 panel under line load

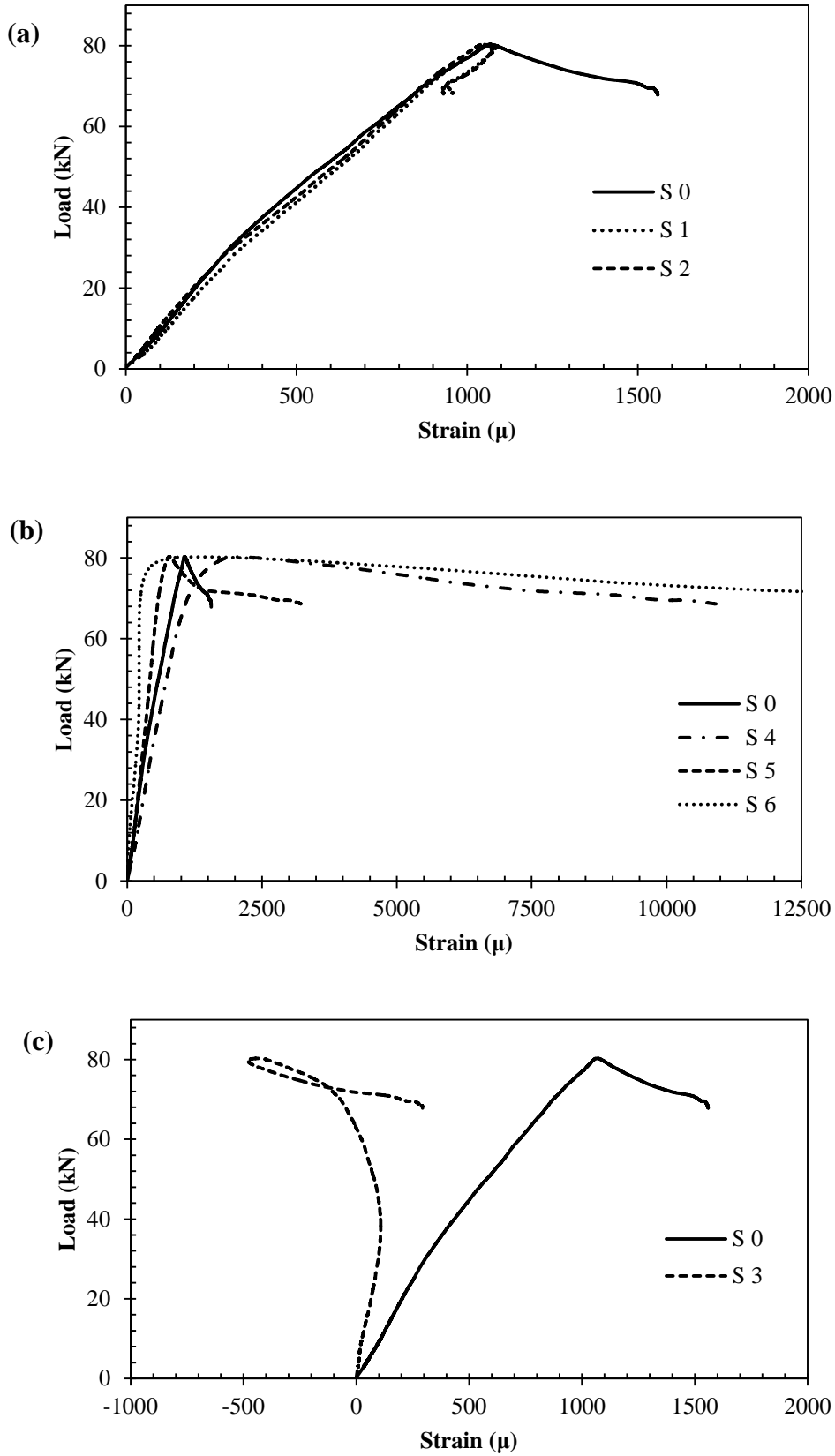


Fig. 4.22 Load–strain curves of SAS: Strain distribution (a) along span direction (b) along width direction (c) at midpoint

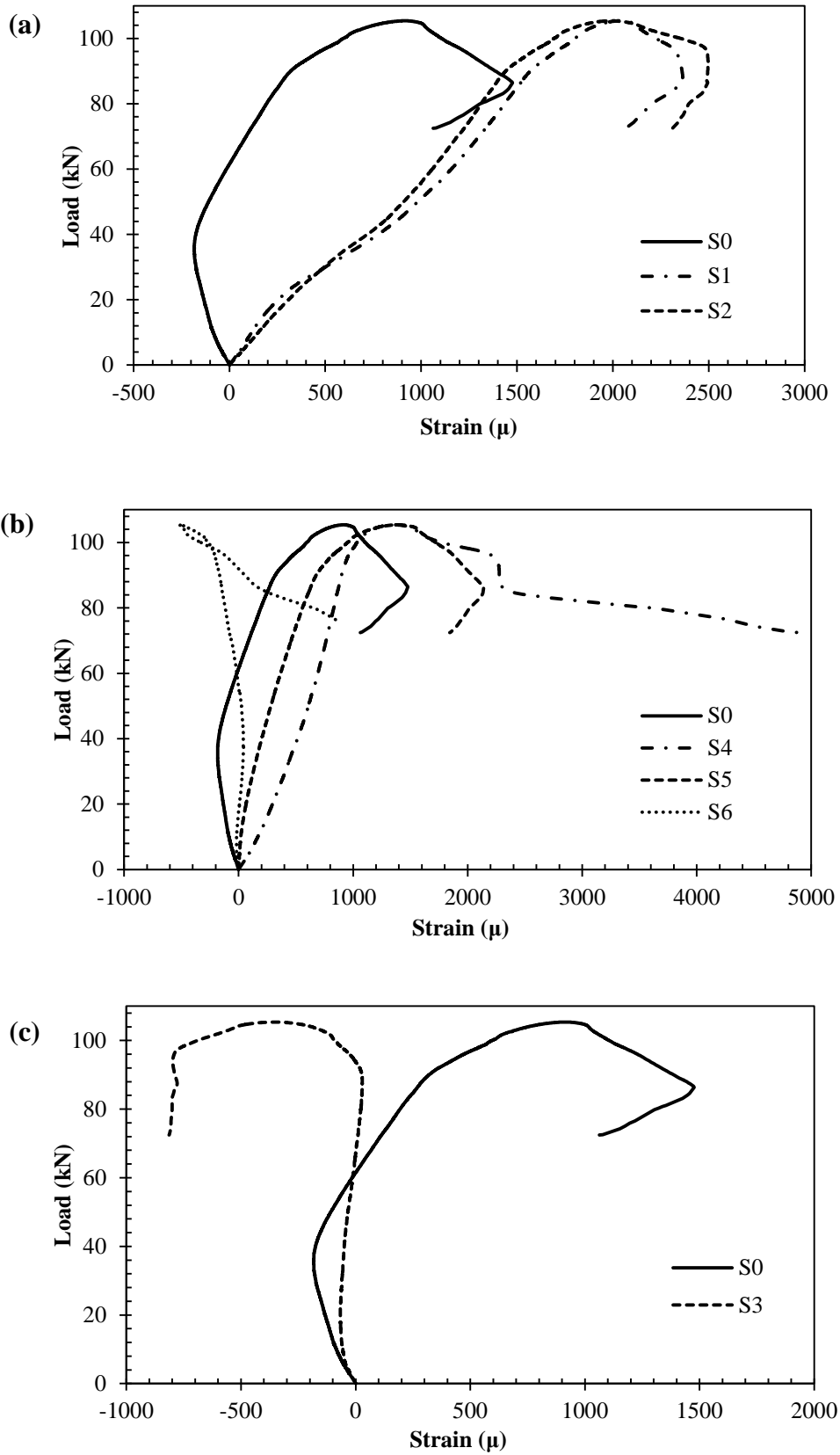


Fig. 4.23 Load–strain curves of SWS: Strain distribution (a) along span direction (b) along width direction (c) at midpoint

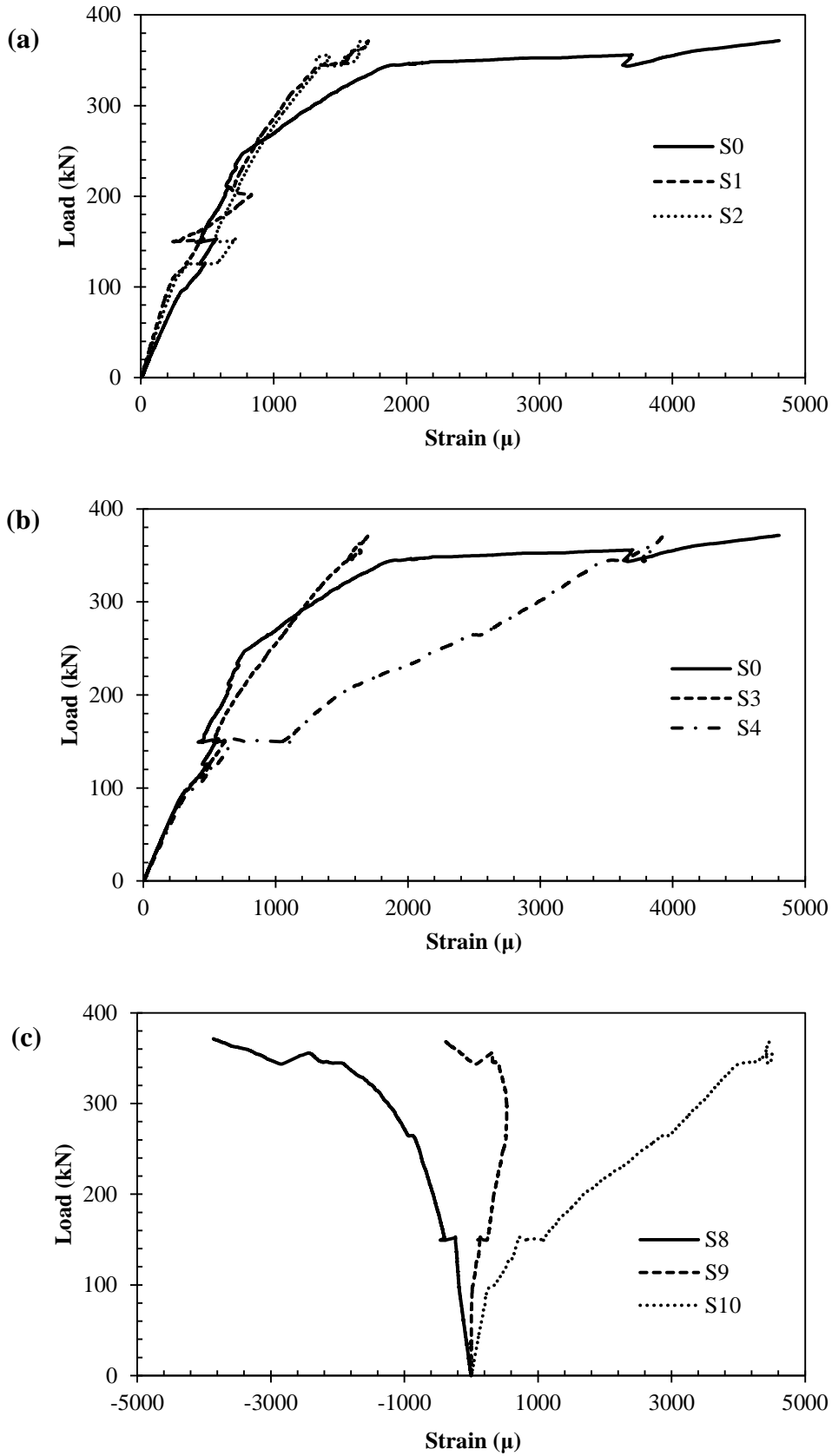


Fig. 4.24 Load–strain curves of SCS50: Strain distribution (a) along span direction (b) along width direction (c) in side plate

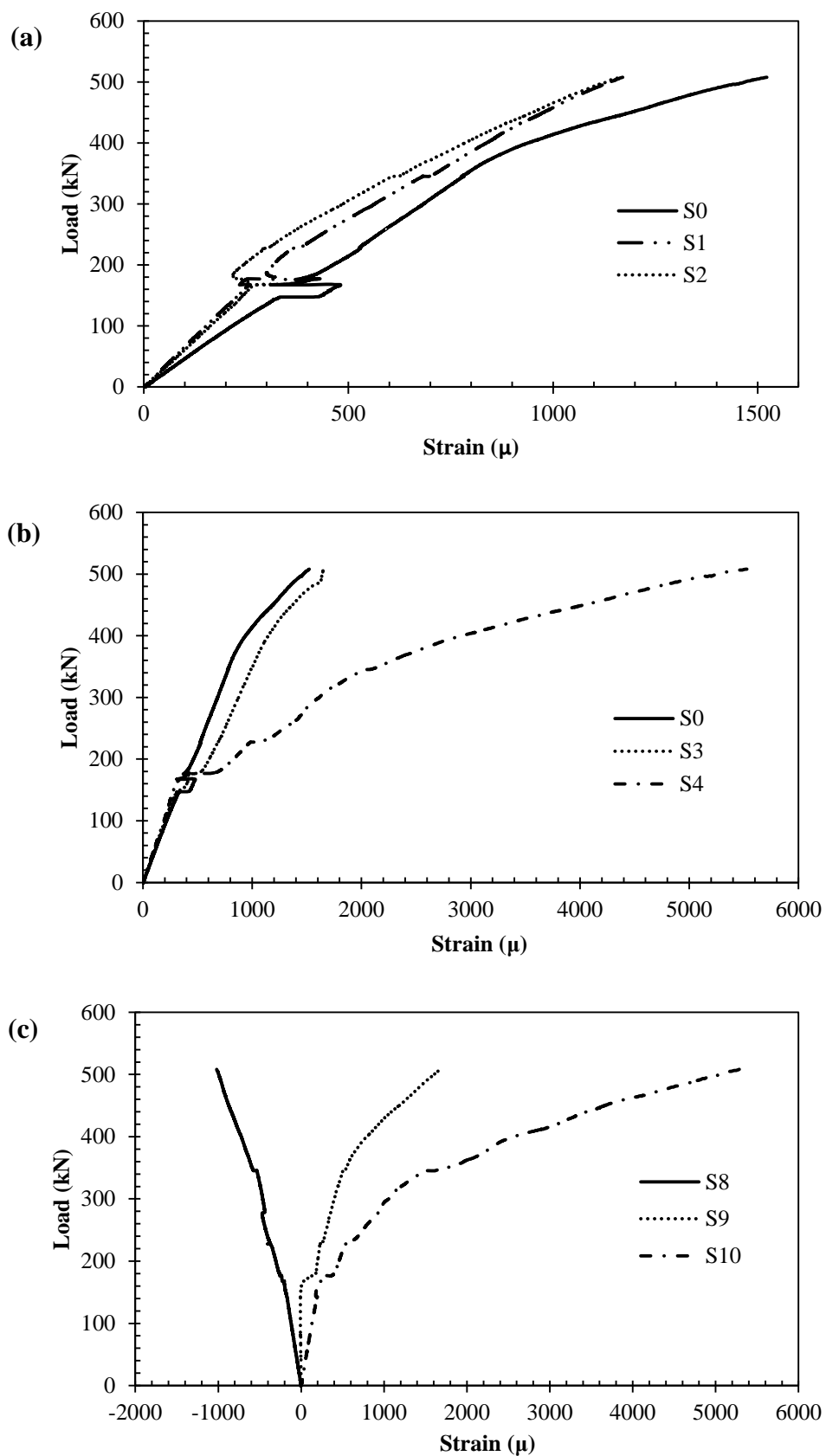


Fig. 4.25 Load–strain curves of SCS75: Strain distribution (a) along span direction (b) along width direction (c) in side plate

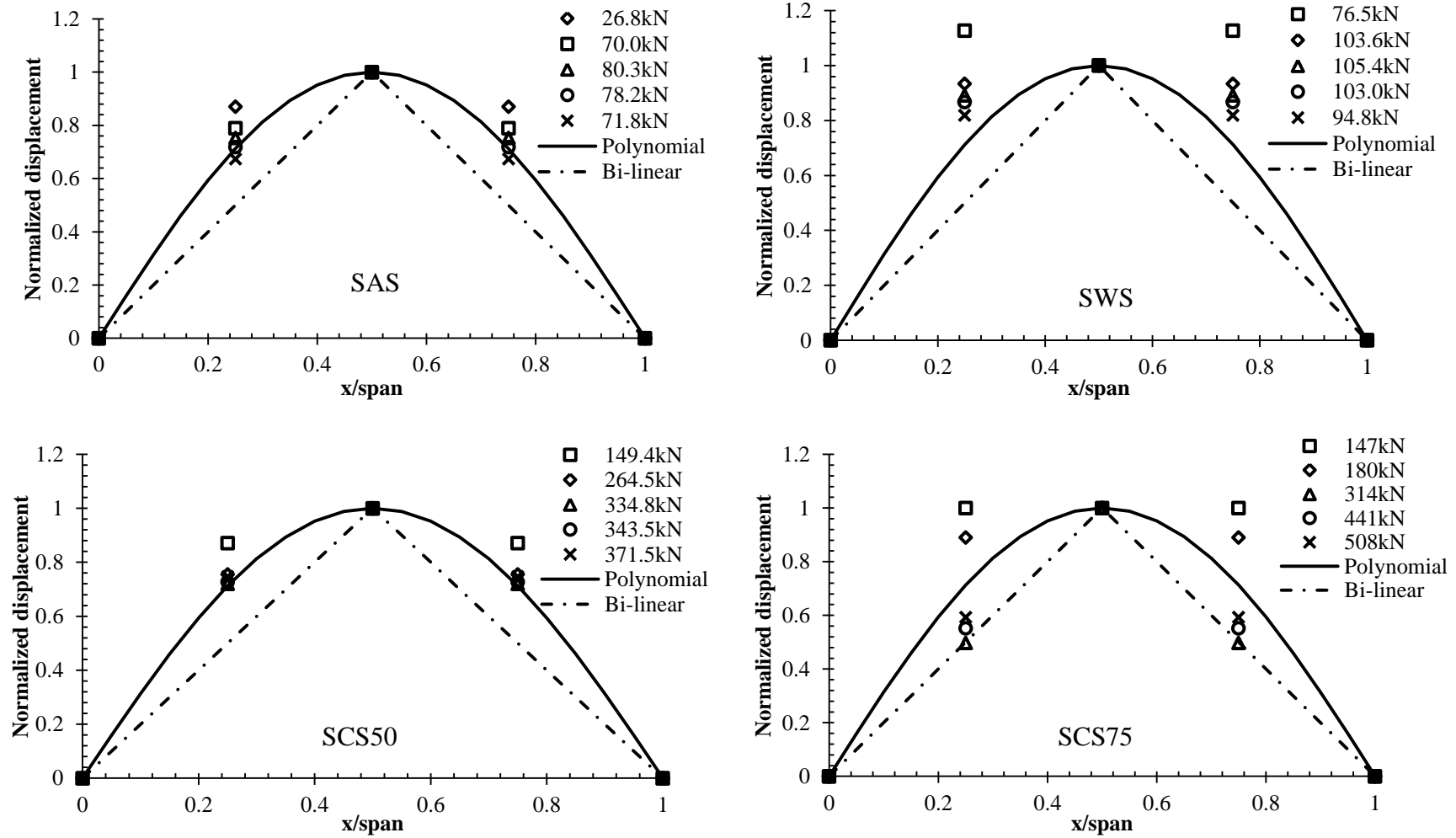


Fig. 4.26 Deflection shape in span direction

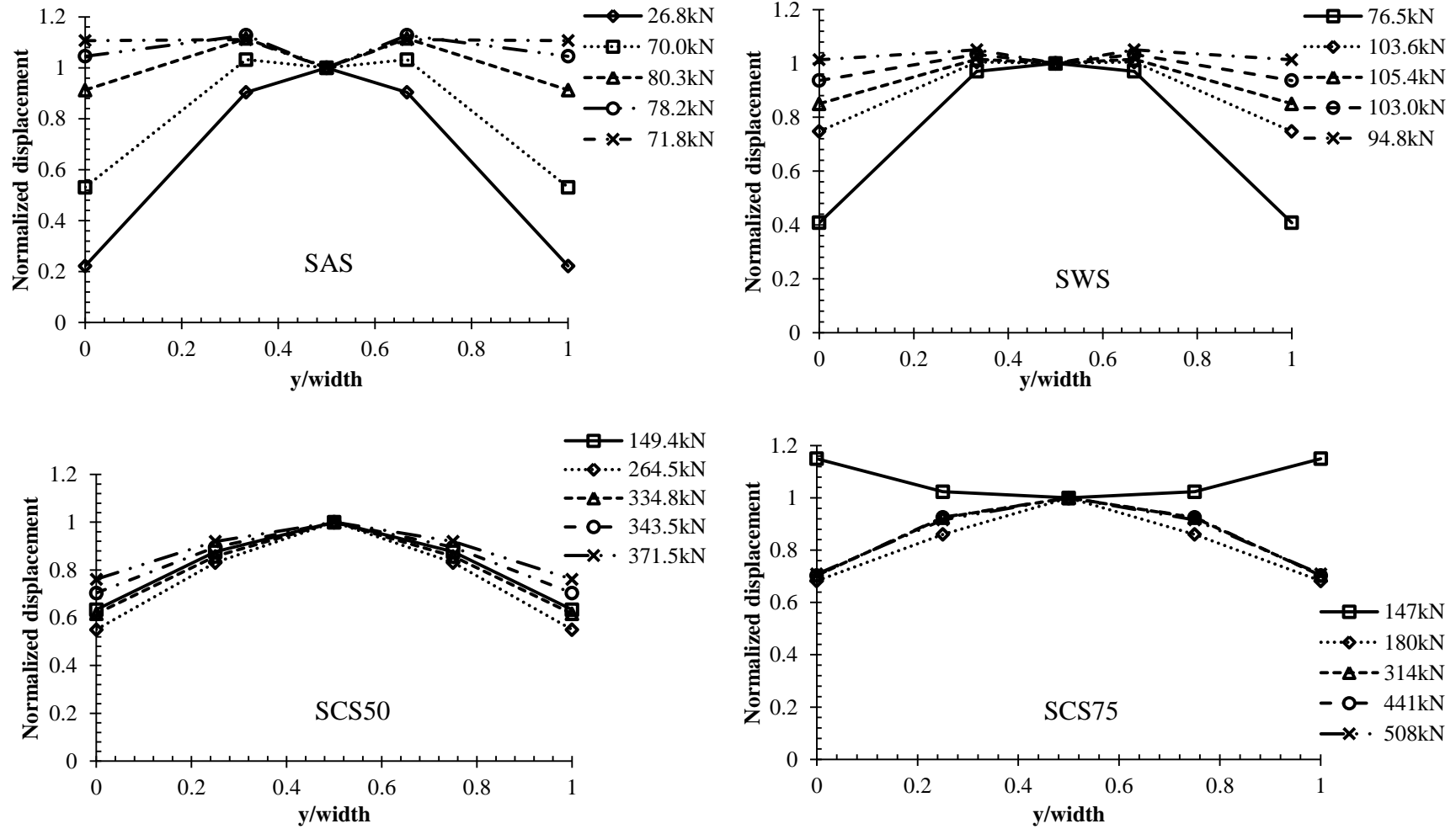


Fig. 4.27 Deflection shapes in width direction

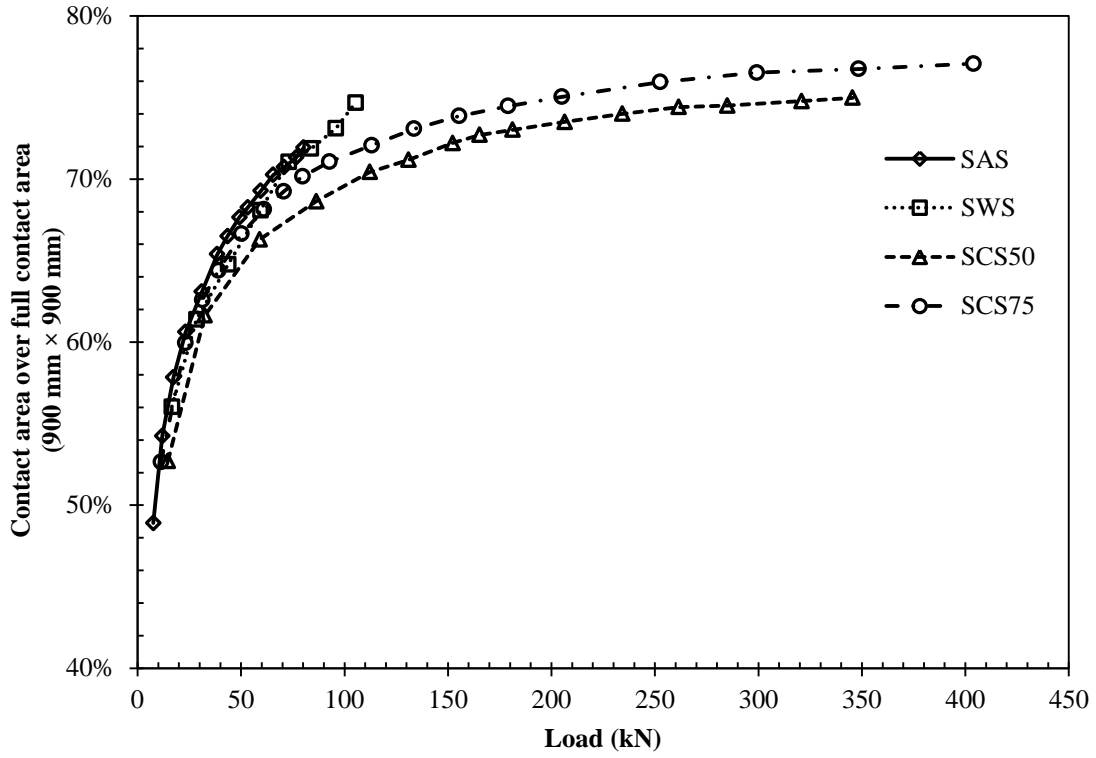


Fig. 4.28 Contact area–load curves

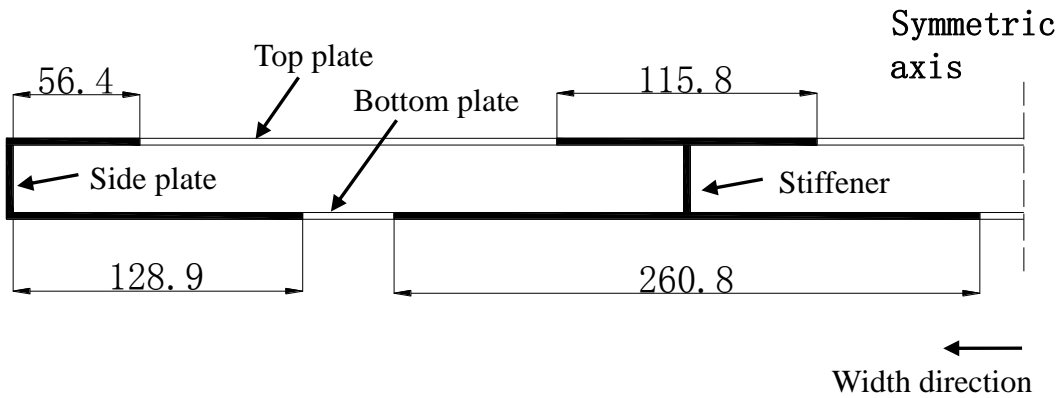


Fig. 4.29 Effective cross-section of SAS under bending (in mm)

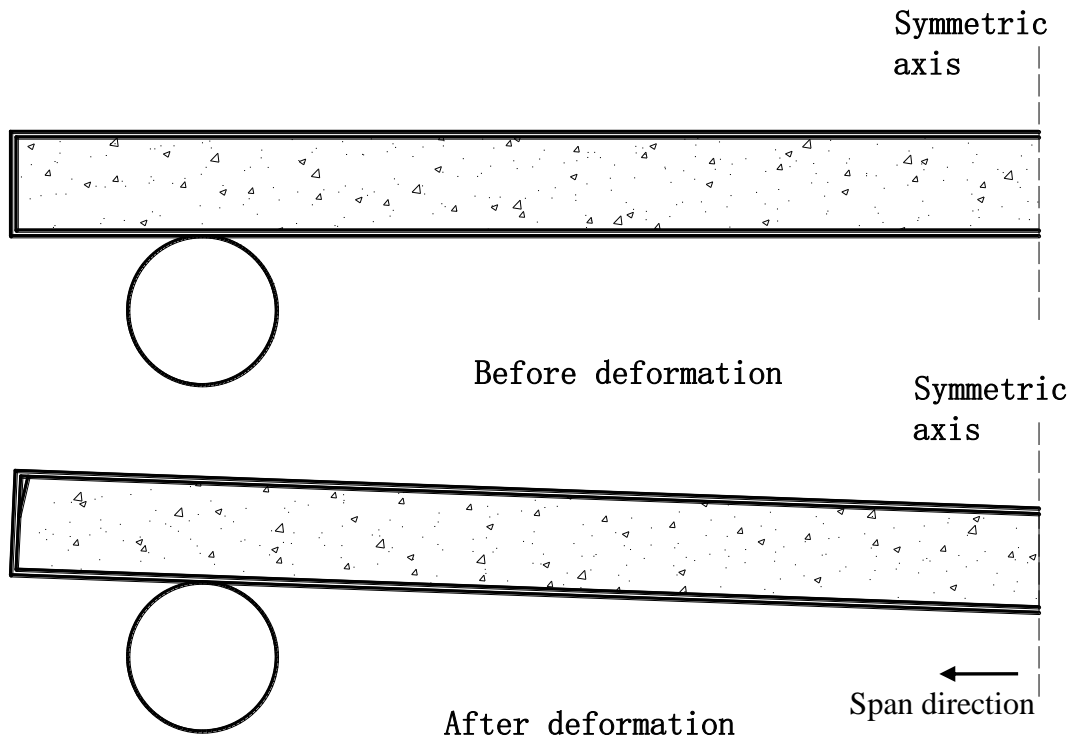


Fig. 4.30 Deformation of SCS sandwich panel under lateral pressure load

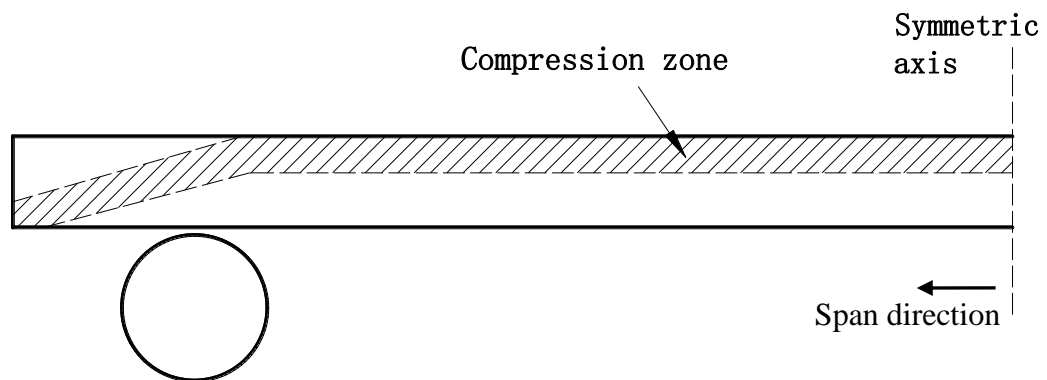


Fig. 4.31 Compression zone along the concrete core

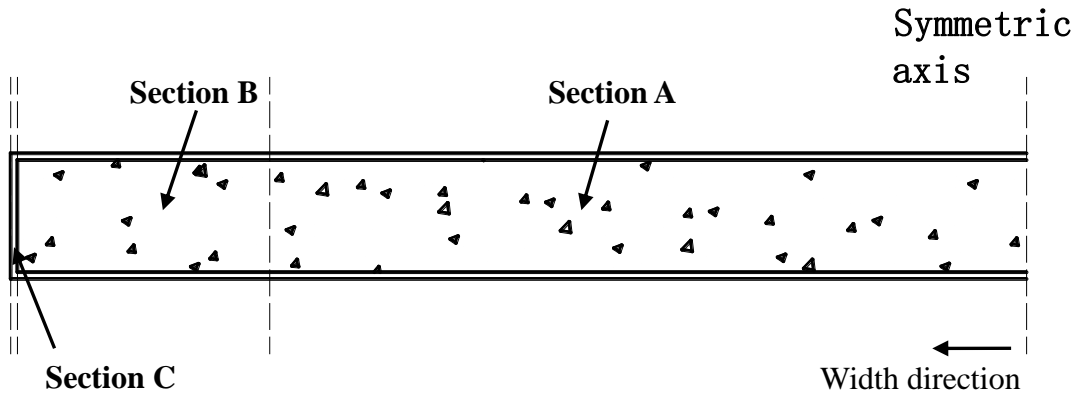


Fig. 4.32 Cross-section of SCS sandwich panel at mid-span

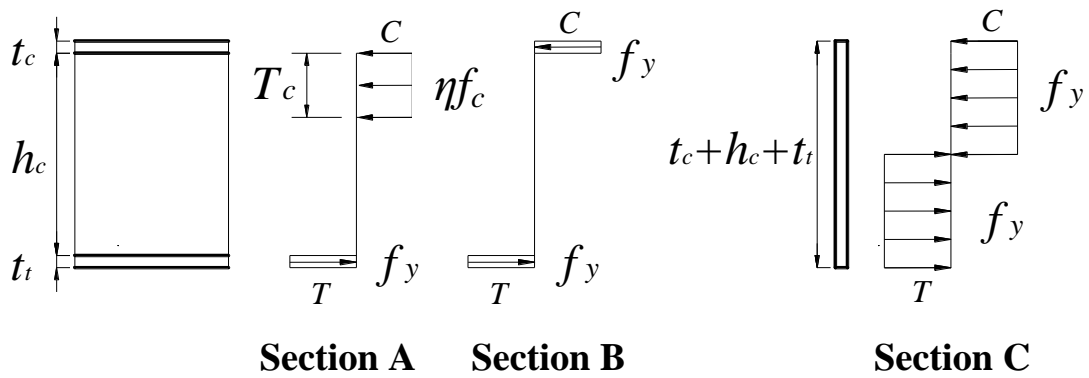


Fig. 4.33 Force distribution on each section

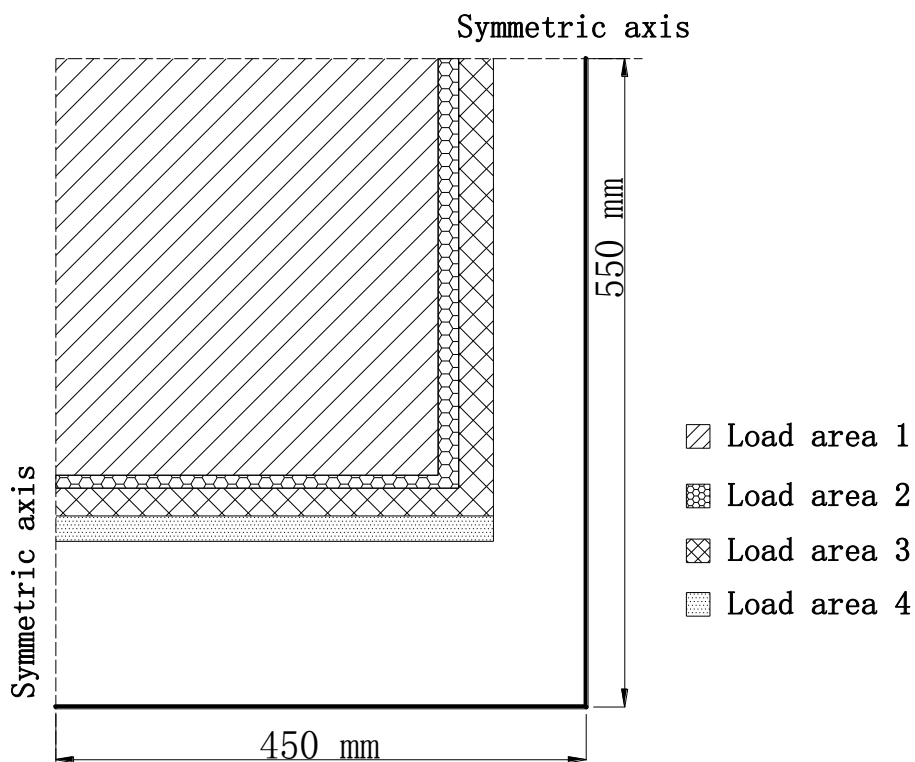


Fig. 4.34 Varying contact area in the FE model of SAS (quarter model)

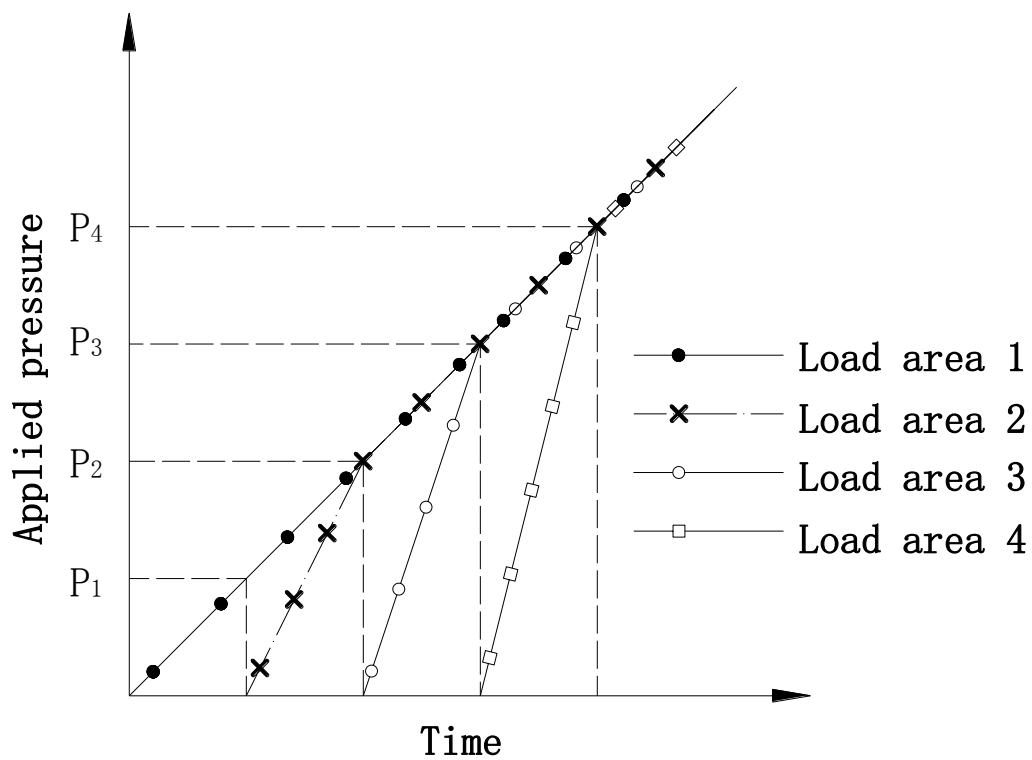


Fig. 4.35 Applied loading curves in FE model

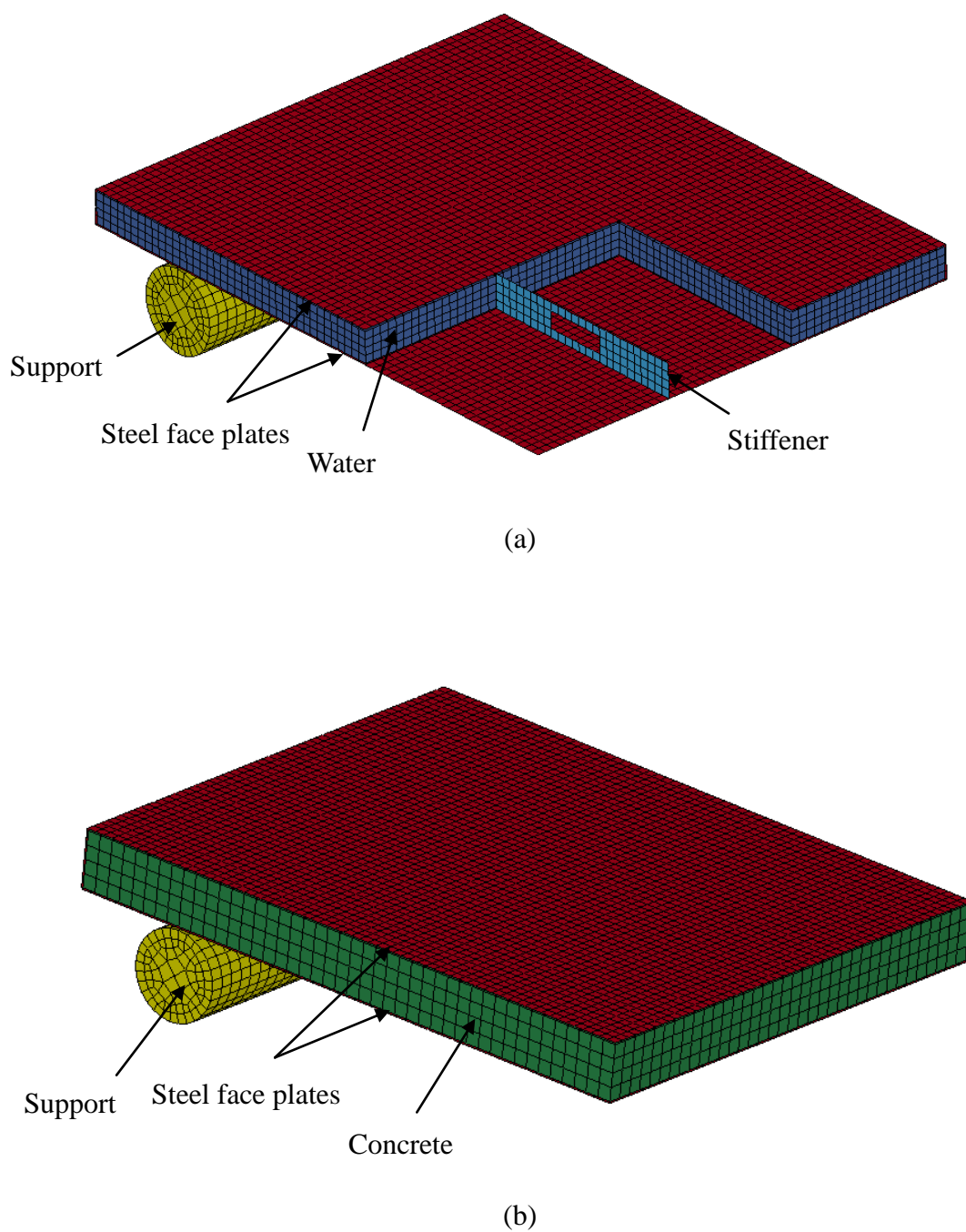


Fig. 4.36 FE model of (a) water tank and (b) SCS sandwich panel in lateral pressure test (quarter model)

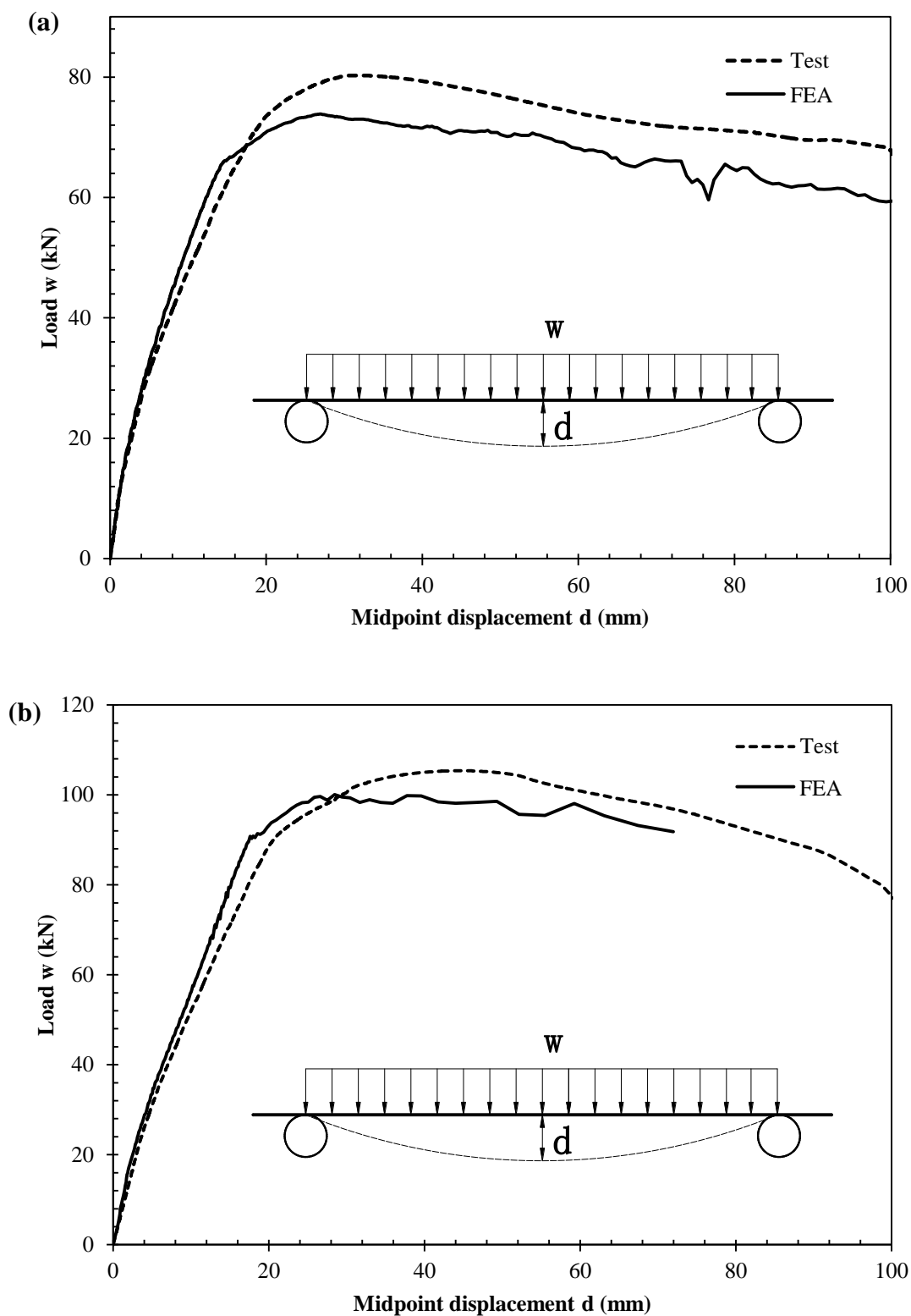
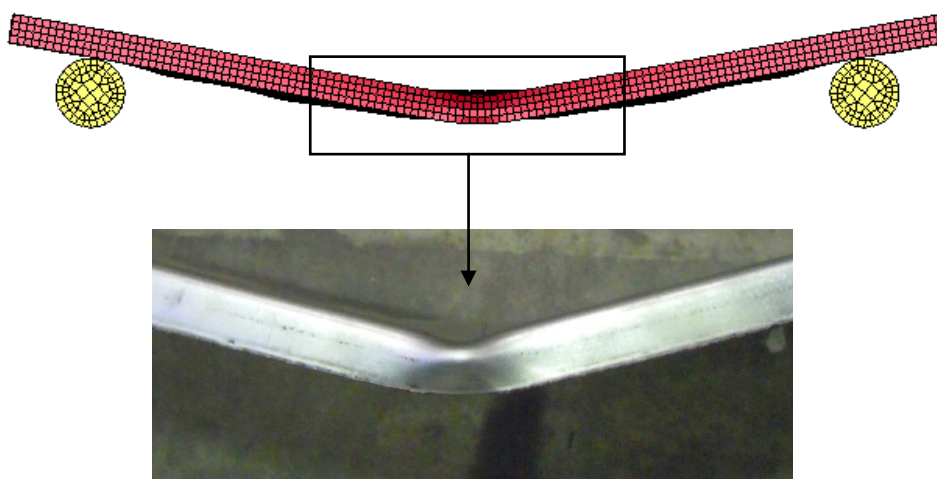
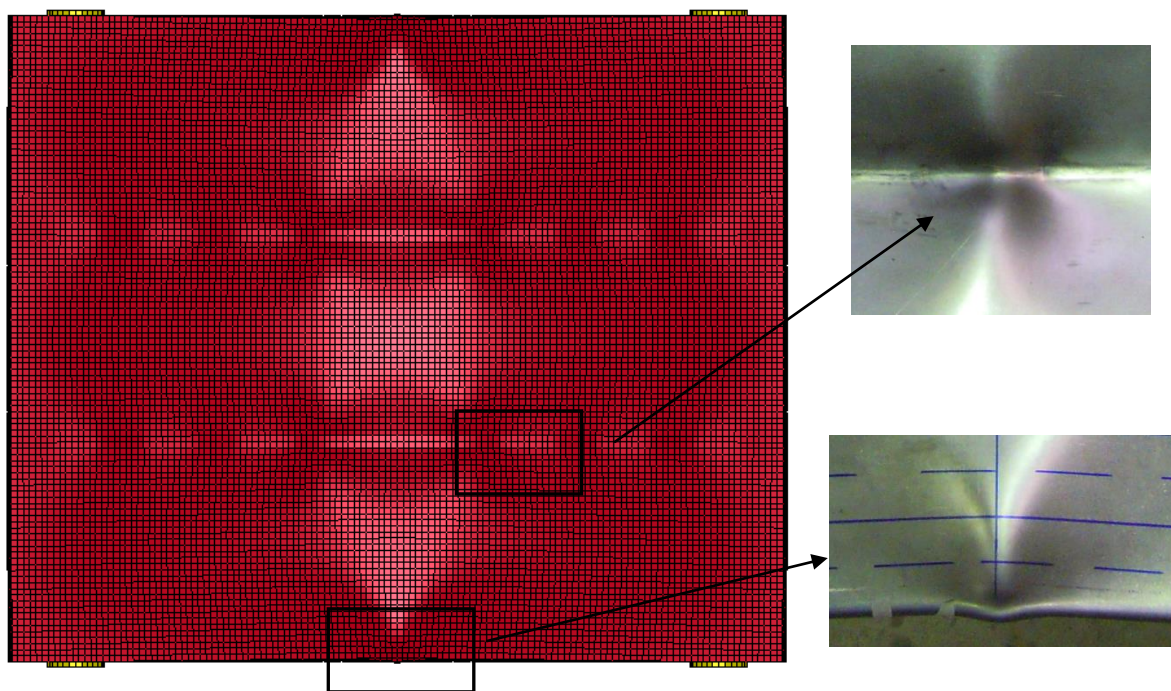


Fig. 4.37 Comparison of FE predicted load–midpoint displacement with test results:

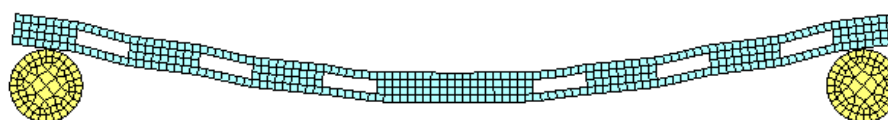
(a) SAS (b) SWS



(a)



(b)



(c)

Fig. 4.38 Deformation of SAS in the FE analysis (top surface): (a) Plastic hinge at mid-span (b) Buckling in the top surface (c) Deformation of stiffener

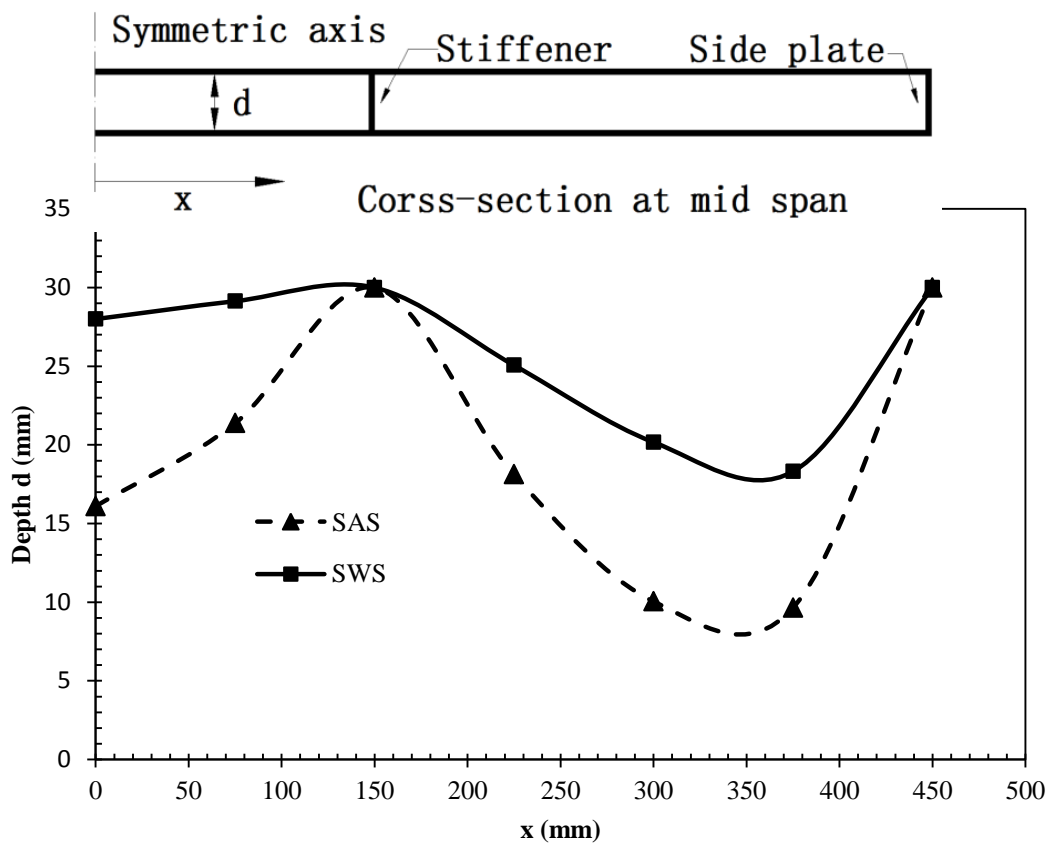


Fig. 4.39 Comparison of face plate depth between SAS and SWS

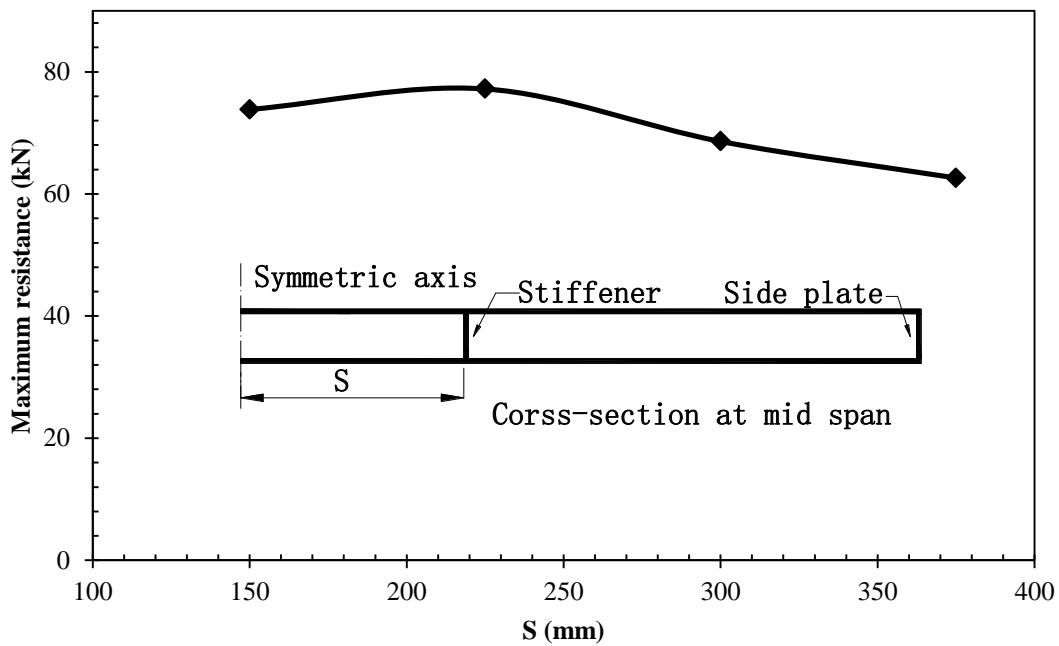
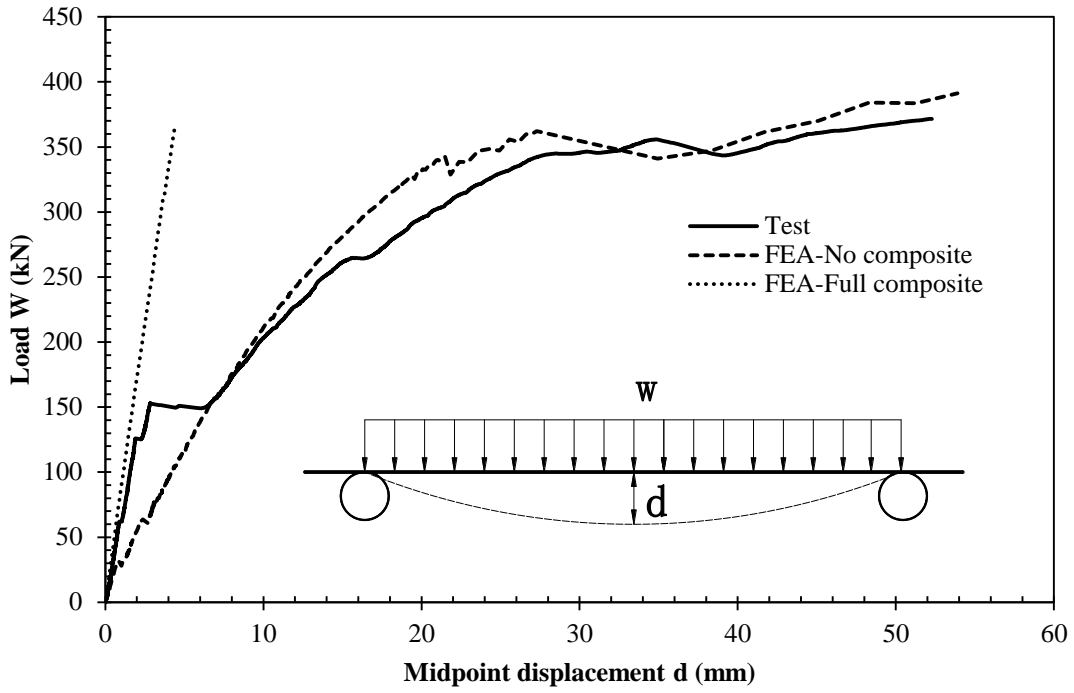
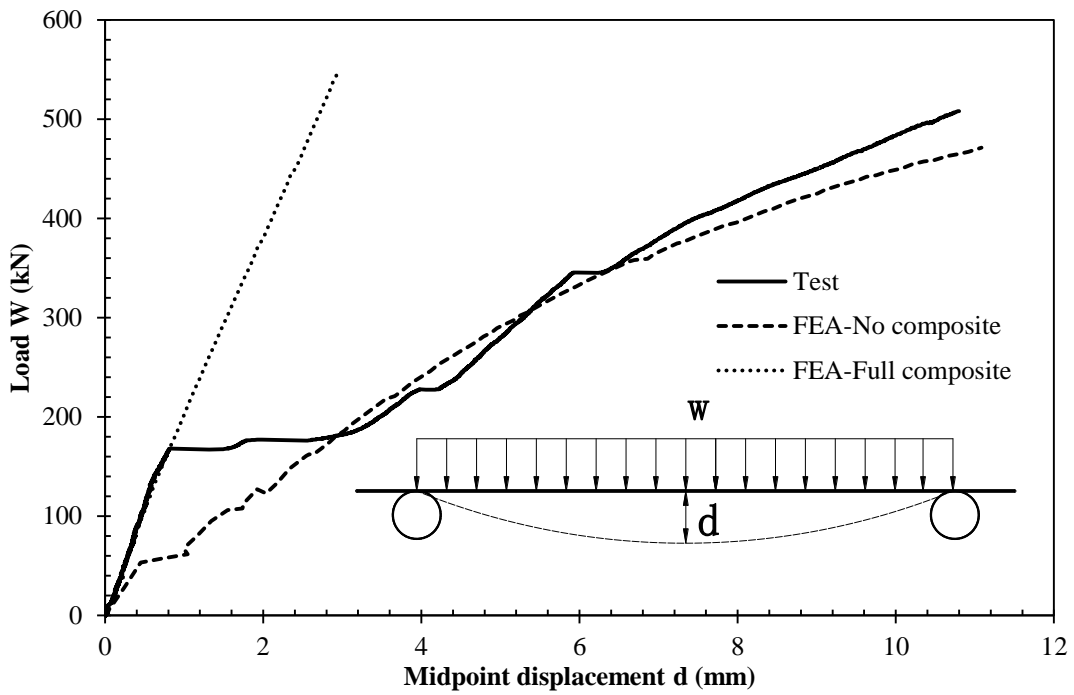


Fig. 4.40 Variation of the resistance of SAS with moving stiffener



(a)



(b)

Fig. 4.41 Comparison of FE predicted load–midpoint displacement with test results:

(a) SCS50 (b) SCS75

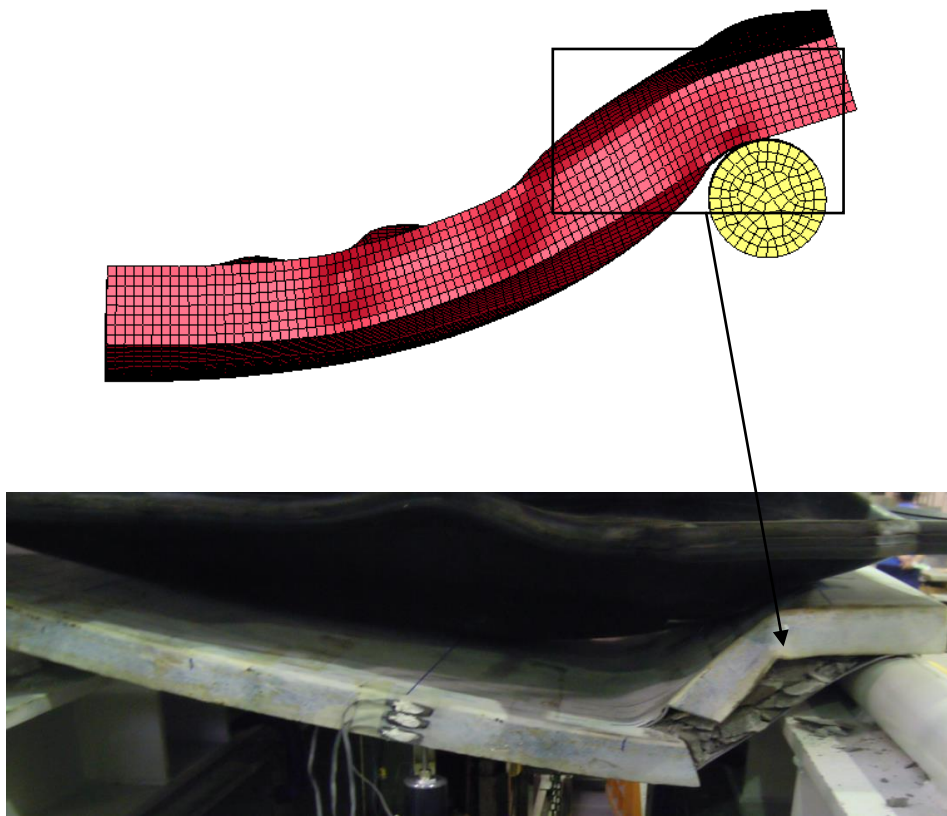


Fig. 4.42 Shear failure of SCS50

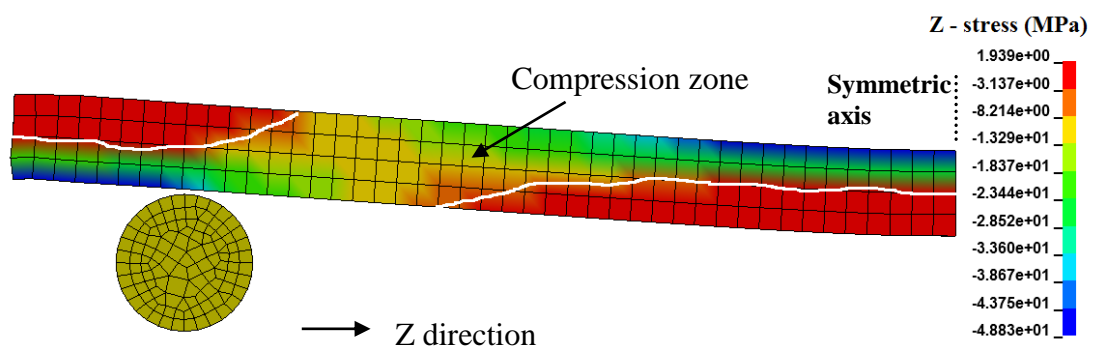


Fig. 4.43 Compression zone of the concrete core along span direction

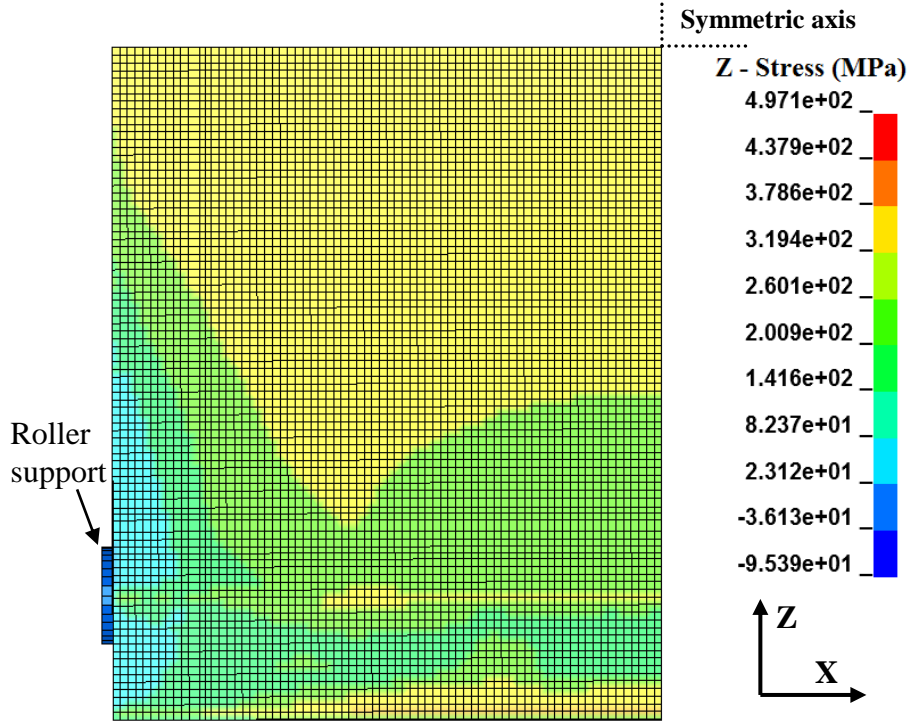


Fig. 4.44 Axial stress distribution (Z-direction) in the bottom plate (quarter model)

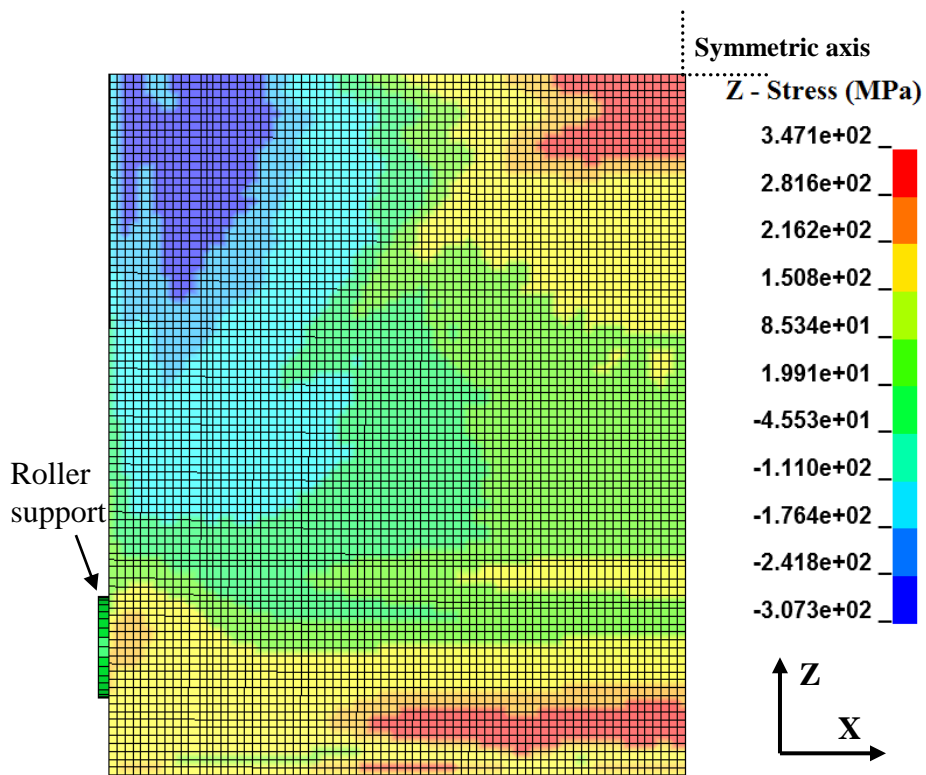


Fig. 4.45 Axial stress distribution (Z-direction) in top plate (quarter model)

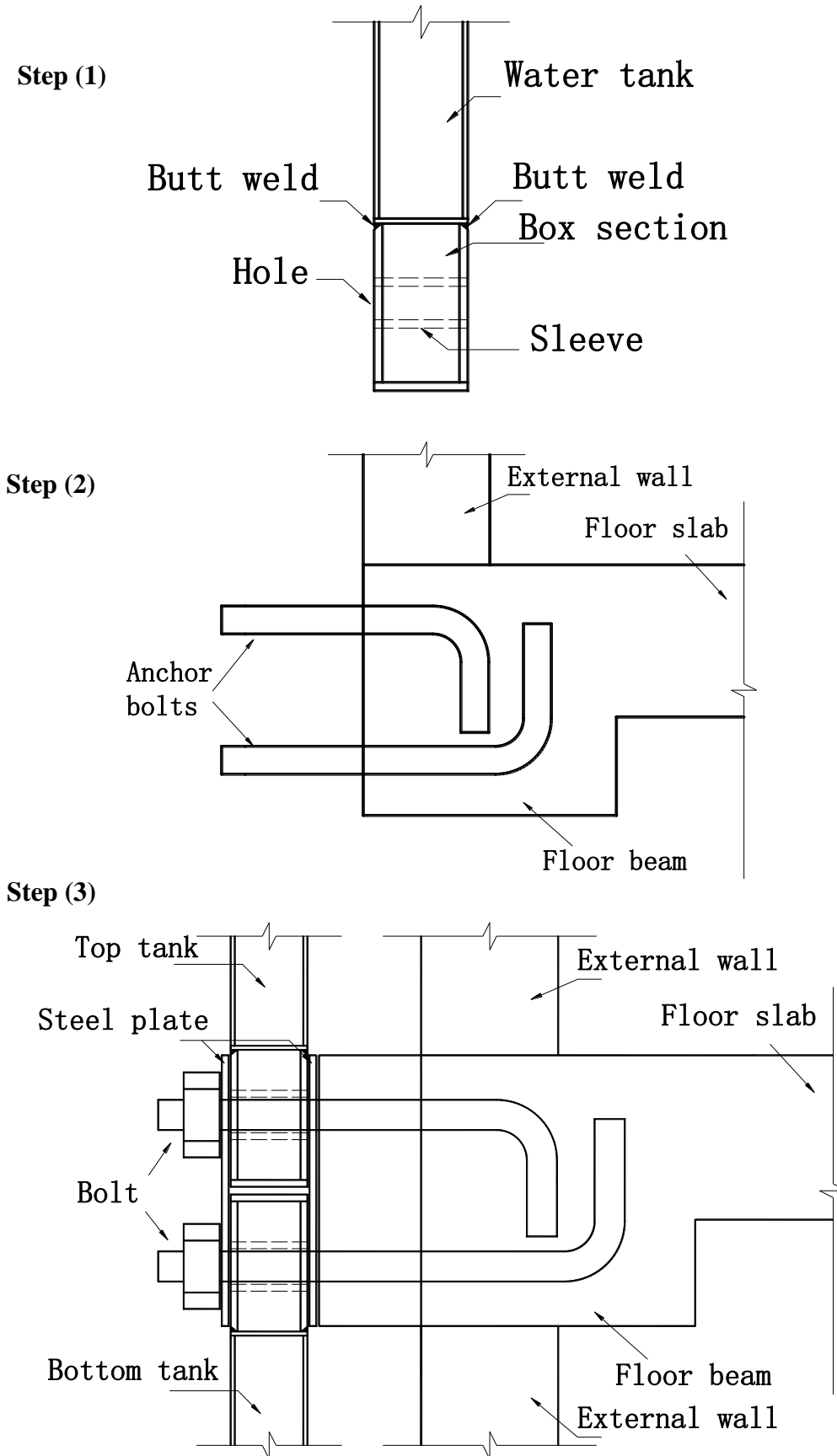


Fig. 4.46 Installation of façade tanks to floor beam

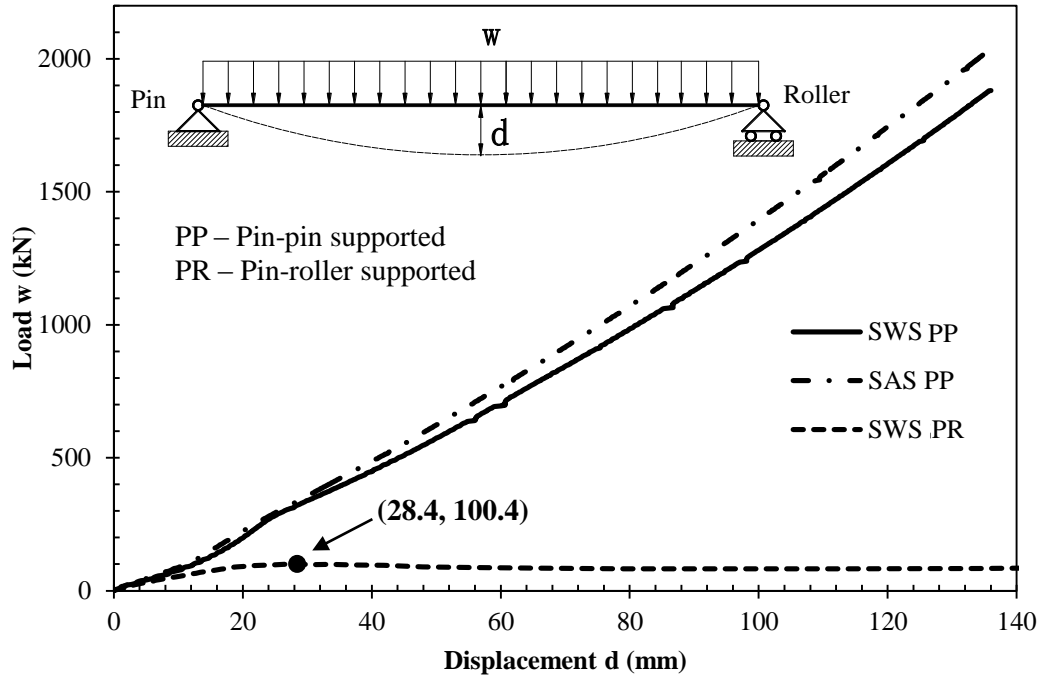


Fig. 4.47 Load–displacement curves of SAS and SWS tanks

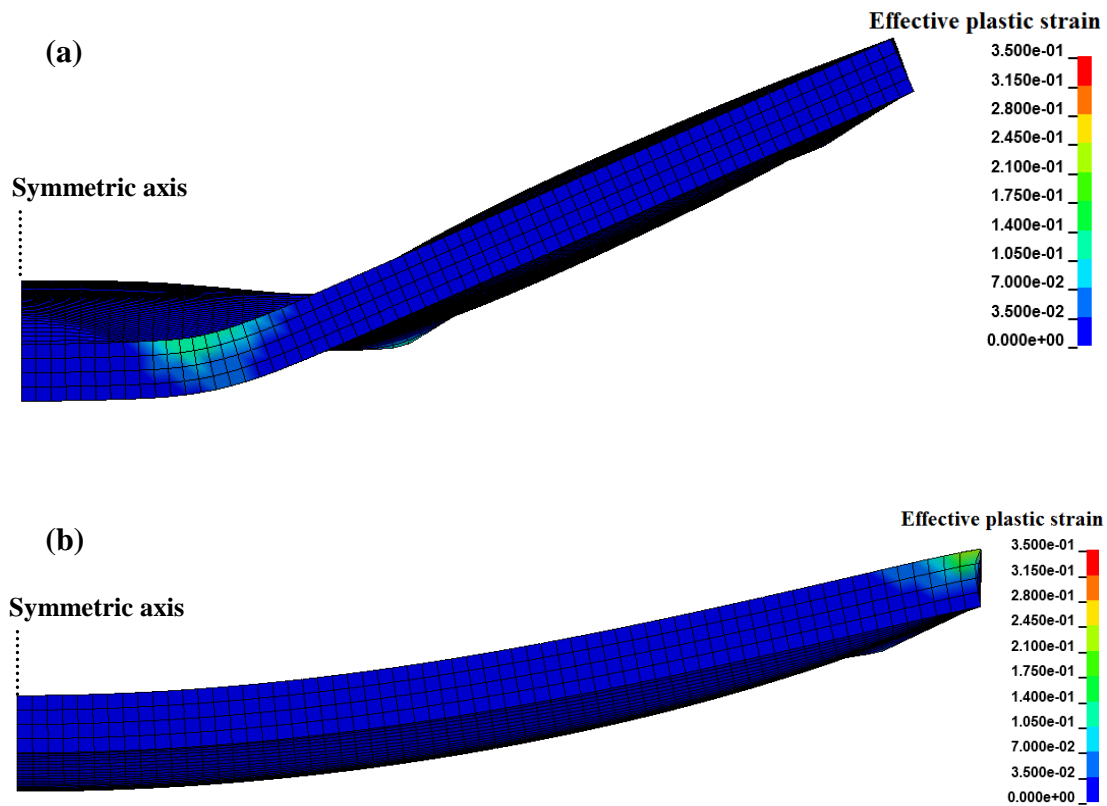


Fig. 4.48 Failure modes of SWS: (a) pin-roller supported (b) pin-pin supported

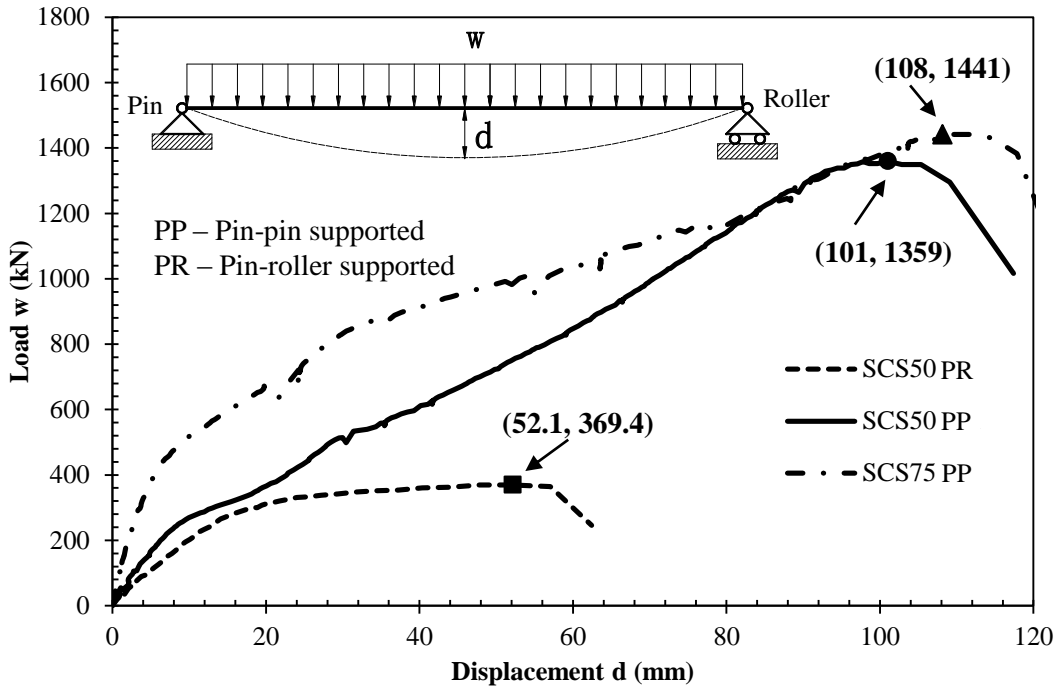


Fig. 4.49 Load–displacement curves of SCS sandwich panels

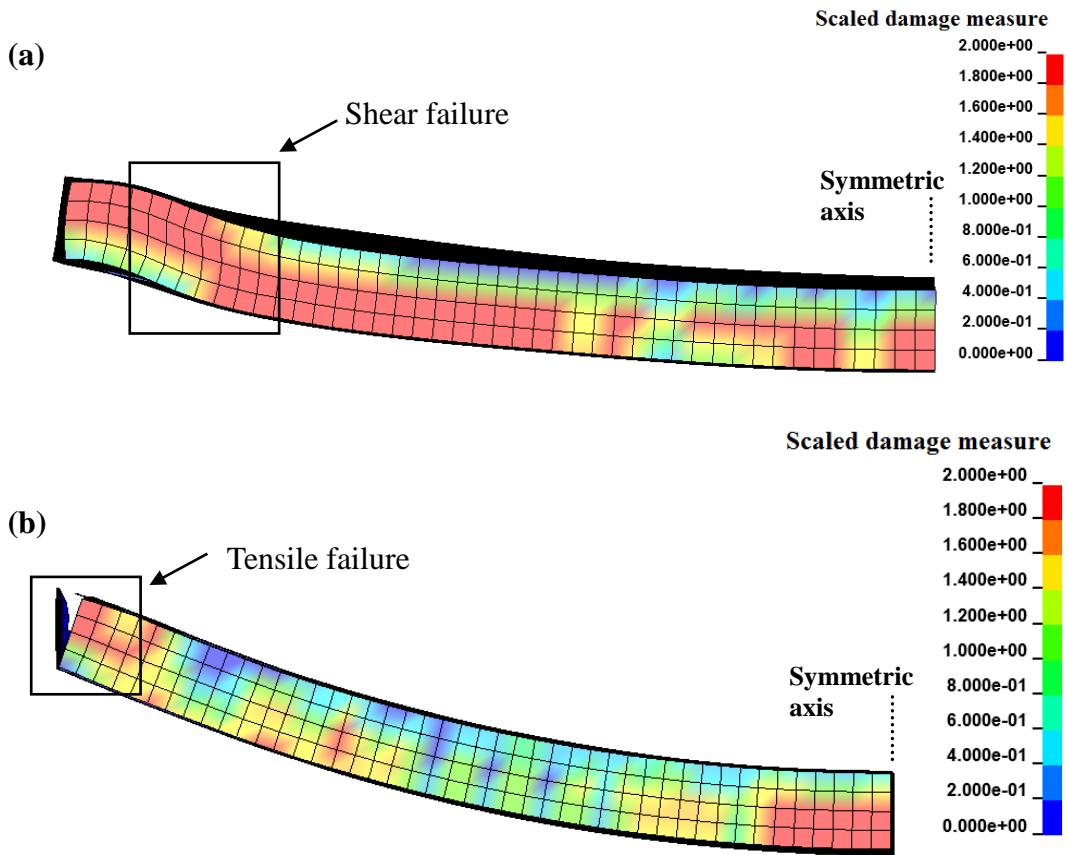


Fig. 4.50 Failure modes of SCS50: (a) pin-roller supported (b) pin-pin supported

Chapter 5 Performance of Water Façade Systems under Dynamic Pressure Load

5.1 Introduction

The structural responses of the water façade systems under dynamic pressure loading were experimentally, analytically and numerically studied in this chapter. The loading was applied using dropped projectile on an inflated high pressure airbag to assert dynamic pressure on the specimens in the experimental study. The measured deformation modes, impact force and air pressure as well as displacement and strain responses of the water tank and SCS panel specimens were analyzed to understand their behaviors under dynamic pressure loading. Equivalent SDOF method was adopted to predict the displacements of the test specimens under dynamic pressure loading. In addition, the FE models were also constructed to simulate the responses of the test specimens and the experimentally-verified FE models were applied to predict the performance of the specimens under blast loading.

5.2 Preparation of Specimens

An identical set of the four specimens described in Chapter 4 for the lateral pressure load test was tested against dynamic pressure loading. The dynamic pressure was generated through drop-weight impact on the same high pressure airbag that was used in the lateral pressure load test. The effects of water on the response of SWS tank and

core depth on the response of SCS panels under dynamic pressure loading were investigated.

5.3 Test Setup and Instrumentation

Impact test was carried out using an instrumented drop-weight impact test machine as shown in Fig. 5.1. A hydraulic controlled mechanical hoisting system is used to raise the projectile up to 4 m drop height. Once the winch brake is released, the projectile, which has an adjustable weight of 500 to 1200 kg, will slide freely along the vertical guide rails towards the specimen below it. Similar to the lateral pressure load test, the drop-weight test specimens were also roller-supported on two 80 mm (diameter) bars support with clear span of 900 mm as shown in Fig. 5.2. The inflated height of the high pressure airbag between the 30 mm thick impact plate and specimen was kept at 160 mm by using two wood blocks. The blocks were inserted between the frame and impact plate and the airbag was charged with initial air pressure of 0.04 MPa for the SAS and SWS tanks and 0.1 MPa for the SCS50 and SCS75 sandwich panels. The initial inflated height and pressure of airbag were carefully selected to reduce variation in contact area between airbag and specimen and shorten the duration of pressure loading. Even though it was expected that the change in contact area would be less significant with increasing load or pressure based on the lateral pressure load test observations, the initial pressure was selected such that midpoint displacement of the specimen was minimal (less than 2 mm) and well within the elastic range. Since the contact area will be varying during test, the initial contact area was measured and wet paint was applied to the bottom surface of the inflated airbag which was not in contact with the specimen before test. The wet paint would leave a marking on the

specimen after impact to indicate the maximum contact area. Since the inflated airbag with lower compressibility, which can be defined as the ratio of compression distance of airbag, ΔH , to change of air pressure, ΔP , will generate dynamic pressure load with shorter duration, the inflated height was kept as small as possible and the current inflated height was selected based on trial tests.

A digital circuit in combination with laser emitters and photodiodes was used to measure the velocity of projectile just before impact and also to trigger the data acquisition by the 16-channels Oscilloscope 1 with sampling rate setting of 1 MHz as shown in Fig. 5.3. The Dytran high frequency 2300V Low Impedance Voltage Mode (LIVM) pressure sensor was connected to the inlet pipe of airbag to capture the air pressure while three quartz force rings on the same plane with total capacity 1050 kN were attached to the projectile to record the impact force. The deformation and strain readings of specimen were respectively measured by using potentiometers and strain gauges at the positions shown in Fig. 5.4. In addition to these instruments, high speed camera images of the impact were also recorded during test. The signals from photodiodes, pressure sensor, quartz force rings and potentiometers were captured using Oscilloscope 1 while the strain gauge readings were recorded by the 16-channel Oscilloscope 2 with the same sampling rate setting of 1 MHz. The Oscilloscope 2 was triggered by strain gauge S0 at the mid-span.

5.4 Discussion on Test Results

The SAS and SWS tanks were at first tested under drop-weight impact by a 500 kg projectile that was dropped from 1.7 m height. However, the maximum displacement

was found to be relatively small and the test specimen survived after the impact with only small deformation. Hence, the tanks were re-subjected to second impact at higher drop height of 2.0 m in order to study their responses under larger deformation. On the other hand, the SCS50 and SCS75 sandwich panels were tested once with an 800 kg projectile that was dropped from the height of 3.7 m.

5.4.1 Deformation Modes

5.4.1.1 SAS and SWS Tanks

The impact plate and airbag were removed after each test to measure the permanent deformation of specimens. Fig. 5.5 compares the images of the SAS tank after the first and second impacts. It can be seen that the tank deformed in a flexural manner with plastic hinge at mid-span after the first impact and the plastic hinge was further developed in the second impact. A concave zone on the top steel plate between stiffeners and side plates was observed after both impacts and the image taken after the second impact is shown in Fig. 5.6. Buckling of side plate could be seen near the mid-span and the top plate buckled along the stiffeners at the weaker cut-out locations after the second impact. These deformation modes are similar to the observed responses in the lateral pressure load test, which indicates that the failure modes of SAS tank under dynamic pressure loading could be related to its response under lateral pressure loading.

The deformed shapes of the SWS tank after the first and second impacts were also under flexural mode as shown in Fig. 5.7. It was noted that the concave zone on the top steel plate was reduced as compared to the SAS tank and was accompanied by a convex zone next to it as seen in Fig. 5.8. Since water is nearly incompressible, the

observed deformed shape can be explained by the change in volume of water from the concave zone to the convex zone in order to maintain a constant total volume of water.

The side view of the SAS and SWS tanks after second impact are compared in Fig. 5.9 and the effect of water in reducing the permanent deformation of the SWS tank can be clearly seen as compared to the empty SAS tank. Besides changes in the load distribution, the improved impact/dynamic pressure resistance could be attributable to the increase in overall mass of the SWS tank with addition of water. As shown in Eq. (5.1), the influence of mass on the response of elastic spring-mass system subjected to impulsive load has the same effect as the stiffness in reducing the maximum displacement:

$$\frac{x_{\max}}{I} = \sqrt{\frac{1}{k_s m}} \quad (5.1)$$

where x_{\max} is maximum displacement, I is impulse, k_s is stiffness and m is mass. However, the effect of mass will be reduced with the increase in ratio of loading duration to natural period of specimen and will disappear when the specimen's response is within quasi-static regime. Meanwhile, the effect of mass cannot be quantified in the dynamic response regime, which was the response regime of the SWS tank in current study.

5.4.1.2 SCS50 and SCS75 Sandwich Panels

The deformation mode of the SCS50 sandwich panel under dynamic pressure loading was a combination of flexure and shear deformation as shown in Fig. 5.10. Bulging near the support line was visible which could be due to the expansion of grout after

cracking under high shear force at the support. Comparison of the permanent deformation of SCS50 and SCS75 sandwich panels in Fig. 5.11 shows that the deformation was considerably reduced by increasing the core depth due to the increase in resistance and mass. However, according to design formulae in Eurocode 4 (2004), the possibility of brittle shear failure may be increased with increasing core depth since the ratio of shear resistance to bending resistance will be reduced. Therefore, it is important to ensure that SCS sandwich panel with thicker core has sufficient shear resistance to avoid shear failure as discussed in Chapter 4.

5.4.2 Impact Force and Air Pressure

The recorded impact force–time histories between the projectile and impact plate are plotted in Fig. 5.12. Multiple contacts between projectile and impact plate with clear separation time can be seen from the plots for the SAS and SWS tanks in both tests while the multiple contacts for the SCS sandwich panels occurred much closer in time to each other. The reason for multiple contacts is that the mass of projectile is larger than impact plate and projectile still moved downward after the first contact with the impact plate.

The pressure–time histories in the airbag, which represents the dynamic pressure loading acting on the specimen, are plotted in Fig. 5.13 for the SAS and SWS tanks. Multiple peak pressures were observed from the curves. From Fig. 5.14 showing the pressure–time history together with the impact force–time history for the SAS tank, it can be seen that the change in pressure was dependent on the contact between the projectile and impact plate. Each contact causes the sudden increase in pressure except for the last contact with smaller impact force. The loading duration on the SAS

tank in the first and second impacts from the pressure–time histories were 0.078 s and 0.076 s, respectively, while the SWS tank was loaded for 0.066 s and 0.065 s in the first and second impacts.

Fig. 5.15 shows the pressure–time histories for the two SCS sandwich panels and the pressure is also dependent on the contact between projectile and impact plate as plotted in Fig. 5.16 for the SCS50 sandwich panel. One notable difference between the impact force–time histories of the tanks and sandwich panels is the shorter time gap between the multiple contacts in each test. This resulted in shorter loading duration of 0.049 s and 0.042 s for the SCS50 and SCS75 sandwich panels, respectively. Besides this, there was less variation in the pressure–time histories as compared to the SAS and SWS tanks.

The recorded impact velocity (V), maximum impact force (F_{\max}), impact impulse (I) and maximum air pressure (P) in each test on the four specimens are summarized in Table 5.1. The impact impulse was obtained by integrating the full impact force–time history, which was shown in Fig. 5.12. From Table 5.1, it appeared that specimens with higher resistance and mass absorbed higher impact impulse under the same impact condition.

5.4.3 Displacement Response

5.4.3.1 SAS and SWS Tanks

The midpoint displacement–time histories of the SAS and SWS tanks from the first and second impact tests are plotted in Fig. 5.17. The maximum displacements occurred at the second peaks in all four tests and are consistent with the recorded

pressure–time histories as compared in Fig. 5.18 for the SWS tank. Both the SAS and SWS tanks experienced plastic deformation in the first and second impacts and their permanent deformations can be seen in Fig. 5.17 except for the SAS tank in the first impact. This is because the potentiometer at the midpoint of SAS tank was separated from the bottom plate halfway during test and hence the curve was abruptly terminated as shown in Fig. 5.17. However, the permanent deformations of all specimens were physically measured and are listed in Table 5.2.

The maximum and permanent displacements of the SAS and SWS tanks are compared in Table 5.2. The SWS tank exhibited lower maximum and permanent displacement by 5.6 % and 14.9 %, respectively, as compared to the SAS tank in the first impact and the difference was further increased to 29.0 % and 38.5 % in the second impact. This demonstrates the better performance of SWS tank against dynamic pressure loading as compared to the SAS tank. The maximum displacements of the two tanks are tracked along their respective resistance–deflection curves, which was obtained in the lateral pressure load test as shown in Fig. 5.19. It can be seen that the maximum displacements of SAS and SWS tanks in the first impact occurred at load hardening stage. In the second impact, the maximum displacement of the SAS tank fell in the load softening stage while the SWS tank was still within load hardening stage. This could explain the larger deformation of SAS tank in the second impact as it needed to deform more to absorb the impact energy as compared to the SWS tank.

5.4.3.2 SCS50 and SCS75 Sandwich Panels

Fig. 5.20 compares the midpoint displacement–time histories of the SCS50 and SCS75 sandwich panels and the maximum displacement of the SCS50 sandwich

panel is about 3.5 times higher than the SCS75 sandwich panel. The maximum displacements occurred at the first peak in the curves, which are consistent with the recorded pressure–time histories of the panels. As compared in Table 5.3, the permanent midpoint displacement of the SCS75 sandwich panel was significantly less than that of the SCS50 sandwich panel.

5.4.4 Strain Response

5.4.4.1 SAS and SWS Tanks

The mid-span longitudinal strain reading (S0) of the SAS tank was larger than the quarter-span strain readings (S1 and S2) throughout the impact as shown in Fig. 5.21(a). This is because the moment at mid-span is larger than the quarter-spans under pressure loading. The non-uniformity of strain readings at quarter-spans was observed under the dynamic pressure loading, which is likely due to the geometric imperfection of the specimen. Since the specimen was one-way supported, the transverse strain reading at mid-span (S3) was smaller than the longitudinal strain reading (S0). Fig. 5.21(b) compares the strains along the width direction and the strain readings of S0 at mid-span and S5 between side plate and stiffener were smaller than the strain readings near side plate (S6) and stiffener (S4), which can be attributed to the shear lag effect.

The mid-span longitudinal strain reading (S0) of the SWS tank was also larger than those at quarter-spans as shown in Fig. 5.22(a). Unlike the SAS tank, the mid-span transverse strain gauge S3 recorded significant strain, which indicates that the bottom plate was subjected to stress in both direction at mid-span with the addition of water. The strain distribution along the width direction was also changed due to addition of

water, as seen from the comparison of Fig. 5.21(b) and Fig. 5.22(b). For the SAS tank, load distribution through stiffener and side plate was evident whereas the load was more globally transferred for the SWS tank. The variation of strain readings at the bottom plate of SWS tank was less pronounced as compared to the SAS tank, which could be related to the change in load distribution through water.

5.4.4.2 SCS50 and SCS75 Sandwich Panels

Fig. 5.23 compares the longitudinal strain distribution (S0, S4 and S5) along the width direction of SCS50 sandwich panel. It can be seen that these three strain readings were similar at the beginning of loading. As the load increases, the strain S5 near the side plate continued to increase while there were no significant changes to the S0 and S4 readings after a sudden drop in strain at 0.187 s. The difference in the strain development between the three strain gauges and the sudden drop was likely due to the weakened composite action after debonding between the grout core and bottom plate. Another sudden drop was also observed at 0.190 s which indicates the progressive debonding between the grout core and bottom plate under impact. Similarly for the SCS75 sandwich panel, the strain reading of S5 near side plate continued to rise at higher rate than those of S0 and S4 after the sudden drop caused by debonding as shown in Fig. 5.24. As for the strain distribution along the span direction, the peak and residual mid-span strain readings of S0 were smaller than the quarter-span strains of S1 and S2 for both SCS50 and SCS75 sandwich panels after the sudden drop. This indicates that the debonding between grout core and bottom plate could affect the strain development at the bottom plate of SCS panel.

5.5 Analysis of Specimens under Dynamic Pressure Load

The equivalent SDOF method proposed by Biggs (1964) is usually adopted by the design guidelines (UFC, 2008; ASCE, 2010; ASCE 2011) as a simple method to predict the displacement of structural member against blast load and was adopted in the current study to analyze the responses of the specimens under dynamic pressure loading. Only one primary deflection mode can be represented in the SDOF system, which is established based on the conservation of energy, i.e. the internal energy, kinetic energy and work done between the actual structure and SDOF system being the same. The strain rate effect on the material strength can be taken into account in the SDOF model by scaling up the resistance. The resistance–deflection and deflection shape functions of water tanks and SCS sandwich panels, which are necessary to establish the SDOF system, were obtained from the lateral pressure load test in Chapter 4.

5.5.1 SDOF System Establishment

The equation of motion for the SDOF system is given as

$$M_e \ddot{z} + R_e(z) = F_e(t) \quad (5.2)$$

where M_e , R_e and F_e are the equivalent mass, resistance and force and can be obtained from Eqs. (5.3) to (5.5) by equating the kinetic energy, internal energy and work done between the SDOF system and actual structure. Since the specimens and load are symmetric, only quarter model is considered when constructing the SDOF system.

$$M_e = \iint m_a [\phi_1(x)\phi_2(y)]^2 dx dy + \sum_{i=1}^n \int m_{xi} [\phi_1(x)\phi_2(y_i)]^2 dx + \sum_{i=1}^l \int m_{yi} [\phi_1(x_i)\phi_2(y)]^2 dy$$

(5.3)

where m_a is the mass per unit area and represents the uniform distributed mass on the surface, i.e. top/bottom plate, water and concrete; m_{xi} and m_{yi} are the mass per unit length in x (span) and y (width) direction and represents the distributed mass along the line, i.e. stiffener and side plate along x direction and end plate along y direction; $\phi_1(x)$ and $\phi_2(y)$ are the deflection shape along x and y direction, respectively.

$$R_e(z) = \int_0^{l(z)} \int_0^{w(z)} r(z)\phi_1(x)\phi_2(y)dxdy \quad (5.4)$$

where $r(z)$ is pressure–deflection function, which was calculated by dividing the resistance by contact area; $l(z)$ and $w(z)$, which are the functions of midpoint displacement z , are the half length of contact area in span and width direction.

$$F_e(t) = \int_0^{l(t)} \int_0^{w(t)} p(t)\phi_1(x)\phi_2(y)dxdy \quad (5.5)$$

where $p(t)$ is the applied pressure–time history; $l(t)$ and $w(t)$, which are the functions of time t , are the half length of applied pressure in span and width direction.

5.5.2 Parameters Calculation

To establish the equivalent mass, resistance and force, the required parameters/functions listed in Eqs. (5.3) to (5.5) are discussed in the followings.

Deflection shape functions in span direction $\phi_1(x)$ and width direction $\phi_2(y)$ are necessary to establish the equivalent mass, resistance and force. As suggested by Biggs (1964), the deflection shape function is usually obtained by analyzing the structural member under lateral pressure loading. Therefore, the deflection shape

obtained from the lateral pressure load test was adopted as the deflection shape for the SDOF system. As discussed in Chapter 4, the deflection shape was varying with the pressure load. Hence, the adopted deflection shape function was obtained by averaging the deflection shapes at the selected load levels. Then, the equivalent mass can be obtained by Eq. (5.3).

As shown in Eq. (5.4), the resistance–deflection and deflection shape functions as well as the length and width of contact area in terms of midpoint displacement are necessary to determine the equivalent resistance and these parameters/functions were obtained from the lateral pressure load test. The DIF is also included in the SDOF system to capture the increased material strength behavior under high strain rates. The DIF depends on the strain rate of the element and increases with increasing strain rate. Hence, the design values of DIF given by design guidelines (UFC, 2008; ASCE, 2010) are varying not only for the design ranges and type of material but also with the state of stress (bending, diagonal tension, direction shear, bond and compression) in the material. The adopted values of DIF for stainless steel, mild steel and concrete are 1.18, 1.1 and 1.19 (ASCE, 2010). It is noted that the SCS sandwich panels include two materials (mild steel and concrete) and the lower DIF value of the two materials (1.1) is adopted for the conservative concern.

The applied pressure–time history, deflection shape function and the length and width of applied pressure are necessary to determine the equivalent force as shown in Eq. (5.5). The applied pressure–time history was obtained in the dynamic pressure test by recording the variation of air pressure. The applied pressure area was changing during test and only the initial and maximum length and width of applied pressure were

measured. The linear relationship between the applied pressure area and applied pressure was assumed to approximate the varying applied pressure area in the test and the validity of this assumption will be discussed in Section 5.6.3. Since the applied pressure–time history is known, the length and width of applied pressure in terms of time can be determined. Then, the equivalent force is determined.

5.5.3 Comparison with Test Results

The displacement–time histories of SAS and SWS tanks, and SCS50 and SCS75 sandwich panels obtained from test and SDOF analysis are compared in Fig. 5.25 and reasonable agreement can be observed. The higher magnitude of fluctuating is observed for the displacement–time curves from SDOF analysis, which may be caused by the omission of damping in the SDOF system. Damping was not taken into consideration as it has no significant effect on the maximum displacement and therefore is usually neglected in the blast resistant design. Table 5.4 compares the maximum displacements between the test and SDOF analysis. All the maximum displacements from the SDOF analysis are generally larger than the test results and the maximum difference for the four specimens is 16.0%. This difference may be caused by the limitation of the SDOF analysis, i.e. the constant deflection shape and DIF value being considered. Based on above discussion, the SDOF method is a simply alternative which can be used to predict the displacements of the specimens under dynamic pressure loading and the results are acceptable.

5.6 Finite Element Analysis of Specimens under Dynamic Pressure Load

5.6.1 Material Models

5.6.1.1 Concrete Material Model

The Karagozian & Case concrete model (MAT_72R3 in LS-DYNA) was adopted to simulate the behaviors of concrete and the failure surfaces, damage features and equation of state of this material model were discussed in Section 4.7.1.1. The strain rate effects have also been discussed and the DIF–strain rate in Eq. (5.6) (Grote *et al.*, 2001) was adopted in this analysis for grout in compression.

$$DIF = \begin{cases} 0.0235 \log \dot{\epsilon} + 1.07 & (\dot{\epsilon} < 250) \\ 0.882(\log \dot{\epsilon})^3 - 4.48(\log \dot{\epsilon})^2 + 7.22 \log \dot{\epsilon} - 2.64 & (\dot{\epsilon} \geq 250) \end{cases} \quad (5.6)$$

and DIF–strain rate in Eq. (5.7) by fitting the experimental data from Ross *et al.*, (1989) was adopted in this analysis for grout in tension. The fitted curve is compared with the experimental data in Fig. 5.26.

$$DIF = \exp \left\{ 0.0513 * [\log(\dot{\epsilon}/\dot{\epsilon}_s)]^{1.35} \right\} \quad (5.7)$$

where $\dot{\epsilon}_s = 1E-7$.

5.6.1.2 Steel Material Model

The Piecewise_Linear_Plasticity material model (Mat_24) was adopted to simulate the stainless steel and mild steel in the dynamic pressure test. As mentioned in Section 4.7.1.2, the Cowper-Symonds model is utilized to consider the strain rate effects. Jones (1988) obtained the values of D and q of 40.4 and 5 for mild steel by fitting the experimental data assembled by Symonds (1967). However, the experimental data

have considerable scatter, which may be related to the different mild steels used in the experiments. Using these values may, undoubtedly, overestimate the strain rate effects of some mild steels. More recently, the values of D and q of 802 and 3.585 were determined by Abramowicz and Jones (1986) from dynamic uniaxial tensile experiments. Hence, the values of D and q given by Abramowicz and Jones (1986) were adopted for mild steel in this study to reduce the possibility of overestimating the strain rate effects due to the lack of dynamic experimental data for the current mild steel. The values of D and q of 240 and 4.74 for stainless steel 316 suggested by Boh *et al.*, (2004) were applied in this study.

5.6.1.3 Water Material Model

The material model MAT_NULL (MAT_9) together with the Gruneisen equation of state (EOS_GRUNEISEN) with cubic shock velocity–particle velocity (V_s – P_s) in LS-DYNA (Hallquist, 2012) was adopted for modeling water. The MAT_NULL is used to describe the deviatoric response of water, in which a deviatoric (viscous) stress is given as

$$\sigma'_{ij} = 2\bar{\mu}\dot{\epsilon}'_{ij} \quad (5.8)$$

where $\bar{\mu}$ is the dynamic viscosity. The Gruneisen EOS, which is used to simulate the volumetric response of water, is written as follow

$$p = \frac{\rho_0 C^2 \mu [1 + (1 - \gamma_0/2)\mu - a/2 \mu^2]}{[1 - (S_1 - 1)\mu - S_2 \frac{\mu^2}{\mu + 1} - S_3 \frac{\mu^3}{(\mu + 1)^2}]^2} + (\gamma_0 + a\mu)E \quad (5.9)$$

for compressed material and is given by Eq. (5.10) for expanded materials

$$p = \rho_0 C^2 \mu + (\gamma_0 + a\mu)E \quad (5.10)$$

where C is the intercept of the V_s – P_s curve; S_1 , S_2 , and S_3 are the coefficients of the

slope of the V_s-P_s curve; γ_0 is the Gruneisen gamma; a is the first order volume correction to γ_0 ; and $\mu = \rho/\rho_0 - 1$. The parameters of C , S_1 , S_2 , S_3 and γ_0 defined here are 1.647E6, 1.921, -0.096, 0.0 and 0.35 (Hertel, 1992), respectively. Fig. 5.27 compares the pressure–relative volume curve obtained by the parameters from Hertel (1992) with the experimental data. The present curve matches well with the experimental data and lies between the experimental data of 20 °C and 40 °C. The water temperature in this test is within this range. Hence, the selected parameters for Gruneisen equation of state are reasonable.

5.6.2 Element Type and Formulation

The S/R Hughes-Liu shell element (Hallquist, 2012) was employed for the face plates of water tank and SCS sandwich panel, and water and cement grout core were both meshed using eight-point solid element with reduced integration. The Lagrangian formulation was adopted for the stainless steel, mild steel and cement grout. The Eulerian formulation, which is ideal for modeling fluid flow problems, was adopted for water in dynamic pressure test and the penalty Fluid-Structure coupling method in LS-DYNA was utilized to model the interaction between face plates and water.

5.6.3 Contact and Loading Approach

Similar to the FE analysis on specimens under lateral pressure load, the penalty-based approach was adopted for the contact between face plate and support and the soft constraint-based approach was employed for the contact between face plate and cement grout.

Since the airbag was not fully inflated during the dynamic pressure test, the contact

area between airbag and specimen would vary continuously due to the varying air pressure inside the airbag. The contact areas corresponding to initial pressure and maximum pressure were recorded in the test to capture the varying contact area. The ratios of maximum contact area to initial contact area ranged from 1.52 to 1.62 for all the four specimens and the variation of the contact area is not significant. Hence, a linear relationship between the contact area and air pressure from initial to maximum value and from maximum to residual value is assumed to approximate the varying contact area in the test and the error of this approximation is acceptable in the preliminary FE studies, which are described in Appendix B. The applied force–time history was then obtained by multiplying the air pressure with contact area. Similar to the FE model in the lateral pressure load test, four contact areas were also adopted to represent the varying contact area in the FE model of dynamic pressure test. The pressure–time history applied on each loading area was obtained by ensuring that the applied force–time history in the FE model was identical to that obtained using linear approximation between contact area and air pressure. Taking the SAS tank for instance, the applied pressure–time history on each loading area is given in Fig. 5.28. The pressure–time curve for load area 1 is same with the air pressure–time history obtained from the test since the load area 1 is always within the contact area during the test. The pressure–time curves for other three load areas are all increasing from zero to maintain the increasing applied load. The explicit solver in LS-DYNA (Hallquist, 2006) was adopted to simulate the specimens under dynamic pressure load and dynamic relaxation approach was utilized to simulate the specimens under initial static pressure load before impact test.

5.6.4 Finite Element Model

Due to symmetry, quarter FE model of the specimen and round bars as the support was established as shown in Fig. 5.29. The nodes along the bottom of the round bars support were restricted from translation and rotation in the FE model to simulate the fixed round bars support. Similar to the FE models for lateral pressure load test, the airbag was not explicitly modeled. However, the mass of airbag skin that was in contact with the specimen in the dynamic pressure test should be included in the FE model to accurately simulate the test, because the bottom airbag skin that moved together with the specimen increases the total mass and mass affects the structural response under dynamic loading. This was done by increasing the density of the highlighted elements of top plate in Fig. 5.29 with additional mass.

5.6.5 Discussion on Finite Element Results

5.6.5.1 Empty Steel Tank and Water Filled Tank

The midpoint displacement–time histories of SAS and SWS tanks from FE analyses are compared with test results in Fig. 5.30 and reasonable agreement can be seen from the comparison. The initial disparity between FE and test for SWS tank may be due to the geometric imperfection of the specimen. Since water has negligible resistance against deviatoric response but has strong resistance against volumetric response, the external work released by water as internal energy is negligible as compared to the stainless steel plate as plotted in Fig. 5.31. Although confined water has little contribution to the energy absorbing, it provides the tank with additional mass besides reducing the deformation of water tank by increasing the resistance.

5.6.5.2 SCS Sandwich Panels

The FE simulated midpoint displacement–time histories of the SCS50 and SCS75 sandwich panels are compared to test results in Fig. 5.32. The FE model can predict the displacement–time history of the SCS50 sandwich panel reasonably well. Although the FE model overestimates the maximum displacement of SCS75 by 26.7%, the simulated residual displacement matches closely with test result. The over predictions by FE analyses may be due to the adopted conservative strain rate parameters for mild steel. The midpoint displacements of both SCS50 and SCS75 sandwich panels in the tests continuously increase to their maximum values, while displacement–time histories given by FE analyses show some fluctuating before reaching the maximum values. The reason is that the damping, which may eliminate the fluctuating of specimen in the test, was not incorporated into the FE model. This can also explain the higher magnitude of fluctuating of FE simulated curves as compared to test after the maximum displacement. The internal energies of steel and grout in the SCS50 sandwich panel and their ratios are compared in Fig. 5.33. It can be seen that the internal energies of steel and grout are initially comparable and subsequently more internal energy is taken by steel. This is because steel has much higher strength and ductility as compared to the grout. Although the energy absorbing capacity of grout is much lower as compared to steel, it helps to resist the buckling of steel plate and increase the total mass.

5.6.5.3 Boundary Effects

In the dynamic pressure test, the load durations ranged from 0.042 s to 0.078 s for the four specimens. This load duration is longer compared with typical blast loading. For instance, the load duration of 100 kg TNT charge detonated at 10 m away is 0.0097 s.

The experimentally-verified FE models for the dynamic pressure test were utilized to investigate the performance of the tanks and sandwich panels under blast loading. The same quarter FE model discussed earlier were used in the analysis. The applied loading was modified to blast pressure loading and applied onto the whole top face of the specimen. The adopted blast pressure–time history has an exponential decay from peak pressure P_r to ambient pressure at time t_d . Negative pressure was omitted as it has little effects on the structural response and is normally omitted in the blast resistant design (UFC, 2008; ASCE, 2010; ASCE 2011). The positive phase can be described by the modified Friedlander equation (Baker, 1973) as given in Eq. (2.1). In this analysis, 100 kg TNT charge detonated at 10 m away was adopted and the peak pressure P_r , load duration t_d and decay coefficient $\bar{\theta}$ were obtained as 845.5 kPa, 9.7 ms and 2.4 by using the blast loading predictive tool ConWep (Hyde, 1991).

Both pin-roller and pin-pin supported boundaries, as described in Section 4.7.5.3, were compared in this analysis. Fig. 5.34 shows the simulated midpoint displacement–time histories of SWS tank with pin-roller and pin-pin supported boundaries and SAS tank with pin-pin supported boundary. It can be seen that the maximum displacement of the pin-pin supported SWS tank is reduced by 59% as compared to the pin-roller supported SWS tank due to the increase in resistance by developing tensile membrane force. As shown in Fig. 4.47, the pin-roller supported SWS tank reaches the maximum resistance of 100.4 kN at displacement of 28.4 mm, while the resistance of pin-pin supported SWS tank is 320.8 kN at the same displacement and still shows significant increase thereafter. It appears in Fig. 5.34 that water has little effect in reducing the deformation of SWS tank with pin-pin supported boundary. This is because water can only increase the total mass of SWS tank but

cannot increase the resistance when the pin-pin supported boundary is adopted.

The midpoint displacement–time histories of the SCS50 sandwich panel with pin-roller and pin-pin supported boundaries and SCS75 sandwich panel with pin-pin supported boundary are compared in Fig. 5.35. It can be seen that the maximum displacement of the pin-pin supported SCS50 sandwich panel is reduced by 27% as compared to the pin-roller supported panel. This can be attributed to the increase in resistance and ductility when the pin-pin supported boundary is adopted. As demonstrated in Fig. 4.49, the maximum resistance and corresponding displacement of pin-pin supported SCS50 sandwich panel respectively increase 268.0 % and 93.9 % as compared to the pin-roller supported panel. By comparing both SCS50 and SCS75 sandwich panels with pin-pin supported boundary, it is observed that the deformation of the SCS75 sandwich panel can be reduced by 37% through increasing the grout core depth due to the increase in resistance (as shown in Fig. 4.49) and total mass.

From above analysis, the tank filled with water or SCS sandwich panel with thicker core can reduce the deflection under dynamic loading and the reduction in deflection is caused by higher resistance and mass. Unlike the structure under static loading whose deflection is determined by the resistance–deflection curve, both mass and resistance–deflection curve affect the structural response under dynamic loading. The effects of mass and resistance–deflection curve on the structural response under dynamic loading can be understood by analyzing a spring-mass system. When the system is subjected to dynamic loading, the external work done by dynamic loading will transfer to the internal and kinetic energy of the system. The internal energy and kinetic energy can be transferred between each other during the motion and the

maximum displacement is reached when all the kinetic energy transfers to the internal energy. Hence, the external work done equals to the maximum internal energy. Both increase in mass and resistance can reduce the external work done by dynamic loading. Taking the FE analysis on pin-pin supported SCS75 and SCS50 sandwich panels for instance, the external work of SCS75 sandwich panel is reduced by 47% compared with the SCS50 sandwich panel due to higher mass and resistance. However, the maximum displacement that is needed to store the external work as internal energy is only determined by the resistance–deflection curve. Hence, mass has effect on external work while resistance–deflection curve has effect on both external work and maximum displacement. As discussed earlier in this chapter, mass effect disappears in the quasi-static response regime, while the resistance–deflection curve has no effect on the external work in the impulsive response regime since the energy transfer from external work to kinetic energy finishes before the system developing internal energy. Based on above discussion, mass only has effect on structural response in the impulsive and dynamic response regimens while resistance–deflection curve has effect in all response regimes.

5.7 Summary

Drop-weight impact tests via high pressure airbag have been carried out on the 900 mm (width) × 900 mm (clear span) empty steel tank (SAS), water filled tank (SWS) and sandwich panels (SCS50 and SCS75). In addition, the SDOF and FE methods were adopted to predict the responses of the test specimens. The main findings and key observations from the tests, SDOF and FE analysis are summarized as follow:

- i) Both the SAS and SWS tanks deformed in a flexural manner under the dynamic pressure loading while a combination of shear and flexure deformation was observed for the SCS50 sandwich panel. The deformation of the SCS75 sandwich panel was minimal without any significant permanent deformation.
- ii) The addition of water was shown to improve the performance of SWS tank under dynamic pressure loading in terms of less deformation and more globally distributed loading, especially under higher impact load in the second impact. In comparison, load concentration near stiffeners and side plates was observed for the SAS tank under the same impact loading.
- iii) For the SCS sandwich panels, the maximum and permanent displacement of the SCS75 sandwich panel with thicker core was significantly reduced as compared to SCS50 sandwich panel due to higher resistance and mass.
- iv) The debonding between grout core and steel plate could be identified from the sudden drops in the strain–time histories of the SCS sandwich panels. It was shown that after the observed drops, the load was distributed away from the mid-span, which indicates that the debonding occurred near mid-span. Load concentration near side plate was observed after the debonding for both panels, which indicates the role of side plate in taking the impact force after the weakening of composite action due to debonding.
- v) The SDOF method could provide acceptable predictions on the displacements of specimens under dynamic pressure loading and the differences between the test and SDOF results in terms of maximum displacement were within 16.0%.
- vi) The established FE models were reasonable in predicting the displacement–time responses of water tanks and SCS sandwich panels under dynamic pressure loading. It was observed from the FE investigations that the deformation of

specimens under blast loading could be significantly reduced when the pin-pin supported boundary was adopted due to increased resistance.

Table 5.1 Summary of impact test results

Water tanks	1 st impact (500kg, 1.7 m)				2 nd impact (500kg, 2.0 m)			
	V (mm/s)	F _{max} (kN)	I (Ns)	P (kPa)	V (mm/s)	F _{max} (kN)	I (Ns)	P (kPa)
SAS	5363	497	4588	175	5820	731	5258	178
SWS	5410	484	4958	192	5762	807	5460	211

Sandwich panels	1 st impact (800kg, 3.7 m)			
	V (mm/s)	F _{max} (kN)	I (Ns)	P (kPa)
SCS50	8147	895	12837	617
SCS75	8070	1012	15703	829

Table 5.2 Midpoint displacement of SAS and SWS tanks (mm)

Specimen	SAS 1 st	SAS 2 nd	SWS 1 st	SWS 2 nd
Maximum displacement	30.6	51.2	28.9	36.3
Permanent displacement	16.8	35.8	14.3	22.0

Table 5.3 Midpoint displacement of SCS50 and SCS75 sandwich panels (mm)

Specimen	SCS50	SCS75
Maximum displacement	34.7	9.8
Permanent displacement	20.4	3.9

Table 5.4 Comparison of maximum displacements between test and SDOF (mm)

Specimen	SAS	SWS	SCS50	SCS75
Test (1)	30.6	28.9	34.7	9.8
SDOF (2)	35.5	28.8	37.3	10.8
Difference [(2)-(1)]/(1)×100%	16.0%	0.3%	7.5%	10.2%

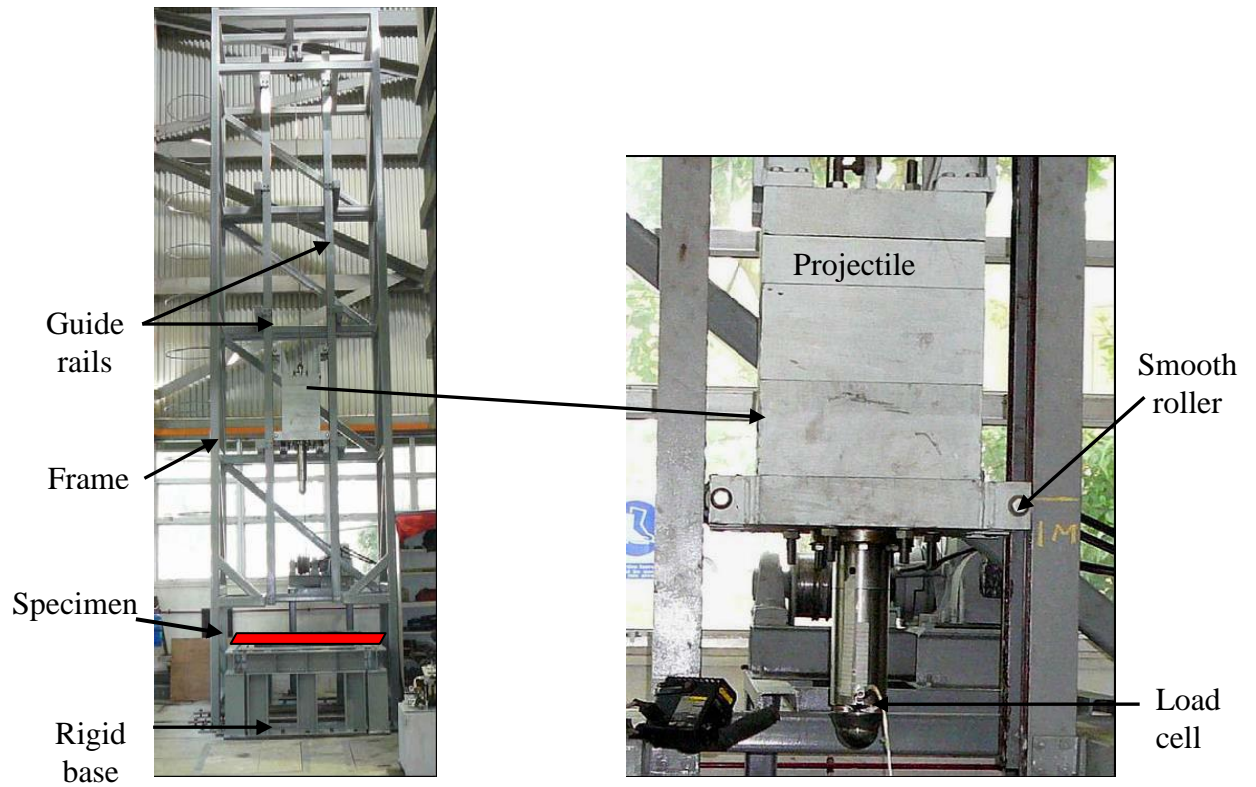


Fig. 5.1 Drop-weight impact test machine

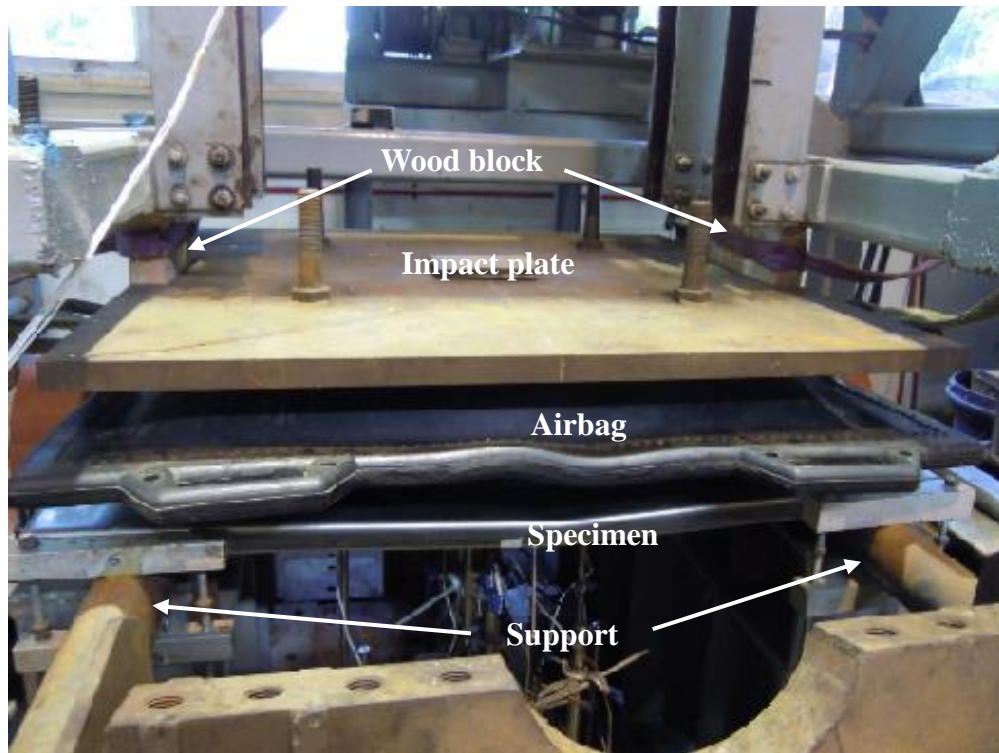


Fig. 5.2 Drop-weight impact test setup

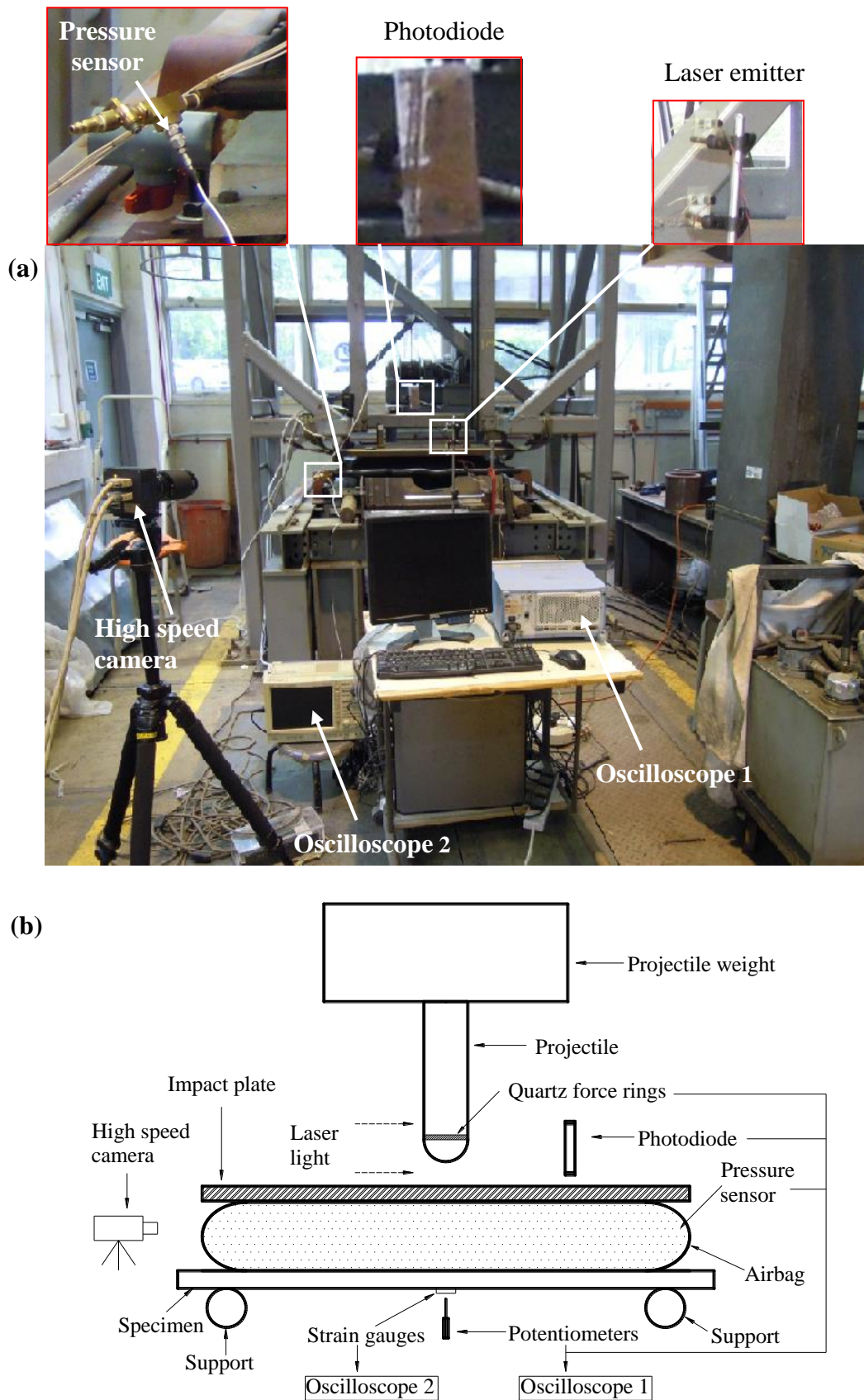


Fig. 5.3 Overview of data acquisition system: (a) photo (b) schematic drawing

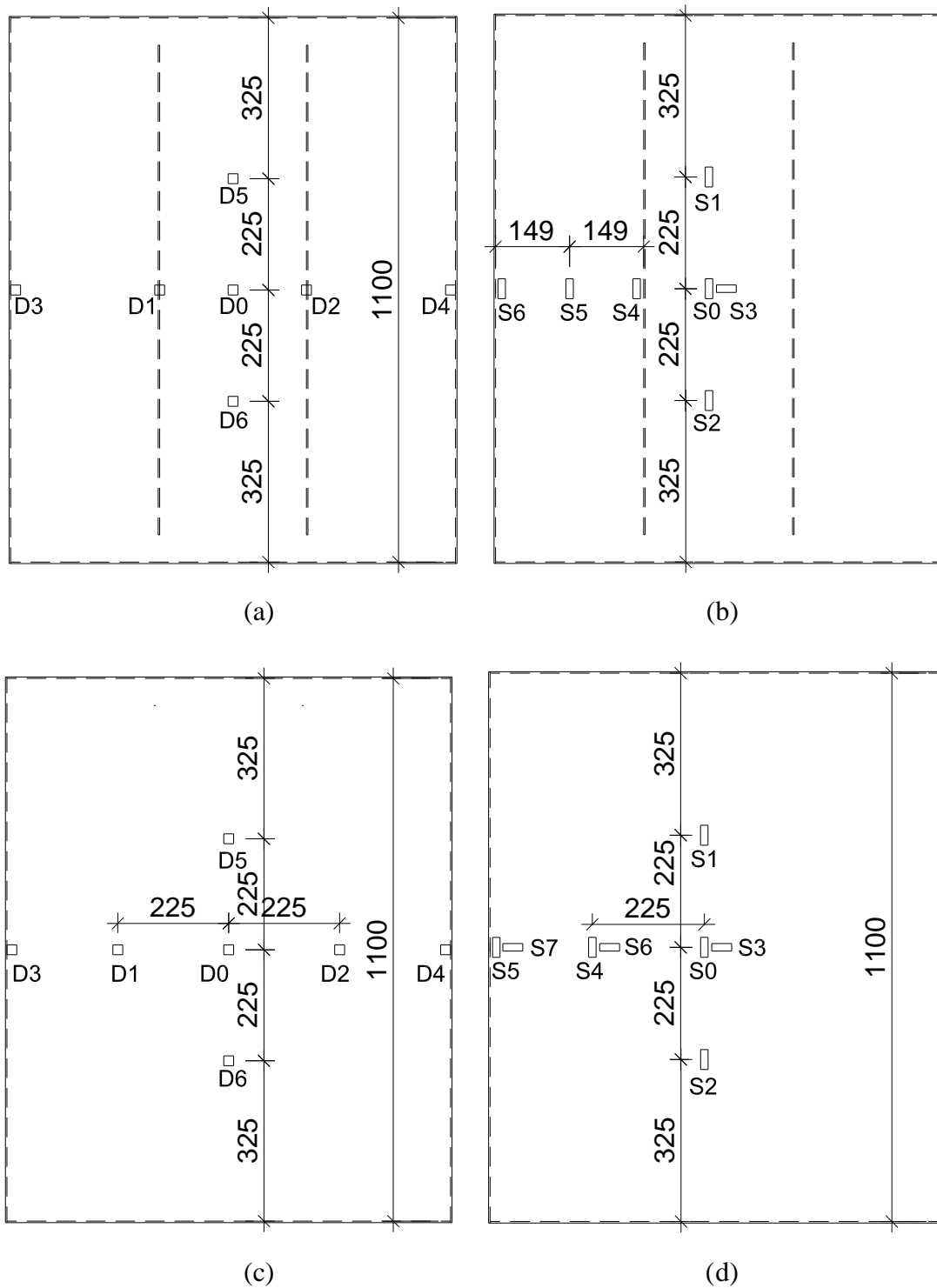


Fig. 5.4 Instrumentation layout: (a) LVDTs on SAS and SWS (b) strain gauges on SAS and SWS (c) LVDTs on SCS50 and SCS75 (d) strain gauges on SCS50 and SCS75 (in mm)

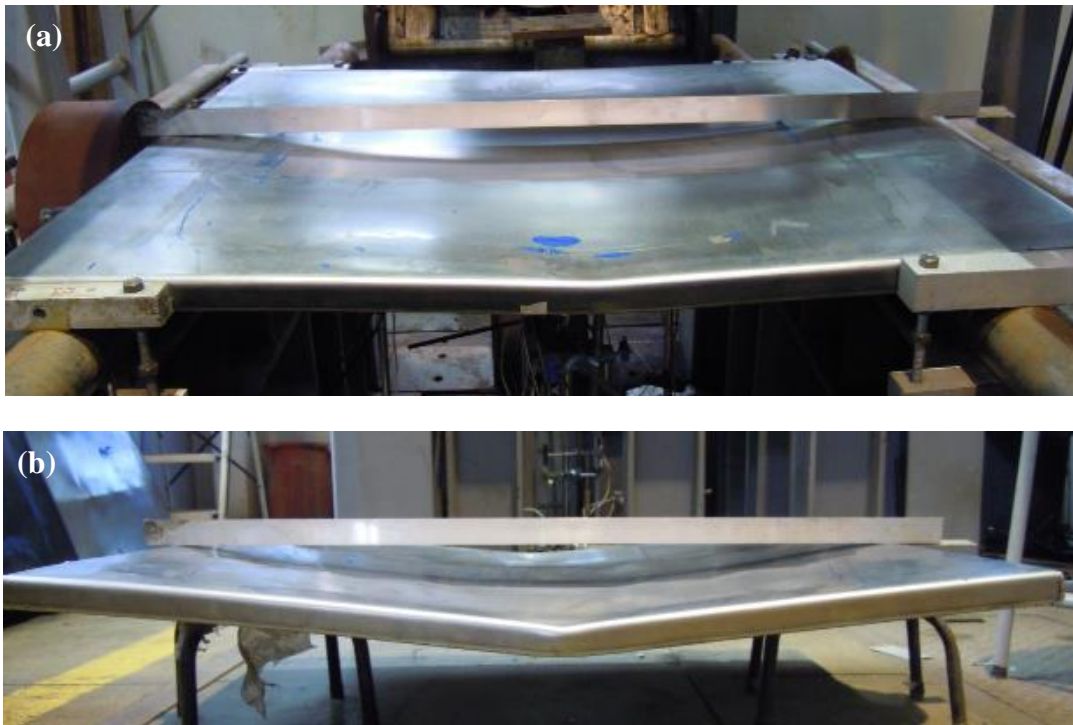


Fig. 5.5 Deformed shape of SAS tank: (a) after 1st impact (b) after 2nd impact

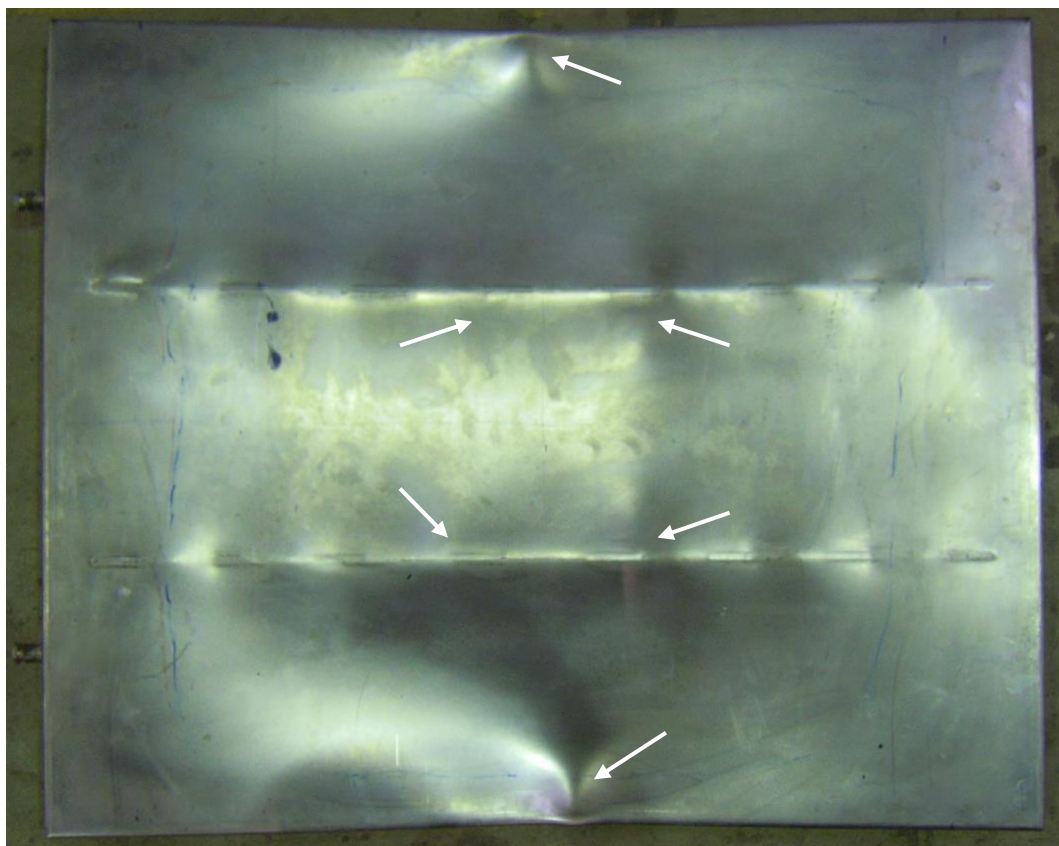


Fig. 5.6 Buckling on top surface of SAS tank after 2nd impact

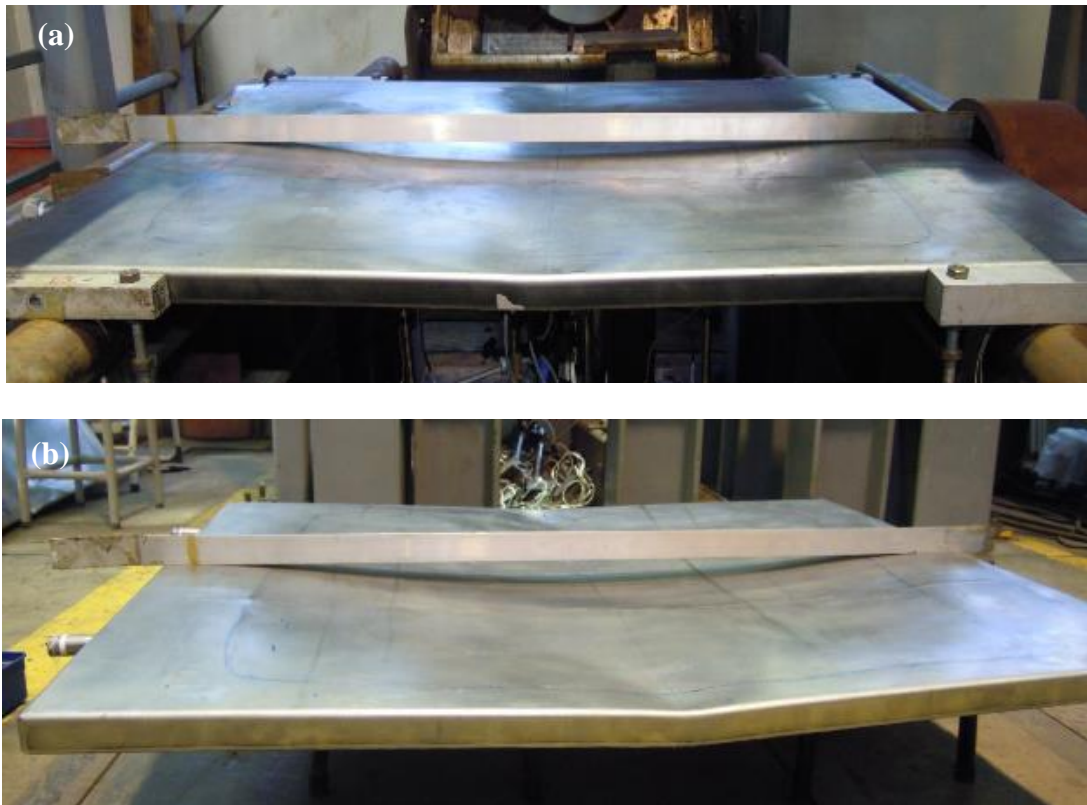


Fig. 5.7 Deformed shape of SWS: (a) after 1st impact (b) after 2nd impact

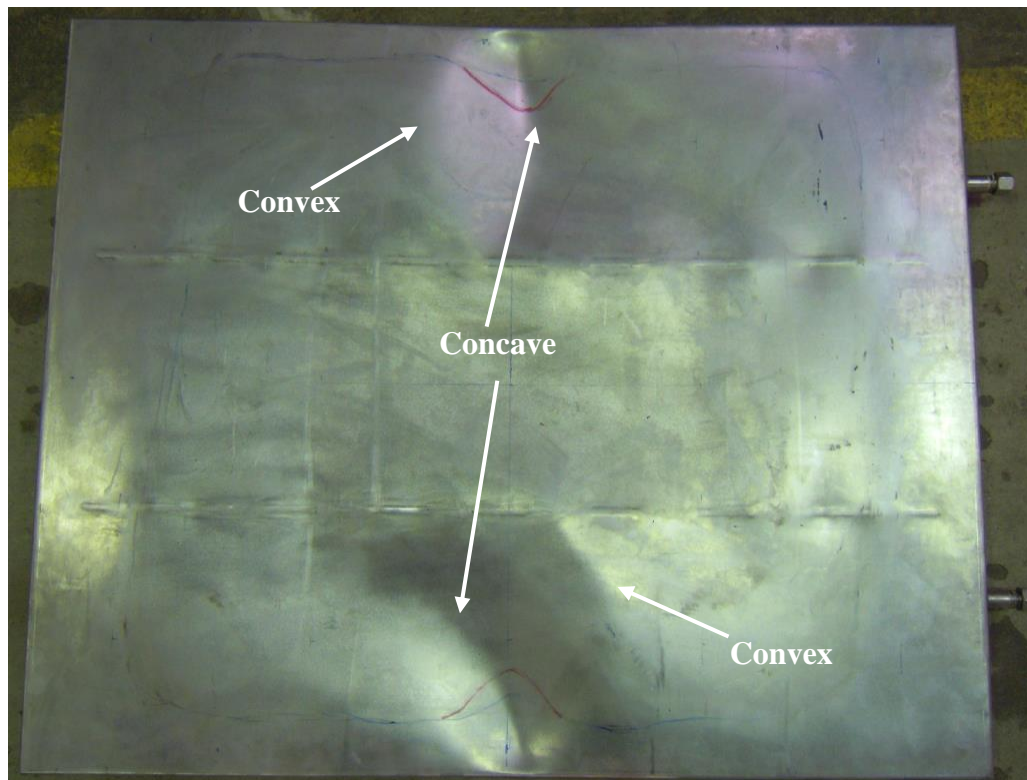


Fig. 5.8 Top surface of SWS after 2nd impact



Fig. 5.9 Permanent deformation of SAS and SWS after 2nd test

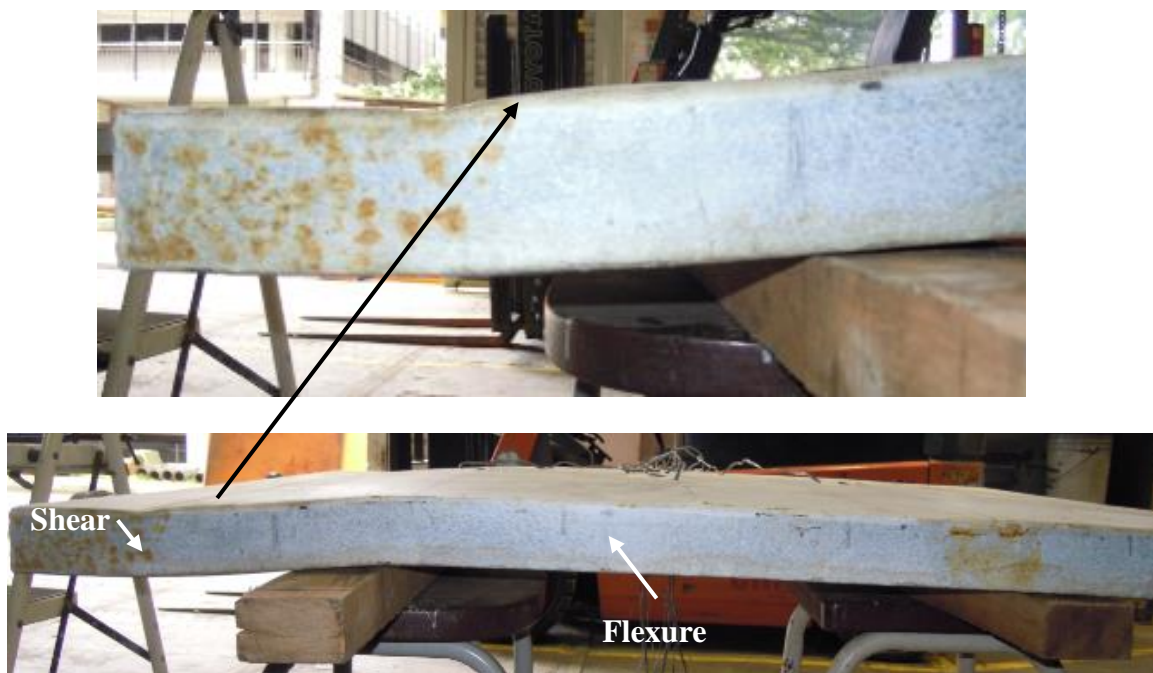


Fig. 5.10 Deformed shape of SCS50 panel after impact



Fig. 5.11 Deformed shape of SCS50 and SCS75 panels after impact

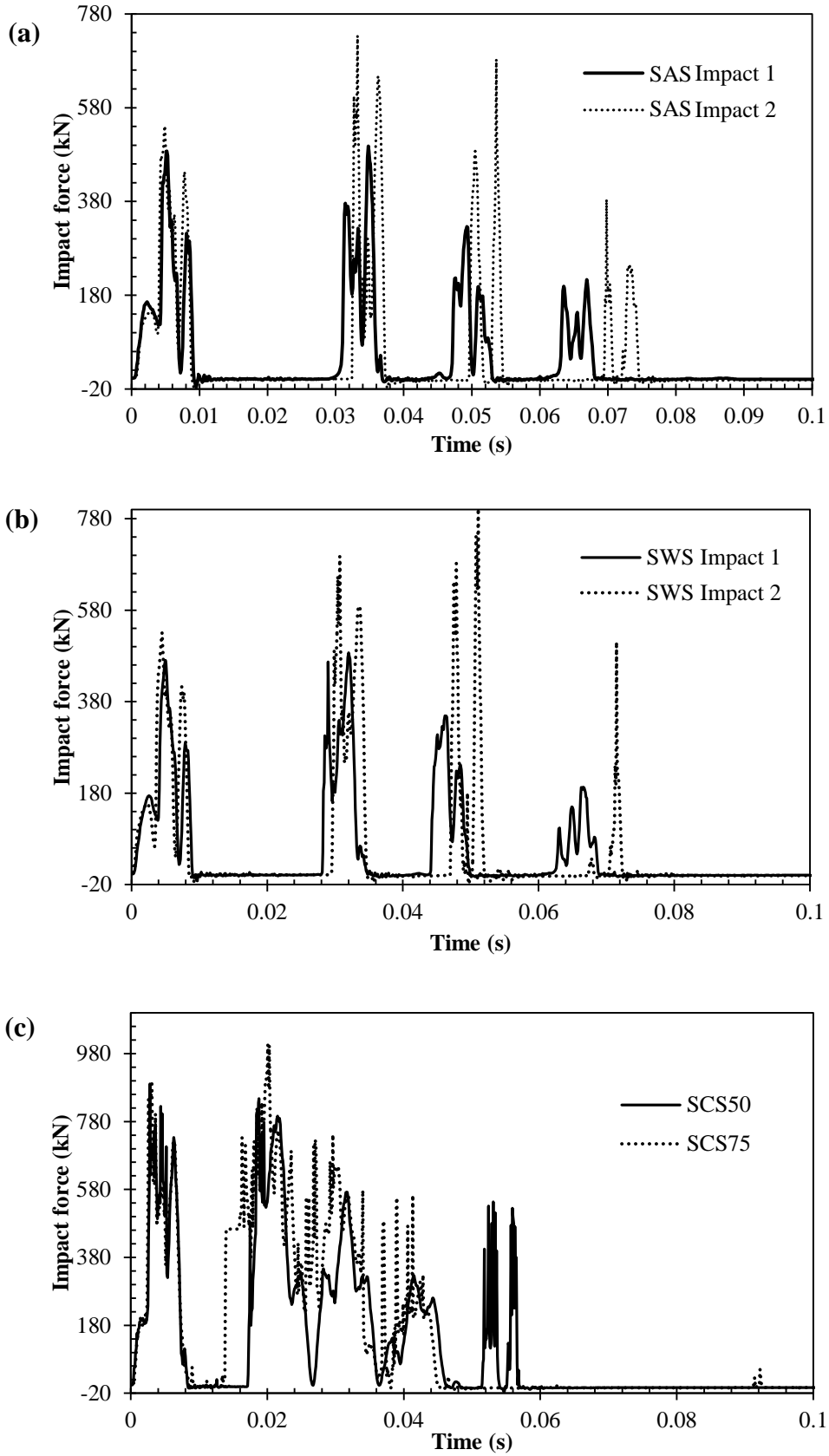


Fig. 5.12 Impact force–time history of (a) SAS (b) SWS (c) SCS sandwich panel

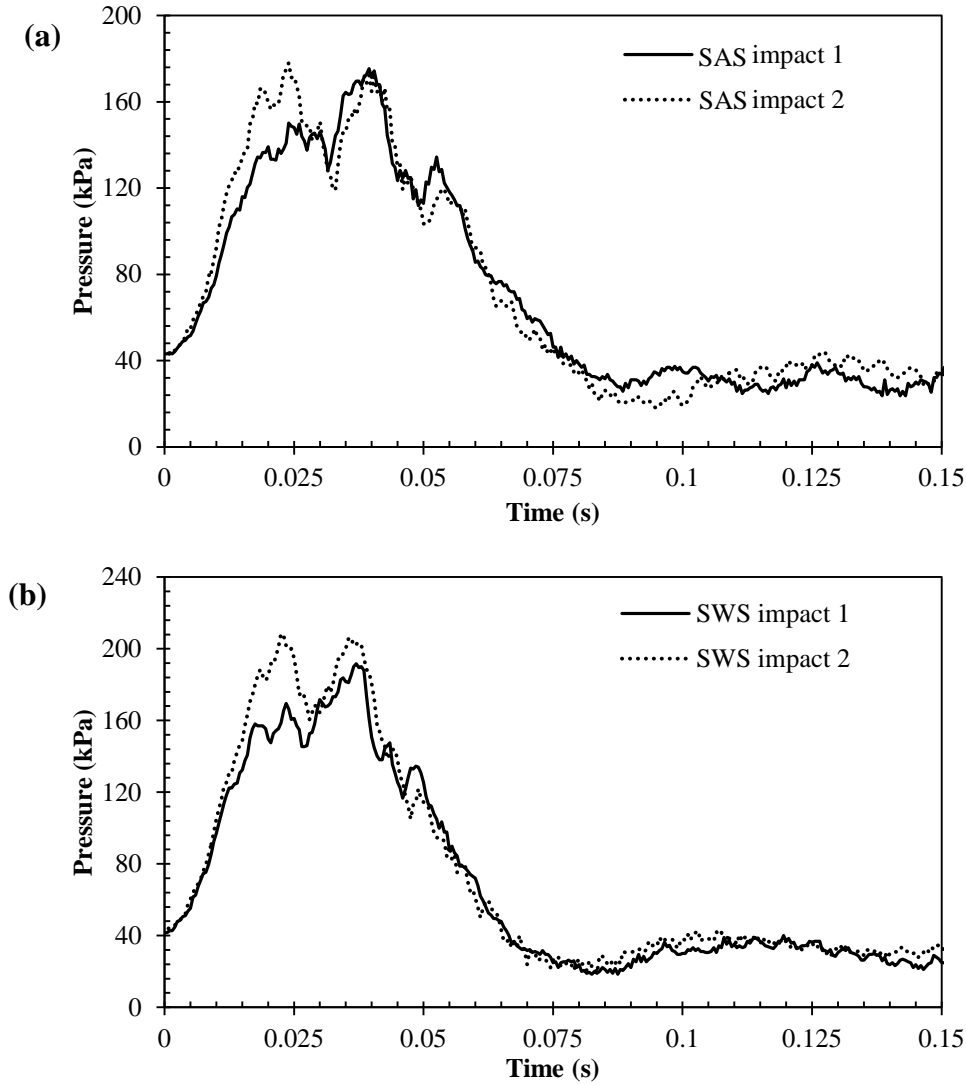


Fig. 5.13 Air pressure–time history of (a) SAS and (b) SWS tanks

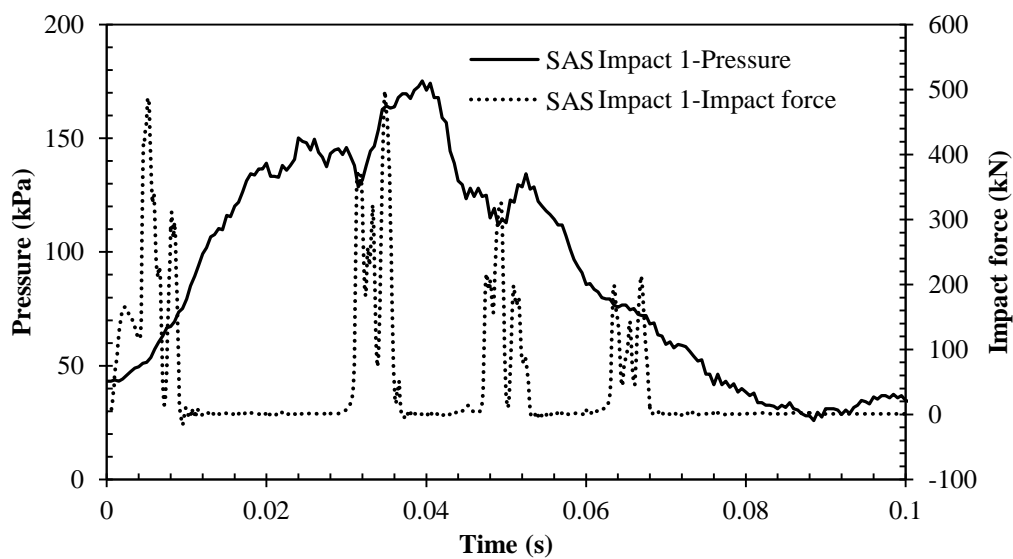


Fig. 5.14 Air pressure and impact force–time history of SAS under first impact

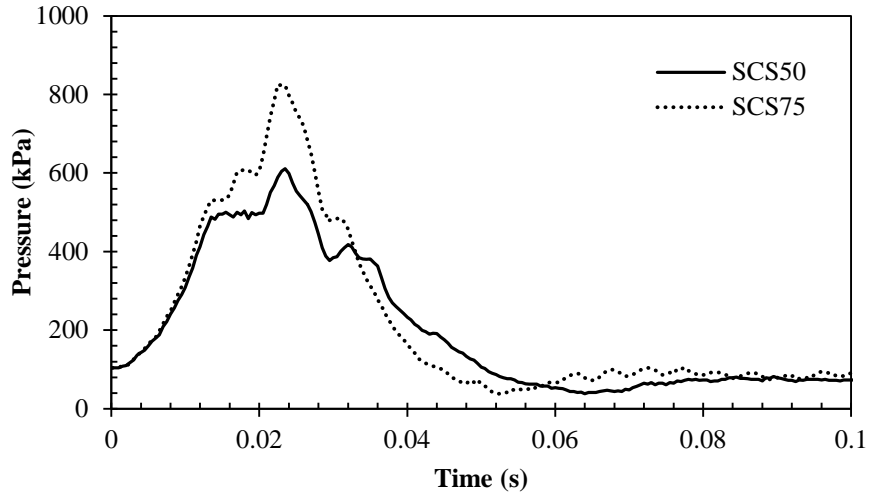


Fig. 5.15 Air pressure–time history of SCS sandwich panel

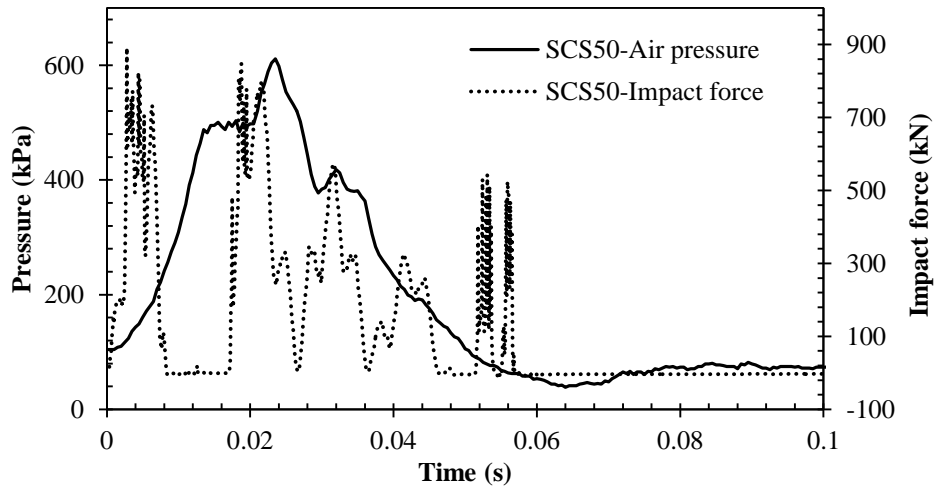


Fig. 5.16 Air pressure and impact force–time history of SCS50 panel

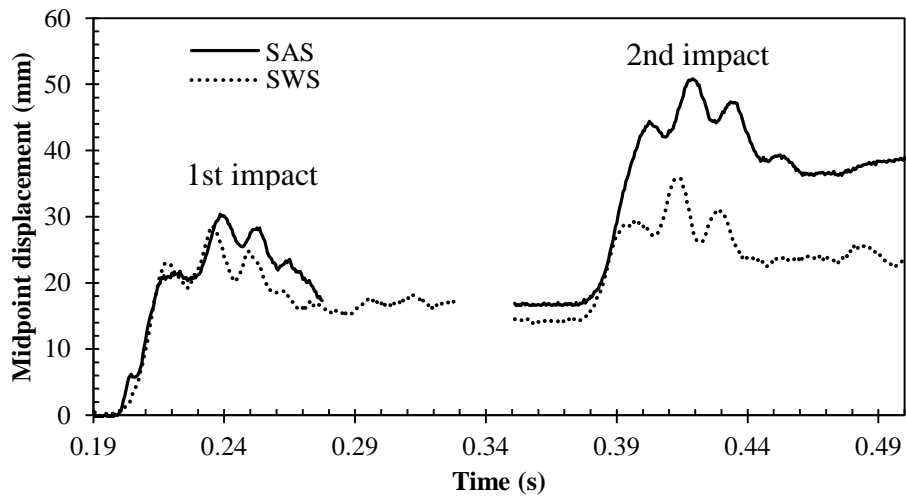


Fig. 5.17 Displacement–time histories of SAS and SWS tanks

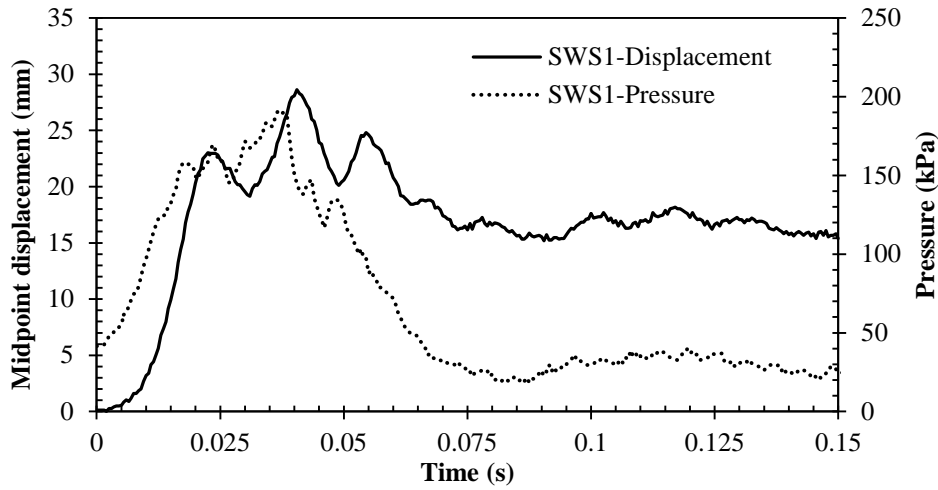


Fig. 5.18 Displacement–time and air pressure–time histories of SWS tank under first impact

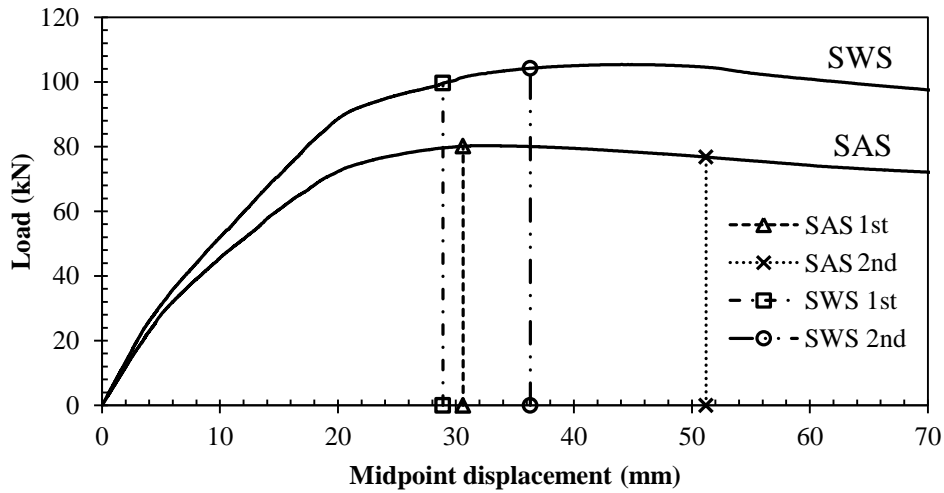


Fig. 5.19 Comparison of maximum displacements of SAS and SWS tanks in the load–deflection curves

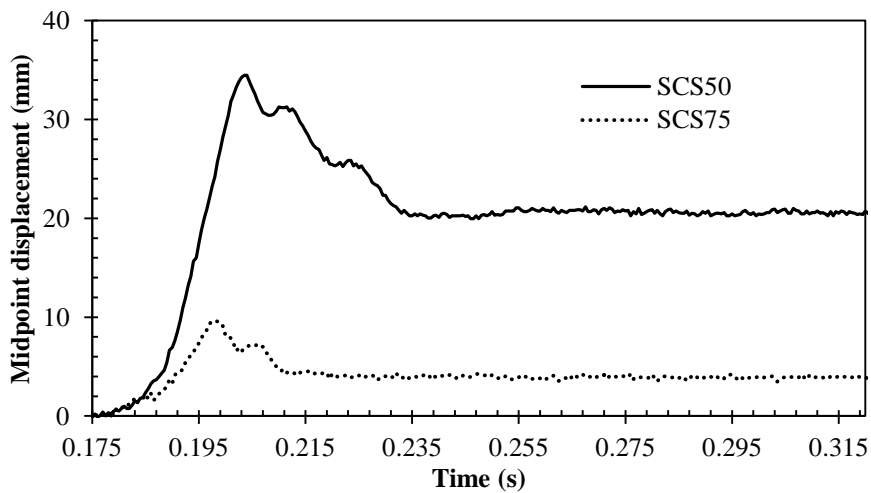
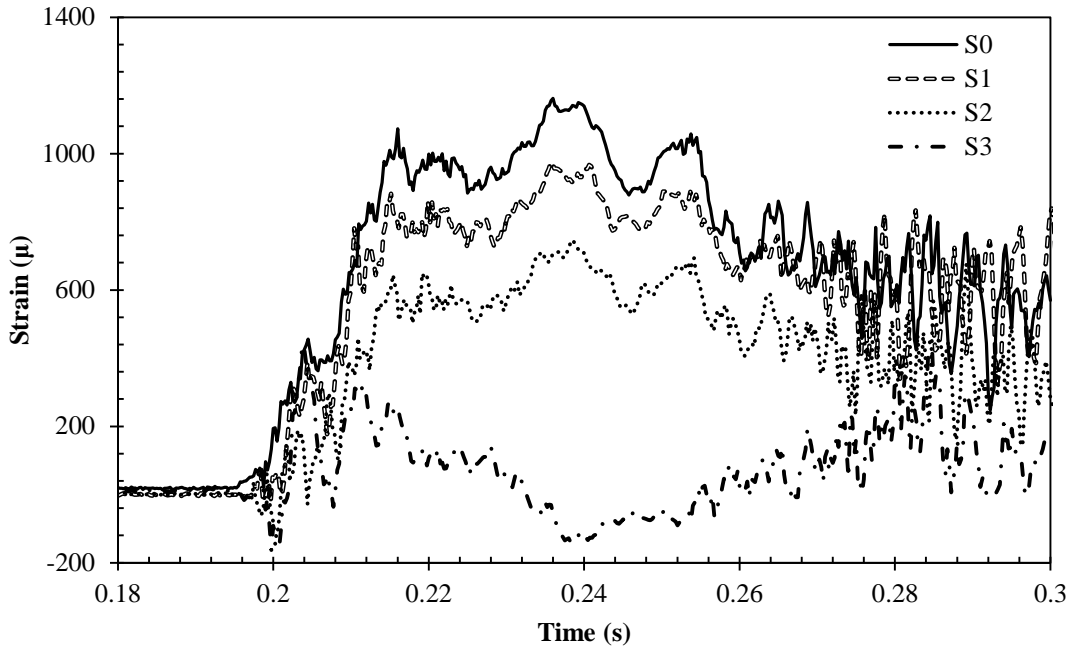
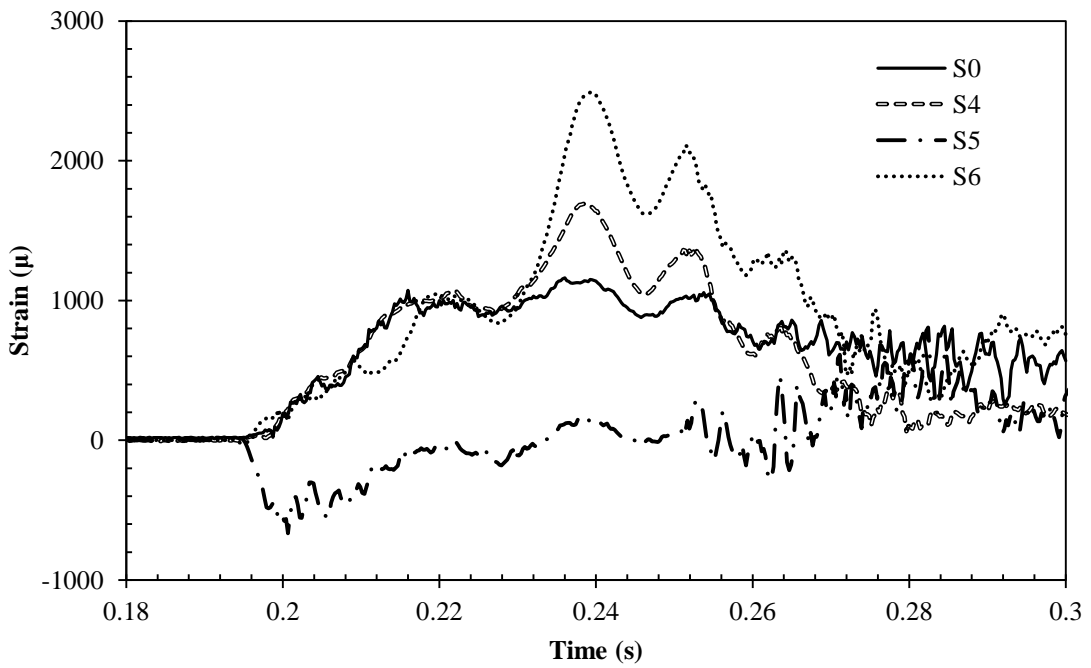


Fig. 5.20 Displacement–time histories of SCS50 and SCS75 sandwich panels

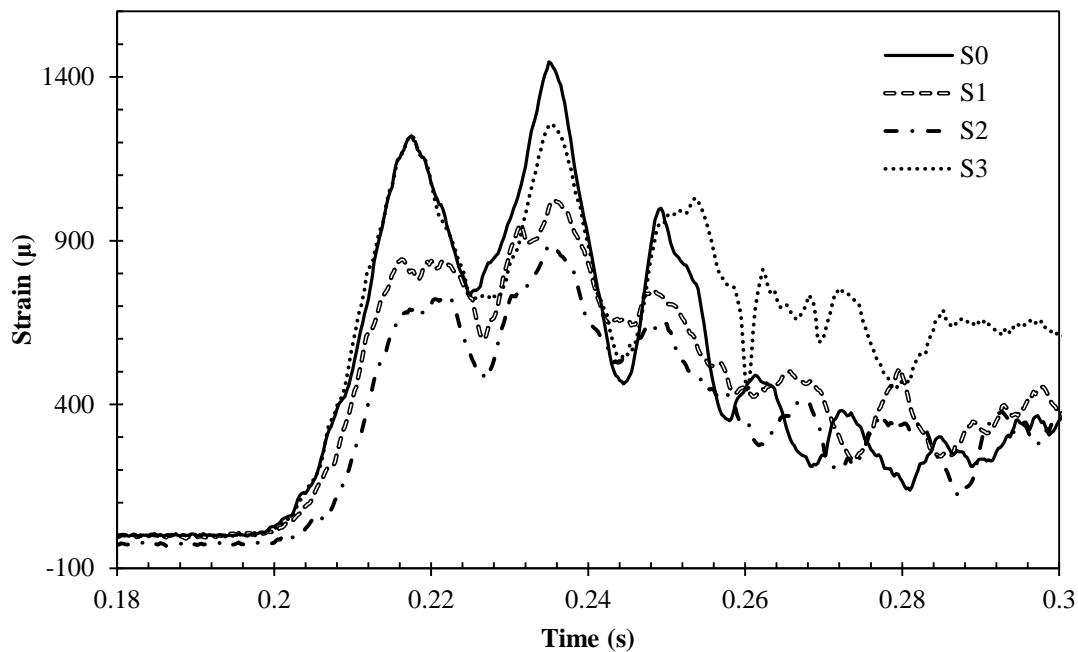


(a)

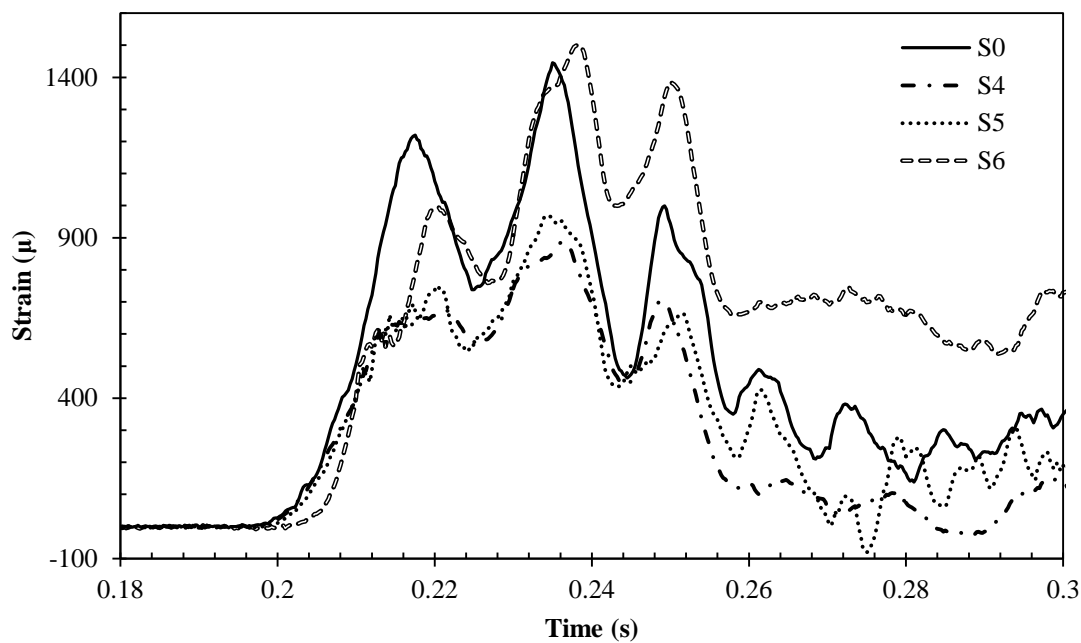


(b)

Fig. 5.21 Strain–time histories of SAS tank under first impact: (a) along span direction (b) along width direction



(a)



(b)

Fig. 5.22 Strain–time histories of SWS tank under first impact: (a) along span direction (b) along width direction

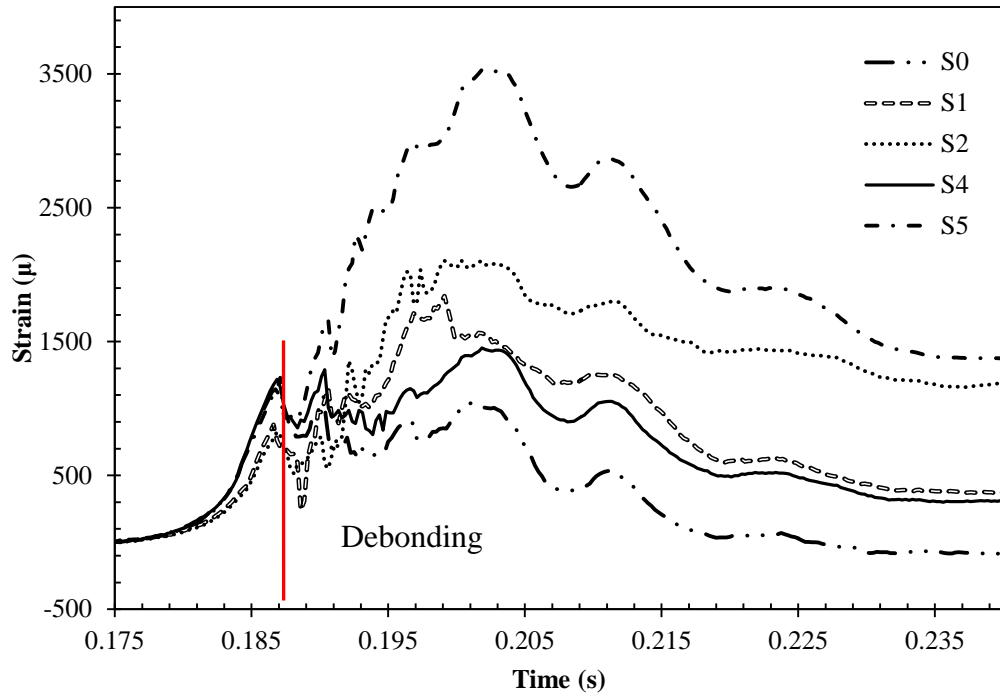


Fig. 5.23 Longitudinal strain–time history of SCS50 under impact

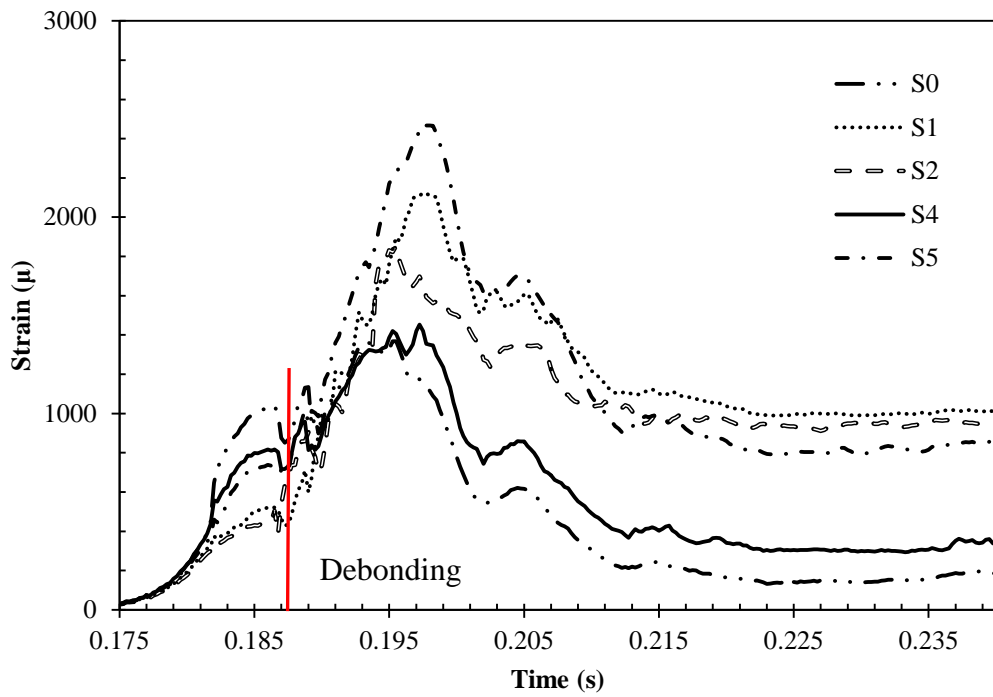
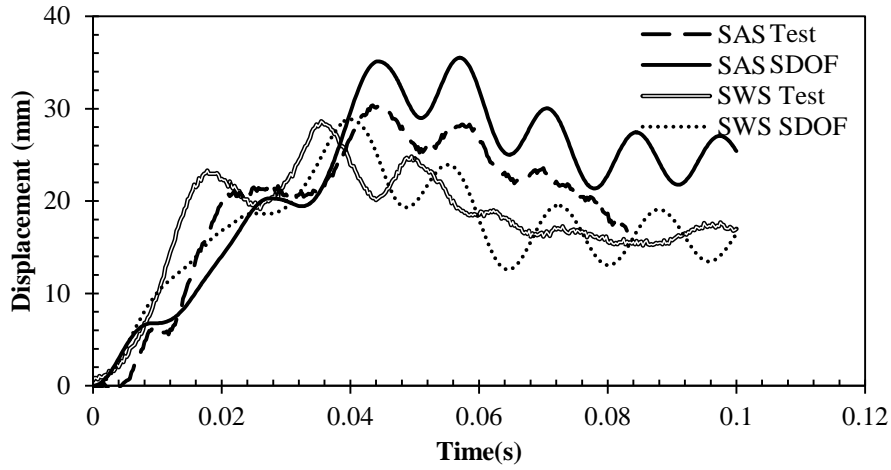
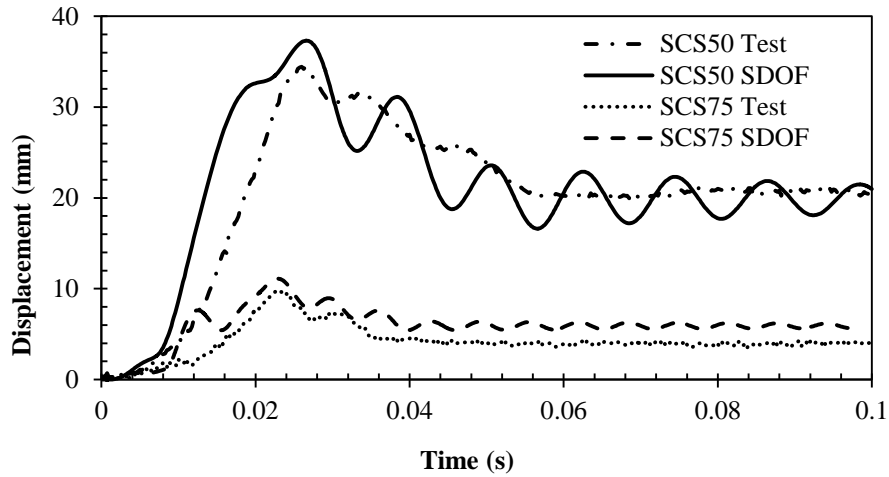


Fig. 5.24 Longitudinal strain–time history of SCS75 under impact



(a) SAS and SWS



(b) SCS50 and SCS75

Fig. 5.25 Comparison of displacement–time histories between test and SDOF

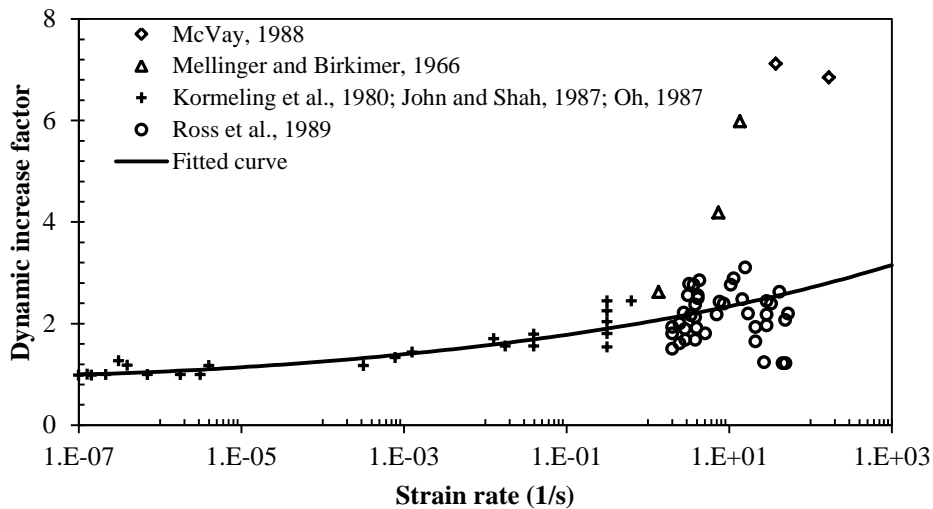


Fig. 5.26 Strain rate effects of mortar under tension

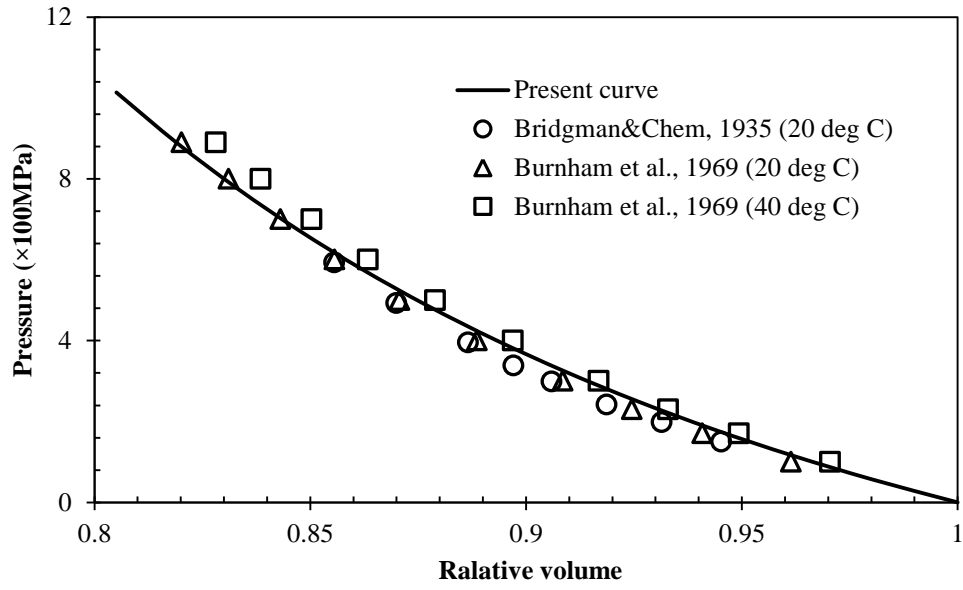


Fig. 5.27 Relationship between pressure and relative volume for water

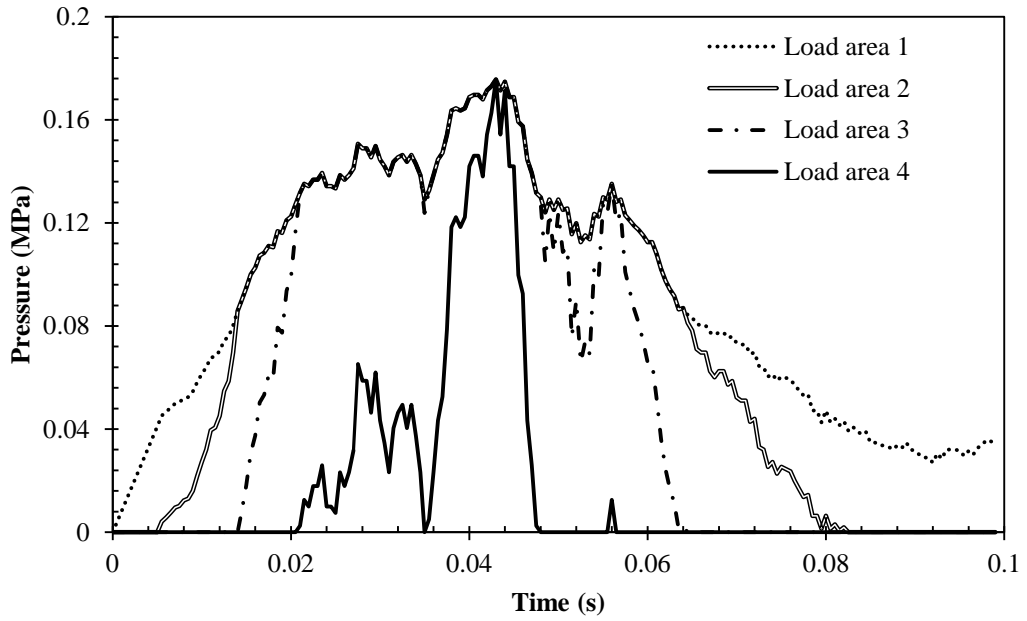


Fig. 5.28 Applied pressure–time history of SAS

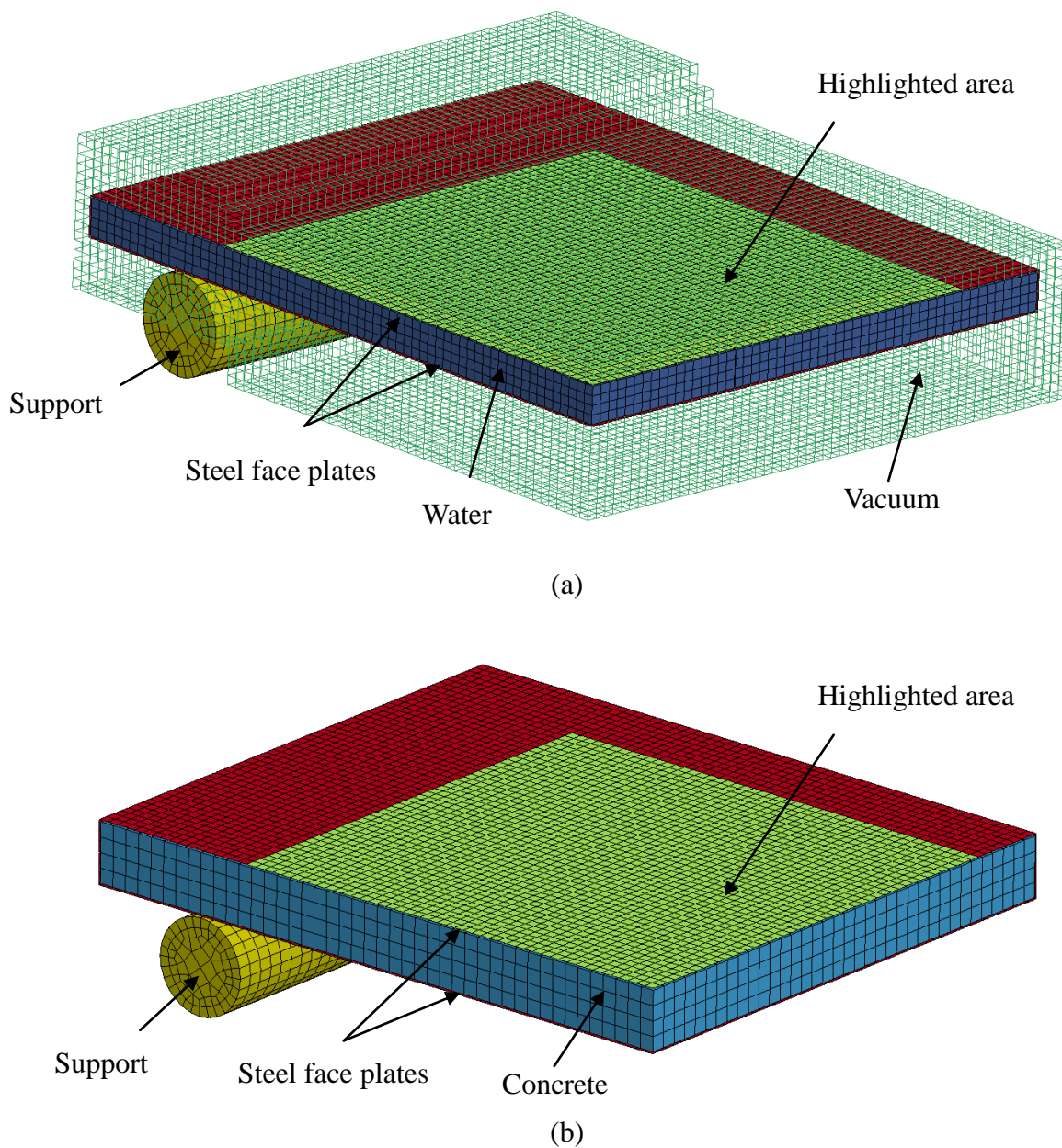


Fig. 5.29 FE model of (a) SWS and (b) SCS sandwich panel in dynamic pressure test

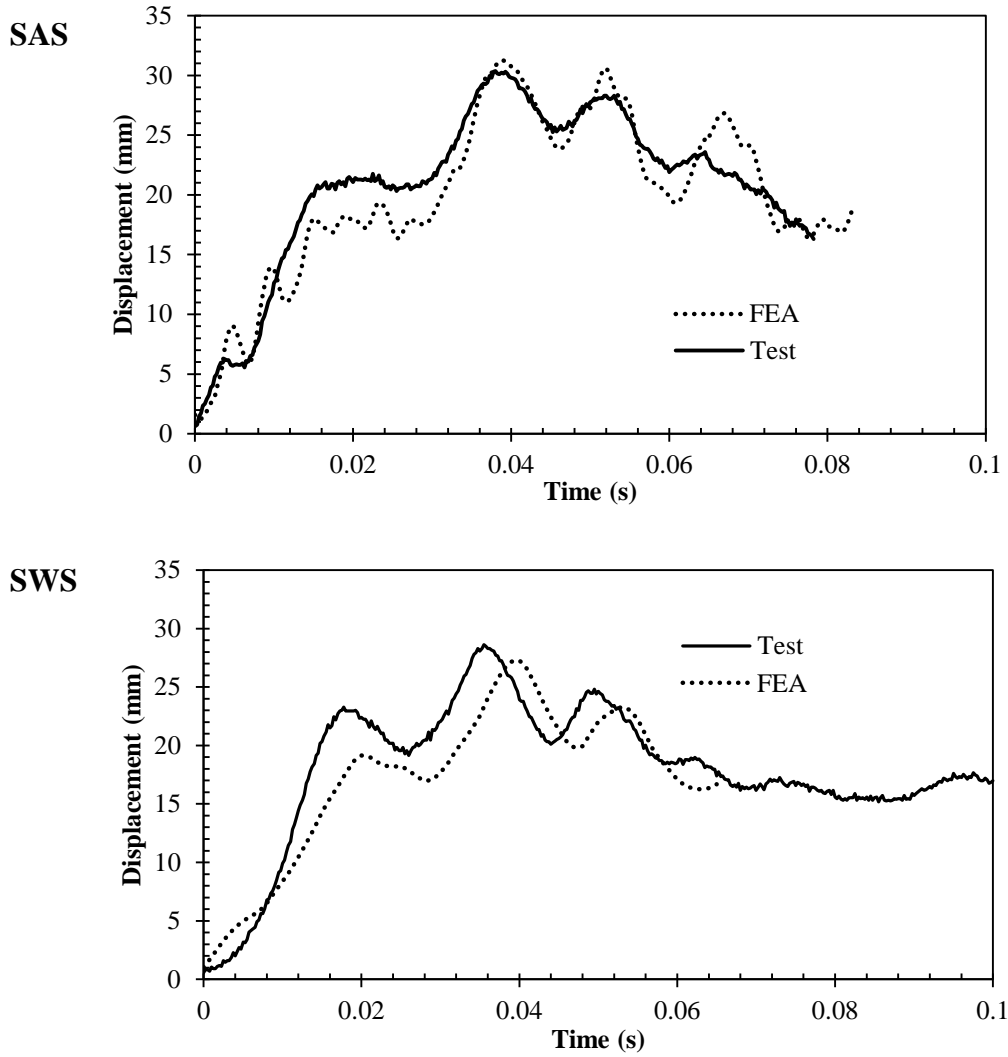


Fig. 5.30 Comparison of FE predicted displacement–time histories with test

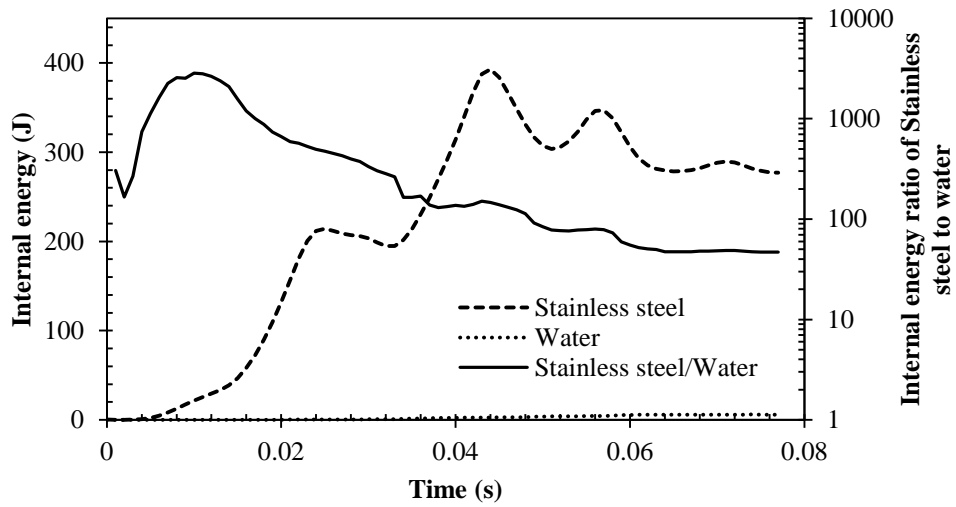


Fig. 5.31 Internal energy of water and stainless steel in FE analysis

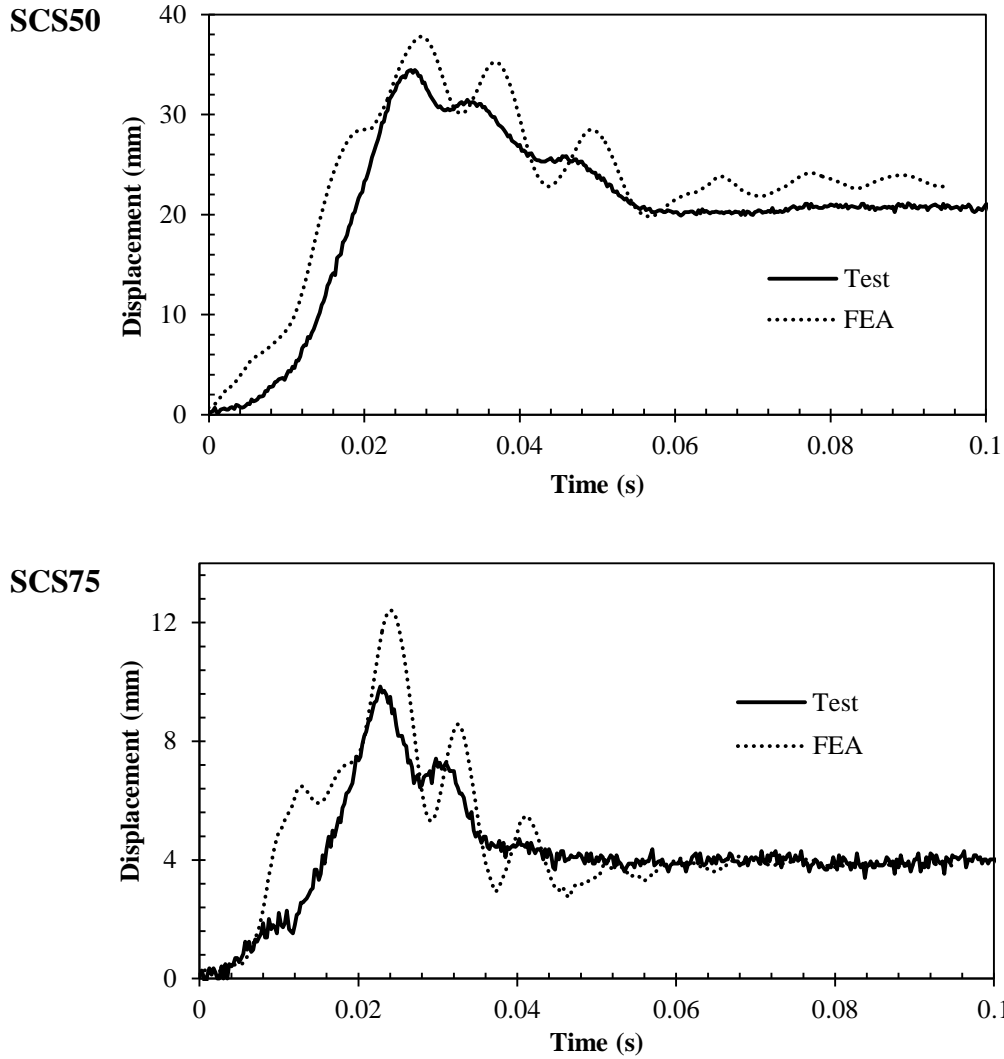


Fig. 5.32 Comparison of FE predicted displacement–time histories with test

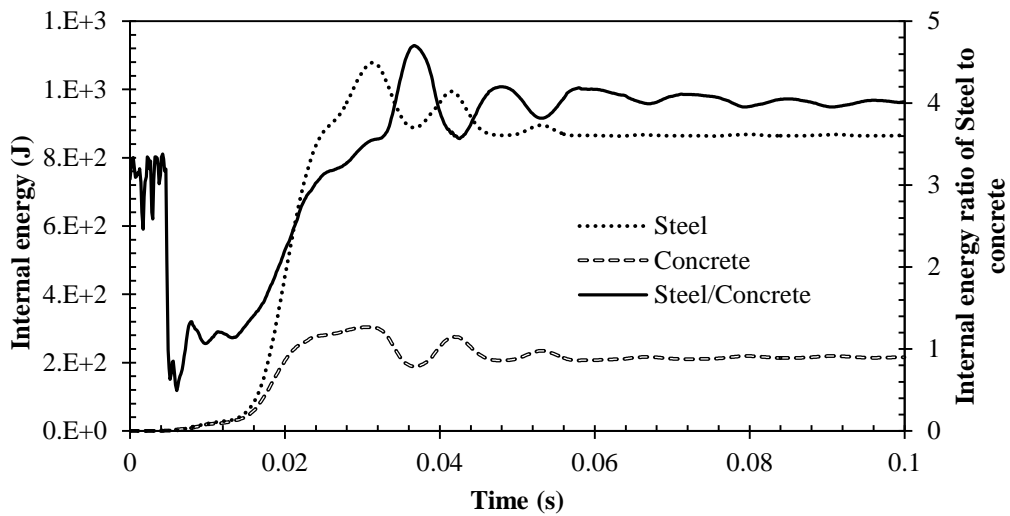


Fig. 5.33 Internal energy of steel and core material of SCS50

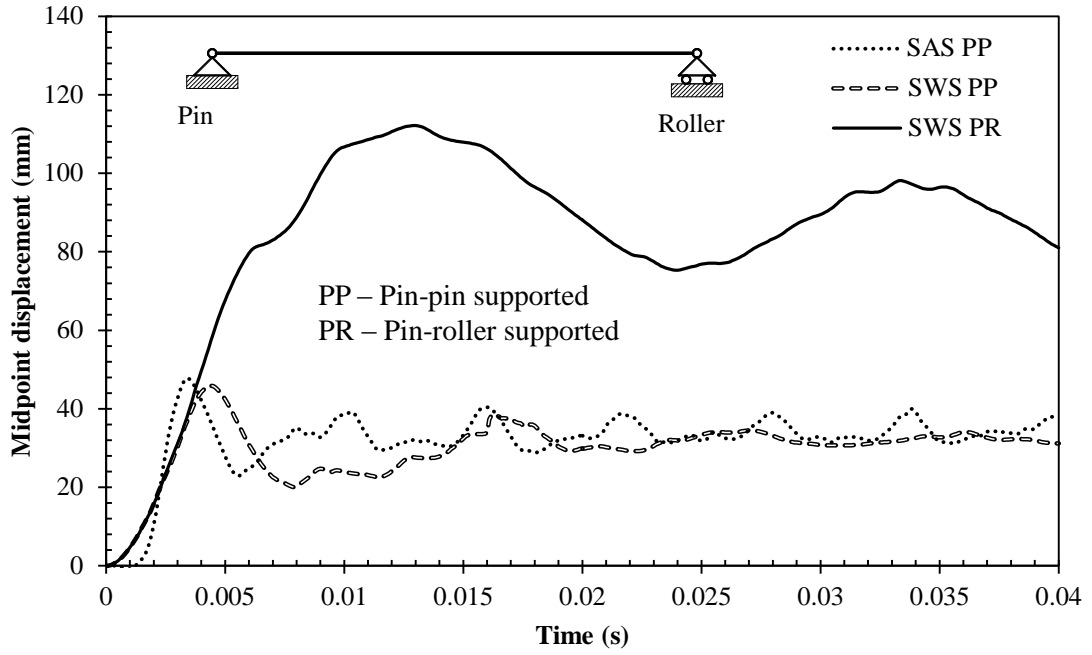


Fig. 5.34 Midpoint displacement–time histories of SAS and SWS

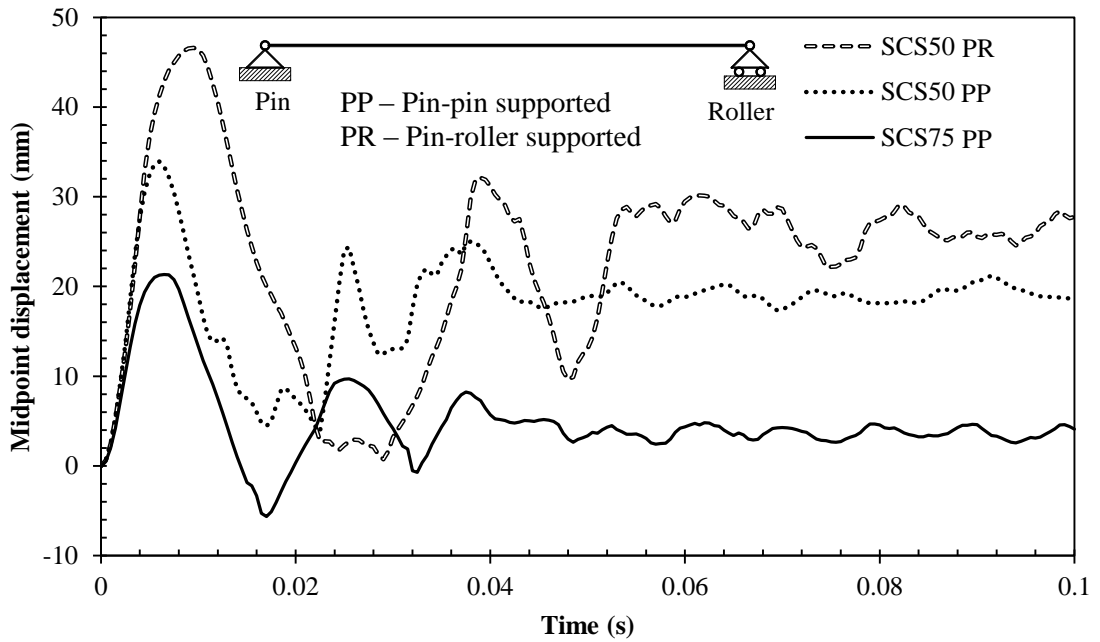


Fig. 5.35 Midpoint displacement–time histories of SCS sandwich panels

Chapter 6 Analytical Methods for Predicting Deformation of Water Façade Systems under Blast Loading

6.1 Introduction

It was demonstrated in Chapter 5 that the blast resistance of water façade systems with pin-pin supported boundary was significantly higher than those with pin-roller supported boundary. Hence, the analytical methods for predicting the deformation of pin-pin supported water façade systems, including SWS and SWS-SCS, under blast loading were developed in this chapter in order to facilitate the blast resistant design of such façade systems.

The SDOF system of the SWS was established, based on which, the shock spectrum and dimensionless P–I diagram were constructed. They can be directly used to gauge the damage level of SWS under given blast load. As for the SWS-SCS, the SDOF system was also established. In contrast, a similar dimensionless P–I diagram was not available for the SWS-SCS, since the relationship between dimensionless pressure and impulse was not established due to the complex material behavior of concrete. Due to the deficiencies of SDOF method, which cannot capture the varying DIF and deflection shape, The Lagrange Equation method with combined deflection shape function and varying DIF was proposed as an improved alternative for predicting the deformation of water façade systems under blast loading

6.2 Analytical Method for Water Filled Tank

6.2.1 SDOF System

For the pin-roller supported SWS tank, the side plates and stiffeners are critical in resisting pressure load. In case where the tank is further axially restrained with pin-pin supported boundary, the top and bottom plates are the key elements to resist pressure load by developing tensile membrane force. Since the deviatoric strength of water is negligible, it is thought to have no contribution to the resistance of SWS under pressure load. Therefore, the SWS tank with pin-pin supported boundary can be simplified as two pin-pin supported steel plates (top and bottom plates) that deform together, as shown in Fig. 6.1. This simplification is conservative and also has wide application since it neglects the side plates and stiffeners and therefore can be applicable for the SWS with different types of stiffeners or connectors between top and bottom plates.

The pin-pin supported SWS tank can be transformed into an equivalent SDOF system by load-mass factor (Biggs, 1964) and the equation of motion of the equivalent SDOF system is given as

$$K_{LM}m\ddot{y} + R(y) = F(t) \quad (6.1)$$

where K_{LM} is the load-mass factor, which can be determined by given deflection shape function. The resistance–deflection and deflection shape functions, which are needed to establish the equation of motion of the equivalent SDOF system in Eq. (6.1), will be discussed in followings.

Since the top/bottom steel plate of SWS is relatively thin and the pressure load is mainly resisted by the tensile membrane force, only axial tension force, T , is considered while bending, shear and compression are negligible, as shown in Fig. 6.2. To satisfy the force equilibrium in y direction, the following equation can be established

$$\bar{T} \frac{dy}{dx} - \bar{T} \frac{d}{dx}(y+dy) = Pdx \quad (6.2)$$

where \bar{T} is the tension force per unit width (N/m) and P is pressure (N/m²). It should be noted that Eq. (6.2) is derived based on the assumption that $\sin\vartheta = \tan\vartheta$. Hence, the support rotation at boundary, ϑ , must be less than 17.75° to ensure that the error introduced by aforementioned assumption is less than 5%. This rotation limitation is only slightly smaller than the maximum allowed support rotation of 20° with lowest protection level (ASCE, 2011). Besides, the error corresponding to support rotation of 20° is 6.42%, which is also acceptable for blast resistant design. The solution of Eq. (6.2) can be obtained as follow by considering the pin-pin supported boundary.

$$y = \frac{P}{2\bar{T}}(Lx - x^2) \quad (6.3)$$

where L is the span. The deflection shape function can then be defined by dividing y by mid-span displacement y_m as

$$\phi(x) = \frac{y(x)}{y_m} = \frac{4}{L^2}(Lx - x^2) \quad (6.4)$$

Then, the load-mass factor can be obtained as 0.8. By equating the resistance $R(y)$ with P in Eq. (6.3) and setting $x=L/2$, the relationship between resistance and mid-span displacement can be obtained as

$$R(y_m) = \frac{8\bar{T}y_m}{L^2} \quad (6.5)$$

The tension force per unit width \bar{T} can be defined as

$$\bar{T} = \begin{cases} Et\varepsilon & \varepsilon \leq \varepsilon_y \\ Et\varepsilon_y + \alpha Et(\varepsilon - \varepsilon_y) & \varepsilon > \varepsilon_y \end{cases} \quad (6.6)$$

where E is Young's modulus, t is plate thickness, ε is strain, ε_y is yield strain and α is the hardening coefficient of the elastic-plastic-hardening constitutive model which is adopted in this study to define the stress-strain relationship of stainless steel beyond elastic range. The strain ε in Eq. (6.6) can be calculated as

$$\varepsilon = \frac{\Delta L}{L} = \frac{1}{4} \sqrt{(8y_m/L)^2 + 4} + \frac{L}{16y_m} \ln \left(\frac{1 + \sqrt{1 + (L/4y_m)^2}}{-1 + \sqrt{1 + (L/4y_m)^2}} \right) - 1 \approx 2.638(y_m/L)^2 \quad (6.7)$$

Therefore, Eq. (6.7) can be adopted to construct the resistance-deflection function as follow:

$$R(y_m) = \begin{cases} \frac{21.104Ety_m^3}{L^4} & y_m \leq L\sqrt{\frac{\varepsilon_y}{2.638}} \\ \frac{8Et\varepsilon_y(1-\alpha)y_m}{L^2} + \frac{21.104\alpha Ety_m^3}{L^4} & y_m > L\sqrt{\frac{\varepsilon_y}{2.638}} \end{cases} \quad (6.8)$$

By substituting Eq. (6.8) and load-mass factor into Eq. (6.1), the equation of motion for the equivalent SDOF system is thus obtained.

Since only tension force is considered in establishing the equilibrium equation in Eq. (6.2) for the steel plate, an energy criterion is adopted to limit its application range. The criterion is that the internal energy per unit width by tension force, as defined in Eq. (6.9), must be more than 95 % of the total internal energy per unit width.

$$E_T = \int_0^{L/2} \int_{-t/2}^{t/2} \frac{1}{2} E \varepsilon_T^2 dt dx \quad (6.9)$$

Substituting the tension strain in Eq. (6.7) into Eq. (6.9) leads to

$$E_T = \int_0^{L/2} \int_{-t/2}^{t/2} \frac{1}{2} E \left[2.638 \left(\frac{y_m}{L} \right)^2 \right]^2 dt dx = 3.48 E t \frac{y_m^4}{L^3} \quad (6.10)$$

Meanwhile, the total internal energy per unit width due to tension and bending is given by

$$E_{T+B} = \int_0^{L/2} \int_{-t/2}^{t/2} \frac{1}{2} E \varepsilon_{T+B}^2 dt dx \quad (6.11)$$

and the total strain ε_{T+B} is obtained by summing the tension and bending strain. The bending strain can be calculated as follow

$$\varepsilon_B = t' \frac{|y''|}{(1+y'^2)^{3/2}} = t' \frac{P/\bar{T}}{\left(1 + \frac{P^2}{4T^2} (L-2x)^2 \right)^{3/2}} \quad (6.12)$$

where P/\bar{T} is obtained from Eq. (6.5) as follow

$$P/\bar{T} = 8y_m/L^2 \quad (6.13)$$

Substituting Eq. (6.13) into Eq. (6.12) and then substituting Eq. (6.12) and Eq. (6.7) into Eq. (6.11) leads to

$$E_{T+B} = 3.48 E t \frac{y_m^4}{L^3} + \frac{8 E t^3 y_m^2}{3 L^3} F\left(\frac{y_m}{L}\right) \quad (6.14)$$

where

$$F\left(\frac{y_m}{L}\right) = \frac{96 \left(\frac{y_m}{L} \right)^2 + 10}{\left(8 \frac{y_m}{L} \right)^4 + 512 \left(\frac{y_m}{L} \right)^2 + 16} + \frac{3 \arctan \left(\frac{4 y_m}{L} \right)}{32 \frac{y_m}{L}} \quad (6.15)$$

Finally, Eq. (6.10) and Eq. (6.14) are substituted into the aforementioned energy criterion limit defined in Eq. (6.16) to obtain the application range in terms of y_m in Eq. (6.17).

$$\frac{E_T}{E_{B+T}} \geq 0.95 \quad (6.16)$$

$$y_m \geq 3.82t\sqrt{F(y_m/L)} \quad (6.17)$$

As mentioned previously, the support rotation should be less than 17.75° , which is equivalent to the ratio of mid-span displacement to span y_m/L being less than 0.08. It is noted that $\sqrt{F(y_m/L)}$ ranges from 1 to 0.95 for y_m/L between 0 and 0.08. The variation is not significant and the maximum value can be applied conservatively in Eq. (6.17) to determine the lower bound application range. Hence, the application range for the constructed SDOF system can be defined as follow:

$$3.82t \leq y_m \leq 0.08L \quad (6.18)$$

It should be mentioned that the lower bound in Eq. (6.18) is derived based on elastic material, while it is proven to be conservative for material in the plastic range. Hence, the application range in Eq. (6.18) can apply for both elastic and elastic-plastic materials. It is noted that when the ratio of plate thickness to span t/L is larger than 0.021, the proposed SDOF system cannot be used. Hence, other approach, like FE analysis, may be needed to solve this kind of problem. However, for practical blast resistance façade panels, the ratio of plate thickness to span is often smaller than 0.021.

The FE model of pin-pin supported SWS tank under lateral pressure load described in Chapter 4 was adopted to verify the resistance–deflection and deflection shape functions derived in this section. Since the analytical model ignored the stiffeners, the FE model of SWS tank without stiffeners was also compared. The comparisons of pressure–mid-span displacement curves are shown in Fig. 6.3. It can be seen that the

analytical method slightly overestimates the deflection of SWS tank with stiffeners due to the exclusion of stiffeners in the analytical model. The discrepancy of pressure–deflection response for small displacement is caused by the bending effects of stiffeners and face plates (top and bottom plates). Herein the stiffeners are the key elements that cause the discrepancy. Because the height of stiffeners (36 mm) is much higher than the thickness of top and bottom plates (3 mm) and therefore larger displacement ($y_m \geq 3.82t$) is needed for the stiffener to eliminate its bending effect. This is also evident from the better agreement between the analytical prediction and FE model without stiffeners. Based on above analysis, the analytical model agrees well with the FE model without stiffeners and provides a conservative prediction for the FE model with stiffeners. The discrepancy is not significant and can be acceptable within its application range ($3.82t \leq y_m \leq 0.08L$). Therefore the analytical model can be used to obtain the resistance–deflection function of SWS tank. The application range in Eq. (6.18) is calculated as $11.46 \text{ mm} \leq y_m \leq 88 \text{ mm}$ for the SWS tank in this analysis. It is noted from Fig. 6.3 that the analytical model can give a close prediction even with the displacement greater than 88 mm.

The deflection shapes from analytical model and FE analysis are compared in Fig. 6.4. It can be seen that the deflection shapes from FE analyses agree well with the analytical prediction when the mid-span displacement equals to 50 and 90 mm. However, when the mid-span displacement equals to 10 mm, the slight disparity of deflection shape is observed. This is because the flexural deformation still has effects on the deflection shape when the mid-span displacement is small (less than $3.82t$). From above comparisons, the analytical model can provide a reasonable prediction on the resistance–deflection and deflection shape functions of the pin-pin supported SWS

tank under pressure loading.

6.2.2 Free Vibration Analysis

Maximum displacement is usually the parameter of concern and is often adopted as the damage level indicator for the structural member. In view of this, the dynamic response of the constructed SDOF system for SWS tank is thus characterized by its free vibration period and maximum displacement. In the elastic range, the equation of motion for the equivalent SDOF system is given by

$$m_e \ddot{\chi} + k_e \chi^3 = P_e(t) \quad (6.19)$$

where $m_e = K_{LM} \rho t L^2$, $\chi = y_m / L$, $k_e = 21.104 E t$ and $P_e(t) = P(t) L$. In order to determine the free vibration period, the SDOF system is analyzed under free vibration where $P_e(t)$ and initial displacement were taken as 0 and initial velocity = v_0 . With these, the equation of motion in Eq. (6.19) can be rewritten as

$$m_e \ddot{\chi} + k_e \chi^3 = 0 \quad (\chi_0 = 0; \dot{\chi}_0 = v_0) \quad (6.20)$$

By equating the kinetic energy to internal energy, the maximum displacement of Eq. (6.20) can be obtained as

$$\chi_{\max} = \sqrt{v_0^4 \sqrt{2m_e/k_e}} \quad (6.21)$$

Since the exact solution of Eq. (6.20) cannot be obtained, fourth-order Runge-Kutta time stepping procedure was adopted to determine the displacement–time history and the free vibration period. It is noted that circular frequency is proportional to initial velocity and inverse proportional to maximum displacement. Hence, the circular frequency can be established by introducing a constant value K as

$$\omega = K v_0 / \chi_{\max} = K \sqrt{v_0^4 \sqrt{k_e/m_e}} \quad (6.22)$$

The value of K is determined by averaging the numerically obtained values as

shown in Fig. 6.5 where κ ranges from 1.0045 to 1.008 with average value of 1.007. Using this average value, the circular frequency and free vibration period are obtained as

$$\omega = 1.007 \sqrt{v_0^4 k_e / m_e}; \quad T = \frac{2\pi}{1.007 \sqrt{v_0^4 k_e / m_e}} \quad (6.23)$$

Eq. (6.23) shows that the free vibration period of the constructed SDOF system is governed by equivalent mass, stiffness and initial velocity, unlike the free vibration period of elastic SDOF system with linearly proportional resistance which depends on only mass and stiffness. This difference is attributed to the different resistance–deflection functions between the two. The resistance in the constructed SDOF system is a three order polynomial of displacement, whereas the resistance in the elastic SDOF system is linear with displacement.

6.2.3 Shock Spectrum

The shock spectrum defines the relationship between the dimensionless maximum displacement and the ratio of blast loading duration to free vibration period of the structure. Following the usual blast resistant design practice, a triangular blast pressure profile with zero rise time is adopted in this paper. Plastic deformation is usually allowed for the blast resistant design. Hence, the shock spectrum of SWS tank with plastic deformation is established in this section.

The equation of motion for the SDOF system under triangular pressure load can be written as

$$\begin{aligned} m_e \ddot{\chi} + R(\chi) &= P_{em} (1 - t/t_d) & t < t_d \\ m_e \ddot{\chi} + R(\chi) &= 0 & t \geq t_d \end{aligned} \quad (6.24)$$

where P_{em} is the initial maximum pressure \times span, t_d is the loading duration and $R(\chi)$ is the resistance. Since it is difficult to find the exact solution for Eq. (6.24), fourth-order Runge-Kutta time stepping procedure was also adopted to obtain the displacement–time history.

For the elastic SDOF system subjected to triangular pressure load, it has been proven that the dimensionless maximum displacement is a function of loading duration to free vibration period ratio (Mays and Smith, 1995). Based on this, it was first assumed that the shock spectrum for the SWS tank considered in this study can also be constructed by adopting a dimensionless maximum displacement of $\frac{\chi_{\max}^3}{P_{em}/k_{ep}}$ as a

function of t_d/T_e . The t_d/T_e ratio can be derived as

$$\frac{t_d}{T_e} = \frac{\kappa t_d \sqrt{v_0} \sqrt[4]{k_{ep}}}{2\pi \sqrt[4]{m_e}} = \frac{\kappa t_d \sqrt{P_{em} t_d} k_{ep}^{0.25}}{2\sqrt{2\pi} m_e^{0.75}} \quad (6.25)$$

In Eq. (6.25), $v_0 = 0.5P_{em}t_d/m_e$ is calculated from conservation of momentum. T_e is the equivalent free vibration period for the SWS in the plastic range and can be defined by replacing k_e with k_{ep} in Eq. (6.23). k_{ep} is the equivalent plastic stiffness and can be calculated by equating the internal energy and maximum displacement as follow:

$$\begin{aligned} \int_0^{\chi_{\max}} R(\chi) d\chi &= Et \left\{ \int_0^{\chi_y} 21.104 \chi^3 d\chi + \int_{\chi_y}^{\chi_{\max}} [8\varepsilon_y(1-\alpha)\chi + 21.104\alpha\chi^3] d\chi \right\} \\ &= \int_0^{\chi_{\max}} k_{ep} \chi^3 d\chi \end{aligned} \quad (6.26)$$

According to Eq. (6.7), the yield strain can be obtained as $\varepsilon_y = 2.638\chi_y^2$. By substituting this into Eq. (6.26), the equivalent plastic stiffness can be expressed as a function of the ratio of yield displacement to maximum displacement and hardening

coefficient, α , as follow:

$$k_{ep} = Et[21.104(\alpha - 1)\left(\frac{\chi_y}{\chi_{\max}}\right)^4 + 42.208(1 - \alpha)\left(\frac{\chi_y}{\chi_{\max}}\right)^2 + 21.104\alpha] \quad (6.27)$$

When $t_d \gg T$, the load can be considered to act in a quasi-static manner since the structure will reach its maximum displacement long before the load has diminished. Equating the external work done by load with the internal energy of the structure leads to

$$\frac{\chi_{\max}^3}{P_{em}/k_{ep}} = 4 \quad (6.28)$$

When $t_d \ll T$, the load can be considered to act in an impulsive manner since the displacement will reach its maximum value only after the impulse has passed. Equating the kinetic energy due to impulse with the internal energy of the structure gives the lower bound of the SDOF displacement response as follow:

$$\frac{\chi_{\max}^3}{P_e/k_e} = \frac{t_d \sqrt{P_{em} t_d} k_{ep}^{0.25}}{(2m_e)^{0.75}} = 2^{0.75} \pi \frac{t_d}{\kappa T_e} \quad (6.29)$$

Eqs. (6.28) and (6.29) describes the quasi-static and impulsive asymptotes, respectively, for the constructed SDOF system under triangular pressure load.

Since the dimensionless maximum displacement of elastic SDOF system can be expressed as a function of t_d/T , its shock spectrum can be directly generated by plotting the function. For the SDOF system constructed for the SWS, the exact solution for its dimensionless maximum displacement cannot be obtained. Hence, the

dimensionless maximum displacement $\frac{\chi_{\max}^3}{P_{em}/k_{ep}}$ and t_d/T_e for varying equivalent peak overpressure, P_{em} , loading duration, t_d , equivalent mass, m_e and equivalent stiffness,

k_{ep} , were calculated and plotted in Fig. 6.6. It can be seen that the calculated values fall in a smooth curve and therefore the assumption that the dimensionless maximum displacement of the SWS is also a function of t_d/T_e is reasonable.

6.2.4 Generation of P–I Diagram

The P–I diagram can be constructed by re-plotting the shock spectrum as a function of dimensionless pressure and impulse. Multiplying the quasi-static asymptote given by Eq. (6.28) by the inverse of the response ratio gives a modified quasi-static asymptote of $4P_{em}/k_{ep}\chi_{\max}^3 = 1 = \bar{P}$ and \bar{P} can be treated as the dimensionless pressure. Similarly, Eq. (6.29) can be rewritten as $2^{0.75} I^{3/2} / (k_{ep} m_e)^{0.75} \chi_{\max}^3 = 1 = \bar{I}$, where $I = 0.5P_{em}t_d$ and \bar{I} can be treated as the dimensionless impulse. These two dimensionless values define the boundaries for the P–I diagram and the dimensionless pressure and impulse asymptotes are both unity. The pressure and impulse asymptotes can also be written as

$$P_{e0} = \frac{k_{ep}\chi_{\max}^3}{4} ; I_0^{3/2} = \frac{(k_{ep} m_e)^{0.75} \chi_{\max}^3}{2^{0.75}} \quad (6.30)$$

The dimensionless P–I diagram of the constructed SDOF system can be obtained by transferring the shock spectrum, which was defined earlier in Section 6.2.3, as shown in Fig. 6.7.

The $\ln(\bar{P} - 1)$ and $\ln(\bar{I} - 1)$, which are approximately linear relationship, were adopted to generate the formula for the dimensionless P–I diagram in Fig. 6.7. The linear and quadratic polynomial fitted formulae are given as follow:

$$\ln(\bar{P} - 1) + 0.59\ln(\bar{I} - 1) + 1.07 = 0 \quad \text{or} \quad (\bar{P} - 1)(\bar{I} - 1)^{0.59} = 0.34 \quad (6.31)$$

$$\ln(\bar{P}-1)+0.026\ln^2(\bar{I}-1)+0.59\ln(\bar{I}-1)+0.97=0 \quad (6.32)$$

Fig. 6.7 shows that both linear and quadratic polynomial fittings agree well with SDOF results and the quadratic polynomial fittings are slightly better.

Both the constructed shock spectrum and P–I diagram can be utilized to assess the damage level of the SWS tank under triangular pressure load. The parameters relationship is directly shown by these equations, which is versatile and convenient for blast resistant design.

The FE model of pin-pin supported SWS tank under dynamic pressure loading in Chapter 5 was adopted to verify the generated dimensionless P–I diagram. Since the strain rate effect was not considered when constructing the P–I diagram, the strain rate effect was also neglected in the FE model for consistency. The generated P–I diagram from FE analysis is compared with the analytical prediction in Fig. 6.8. The prediction is conservative in the quasi-static response regime, because the analytical model overestimates the deflection as shown in Fig. 6.3. However, the prediction is not conservative in the impulsive response regime. This is because the deflection shape function obtained by analyzing the member under lateral pressure loading is more applicable for the member under quasi-static response regime (Baker, 1983). Although difference is observed between the FE result and analytical prediction, the constructed dimensionless P–I diagram can be used to preliminarily predict the damage level of SWS tank under given blast load.

6.2.5 Lagrange Equation Method

Since the equivalent SDOF system cannot capture the varying deflection shape, FE

method is increasingly used to predict the responses of structures under blast loading. However, the FE method is more complex and time-consuming and the established FE model must be verified by test results to prove its accuracy. Hence, the Lagrange Equation method with combined deflection shape function was developed in this section to predict the deflection of SWS tank under blast loading. It is more accurate than equivalent SDOF method, since it is allowed to define more than one deflection functions to capture the varying deflection shape and the varying DIF in terms of transient strain rate was also considered to capture the strain rate effects. This method is easier and needs significantly less computing time than the FE analysis.

6.2.5.1 Equation of Motion

In the Lagrange Equation method, the equations of motion can be formulated as follow:

$$\frac{d}{dt} \left(\frac{\partial K}{\partial \dot{C}_i} \right) + \frac{\partial (U+V)}{\partial C_i} = 0, \quad i = 1, 2, \dots, n. \quad (6.33)$$

where K is kinetic energy, U is strain energy, V is potential energy of loading and C_i is generalized displacement. The fourth-order Runge-Kutta time stepping procedure can be utilized to solve the equations of motion.

For the pin-pin supported SWS tank considering only tensile membrane force to resist blast loading, K , U and V in Eq. (6.33) can be formulated in Eq. (6.34), Eq. (6.36) and Eq. (6.38), respectively.

For kinetic energy,

$$K = \frac{1}{2} \int_0^L \rho A \dot{y}^2 dx \quad (6.34)$$

where L is span, ρ is density, A is cross-section area and \dot{y} is velocity. The deformation, y , with n generalized displacements and deflection shape functions are given by

$$y(x,t) = \sum_{i=1}^n C_i(t) \phi_i(x) \quad (6.35)$$

Similar to resistance $R(\chi)$ in the SDOF method, the strain energy U varies with different loading stages and is defined as follow

$$U = \begin{cases} \frac{1}{2} EA \frac{\Delta L^2}{L}, & \Delta L \leq \Delta L_y \\ \frac{EA}{2L} [\alpha \Delta L^2 + 2(1-\alpha) \Delta L_y \Delta L + (\alpha-1) \Delta L_y^2], & \Delta L > \Delta L_y \end{cases} \quad (6.36)$$

where ΔL is the difference between the developed length and original length of the top/bottom steel plate, which can be approximated using Eq. (6.37).

$$\Delta L = \frac{1}{2} \int_0^L \left(\frac{dy}{dx} \right)^2 dx \quad (6.37)$$

For potential energy,

$$V = - \int_0^L p(x,t) y(x,t) dx \quad (6.38)$$

The FE model of pin-pin supported SWS tank used in Section 6.2.4 was also adopted here to compare with the Lagrange Equation method. In the Lagrange Equation method, the displacement is defined in Eq. (6.39) by combining three different deflection shape functions.

$$y = C_1(t) \sin \frac{\pi}{L} x + C_2(t) \sin \frac{3\pi}{L} x + C_3(t) \sin \frac{5\pi}{L} x \quad (6.39)$$

Fig. 6.9 compares the maximum displacements obtained from FE, SDOF and Lagrange Equation methods. The SDOF method overestimates the maximum displacements in the dynamic and quasi-static response regimes and underestimates the maximum displacement in the impulsive response regime. This indicates that utilizing SDOF method may result in unsafe design for SWS tank in the impulsive response regime. However, the Lagrange Equation method overestimates the maximum displacements in all response regimes. The over prediction is reasonable, since the stiffeners are not included in the Lagrange Equation model. From above comparison, it is demonstrated that by capturing the varying deflection shape during motion, the Lagrange Equation method is able to provide better predictions than the SDOF method in terms of providing conservative predictions in all response regimes.

6.2.5.2 Dynamic Increase Factor

It has been widely accepted that strain rate effects on material strength can be considered in the blast resistant design. The effect is normally included by means of the material strength's DIF, which can be defined as a function of strain rate. In the FE method, the DIF–strain rate relationship can be directly specified in the constitutive model and varying values of DIF depending on strain rate can be applied in the FE calculation (Hallquist, 2006). For the SDOF method, a constant DIF value is usually adopted to scale either the yield strength, ultimate strength or both of them depending on the mode of deformation (UFC, 2008). It has been argued that a single DIF value may not accurately capture the strain rate effect for highly varying strain rates. Therefore, varying DIF in terms of strain rate is included into the Lagrange Equation method to better capture the strain rate effect. Since strain rate has little effect on the Young's modulus of stainless steel, it can be kept unchanged during calculation while

both yield stress and strain vary with the strain rate.

The energy principle is utilized to introduce the varying DIF into the Lagrange Equation method. By applying the differential operator on internal energy with and without consideration of strain rate effect, that is U and U_D , respectively, for the pin-pin supported top/bottom steel plate, the following equations are obtained

$$dU = \iiint_{\tilde{V}} \sigma d\varepsilon d\tilde{V} = \tilde{V} \sigma d\varepsilon \quad (6.40)$$

$$dU_D = \tilde{V} f(\dot{\varepsilon}_p) \sigma d\varepsilon = f(\dot{\varepsilon}_p) dU \quad (6.41)$$

where \tilde{V} is the volume of the top/bottom steel plate. Eq. (6.41) can be rewritten as

$$\sum_{i=1}^n \left(\frac{\partial U_D}{\partial C_i} - f(\dot{\varepsilon}_p) \frac{\partial U}{\partial C_i} \right) dC_i = 0 \quad (6.42)$$

Setting $\frac{\partial U_D}{\partial C_i} = f(\dot{\varepsilon}_p) \frac{\partial U}{\partial C_i}$ ($i=1, 2, \dots, n$) satisfies Eq. (6.42) and substituting them in

Eq. (6.33) gives the Lagrange Equation with varying DIF consideration.

Since the elongation of the top/bottom steel plate ΔL is a function of C_1, C_2, \dots, C_n ,

i.e.

$$\Delta L = g(C_1, C_2, \dots, C_n) \quad (6.43)$$

the plastic strain rate can be derived as

$$\dot{\varepsilon}_p = \frac{\Delta \dot{L}}{L} = \frac{1}{L} \left(\frac{\partial g}{\partial C_1} \dot{C}_1 + \frac{\partial g}{\partial C_2} \dot{C}_2 + \dots + \frac{\partial g}{\partial C_n} \dot{C}_n \right) \quad (6.44)$$

By adopting the Cowper-Symonds model (Jones, 1988) to establish the relationship between strain rate and DIF, the following equation is obtained

$$\frac{\partial U_D}{\partial C_i} = \left[1 + \left(\frac{\dot{\epsilon}_p}{D} \right)^{1/q} \right] \frac{\partial U}{\partial C_i} \quad (6.45)$$

The FE model of pin-pin supported SWS tank was used to evaluate the accuracy of the proposed varying DIF in Lagrange Equation method. The Cowper-Symonds model with $D = 240$ and $q = 4.74$ (Boh *et al.*, 2004) was adopted to scale the yield stress. The ratios of the maximum displacements with and without DIF obtained from FE and Lagrange Equation models are compared in Fig. 6.10. It can be seen that the predictions using the Lagrange Equation method with varying DIF are in good agreement with the FE results and the predictions are little conservative. This discrepancy could be attributed to the omission of stiffener and assumption of uniform stress along the span in the Lagrange Equation model.

6.3 Analytical Method for Water Filled Tank-Sandwich Panel

6.3.1 SDOF System

Similar to the pin-pin supported SWS tank, the face plates of SWS-SCS are the key elements to resist pressure load by developing tensile membrane force. Hence, the SWS-SCS with pin-pin supported boundary can be simplified as four pin-pin supported steel plates and a concrete core as shown in Fig. 6.11. Similar to the pin-pin supported SWS tank, this simplification is also conservative and has wide application for the SWS-SCS with different types of stiffeners or connectors.

The deflection shape and resistance–deflection function, which are necessary to establish the SDOF system, are usually derived by solving the differential equations

established based on force equilibriums. However, for the SWS-SCS, it is difficult to establish the force equilibrium equations due to the undetermined composite action between steel plate and concrete core and the complex stress–strain relationship of concrete. Hence, the resistance–deflection function of SWS-SCS is divided into two parts, i.e. steel plates and concrete core. The deflection shape and resistance–deflection function of pin-pin supported steel plate considering tensile membrane action have been derived by utilizing force equilibrium equations which are given in Eqs. (6.4) and (6.8), respectively.

The deflection shape function of the steel plate in Eq. (6.4) is also adopted as the deflection shape function for SWS-SCS. This is because the deflection shape function has little effect on the structure's response (Baker *et al.*, 1983) and the steel plates in the SWS-SCS absorb most of the blast energy under large deformation due to its high ductility. Another reason is that the constant curvature along the span can be derived based on this deflection shape function, which will significantly simplify the calculation.

The energy principle is adopted to derive the resistance–deflection function contributed by concrete core. The procedure is: a) obtain the strain distribution of concrete core and establish the relationship between strain and mid-span displacement; b) derive the relationship between the internal energy of concrete core and mid-span displacement; c) differentiate the internal energy with mid-span displacement and divided by load factor K_L to obtain the resistance–deflection function of concrete core

6.3.1.1 Resistance–Deflection Function by Concrete Core

To simplify the derivation of resistance–deflection function contributed by concrete core, the following assumptions are made.

- a) The tensile strength of concrete is ignored.
- b) The confinement effect given by face plates on the compressive strength of concrete is ignored.
- c) The bond and friction between steel plates and concrete core is ignored.

The force distribution on the concrete core and the compression zone along the span are shown in the Fig. 6.12, together with the neutral axis along the span. According to the force equilibrium in horizontal direction, the compression force given by the end plate equals to the compression force at mid-span, i.e.

$$F_{end} = F_c \quad (6.46)$$

Therefore, it is reasonable to assume that the compression depth (the distance between maximum compression layer and neutral axis) at the end and mid-span is the same. Fig. 6.13 shows the deformation profile across the concrete depth and the compression depth at mid-span t_2 equals to t_1 at the end. t_1 is determined by ensuring that the extension of concrete core within t_1 zone is larger than that of the steel plates so that it can be compressed by the end plate. Meanwhile, the following relationship is established.

$$\frac{\Delta L_s}{t_n - t_1} = \frac{\Delta L_c}{t_2} \quad (6.47)$$

where ΔL_s is the difference between developed length and original length of steel plate and ΔL_c is the difference between compressed length and original length of

concrete in the top layer. By adopting the deflection shape function in Eq. (6.4), the curvature of concrete core can be calculated as

$$K_c = \frac{|y''|}{(1+y'^2)^{3/2}} = \frac{8y_m/L^2}{\left\{1 + \left[\frac{4y_m}{L^2}(L-2x)\right]^2\right\}^{3/2}} \quad (6.48)$$

When y_m/L is small, Eq. (6.48) can be simplified as

$$K_c = 8y_m/L^2 \quad (6.49)$$

Therefore, ΔL_c can be obtained as

$$\Delta L_c = K_c (L - 2t_c / \tan \theta) t_2 \quad (6.50)$$

And the elongation of steel plate ΔL_s can be obtained as

$$\Delta L_s = \frac{1}{2} \int_0^L \left(\frac{dy}{dx} \right)^2 dx = \frac{8y_m^2}{3L} \quad (6.51)$$

From above equations, the neutral axis is determined as

$$t_n = \frac{t_c}{2} + \frac{y_m \xi}{6} \quad (6.52)$$

where $\xi = L / (L - 2t_c / \tan \theta)$. The θ normally ranges from 26.6° to 45° . In this study, θ is taken as 26.6° in accordance with Eurocode 2 (2004). Therefore, the strain expression above the neutral axis is derived as

$$\varepsilon = K(t - t_n) = \frac{8}{L_2} \left[\left(t - \frac{t_c}{2} \right) y_m - \frac{y_m^2 \xi}{6} \right] \quad (6.53)$$

Since it is complex to derive the internal energy of concrete core based on current neutral axis which varies with the mid-span displacement, the unchanging neutral axis is proposed, based on which, the equivalent curvature is then derived. If the internal energy of concrete core keeps increasing with the mid-span displacement rising from

0 to $y_{m,n}$, the neutral axis t_n in Eq. (6.52) ranges from $t_c/2$ to $t_c/2 + y_{m,n}\xi/6$. Therefore, it is rational to take the average neutral axis $t_c/2 + y_{m,n}\xi/12$ as unchanging neutral axis. $y_{m,n}$ is the minimum of the maximum mid-span displacement $y_{m,max}$ and $y_{m,m}$, where $y_{m,m}$ is a value of the mid-span displacement. When the mid-span displacement exceeds $y_{m,m}$, the equivalent curvature starts to decrease with increasing of mid-span displacement. $y_{m,m}$ will be given later after deriving the equivalent curvature.

The equivalent curvature K_e is derived based on the criteria that the internal energy of concrete core calculated by using original and equivalent strain expression is the same in elastic material range. The internal energy of concrete core per unit area is given as

$$u = \int_0^{\eta_m} \frac{1}{2} E \varepsilon^2 d\eta = \frac{1}{6} EK^2 \eta_m^3 \quad (6.54)$$

where η is the distance between compressive layer and the neutral axis, and

$$\eta_m = T/2 - y_{m,n}\xi/12.$$

Then, the equivalent curvature is obtained as

$$K_e = \frac{8y_m}{L^2} \left(\frac{1 - y_m\xi/3t_c}{1 - y_{m,n}\xi/6t_c} \right)^{3/2} \quad (6.55)$$

and the strain can be expressed as

$$\varepsilon = K_e \eta = \frac{8y_m \eta}{L^2} \left(\frac{1 - y_m\xi/3t_c}{1 - y_{m,n}\xi/6t_c} \right)^{3/2} \quad \left(0 \leq \eta \leq \frac{t_c}{2} - \frac{y_{m,n}\xi}{12} \right) \quad (6.56)$$

Differentiating the equivalent curvature K_e with mid-span displacement y_m and setting it to zero leads to

$$\frac{dK_e}{dy_m} = \frac{8}{L^2} \left(\frac{1 - y_m \xi / 3t_c}{1 - y_{m,n} \xi / 6t_c} \right)^{3/2} - \frac{4y_m \xi}{L^2 t_c} \frac{(1 - y_m \xi / 3t_c)^{1/2}}{(1 - y_{m,n} \xi / 6t_c)^{3/2}} = 0 \quad (6.57)$$

The solution of mid-span displacement $y_{m,m} = 6t_c / 5\xi$ from Eq. (6.57) indicates that when the mid-span displacement is larger than $y_{m,m}$, the equivalent curvature K_e starts to decrease with increasing mid-span displacement. In other words, the internal energy of concrete core stops increasing when the mid-span displacement is larger than $y_{m,m}$.

The stress–strain curve of concrete under uniaxial compression is given by Eurocode 2 (2004) as

$$\frac{\sigma_c}{f_{cm}} = \frac{k \varepsilon / \varepsilon_o - (\varepsilon / \varepsilon_o)^2}{1 + (k - 2) \varepsilon / \varepsilon_o} \quad \text{for } |\varepsilon| < |\varepsilon_c| \quad (6.58)$$

where k , f_{cm} , ε_o and ε_c can be found in Eurocode 2 (2004).

When all the compression strains above the neutral axis are smaller than the crush strain of concrete ε_c , the stress–strain relationship given in Eq. (6.58) can be used for all the compression concrete above the neutral axis. Hence, the internal energy of concrete core per unit volume can be calculated as

$$u_c(\varepsilon) = \int_0^\varepsilon \sigma d\varepsilon' = \int_0^\varepsilon f_{cm} \frac{k \varepsilon' / \varepsilon_o - (\varepsilon' / \varepsilon_o)^2}{1 + (k - 2) \varepsilon' / \varepsilon_o} d\varepsilon' = \varepsilon_o f_{cm} g_1\left(\frac{\varepsilon}{\varepsilon_o}\right) \quad (6.59)$$

$$\text{where } g_1\left(\frac{\varepsilon}{\varepsilon_o}\right) = \left[\frac{(k-1)^2 \varepsilon / \varepsilon_o}{(k-2)^2} - \frac{(\varepsilon / \varepsilon_o)^2}{2(k-2)} - \frac{(k-1)^2 \ln((k-2) \varepsilon / \varepsilon_o + 1)}{(k-2)^3} \right].$$

Provided that the internal energy per unit cross-section of concrete core along the compressive zone is the same, the internal energy of concrete core is calculated as

$$U_c^u = L_e B \int_0^{\eta_m} u_c(K_e \eta) d\eta = \frac{L_e B \varepsilon_o^2 f_{cm}}{K_e} g_2\left(\frac{K_e \eta_m}{\varepsilon_o}\right) \quad (6.60)$$

where B is the width of concrete core, L_e is the length of compression zone and can be calculated as $L_e = L + 2t_c (1/\sin \theta - 1/\tan \theta)$,

$$g_2\left(\frac{K_e \eta_m}{\varepsilon_o}\right) = \bar{A} \left(\frac{K_e \eta_m}{\varepsilon_o}\right)^2 - \bar{B} \left(\frac{K_e \eta_m}{\varepsilon_o}\right)^3 - \bar{C} \frac{K_e \eta_m}{\varepsilon_o} \left\{ \ln \left[(k-2) \frac{K_e \eta_m}{\varepsilon_o} + 1 \right] - 1 \right\} - \bar{D} \ln \left[(k-2) \frac{K_e \eta_m}{\varepsilon_o} + 1 \right]$$

, where $\bar{A} = \frac{(k-1)^2}{2(k-2)^2}$, $\bar{B} = \frac{1}{6(k-2)}$, $\bar{C} = \frac{(k-1)^2}{(k-2)^3}$, $\bar{D} = \frac{(k-1)^2}{(k-2)^4}$.

Thus, differentiating the internal energy of concrete core with mid-span displacement leads to

$$\frac{dU_c^u}{dy_m} = \frac{L_e B \varepsilon_o^2 f_{cm}}{K_e} K_e' \left\{ -g_2\left(\frac{K_e \eta_m}{\varepsilon_o}\right) \frac{1}{K_e} + 2\bar{A} \left(\frac{\eta_m}{\varepsilon_o}\right)^2 K_e - 3\bar{B} \left(\frac{\eta_m}{\varepsilon_o}\right)^3 K_e^2 - \bar{C} \frac{\eta_m}{\varepsilon_o} \left[\ln \left[(k-2) \frac{K_e \eta_m}{\varepsilon_o} + 1 \right] - 1 \right] \right. \\ \left. - \bar{C} \frac{k-2}{(k-2) K_e \eta_m / \varepsilon_o + 1} \frac{K_e \eta_m^2}{\varepsilon_o^2} - \bar{D} \frac{k-2}{(k-2) K_e \eta_m / \varepsilon_o + 1} \frac{\eta_m}{\varepsilon_o} \right\} \quad (6.61)$$

where $K_e' = \frac{dK_e}{dy_m}$.

The resistance–deflection function of concrete core without crushing can be obtained as

$$R_{c1}(y_m) = \frac{dU_c^u}{dy_m} \frac{1}{BLK_L} \quad (6.62)$$

where K_L is the load factor and can be calculated based on the given deflection shape function in Eq. (6.4).

When some parts of the compression strains exceed crush strain of concrete ε_c , the internal energy of concrete core can be divided into two parts, i.e. concrete with crushing and concrete without crushing. The internal energy of concrete core without

crushing can be calculated as

$$U_{c,1} = L_e B \int_0^{\eta_0} u_c(K_e \eta) d\eta = \frac{L_e B \varepsilon_o^2 f_{cm}}{K_e} g_2\left(\frac{K_e \eta_0}{\varepsilon_o}\right) \quad (6.63)$$

where $\eta_0 = \frac{\varepsilon_c L^2}{8 y_m} \left(\frac{1 - y_{m,n} \xi / 6 t_c}{1 - y_m \xi / 3 t_c} \right)$, which is calculated by setting strain expression in

Eq. (6.56) to crush strain ε_c . The internal energy of concrete core with crushing can be calculated as

$$U_{c,2} = L_e B (\eta_m - \eta_0) \varepsilon_o f_{cm} g_1\left(\frac{\varepsilon_c}{\varepsilon_o}\right) \quad (6.64)$$

Hence, the total internal energy of concrete core after crushing is given by

$$U_c^c = U_{c,1} + U_{c,2} \quad (6.65)$$

Similarly, differentiating the internal energy of concrete core with mid-span displacement leads to

$$\frac{dU_c^c}{dy_m} = -\frac{L_e B \varepsilon_o^2 f_{cm}}{K_e^2} K_e' g_2\left(\frac{\varepsilon_c}{\varepsilon_o}\right) - L_e B \varepsilon_o f_{cm} g_1\left(\frac{\varepsilon_c}{\varepsilon_o}\right) \eta_0' \quad (6.66)$$

where $\eta_0' = \frac{\varepsilon_c L^2}{8} \left(1 - \frac{y_{m,n} \xi}{6 t_c} \right)^{3/2} \left[-\frac{1}{y_m^2 (1 - y_m \xi / 3 t_c)^{3/2}} + \frac{\xi}{2 t_c y_m (1 - y_m \xi / 3 t_c)^{5/2}} \right]$

In the same way, the resistance–deflection function of concrete core after crushing can be obtained as

$$R_{c2}(y_m) = \frac{dU_c^c}{dy_m} \frac{1}{BLK_L} \quad (6.67)$$

The procedure of calculating the resistance–deflection function of concrete core is summarized as follow:

a) Calculating the maximum strain of concrete core by using Eq. (6.68).

$$\varepsilon_{\max} = \frac{8y_{m,m}}{L^2} \left(\frac{1 - y_{m,m}\xi/3t_c}{1 - y_{m,n}\xi/6t_c} \right)^{3/2} \left(\frac{t_c}{2} - \frac{y_{m,n}\xi}{12} \right) \quad (6.68)$$

b) For $\varepsilon_{\max} \leq \varepsilon_c$, there is no concrete crushing. Then, resistance–deflection function is given as

$$R_c = \begin{cases} R_{c1} & (y_m \leq y_{m,m}) \\ 0 & (y_m > y_{m,m}) \end{cases} \quad (6.69)$$

c) For $\varepsilon_{\max} > \varepsilon_c$, calculating y_o by solving the Eq. (6.70).

$$\frac{8y_m}{L^2} \left(\frac{1 - y_m\xi/3t_c}{1 - y_{m,n}\xi/6t_c} \right)^{3/2} \left(\frac{t_c}{2} - \frac{y_{m,n}\xi}{12} \right) = \varepsilon_c \quad (6.70)$$

Then, the resistance–deflection function is given as

$$R_c = \begin{cases} R_{c1} & (y_m \leq y_o) \\ R_{c2} & (y_o < y_m \leq y_{m,m}) \\ 0 & (y_m > y_{m,m}) \end{cases} \quad (6.71)$$

The total resistance of SWS-SCS is obtained by summing the resistance of steel plates and concrete core. Fig. 6.14 compares the analytical pressure–mid-span displacement of SWS-SCS with that obtained from FE analysis. The FE model used here was the combined FE models of pin-pin supported SWS and SCS50 in Section 4.7.5.3. It should be mentioned that the side plates of SCS50 was removed from the FE model to be consistent with the analytical model. It can be seen from the comparison that the analytical model agrees well with the FE model with slightly over predicted deflection. The deflection shapes obtained from analytical model and FE analysis are compared in Fig. 6.15. It can be seen that the deflection shapes from analytical model is also in good agreement with the FE results and their differences reduce with increasing displacement. This is likely due to the increasing damage of concrete under large deformation, which reduces its contribution to the deflection shape.

6.3.1.2 Dynamic Increase Factor

Steel Plates

The varying DIF can be taken into consideration during transformation of actual structural member to its equivalent SDOF system through energy conservation. The variation for internal energy of a pin-pin supported steel plate and its equivalent SDOF system at arbitrary moment is given by Eqs. (6.72) and (6.73), respectively.

$$dU_a = \int_0^L f(\dot{\epsilon}_p) \sigma(y_m) A d\epsilon dx \quad (6.72)$$

$$dU_e = DIF_s * K_R * R(y_m) dY = DIF_s * \int_0^L \sigma(y_m) A d\epsilon dx \quad (6.73)$$

where K_R is the resistance factor. By assuming that the internal energy along the span is constant and equating the above two equations leads to

$$DIF_s = \frac{\int_0^L f(\dot{\epsilon}_p) dx}{L} \quad (6.74)$$

The configuration of infinitesimal element dx is shown in Fig. 6.16 at t and $t+\Delta t$. The variation of plastic strain can be derived as

$$\Delta\epsilon_p = \frac{[\phi(x)]^2 (y_m + \dot{y}_m \Delta t) \dot{y}_m \Delta t}{1 + [\phi(x)]^2 y_m (y_m + \dot{y}_m \Delta t)} \quad (6.75)$$

When $\Delta t \rightarrow 0$, $\dot{y}_m \Delta t \rightarrow 0$, thus

$$\dot{\epsilon}_p = \frac{\Delta\epsilon_p}{\Delta t} = \frac{[\phi(x)]^2 y_m \dot{y}_m}{1 + [\phi(x) y_m]^2} \quad (6.76)$$

Eq. (6.76) defines the plastic strain rate in terms of shape function, generalized displacement and velocity. For steel material, the following Eq. (6.77) can be obtained by using the Cowper-Symonds model (Jones, 1988) to define the DIF as a function of plastic strain rate

$$f(\dot{\epsilon}_p) = 1 + \left(\frac{[\phi(x)]^2 \dot{y}_m y_m}{D + D[\phi(x) y_m]^2} \right)^{1/q} \quad (6.77)$$

where D and q are the Cowper-Symonds parameters. Substituting Eq. (6.76) and shape function in Eq. (6.4) into Eq. (6.74), the DIF can be calculated as follow

$$DIF = 1 + \frac{\int_0^L \left(\frac{\dot{\chi} \chi}{D \chi^2 + D/16(1-2x/L)^2} \right)^{1/q} dx}{L} \quad (6.78)$$

where $\chi = y_m/L$ is the mid-span displacement to span ratio.

Concrete Core

The variation for the internal energy of concrete core without considering strain rate effect is given as

$$dU_c = BL_e \int_0^{\eta_m} \sigma_c d\epsilon d\eta = BL_e f_{cm} \int_0^{\eta_m} \frac{k K_e \eta / \epsilon_o - (K_e \eta / \epsilon_o)^2}{1 + (k-2) K_e \eta / \epsilon_o} \eta d\eta dK_e \quad (6.79)$$

Then, we have

$$\frac{dU_c}{dy_m} = \frac{dU_c}{dK_e} \frac{dK_e}{dy_m} = BL_e f_{cm} \int_0^{\eta_m} \frac{k K_e \eta / \epsilon_o - (K_e \eta / \epsilon_o)^2}{1 + (k-2) K_e \eta / \epsilon_o} \eta d\eta \frac{dK_e}{dy_m} \quad (6.80)$$

The variation of the internal energy of concrete core considering strain rate effect is given as

$$dU_{c,dyn} = BL_e \int_0^{\eta_m} D_c(\dot{\epsilon}) \sigma_c d\epsilon d\eta = BL_e f_{cm} \int_0^{\eta_m} D_c(\eta \dot{K}_e) \frac{k K_e \eta / \epsilon_o - (K_e \eta / \epsilon_o)^2}{1 + (k-2) K_e \eta / \epsilon_o} \eta d\eta dK_e \quad (6.81)$$

Then,

$$\frac{dU_{c,dyn}}{dy_m} = \frac{dU_{c,dyn}}{dK_e} \frac{dK_e}{dy_m} = BL_e f_{cm} \int_0^{\eta_m} D_c(\eta \dot{K}_e) \frac{k K_e \eta / \epsilon_o - (K_e \eta / \epsilon_o)^2}{1 + (k-2) K_e \eta / \epsilon_o} \eta d\eta \frac{dK_e}{dy_m} \quad (6.82)$$

Therefore, the dynamic increased resistance for concrete core is obtained as

$$DIF_{c1} = \frac{R_{c,dyn}}{R_c} = \frac{dU_{c,dyn}/dy_m}{dU_c/dy_m} = \frac{\int_0^{\eta_m} D_c(\eta \dot{K}_e) \frac{k K_e \eta / \varepsilon_o - (K_e \eta / \varepsilon_o)^2}{1 + (k-2) K_e \eta / \varepsilon_o} \eta d\eta}{\int_0^{\eta_m} \frac{k K_e \eta / \varepsilon_o - (K_e \eta / \varepsilon_o)^2}{1 + (k-2) K_e \eta / \varepsilon_o} \eta d\eta} \quad (6.83)$$

The Eq. (6.83) is only used to scale up the R_{c1} , the DIF for scaling up R_{c2} is given in Eq. (6.84).

$$DIF_{c2} = \frac{\int_0^{\eta_0} D_c(\eta \dot{K}_e) \frac{k K_e \eta / \varepsilon_o - (K_e \eta / \varepsilon_o)^2}{1 + (k-2) K_e \eta / \varepsilon_o} \eta d\eta}{\int_0^{\eta_0} \frac{k K_e \eta / \varepsilon_o - (K_e \eta / \varepsilon_o)^2}{1 + (k-2) K_e \eta / \varepsilon_o} \eta d\eta} \quad (6.84)$$

In above equations, $D_c(\dot{\varepsilon})$ defines the relationship between DIF and strain rate of concrete core.

6.3.1.3 Equation of Motion

Since there is no connection between SWS and SCS, the separation may occur during the calculation. The same situation may also applicable for the top steel plate of SCS and concrete core. Therefore, the SWS-SCS can be divided into three components, i.e. SWS (A), top plate of SCS (B), concrete core + bottom plate of SCS (C). These three components may separate from each other during the calculation. Hence, the flow chart of determining the equation of motion is given in Fig. 6.17, in which the three equations of motion (EOM1, EOM2 and EOM3) are given in Eqs. (6.85) to (6.87) and they are representing no separation, component C separating from component B and A, and component A separating from component B and C, respectively.

$$K_{LM} [\rho_{ss}(t_{s1} + t_{s2}) + \rho_w t_w + \rho_{ms}(t_{s3} + t_{s4}) + \rho_c t_c] \ddot{y}_m + R_{ss} + R_{s1} + R_{s2} + R_c = P(t) \quad (6.85)$$

$$K_{LM} [\rho_{ms} t_{s4} + \rho_c t_c] \ddot{y}_m + R_{s2} + R_c = 0 \quad (6.86)$$

$$K_{LM} [\rho_{ms}(t_{s3} + t_{s4}) + \rho_c t_c] \ddot{y}_m + R_{s1} + R_{s2} + R_c = 0 \quad (6.87)$$

where ρ_{ss} , ρ_{ms} and ρ_c are densities of stainless steel, mild steel and concrete; t_{s1} , t_{s2} , t_{s3} , t_{s4} , t_w and t_c are thicknesses of top plate of SWS, bottom plate of SWS, top plate of SCS, bottom plate of SCS, water layer and concrete core; R_{ss} , R_{s1} , R_{s2} and R_c are the resistances of SWS, top plate, bottom plate and concrete core; $P(t)$ is pressure–time history of blast loading.

6.3.2 Lagrange Equation Method

In the Lagrange Equation method, the equations of motion has been given in Eq. (6.33) and the kinetic energy, internal energy and potential energy of face plates have been discussed in Section 6.2.5. It should be noted that the separation may occur for the SWS-SCS under blast loading. Therefore, the separating components must be removed during the calculation. Similar to the SDOF method, the criterion that determines the separation in SDOF method is also adopted for the Lagrange Equation method.

For the concrete core in the SWS-SCS, the calculation of kinetic energy T and potential energy V is same with face plates. However, the derivation of the internal energy of concrete core U_c and its differential with generalized displacements are complex. Hence, the simplified method is adopted and illustrated as follow. To avoid recalculating the internal energy of concrete core, it is assumed that the combined deflection shape function in Lagrange Equation method is same with that in SDOF method. In reality, the combined deflection shape function in the Lagrange Equation method is varying during calculation. However, this assumption is reasonable for the pin-pin supported SWS-SCS under blast loading, since the internal energy of concrete

core is relatively small as compared to the face plates, especially under large deformation. Therefore, the mid-span displacement of SWS-SCS is calculated as

$$y_m = \sum_{i=1}^n C_i(t) \phi_i(L/2) \quad (6.88)$$

Hence, the differential of the internal energy of concrete core U_c with generalized displacement C_i is derived as

$$\frac{\partial U_c}{\partial C_i} = \frac{\partial U_c}{\partial y_m} \frac{\partial y_m}{\partial C_i} \quad (6.89)$$

The DIF for concrete core in Lagrange Equation method is the same as that in SDOF method, since the same deflection shape function is assumed in the calculation of the internal energy of concrete core. The DIF for face plates in the Lagrange Equation method has been derived in Section 6.2.5.2.

6.3.3 Comparison with Finite Element Results

Table 6.1 compares the maximum displacements obtained from FE, SDOF and Lagrange Equation models. The combined deflection shape function in Eq. (6.39) was adopted for the Lagrange Equation model. The FE model used here was the combined FE model of pin-pin supported SWS and SCS50 in Section 5.6.5.3. Similar to the FE model in Section 6.3.1.1 for the resistance–deflection comparison, the side plates of SCS50 were also removed from the FE model. It can be seen from the comparison that both SDOF and Lagrange Equation model can predict the maximum displacements of SWS-SCS with reasonable accuracy and the maximum difference is less than 12%. Both the two models overestimate the displacement of SWS-SCS except for the SDOF model under impulsive response regime. The overestimation is expected, since the analytical resistance–deflection curve is slightly conservative as

discussed in Section 6.3.1.1. Similar to the SDOF model for the SWS tank under impulsive loading, the underestimation of deformation under impulsive loading is because the deflection shape function obtained by analyzing the member under lateral pressure loading is not applicable for the SWS-SCS in impulsive response regime. However, the Lagrange Equation model, which can capture the varying deflection shape, is able to provide better predictions than SDOF method and the predictions are conservative for all the response regimes.

6.4 Design implications

The Lagrange Equation method with combined deflection shape and varying DIF is adopted in this section to develop the design table for the SWS and SWS-SCS façade systems under blast loading. The design table provides the minimum plate thicknesses of the SWS and SWS-SWS façade systems needed to resist given blast load and the preferred façade type is also discussed.

The water façade systems were meant to be installed on the outer skin of the building to achieve both energy saving and blast resistance functions. Attaching the façade to the existing edge beams would be a convenient way of installation. One proposed method to install the façade system has been discussed in Chapter 4 and the assembly was also given in Fig. 4.46. Hence, the span of the façade system is equal to the floor height. In this analysis, the floor height was assumed to be 3 m and the water and concrete core depth was assumed to be 100 mm. The adopted materials that include stainless steel, mild steel and concrete, were same with those in the lateral and dynamic pressure tests and the properties have been given in Chapter 4. Two TNT

explosive weights were adopted, i.e. 100 kg and 250 kg, and six standoff distances of detonation were analyzed, including 5 m, 10 m, 15 m, 20 m, 25 m and 30 m. The parameters, including reflected peak pressure, P_r , and reflected impulse, i_r , were obtained using the blast loading predictive tool ConWep (Hyde, 1991). The triangle pressure profile with zero rise time was adopted, in which the reflected peak pressure was maintained and the load duration t_d was obtained as

$$t_d = \frac{2i_r}{P_r} \quad (6.90)$$

There are four levels of protection (LOP) for buildings against blast attack, i.e. LOP I (Very Low), LOP II (Low), LOP III (Medium) and LOP IV (High) from low to high level of protection. For LOP I, only collapse of building is prevented and for LOP II, life safety is promised and surviving occupants will likely be able to evacuate and then return only temporarily (ASCE, 2011). Since the façade systems are designed to protect the buildings against blast attack and the damage of façade systems after blast load is permitted, the lower two levels of protection, including LOP I and LOP II, were adopted in this analysis. Since the façade systems are nonstructural elements, they were permitted to undergo hazardous and heavy damage for LOP I and LOP II, respectively. Hazardous damage means the element is likely to fail and produce debris and heavy damage means the element is unlikely to fail but will likely have some permanent deflection (ASCE, 2011). The allowed support rotations for one-way supported façade systems with full tension membrane are 12° for hazardous damage and 6° for heavy damage (ASCE, 2011).

In this analysis, the thickness of all the face plates of SWS and SCS is the same and

the values given in Table 2 are the minimum thicknesses of face plates needed to achieve the target levels of protection. It can be seen that thicker face plate is needed to be survived under close in blast load or higher level of protection. Therefore, the thick face plate is observed for the SWS façade with close in blast attack. For practicality of application and economical reason, face plate thickness higher than 20 mm was not considered to achieve the required protection level. In such cases, the SWS-SCS façade is shown to be feasible, including 100 kg @ 5 m with LOP II, 250 kg @ 5 m with LOP I and LOP II, and 250 kg @ 10 m with LOP II. Meanwhile for far range blast load or lower level of protection, the SWS façade could be applied to achieve the required protection level.

6.5 Summary

The analytical methods for predicting the deformation of pin-pin supported water façade systems under blast loading were developed in this chapter and the main conclusions are drawn as follow:

- i) The constructed dimensionless P–I diagram was verified with the FE results and can be used to preliminarily predict the damage level of SWS under given blast load. Whereas, a similar dimensionless P–I diagram was not available for the SWS-SCS, since the relationship between dimensionless pressure and impulse was not established due to the complex material behavior of concrete.
- ii) The Lagrange Equation method with combined deflection shape function was developed as an improved alternative to the SDOF method. It was shown that the Lagrange Equation method consistently predicted the displacement conservatively for all response regimes as compared to the FE analysis results.

- iii) The varying DIF was included in the Lagrange Equation method, which was shown to reasonably capture the strain rate effects by comparing with FE analysis results.
- iv) The Lagrange Equation method with combined deflection shape functions and varying DIF was adopted to develop the design table for the water façade systems against blast loading. It was found that the SWS façade was shown to be suitable for protections against far range blast loads and low level of protection whereas the SWS-SCS façade would be necessary for protections against close in blast loads and high level of protection.

Table 6.1 Maximum displacement comparison

P_{\max} (MPa)	t_d (ms)	Response regime	Max Displacement (mm)			Difference (%)	
			FE	SDOF	LEM	SDOF	LEM
0.9	5000	Quasi-static	64.1	71.7	67.8	11.9	5.8
1.2	12	Dynamic	66.4	69.4	73.6	4.6	10.9
3.5	2	Impulsive	75.0	69.5	77.1	-7.3	2.8

Note: P_{\max} – Peak overpressure, t_d – load duration.

Table 6.2 Minimum plate thickness of façade systems under blast load

100 kg TNT Standoff distance (m)	SWS t_{plate} (mm)		SWS-SCS t_{plate} (mm)	
	LOP I (12°)	LOP II (6°)	LOP I (12°)	LOP II (6°)
5	9.5	27.0	4.0	9.0
10	3.0	10.0	0.4	2.0
15	1.5	5.5	N.A.	N.A.
20	0.7	3.5	N.A.	N.A.
25	0.5	2.5	N.A.	N.A.
30	0.3	2.0	N.A.	N.A.
250 kg TNT				
Standoff distance (m)	SWS t_{plate} (mm)		SWS-SCS t_{plate} (mm)	
5	22.0	N.A.	10.5	21.0
10	7.5	22.0	3.0	6.5
15	4.0	12.0	1.0	2.5
20	2.5	8.0	N.A.	N.A.
25	1.5	5.5	N.A.	N.A.
30	1.0	4.5	N.A.	N.A.

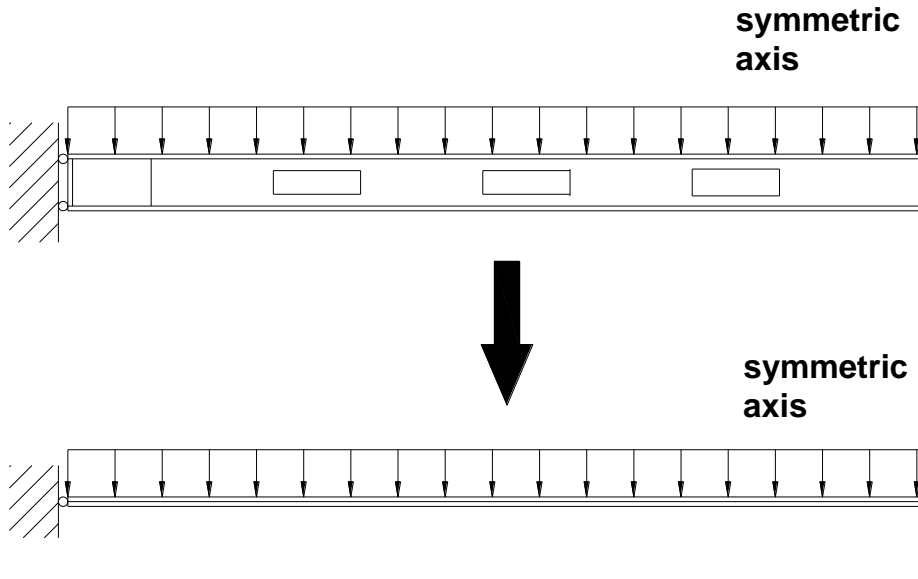


Fig. 6.1 Simplified half model for pin-pin supported SWS tank

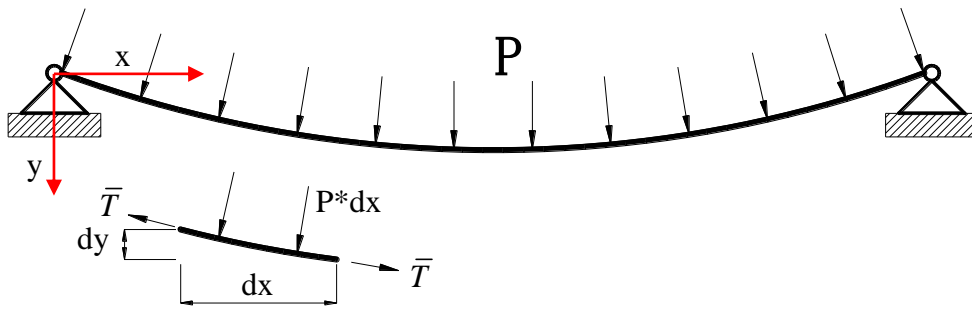


Fig. 6.2 Details of membrane action

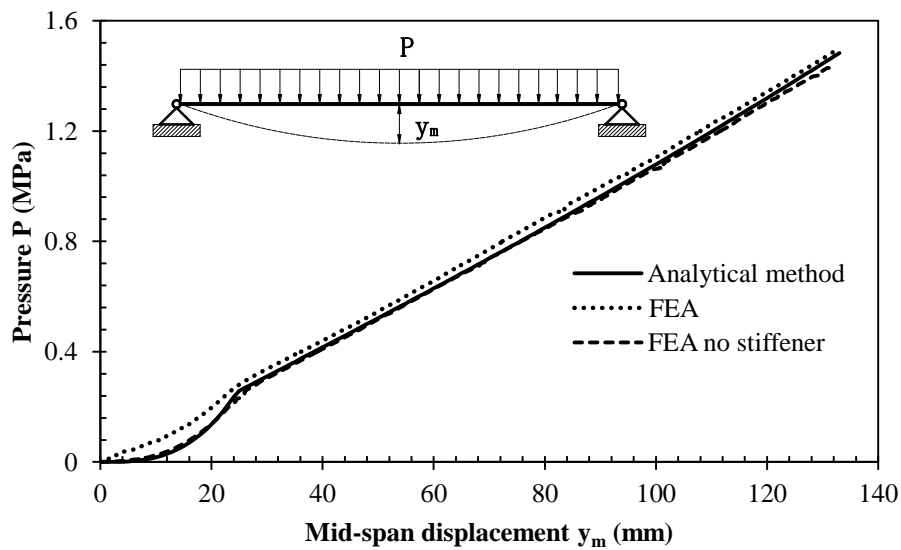


Fig. 6.3 Comparison of pressure–mid-span displacement response

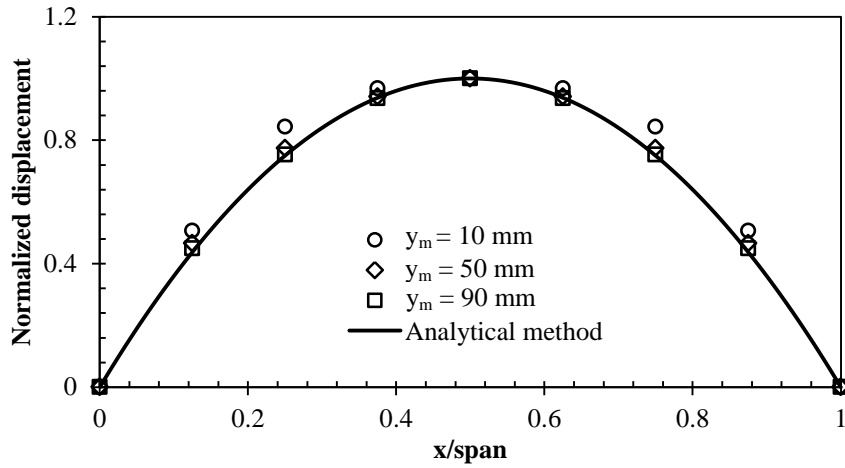


Fig. 6.4 Comparison of deflection shape of SWS tank

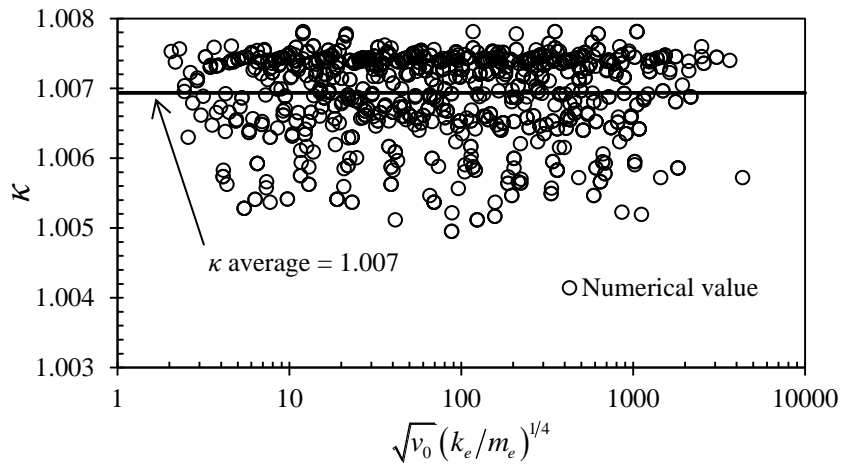


Fig. 6.5 Numerical generated constant value κ

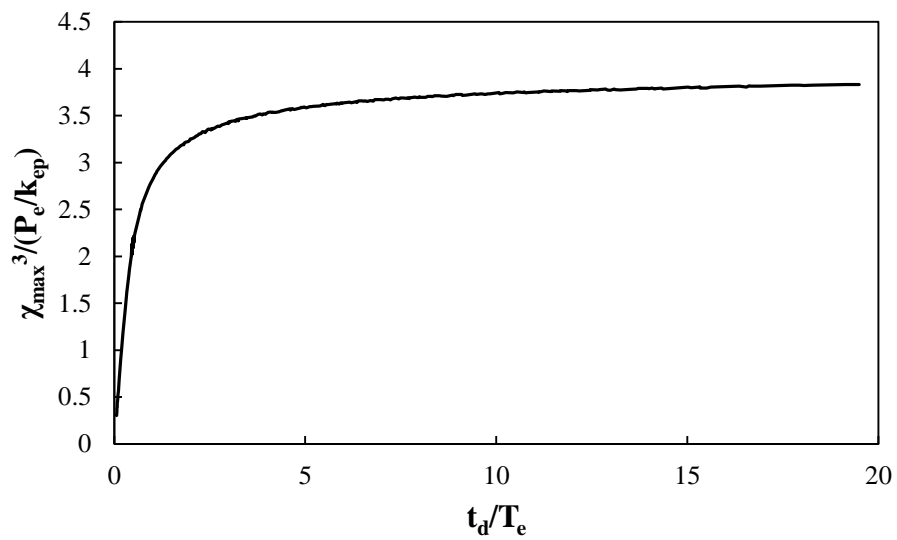


Fig. 6.6 Shock spectrum for SWS tank

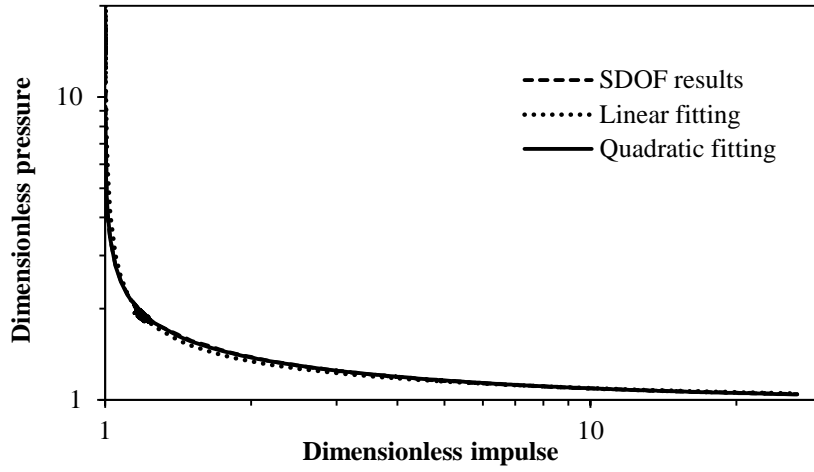


Fig. 6.7 Dimensionless P-I diagram for SWS tank

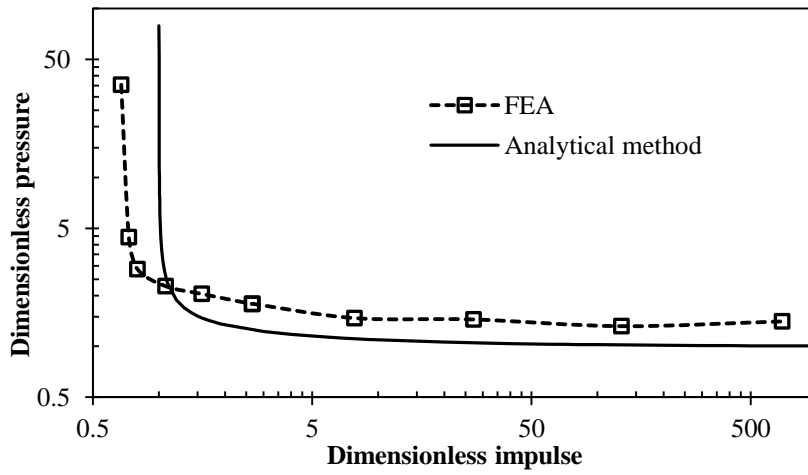


Fig. 6.8 Comparison of dimensionless P-I diagram

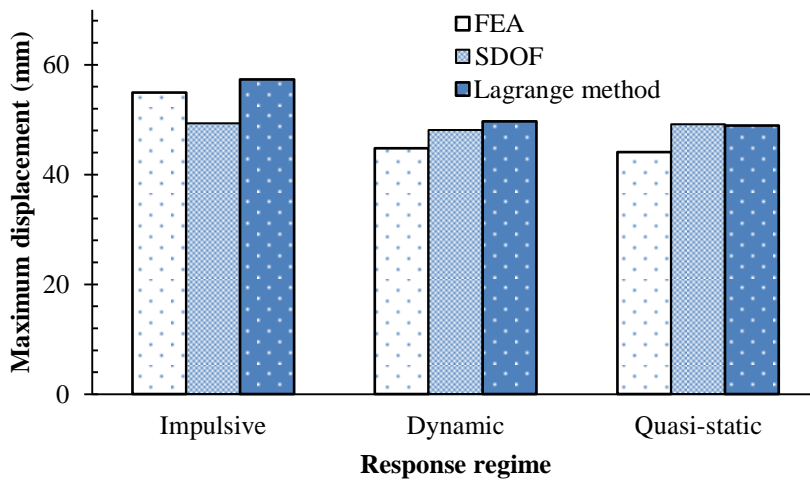


Fig. 6.9 Comparison of maximum displacement

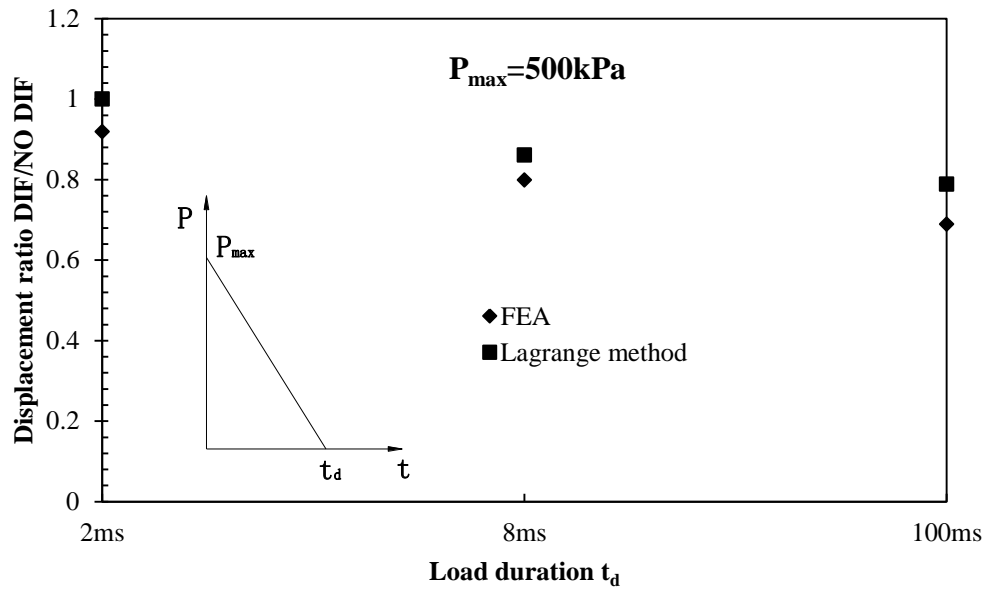


Fig. 6.10 Comparison of strain rate effect

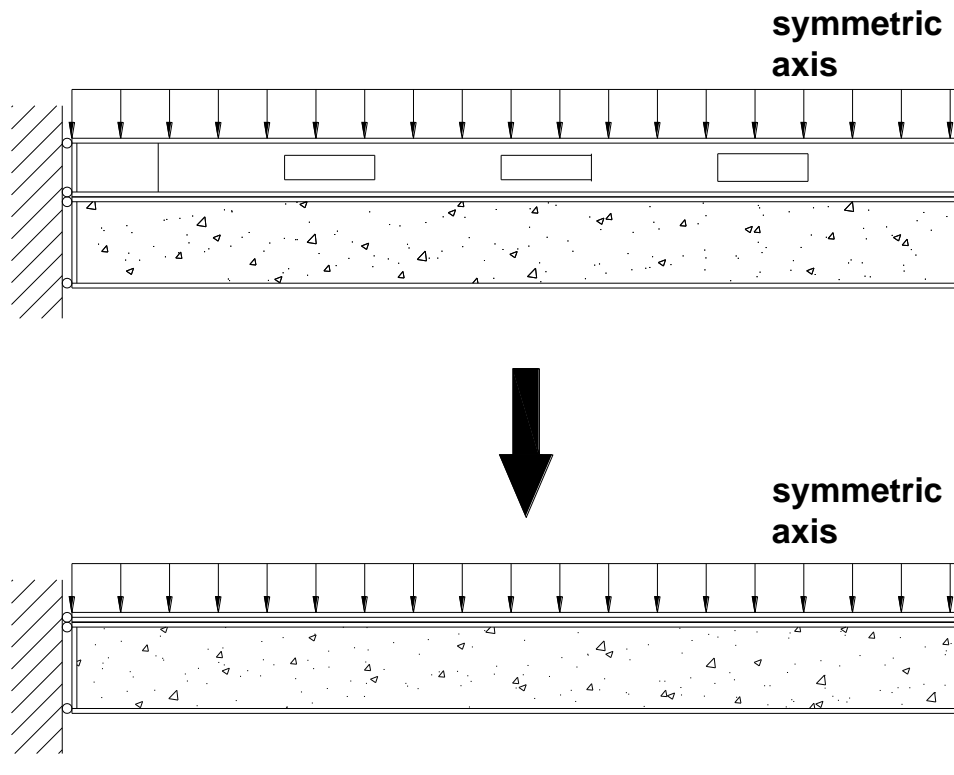


Fig. 6.11 Simplified half model for pin-pin supported SWS-SCS panel

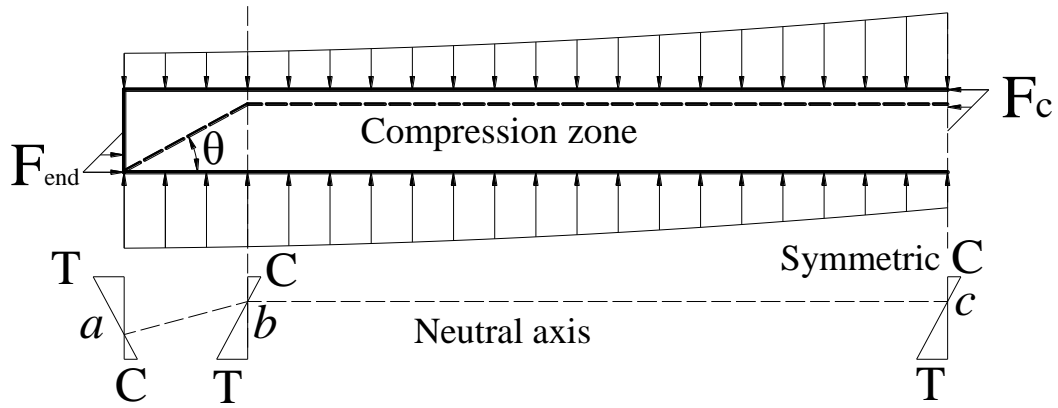


Fig. 6.12 Force distribution and neutral axis on the concrete core

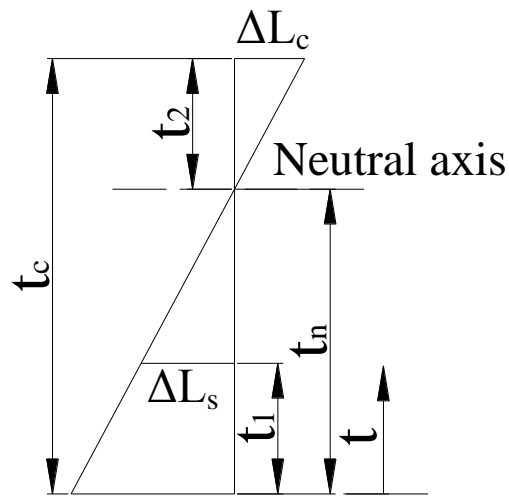


Fig. 6.13 Deformation profile across the concrete core depth

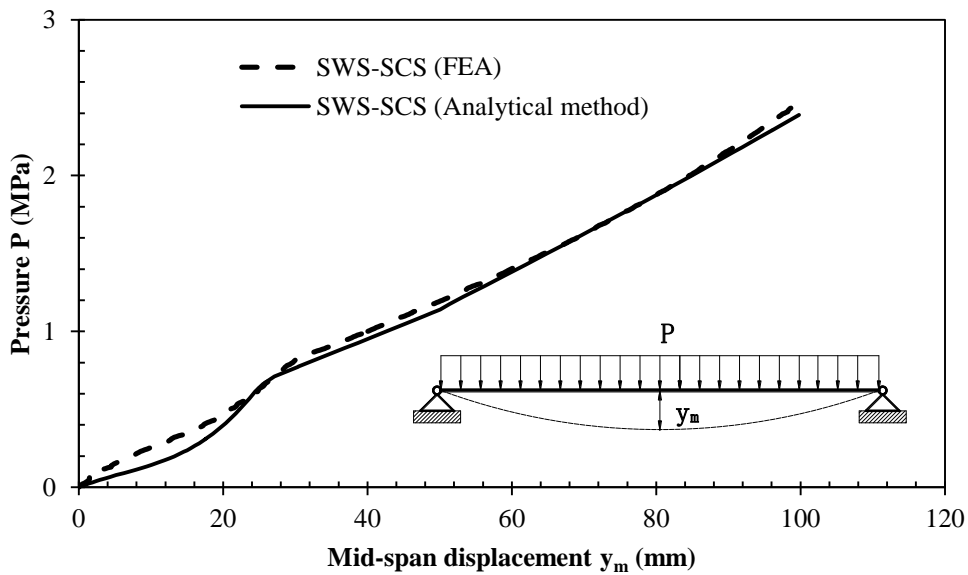


Fig. 6.14 Comparison of pressure–mid-span displacement curves between analytical method and FE analysis

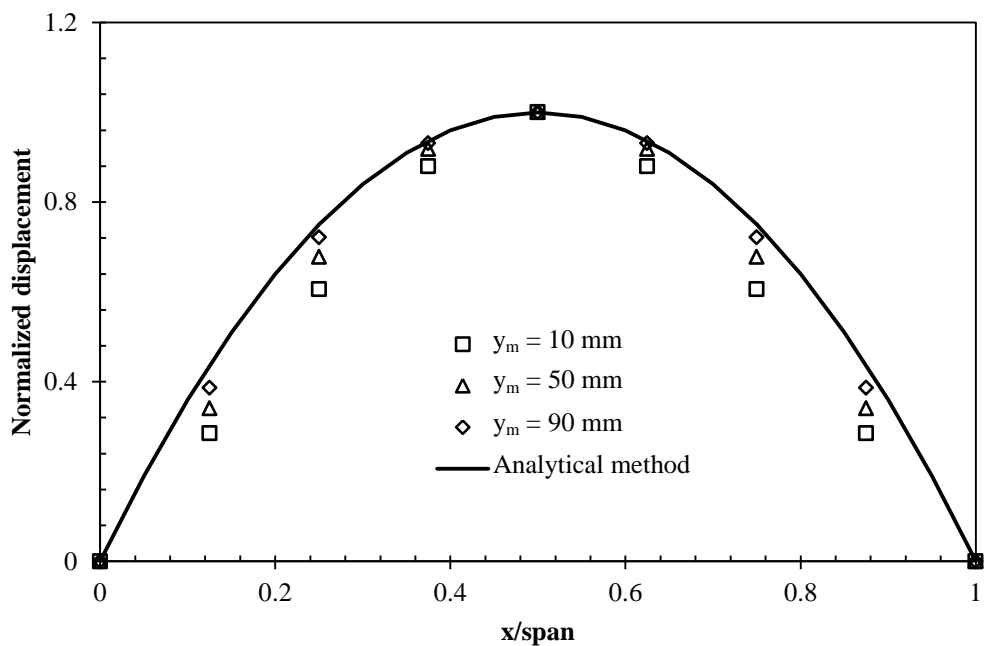


Fig. 6.15 Comparison of deflection shapes of SWS-SCS panel

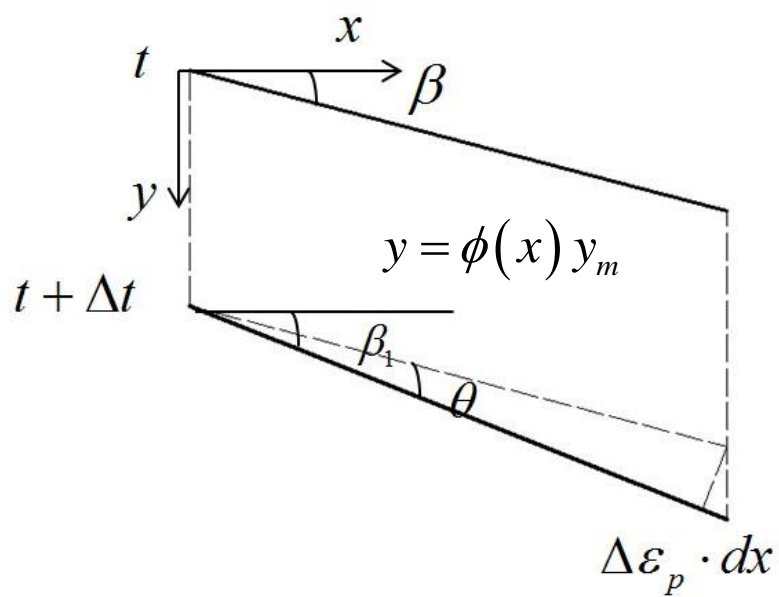


Fig. 6.16 Configuration of infinitesimal element along span

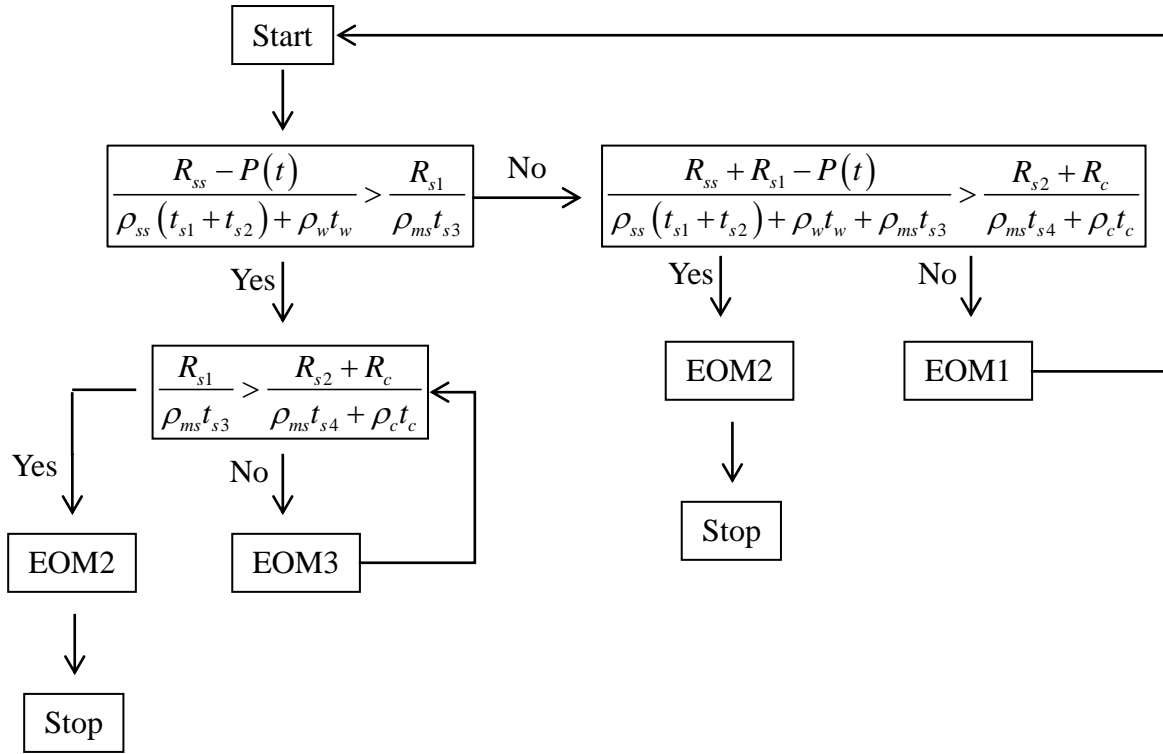


Fig. 6.17 Flow chart for determining equation of motion

Chapter 7 Conclusions and Recommendations

7.1 Review on Completed Research Work

A multi-functional water façade system has been developed to harness the solar energy, reduce solar heat penetration into building and at the same time acts as a protective envelope against blast loading. Experimental and/or numerical investigations were carried out to evaluate the energy savings potential and blast resistant performance of the water facade.

In the first part of this research, mock-ups of the proposed water façade system were designed and fabricated for field monitoring study to determine their thermal efficiency and space cooling load reduction by shielding the building from solar heat penetration. The first mock-up, which was a stainless steel water filled tank, was installed on the west wall of one of two identical rooms of a monitoring station at Tuas, Singapore. The thermal efficiency and space cooling load reduction of the water filled tank mock-up was evaluated in comparison to the control bare wall of the other identical room. After completing the monitoring of the water filled tank mock-up in reference to the bare wall, a second mock-up, denoted as water filled tank-sandwich panel with an additional layer of Steel-Concrete-Steel sandwich panel behind the water filled tank, was installed on the bare wall to compare the energy efficiency of the two mock-ups in terms of thermal efficiency and space cooling load.

The structural responses of the water façade systems under lateral pressure loading were experimentally, analytically and numerically investigated in the second part of this research. The resistance–deflection functions, deflection shapes and failure modes of empty steel tank and water filled tank as well as Steel-Concrete-Steel panels were determined in the test, which were then applied to develop the analytical models for the water façade systems under dynamic pressure loading. The combined configuration of the water filled tank-sandwich panel was not tested due to the limited lifting capacity of airbag, which was used to generate the pressure loading in the experimental study. Based on the test results, Finite Element models of the water tanks and Steel-Concrete-Steel panels under lateral pressure loading were established. The experimentally-verified Finite Element models were applied to investigate the effect of water on the static response of water filled tank and the load transfer mechanism between face plate and concrete core of Steel-Concrete-Steel panel.

The responses of the water façade systems under dynamic pressure loading were also experimentally, analytically and numerically studied in the third part of this research. Drop-weight projectile was dropped from a height onto the inflated high pressure airbag to generate the dynamic pressure loading. The measured deformation modes, impact force– and air pressure–time histories as well as displacement and strain responses of the water tank and Steel-Concrete-Steel panel specimens were analyzed to understand their behaviors under dynamic pressure loading. Equivalent SDOF method was adopted to predict the responses of the specimens. Besides this, the Finite Element models were also constructed to simulate the responses of the test specimens and the experimentally-verified Finite Element models were applied to predict the performance of the specimens under blast loading.

In the last part of this research, analytical methods for pin-pin supported water façade systems against blast loading were developed to facilitate the blast resistant design of such structures. The dimensionless P–I diagram was established for the water filled tank, which can be directly used to gauge the damage level under given blast load. Whereas, a similar dimensionless P–I diagram was not available for the water filled tank-sandwich panel, since the relationship between dimensionless pressure and impulse was not established due to the complex material behavior of concrete. Due to the deficiencies of SDOF method, which cannot capture the varying Dynamic Increase Factor and deflection shape, Lagrange Equation method with combined deflection shape function and varying Dynamic Increase Factor was proposed as an improved alternative for predicting the responses of water façade systems under blast loading.

7.2 Conclusions

Within the scopes of the experimental, numerical and analytical investigations reported in this thesis on the proposed water façade systems, the key conclusions are drawn as follow:

- i) Automated circulation of warm water at target temperature of 38 °C from the mock-ups of the water façade to storage followed by immediate replacement with cold water was demonstrated in the field monitoring study. The water filled tank-sandwich panel mock-up with additional Steel-Concrete-Steel layer was shown to be more effective in storing the solar energy as compared to the water filled tank mock-up due to the thermal mass of the Steel-Concrete-Steel layer.

The thermal efficiency of the two mock-ups were found to range from 12.87% to 40.62% for the selected two months of monitoring data with water filled tank-sandwich panel being higher under the same weather condition. Generally, the thermal efficiency increases with increasing solar energy.

- ii) The temperature of external west wall behind the water filled tank mock-up was reduced significantly as compared to the control bare wall, which indicates that the proposed water façade system is effective in minimizing solar heat penetration into the building to reduce the space cooling load. However, the shielded wall cooled down at a slower rate at night due to the heat barrier effect of the mock-up, and this adversely affected the total space cooling load reduction. In comparison, the water filled tank-sandwich panel mock-up with additional Steel-Concrete-Steel layer performed better than the water filled tank mock-up in reducing the space cooling load.
- iii) In the lateral pressure test, both of the empty steel tank and water filled tank failed under ductile flexure mode and the resistance of the water filled tank was 31% higher than the empty steel tank due to the effect of water in maintaining the section modulus and delaying the local buckling of the tank. It was also observed that the shear lag of strain in between the stiffener and side plate of the water filled tank was less obvious as compared to the empty steel tank due to addition of water.
- iv) The 50 mm thick Steel-Concrete-Steel panel failed in brittle shear mode with tearing of side and top plates as well as spalling of the grout core under the lateral lateral pressure loading. Such failure mode is undesirable and should be avoided by improving the shear resistance within the high shear stress zone near the

- support before the Steel-Concrete-Steel panel could be applied as an add-on layer layer to improve the blast resistance of the water filled tank.
- v) The lateral pressure resistance of all specimens was closely predicted by the analytical solution except for the water filled tank, since water effects in resisting local buckling of compression plate was not quantified. This quantification is out of the current research scope because there is no compression plate for the water filled tank with pin-pin supported boundary and this boundary was suggested for actual connections to improve its resistance by developing tensile membrane force. The analytical method to calculate the bending resistance of Steel-Concrete-Steel sandwich panel under lateral pressure load was proposed and the prediction was conservative in comparison to the test results.
- vi) Finite Element models for the specimens subjected to lateral pressure load were established and verified against the test data. With the verified Finite Element models, it was shown that water helped to transfer the lateral pressure loading from the top to the bottom plates of the water filled tank and maintain its section modulus. This led to the higher resistance of the water filled tank. It was also found that the lateral pressure resistance of the tanks and Steel-Concrete-Steel panels could be significantly increased by changing the boundary from pin-roller supported to pin-pin supported. Flexure or shear failure mode was observed for the pin-roller supported specimens, while tensile membrane failure was evident in the pin-pin supported specimens. The magnitude of improvement in lateral pressure resistance depended on the tensile strength of the face plate.
- vii) Both of the empty steel tank and water filled tank deformed in a flexural manner under the dynamic pressure loading. The pressure load was more globally

distributed in the water filled tank while load concentration near stiffeners and side plates were observed for the empty steel tank under the same impact. This and the mass effect could be attributed to the improved resistance of the water filled tank, which deformed less as compared to the empty tank, especially under higher impact load. As for the 50 mm thick Steel-Concrete-Steel panel, a combination of shear and flexure deformation was observed under the dynamic pressure loading while the 75 mm thick Steel-Concrete-Steel panel displayed significantly less maximum and permanent displacements due to its larger resistance and mass.

- viii) The maximum displacements of the specimens under dynamic pressure loading were reasonably approximated using the SDOF method, with differences within 16.0%. Other than this, Finite Element models of the test specimens were also established and verified against the test results. The verified models were used to investigate the performance of the same specimens under blast loading. It was shown that the deformation of the specimens was reduced with pin-pin supported boundary as compared to the pin-roller supported specimens. This is because of the mobilization of tensile membrane action which gives higher resistance to blast loading.
- ix) The dimensionless P-I diagram was established for predicting the damage level of the water filled tank under given blast loading. The diagram was built based on the SDOF method and its accuracy was verified with the Finite Element results.
- x) The Lagrange Equation method with combined deflection shape function and varying Dynamic Increase Factor was developed as a simplified analysis tool to predict the blast response of the water façade system under all response regimes.

The proposed method was shown to provide better predictions than the SDOF method.

Since the probability of blast threat on buildings is usually very low, it is of significance advantage to carry out the investigation on the multi-functional water façade system in order to maximize the benefits of adopting a blast-mitigating design while improving the building performance in terms of energy usage. Through this research, the energy efficiency and blast response of the proposed water façade systems have been investigated and discussed. The findings of this research would serve as a strong foundation to further develop and/or optimize the proposed water façade system for actual applications in the foreseeable future.

7.3 Recommendations for Future Studies

In order to attain a better insight into the proposed multi-functional blast resistant water façade systems, further studies are recommended in the following areas:

- i) Field temperature monitoring on the mock-ups of the water façade systems has been conducted to evaluate the energy efficiency of the proposed systems. Numerical analysis is thus recommended to further complement the test findings and parametric studies using experimentally-verified numerical models should be carried out to investigate the effects of absorptivity, plate thickness, frequency of draining, etc. in order to optimize the current design.
- ii) Since the analytical solution for predicting the effect of water on the resistance the SWS tank is yet available, studies on this aspect could be attempted to quantify the increase in resistance of SWS tank by water.

- iii) Actual field blast test would be a very valuable addition to existing research works that have been carried out on the proposed water façade system, particularly because similar test on confined water is not found in the literature.
- iv) For ease of maintenance of the water façade tanks, further research could be carried out to develop feasible and yet robust connection methods between the façade and supporting structures.

References

- Abramowicz W, Jones N (1986), Dynamic progressive buckling of circular and square tubes, *International Journal of Impact Engineering*, 4:243-270.
- Absil LHJ, Weerheijm J et al (2000), Water mitigation of explosion effects experimental parametric study, In: *Proceedings of the 29th Department of Defence Explosives Safety Seminar*. Orlando, FL, USA.
- Arora H, Hooper PA, Dear JP (2011), Dynamic response of full-scale sandwich composite structures subject to air-blast loading, *Composites: Part A*, 42: 1651-1662.
- Astarlioglu S, Krauthammer T, Morency D, Tran TP (2013), Behavior of reinforced concrete columns under combined effects of axial and blast-induced transverse loads, *Engineering Structures*, 55:26-34.
- ASCE (2010), *Design of blast-resistant buildings in petrochemical facilities*, Reston, Virginia: American Society of Civil Engineers.
- ASCE (2011), *Blast protection of buildings*, Reston, Virginia: American Society of Civil Engineers.
- Baer SC and Mingenbach W (2002), *Passive heating and cooling system*, Patent No. US 6,357,512.
- Baker WE (1973), *Explosions in air*, Austin, TX, USA: University of Texas Press.
- Baker WE, Cox PA, Westine PS, Kulesz JJ, Strehlow RA (1983), *Explosion and hazards and evaluation*, Amsterdam: Elsevier scientific publishing company.
- Baylot JT, Bullock B, Slawson TR, Woodson SC (2005), Blast response of lightly attached concrete masonry unit wall, *Journal of Structural Engineering*, 131(8): 1186-1193.
- Biggs JM (1964), *Introduction to structural dynamics*, New York: McGraw-Hill.
- Birnbaum NK, Fairlie GE, Francis NJ (1998), Numerical modelling of small scale water mitigation feasibility tests, In: *Proceedings of the 28th DoD Explosives Safety Seminar*. Orlando, FL, USA.
- Boh JW, Louca LA, Choo YS (2004), Strain rate effects on the response of stainless steel corrugated firewalls subjected to hydrocarbon explosions, *Journal of Constructional Steel Research*, 60:1-29.

Boh JW, Louca LA, Choo YS (2005), Energy absorbing passive impact barrier for profiled blastwalls. *International Journal of Impact Engineering*, 31: 976-995.

Carta G, Stochino F (2013), Theoretical models to predict the flexural failure of reinforced concrete beams under blast loads, *Engineering structures*, 49:306-15.

CEB (1993), CEB-FIP Model Code 1990, Trowbridge, Wiltshire, UK: Comite Euro-International du Beton, Redwood Books.

Chabin P, Pitiot F (1998), Blast wave mitigation by water. In: *Proceedings of the 28th Department of Defence Explosives Safety Seminar*, Orlando, FL, USA.

Chen WF (1982), *Plasticity in reinforced concrete*, McGraw Hill, New York.

Chen WF, Han D (1990), *Plasticity for structural engineers*, Elsevier, Amsterdam.

Chen W, Hao H (2014), Experimental investigations and numerical simulations of multi-arch double-layered panels under uniform impulsive loadings, *International Journal of Impact Engineering*, 63:140-157.

Cheng M, Hung KC, Chong OY (2005), Numerical study of water mitigation effects on blast wave, *Shock Waves*, 14(3):217-223.

Cheng M, Liu ZJ, Hung KC, Chong OY (2002), Blast wave mitigation by water wall, In: *Proceedings of the International Conference on Protection of Structures against Hazards*, Singapore.

Chong WK, Lam KY, Yeo KS, Liu GR, Chong OY (1999), A comparison of simulation's results with experiment on water mitigation of an explosions, *Shock and Vibration*, 6, 73-80.

Chow TT, Chan ALS, Fong KF, Lin Z et al. (2009), Annual performance of building-integrated photovoltaic/water-heating system for warm climate application, *Applied Energy*, 86(5):689-96.

Chow TT, He W, Chan ALS, Fong KF et al. (2008), Computer modeling and experimental validation of a building-integrated photovoltaic and water heating system, *Applied Thermal Engineering*, 28(11-12):1356-64.

Chow TT, He W and Ji J (2007), An experimental study of façade-integrated photovoltaic/water heating system, *Applied Thermal Engineering*, 27:37-45.

Clubley SK (2014), Non-linear long duration blast loading of cylindrical shell structures, *Engineering Structures*, 59:113-126.

Cormie D, Mays GC, Smith PD (2009), *Blast effects on buildings*, London: Thomas Telford.

Crawford JE, Wu Y, Magallanes JM, Lan S (2012), *Modeling of concrete materials under extreme loads*, *Advances in Protective Structures Research*, Taylor & Francis Group, London.

-
- Davidson JS, Fisher JW, Hammons MI, Porter JR, Dinan RJ (2005), Failure mechanisms of polymer-reinforced concrete masonry walls subjected to blast, *Journal of Structural Engineering*, 131(8): 1194-1205.
- Derakhshan H, Griffith MC, Ingham JM (2013), Airbag testing of multi-leaf unreinforced masonry walls subjected to one-way bending, *Engineering Structures*, 57: 512-522.
- Dragos J, Wu C (2013), A new general approach to derive normalised pressure impulse curves, *International Journal of Impact Engineering*, 62:1-12.
- Egan B, McCarthy CT, McCarthy MA, Gray PJ, Frizzell RM (2012), Modelling of a single-bolt countersunk composite joint using implicit and explicit finite element analysis, *Computational Materials Sciences*, 64: 203-208.
- Eicker U (2003), *Solar technologies for buildings*, West Sussex: John Wiley&Sons.
- Eurocode 2 (2004), *Design of concrete structures*, EN 1992-1-1.
- Eurocode 3 (2005), *Design of steel structures-Part 1-1: General rules and rules for buildings*, BS EN 1993-1-1.
- Eurocode 3 (2006), *Design of steel structures-Part 1-5: Plated structural elements*, BS EN 1993-1-5.
- Eurocode 4 (2004), *Design of composite steel and concrete structures-Part 1.1: General rules and rules for buildings*, BS EN 1994-1-1.
- Fallah AS and Louca LA (2006), Pressure-impulse diagrams for elastic-plastic-hardening and softening single-degree-of-freedom models subjected to blast loading, *International Journal of Impact Engineering*, 34: 823-42.
- Foglar M, Kovar M (2013), Conclusions from experimental testing of blast resistance of FRC and RC bridge decks, *International Journal of Impact Engineering*, 59: 18-28.
- Foundoukos N (2005), *Behavior and design of steel-concrete-steel sandwich construction*, PhD thesis, Department of Civil and Environmental Engineering, University of London.
- Grote DL, Park SW, Zhou M (2001), Dynamic behavior of concrete at high strain rate and pressures: I. experimental characterization, *International Journal of Impact Engineering*, 25: 869-886.
- Gurtman GA, Kirsch JW, Hastings CR (1971), Analytical equation of state for water compressed to 300 Kbar, *Journal of Applied Physics*, 42(2): 851-857.
- Hallissy G, Higbie WG and Fyfe ER (2005), *Blast Resistant Prefabricated Wall Unit*, Patent No. US 2005/0144900 A1, US.
- Hallquist JO (2006), *LS-DYNA theory manual*, Livermore, California: Livermore Software Technology Corporation, Livermore, California.

Hallquist JO (2012), LS-DYNA keyword user's manual, Livermore, California: Livermore Software Technology Corporation, Livermore, California.

Hertel ES (1992), The CTH data interface for Equation-of-State and constitutive model parameters, Sandia Report SAND92-1297.

Hyde D (1991), Conventional Weapons program (ConWep), Vicksburg, MS, USA: US Army Waterways Experimental Station.

Ishiguro S (2007), Experiments and analyses of fracture properties of grouting mortars, In: Proceedings of the 6th international conference on fracture mechanics of concrete and concrete structures.

Joachim CE, Lunderman CV (1997), Blast suppression with water-results of small-scale test program, In: Proceedings of the 15th International Symposium on the Military Aspects of Blast and Shock, Banff, Alberta, Canada.

John R, Shah SP (1987), Effects of High Strength and Rate of Loading on Fracture Parameters of Concrete, Proceedings of SEMRILEM International Conference on Fracture of Concrete and Rock, Society for Experimental Mechanics, Bethel.

Jones N (1988), Structural impact, New York: Cambridge University Press.

Jones J, Wu C, Oehlers DJ, Whittaker AS, Sun W, Marks S, Coppola R (2009), Finite difference analysis of simply supported RC slabs for blast loadings, Engineering structures, 31:2825-32.

Kang KK (2012), Blast resistance of steel-concrete composite structures, PhD thesis, National University of Singapore.

Keenan WA, Wager PC (1992), Mitigation of confined explosion effects by placing water in proximity of explosions, In: Proceedings of the 25th DoD Explosives Safety Seminar, Anaheim, CA, USA.

Kormeling HA et al. (1980), Experiments on Concrete and Single and Repeated Uniaxial Impact Tensile Loads, Report No. 50-80-3, Stevin Laboratory, Delft University of Technology, 1980.

Krauthammer T, Astarlioglu S, Blasko J, Soh TB and Ng PH (2008), Pressure-impulse diagrams for the behaviour assessment of structural components, International journal of impact engineering, 35: 771-83.

Krauthammer T, Bazeos N, Holmquist TJ (1986), Modified SDOF analysis of box-type structures, Journal of Structural Engineering , 112: 726-744.

Lacroix DN, Doudak G, EI-Domiaty K (2014), Retrofit options for light-frame wood stud walls subjected to blast loading, Journal of Structural Engineering, 140(4): 04013104.

Lan S, Lok TS, Heng L (2005), Composite structural panels subjected to explosive loading, Construction and Building Materials, 19: 387-395.

-
- Langdon GS, Schleyer GK (2005a), Inelastic deformation and failure of profiled stainless steel blast wall panels, Part I: experimental investigations, *International Journal of Impact Engineering*, 31:341-369.
- Langdon GS, Schleyer GK (2005b), Inelastic deformation and failure of profiled stainless steel blast wall panels, Part II: analytical modelling considerations, *International Journal of Impact Engineering*, 31:371-399.
- Lei M, Barnett S et al. (2014), Numerical simulation of ultra high performance fibre reinforced concrete panel subjected to blast loading, *International Journal of Impact Engineering*, 64: 91-100.
- Lee CH, Liu TJ, Lee DJ (2005), Passive energy saving system for a building, Patent No. US 2005/0103337 A1, Taiwan.
- Li QM, Meng H (2002a), Pressure-impulse diagram for blast loads based on dimensional analysis and single-degree-of-freedom mode, *Journal of engineering mechanics*, 1(87):87-92.
- Li QM, Meng H (2002b), Pulse loading shape effects on pressure-impulse diagram of an elastic-plastic, single-degree-of-freedom structural model, *International Journal of Mechanical Sciences*, 44:1985-1998.
- Liew JYR, Wang TY, Sohel KMA (2008), Tensile capacity of short anchor bolts and welded sandwich composite structures, US Provisional Patent 61/047, 130.
- Liew JYR, Sohel KMA (2009), Lightweight steel-concrete-steel sandwich system with J-hook connectors, *Engineering Structures*, 31(5): 1166-1178.
- Liew JYR, Wang TY (2011), Novel Steel-Concrete-Steel sandwich composite plates subject to impact and blast load, *Advances in Structural Engineering*, 14(4), 673-687.
- Lin X, Zhang YX, Hazell PJ (2014), Modelling the response of reinforced concrete panels under blast loading, *Materials and Design*, 56: 620-628.
- Magallanes JM, Wu Y, Malvar LJ, Crawford JE (2010), Recent improvements to release III of the K&C concrete model. In: the 11th international LS-DYNA users conference.
- Malek N, Machida A, Mutsuyoshi H, Makabe T (1992), Steel-concrete sandwich members without shear reinforcement, *Transactions of Japan Concrete Institute*, 15(2): 1279-1284.
- Maloney T (1981), Environmentally driven heating and cooling system, Patent No. US 4,257,477, US.
- Malo KA (2001), Water pressure chamber for static testing of panels, *International Journal of Mechanical Sciences*, 43:1209-1228.
- Malvar LJ, Crawford JE, Wesevich JW, Simons D (1997), A plasticity concrete material model for DYNA3D, *International Journal of Impact Engineering*, 19:

847-873.

Malvar LJ, Morrill KB, Crawford JE (2004), Numerical modeling of concrete confined by fiber-reinforced composites, *Journal of composites for construction*, 8(4): 315-322.

Malvar LJ, Tancreto JE (1998), Analytical and test results for water mitigation of explosion effects, In: *Proceedings of the 28th DoD Explosives Safety Seminar*, Orlando, FL, USA.

Mao L, Barnett S, Begg D, Schleyer G, Wight G (2014), Numerical simulation of ultra high performance fibre reinforced concrete panel subjected to blast loading, *International Journal of Impact Engineering*, 64:91-100.

Marais ST, Tait RB, Cloete TJ, Nurick GN (2004), Material testing at high strain rate using the split Hopkinson pressure bar, *Latin American Journal of Solids and Structures*, 1: 319-339.

Mayrhofer (2002), Reinforced masonry walls under blast loading, *International Journal of Mechanical Sciences*, 44:1067-1080.

McVay MK (1988), Spall Damage of Concrete Structures, Technical Report No. SL-88-22, US Army Engineer Waterways Experiment Station, Vicksburg.

Mellinger FM, Birkimer DL (1966), Measurements of stress and strain on cylindrical test specimens of rock and concrete under impact loading, Technical Report No. 4-46, US Army Corps of Engineers, Ohio River Division Laboratories, Cincinnati.

Morison CM (2006), Dynamic response of walls and slabs by single-degree-of-freedom analysis-a critical review and revision, *International Journal of Impact Engineering*, 32: 1214-1247.

Mostaghel N (2003), Blast load simulation system, US Patent US6536258 B1, US Patent.

Mutalib AA and Hao H (2011), Development of P-I diagrams for FRP strengthened RC columns, *International journal of impact engineering*, 38: 290-304.

Naito CJ, Wheaton KP (2006), Blast assessment of load-bearing reinforced concrete shear walls, *Practice periodical on structural design and construction*, 11(2), 112-121.

Nassr AA, Razaqpur AG, Tait MJ, Campidelli M, Foo S (2012), Single and multi degree of freedom analysis of steel beams under blast loading, *Nuclear Engineering and Design*, 242(1):63-77.

Nanayakkara L (2004), Blast Protective Barrier System, Patent No. US 2004/0261332 A1, US.

Ngo T, Mendis P, Krauthammer T (2007), Behavior of ultrahigh-strength prestressed concrete panels subjected to blast loading, *Journal of Structural Engineering*, 133(11):1582-1590.

Oduyemi TOS, Wright HD (1989), An experimental investigation into the behavior of double skin sandwich beams, *Journal of Constructional Steel Research*, 14(3):197-220.

Oh BH (1987), Behavior of concrete under dynamic tensile loads, *ACI Materials Journal*, 84(1):8-13.

Patoary MKH (2004), Strengthening of masonry walls against out-of-plane loads using FRP systems, PhD thesis, National University of Singapore.

Remennikov AM, Liew JYR, Kong SY, Kang KW (2009), Simulation of impulsive loading on columns using an inflatable airbag technique, In: *Proceedings of the 8th International Conference on Shock & Impact Loads on Structures*, Adelaide, Australia.

Rigby SE, Tyas A, Bennett T (2014), Elastic-plastic response of plates subjected to cleared blast loads, *International Journal of Impact Engineering*, 66:37-47.

Ross CA, Thompson PY, Tedesco JW (1989), Split-Hopkinson pressure-bar tests on concrete and mortar in tension and compression, *ACI Material Journal*, 86(5): 475-481.

Ross CA, Jerome DM, Tedesco JW, Hughes ML (1996), Moisture and strain rate effects on concrete strength, *ACI Materials Journal*, 93(3):293-300.

Rust W, Schweizerhof (2003), Finite element limit load analysis of thin-walled structures by ANSYS (implicit), LS-DYNA (explicit) and in combination, *Thin-Walled Structures*, 14: 227-244.

Schleyer GK, Lowak MJ, Polcyn MA, Langdo GS (2007), Experimental investigation of blast wall panels under shock pressure loading, *International Journal of Impact Engineering*, 34:1095-1118.

Shi Y, Hao H, Li ZX (2008), Numerical derivation of pressure-impulse diagrams for prediction of RC column damage to blast loads, *International journal of impact engineering*, 35: 1213-27.

Shin YS, Lee M et al. (1998), Modelling mitigation effects of watershield on shock waves, *Shock and Vibration*, 5: 225-234.

Silva PF, Lu B (2009), Blast resistance capacity of reinforced concrete slabs, *Journal of structural engineering*, 135(6): 708-716.

Smith PD, Hetherington JG (1994), *Blast and ballistic loading of structures*, Butterworth-Heinemann, Oxford.

Smith SJ, McCann DM, Kamara ME (2009), *Blast resistant design guide for reinforced concrete structures*, Skokie, IL: Portland Cement Association.

Swartz A J, Kulpa G, Elliott A C (2009), *Energy Absorbing Blast Wall for Building Structure*, Patent No. US 2009/0158679 A1, US.

Symonds PS (1967), *Survey of methods of analysis for plastic deformation of*

structures under dynamic loading, Brown University, Division of Engineering Report BU/NSRDC/1-67.

Tabatabaei ZS, Volz JF et al. (2013), Experimental and numerical analysis of long carbon fiber reinforced concrete panels exposed to blast loading, *International Journal of Impact Engineering*, 57: 70-80.

Tan K. H., Patoary M. K. H. (2009), Blast resistance of FRP-strengthened masonry walls. I: approximate analysis and field explosion tests, *Journal of Composites for Construction*, 13(5): 422-430.

Tanapornraweekit G, Haritos N, Mendis P (2011), Behavior of FRP-RC slabs under multiple independent air blasts, *Journal of Performance of Constructed Facilities*, 25:433-440.

Urgessa G. S., Maji A. K. (2010), Dynamic response of retrofitted masonry walls for blast loading, *Journal of Engineering Mechanics*, 136(7): 858-864.

UFC 3-340-02 (2008), Structures to resist the effects of accidental explosions, Washington, DC: US Department of Army, Navy and the Air Force.

Vretblad B, Eriksson S (1994), Blast mitigation in confined spaces by energy absorbing materials, In: *Proceedings of the 26th DoD Explosives Safety Seminar*, Miami, FL, USA.

Wang M, Hao H, Ding Y, Li ZX. (2009), Prediction of fragment size and ejection distance of masonry wall under blast load using homogenized masonry material properties, *International Journal of Impact Engineering*, 36: 808-820.

Wei X., Stewart M. G. (2010), Model validation and parametric study on the blast response of unreinforced brick masonry walls, *International Journal of Impact Engineering*, 37: 1150-1159.

Whisler D, Kim H (2014), A non-explosive test method for generating wide area dynamic blast-type pressure pulse loading on armored panels, *International Journal of Impact Engineering*, 68: 28-40.

White FM (1986), *Fluid mechanics*, McGraw-Hill.

Wu C, Oehlers DJ, Rebentrost M, Leach J, Whittaker AS (2009), Blast testing of ultra-high performance fibre and FRP-retrofitted concrete slabs, *Engineering Structures*, 31:2060-2069.

Xu K, Lu Y (2006), Numerical simulation study of spallation in reinforced concrete plates subjected to blast loading, *Computers and Structures*, 84: 431-438.

Yan JB, Liew JYR, Zhang MH, Sohel KMA (2014), Experimental and analytical study on ultimate strength behavior of steel-concrete-steel sandwich composite beam structures, *Materials and Structures*, In press.

Yun SH, Jeon HK, Park T (2013), Parallel blast simulation of nonlinear dynamics for

References

concrete retrofitted with steel plate using multi-solver coupling, *International Journal of Impact Engineering*, 60: 10-23.

Zhou XQ, Kuznetsov VA, Hao H, Waschl J (2008), Numerical prediction of concrete slab response to blast loading, *International Journal of Impact Engineering*, 35: 1186-1200.

References

Appendix A: Figures of Mock-ups for Monitoring Test

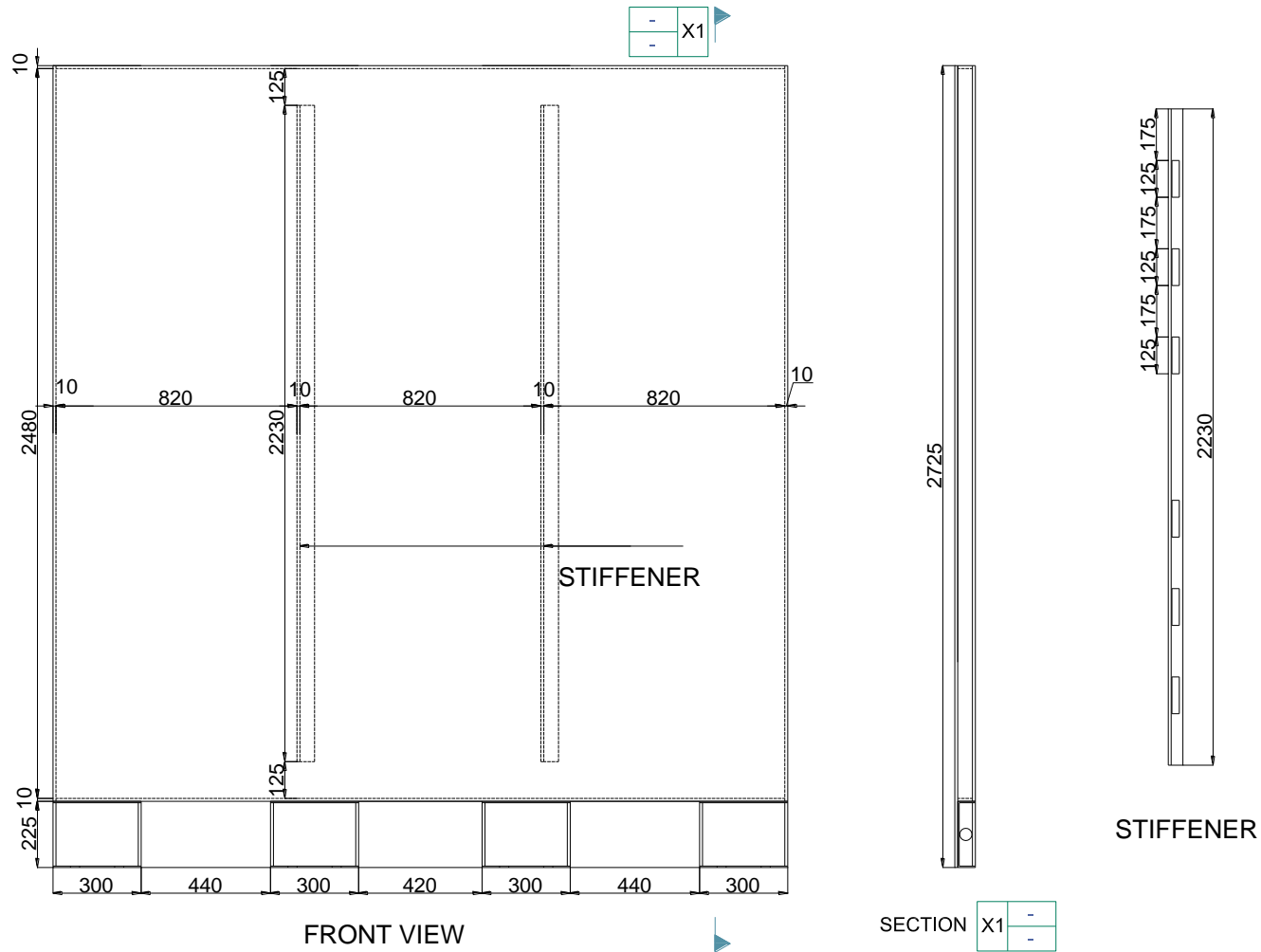


Fig. A.1 SWS tank, in mm

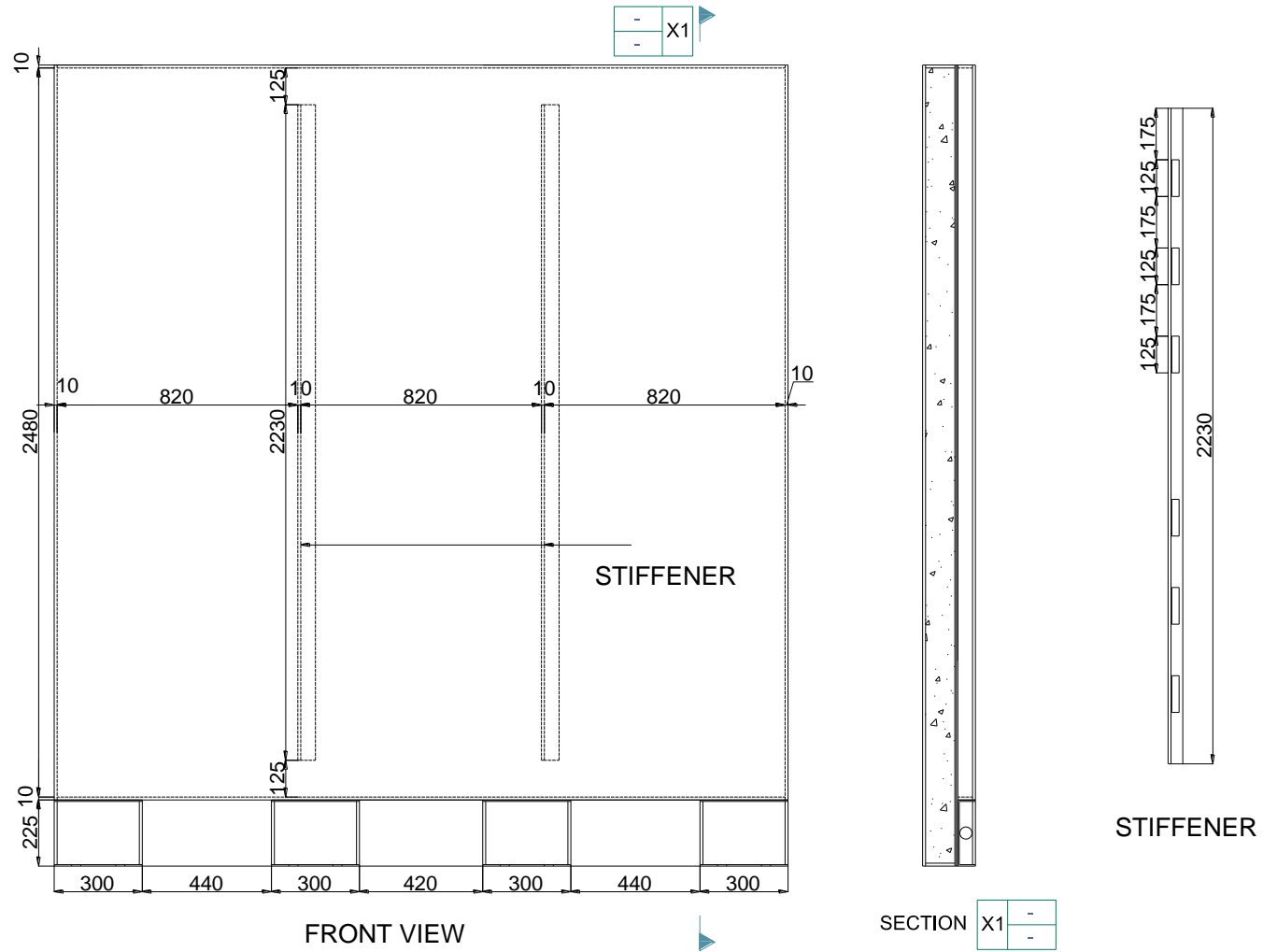


Fig. A.2 SWS-SCS, in mm

Appendix B: Contact Area Approximation

To verify the linear approximation between air pressure and contact area in the drop-weight impact test, the FE model including the SES tank, airbag, force transfer plate and projectile is established, as shown in Fig. B.1. The mass and impact velocity of projectile are 550 kg and 5.5 m/s. The initial air pressure before impact is 0.04 MPa, which is same with the test.

The actual applied force and the calculated applied force by multiplying the air pressure and contact area is compared in Fig. B.2. The actual applied force is the contact force between the airbag and specimen in the FE model. The contact area is obtained by linearly interpolated with air pressure (the same method used in the test as Section 5.6.3). It can be seen that the load–time history by multiplying the linearly interpolated contact area with air pressure is very close to the actual applied force, which verify the accuracy of using linearly interpolation between air pressure and contact area to obtain the contact area–time history in the test.

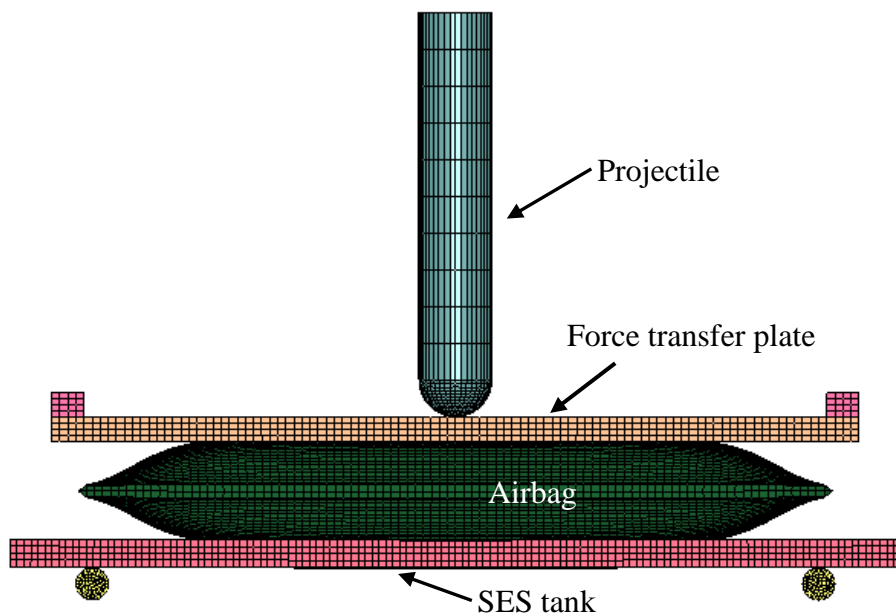


Fig. B.1 FE model of drop-weight impact test

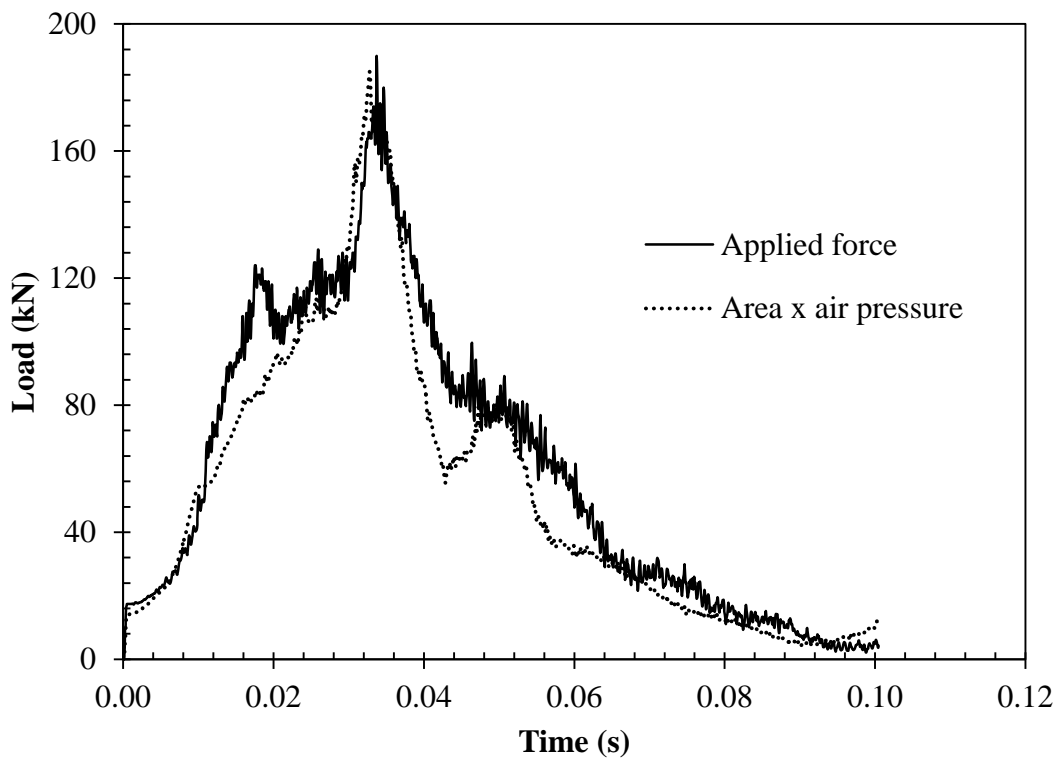


Fig. B.2 Comparison of applied force–time history

Publications

Wang Y, Liew JYR, Lee SC (2015), Theoretical models for axially restrained steel-concrete-steel sandwich panels under blast loading, *International Journal of Impact Engineering*, 76: 221-231.

Wang Y, Liew JYR, Lee SC (2014), Performance of water tank under static and dynamic pressure loads, 6th International Conference on Protection of Structures against Hazards, Tianjin, China.

Wang Y, Liew JYR, Lee SC (2013), Theoretical models for axially-restrained steel-concrete-steel sandwich panels under blast loads, 10th International Conference on Shock & Impact loads on Structures, Singapore.

Wang Y, Liew JYR, Lee SC (2013), High velocity airbag impact test on water tank, 26th KKHTCNN Symposium on Civil Engineering, Singapore.

Zheng M, Lee SC, Wang Y, Liew JYR (2013), Heat transfer analysis of building wall system with water tank attached, The Pacific Structural Conference, Singapore.

Wang Y, Liew JYR, Lee SC (2012), P-I diagram for one-way supported structures considering membrane effect, 5th International Conference on protection of structures against hazards, Singapore.

Wang Y, Liew JYR, Lee SC (2012), Development of P-I diagram for one-way supported structure considering tensile membrane effect, 25th KKHTCNN Symposium on Civil Engineering, South Korea.

Wang Y, Liew JYR, Lee SC (2012), Development of P-I diagrams for stainless steel water tank subjected to blast loading, 10th International Conference on Advances in Steel Concrete Composite and Hybrid Structures, Singapore.